

Proceedings of the Workshop on

**SPECIATION, TECHNIQUES
AND FACILITIES FOR RADIOACTIVE
MATERIALS AT SYNCHROTRON
LIGHT SOURCES**

*4-6 October 1998
Grenoble, France*

co-sponsored by

European Commission
Forschungszentrum Rossendorf
European Synchrotron Radiation Facility
Commissariat à l'Énergie Atomique
US Department of Energy

NUCLEAR ENERGY AGENCY
ORGANISATION FOR ECONOMIC CO-OPERATION AND DEVELOPMENT

ORGANISATION FOR ECONOMIC CO-OPERATION AND DEVELOPMENT

Pursuant to Article 1 of the Convention signed in Paris on 14th December 1960, and which came into force on 30th September 1961, the Organisation for Economic Co-operation and Development (OECD) shall promote policies designed:

- to achieve the highest sustainable economic growth and employment and a rising standard of living in Member countries, while maintaining financial stability, and thus to contribute to the development of the world economy;
- to contribute to sound economic expansion in Member as well as non-member countries in the process of economic development; and
- to contribute to the expansion of world trade on a multilateral, non-discriminatory basis in accordance with international obligations.

The original Member countries of the OECD are Austria, Belgium, Canada, Denmark, France, Germany, Greece, Iceland, Ireland, Italy, Luxembourg, the Netherlands, Norway, Portugal, Spain, Sweden, Switzerland, Turkey, the United Kingdom and the United States. The following countries became Members subsequently through accession at the dates indicated hereafter; Japan (28th April 1964), Finland (28th January 1969), Australia (7th June 1971), New Zealand (29th May 1973), Mexico (18th May 1994), the Czech Republic (21st December 1995), Hungary (7th May 1996), Poland (22nd November 1996) and the Republic of Korea (12th December 1996). The Commission of the European Communities takes part in the work of the OECD (Article 13 of the OECD Convention).

NUCLEAR ENERGY AGENCY

The OECD Nuclear Energy Agency (NEA) was established on 1st February 1958 under the name of OEEC European Nuclear Energy Agency. It received its present designation on 20th April 1972, when Japan became its first non-European full Member. NEA membership today consists of all OECD Member countries, except New Zealand and Poland. The Commission of the European Communities takes part in the work of the Agency.

The primary objective of the NEA is to promote co-operation among the governments of its participating countries in furthering the development of nuclear power as a safe, environmentally acceptable and economic energy source.

This is achieved by:

- *encouraging harmonization of national regulatory policies and practices, with particular reference to the safety of nuclear installations, protection of man against ionising radiation and preservation of the environment, radioactive waste management, and nuclear third party liability and insurance;*
- *assessing the contribution of nuclear power to the overall energy supply by keeping under review the technical and economic aspects of nuclear power growth and forecasting demand and supply for the different phases of the nuclear fuel cycle;*
- *developing exchanges of scientific and technical information particularly through participation in common services;*
- *setting up international research and development programmes and joint undertakings.*

In these and related tasks, the NEA works in close collaboration with the International Atomic Energy Agency in Vienna, with which it has concluded a Co-operation Agreement, as well as with other international organisations in the nuclear field.

© OECD 1999

Permission to reproduce a portion of this work for non-commercial purposes or classroom use should be obtained through the Centre français d'exploitation du droit de copie (CCF), 20, rue des Grands-Augustins, 75006 Paris, France, Tel. (33-1) 44 07 47 70, Fax (33-1) 46 34 67 19, for every country except the United States. In the United States permission should be obtained through the Copyright Clearance Center, Customer Service, (508)750-8400, 222 Rosewood Drive, Danvers, MA 01923, USA, or CCC Online: <http://www.copyright.com/>. All other applications for permission to reproduce or translate all or part of this book should be made to OECD Publications, 2, rue André-Pascal, 75775 Paris Cedex 16, France.

FOREWORD

X-ray spectroscopic and scattering techniques are powerful tools for providing molecular scale information on radionuclides in solution, and in crystalline and amorphous solids. They permit the characterisation of species that are important for chemical processing, waste management and materials identification and are a key link to laboratory-based techniques. Intense monochromatic X-ray photons, which are necessary for such experiments, are available only at synchrotron light sources. In order to study processes utilising radioactive materials with modern X-ray techniques, special procedures and facilities are necessary. At present a few synchrotron laboratories and users have set up procedures and facilities for the use of radioactive materials. Other synchrotron laboratories and user groups are constructing or planning such facilities.

For this reason, the first Euroconference and NEA Workshop on Speciation, Techniques and Facilities for Radioactive Materials at Synchrotron Light Sources, Actinide-XAS-98, was held from 4-6 October 1998 in Grenoble, France, with close to 100 participants from 15 countries (see Annex 1). It was hosted by the European Synchrotron Radiation Facility (ESRF), and organised mainly by the Forschungszentrum Rossendorf, Germany. The European Commission, the CEA (France) and the US DOE co-sponsored the meeting. There were 31 oral presentations and 22 posters covering:

1. Introduction to synchrotron radiation techniques, such as X-ray absorption spectroscopy, X-ray scattering, and X-ray imaging.
2. Results in the field of radionuclide/actinide chemistry and physics obtained by synchrotron radiation:
 - Radionuclides in the environment.
 - Nuclear waste management.
 - Separation technology.
 - General actinide chemistry.
 - Radiopharmaceutical chemistry.
 - Electronic and magnetic properties.
3. Status reports on current and future actinide experimental stations at synchrotron light sources.

These proceedings contain the abstracts and some of the full papers presented at the meeting. The editors, Dr. Edelstein, Dr. Nitsche and Dr. Reich, and other anonymous referees reviewed the full papers. The organising committee (see Annex 2) wishes to acknowledge and thank these reviewers.

TABLE OF CONTENTS

FOREWORD	3
EXECUTIVE SUMMARY	11
Session I: INTRODUCTION TO SYNCHROTRON RADIATION TECHNIQUES	13
<i>Chairs: N.M. Edelstein, C. Madic, S. Tachimori, D.C. Koningsberger</i>	
<i>H. Nitsche, T. Reich, C. Hennig, A. Roßberg, G. Geipel, M.A. Denecke</i>	
<i>L. Baraniak, P. Panak, A. Abraham, B. Mack, S. Selenska-Pobell, G. Bernhard</i>	
Application of Synchrotron Radiation Techniques to Radionuclide Studies.....	15
<i>D.C. Koningsberger</i>	
XAFS Spectroscopy: A Powerful Tool to Investigate Local Structure and Electronic Properties.....	29
<i>J. Goulon</i>	
Experimental Aspects of X-Ray Absorption Spectroscopy	31
<i>A. Filipponi</i>	
Theoretical Framework for Data and Error Analysis as Applied to X-Ray Absorption Spectroscopy	33
<i>V.I. Nefedov</i>	
Introduction to X-Ray Photoelectron Spectroscopy: A Complementary Technique to X-Ray Absorption Spectroscopy	35
<i>D.K. Shuh</i>	
Introduction to Actinide Investigations with X-Ray Techniques Below 2 keV	37
<i>W. Matz</i>	
Introduction to X-Ray Diffraction at Synchrotron Light Sources	39
<i>G.H. Lander</i>	
X-Ray Scattering Applied to Magnetism of the Actinides	51
<i>U. Wahlgren, B. Schimmelpfennig, L. Maron, V. Vallet, I. Grenthe, O. Gropen</i>	
Molecular Modelling of Actinide Complexes	53
Session II: APPLICATIONS OF SYNCHROTRON TECHNIQUES	67
<i>Chairs: P.G. Allen, F.R. Livens, A.M. Scheidegger, N. Baclet, D.K. Smith</i>	
<i>C. Madic, C. Den Auwer, R. Guillaumont</i>	
Application of X-Ray Absorption Spectroscopy (XAS) to Actinide Solution Chemistry.....	69

<i>P.M. Bertsch, D.B. Hunter, M. Duff</i> Micro/Spatially Resolved XRF and XAFS for the In Situ Interrogation of Radionuclide Distribution and Speciation in Environmental Samples	81
<i>T. Reich, H. Moll, M.A. Denecke, C. Hennig, G. Geipel, G. Bernhard, H. Nitsche, P.G. Allen, J.J. Bucher, N.M. Edelstein, D.K. Shuh</i> EXAFS Studies of Uranium(VI) Sorption on Mineral Surfaces.....	83
<i>D.K. Veirs</i> X-Ray Absorption Spectroscopy Studies of Plutonium Nitrate Species in Solution and on Ion Exchange Resins	93
<i>F. David, B. Fourest, S. Hubert, J.F. Le Du, R. Revel, C. Den Auwer, C. Madic, L.R. Morss, G. Ionova, V. Mikhalko, V. Vokhmin, M. Nikonov, J.C. Berthet, M. Ephritikhine</i> Aquo Ions of Some Trivalent Actinides: EXAFS Data and Thermodynamic Consequences.....	95
<i>P.G. Allen, D.K. Shuh, J.J. Bucher, N.M. Edelstein, T. Reich</i> Applications of XAFS Spectroscopy to Speciation Problems in Environmental Radiochemistry	101
<i>C. Den Auwer, R. Revel, M.C. Charbonnel, M.T. Presson, C. Madic, S.D. Conradson, E. Simoni, J.F. Le Du</i> Probing Actinide Atoms in Various Liquid Phase U, Np and Pu Co-ordination Compounds	103
<i>S.W. Swanton, G. Baston, M.M. Cowper, J.M. Charnock</i> EXAFS Study of Uranium(VI) Sorbed to Hematite	111
<i>A. Rogalev, M. Finazzi, J. Goulon, C. Neumann, W. Grange, J.-P. Kappler, J.-P. Sanchez, P. Dalmas, A. Yaouanc, Ph. Sainctavit</i> X-Ray Magnetic Circular Dichroism of Uranium Compounds	119
<i>D.L. Clark, S.D. Conradson, D.W. Keogh, M.P. Neu, P.D. Palmer, W. Runde, B.L. Scott, C.D. Tait</i> X-Ray Absorption and Diffraction Studies of Monomeric Actinide Tetra-, Penta- and Hexavalent Carbonato Complexes.....	121
<i>M.A. Denecke</i> Metal-Oxygen Bond Distance Determination from XANES Spectra.....	135
<i>T.I. Docrat, J.F.W. Mosselmans, J.M. Charnock, M.W. Whiteley, D. Collison, F.R. Livens, C. Jones, M.J. Edmiston</i> X-Ray Absorption Spectroscopy of Carbonate and Catecholate Complexes of Uranium(V) in Aqueous Solution.....	143
<i>A.M. Scheidegger, R. Dähn, B. Baeyens, M.H. Bradbury, D.L. Sparks</i> Use of X-Ray Absorption Fine Structure (XAFS) Spectroscopy at the Nuclear Waste Management Laboratory, PSI	145
<i>L. Desgranges, M. Ripert, M. Beauvy, T. Petit</i> Synchrotron Radiation Studies on Nuclear Fuels	153

Session III: USE OF RADIONUCLIDES AT SYNCHROTRON FACILITIES 161

Chair: G.H. Lander

P.G. Allen, D.K. Shuh, J.J. Bucher, N.M. Edelstein
Experimental Procedures and Safety Considerations for Transuranic Studies
at the Stanford Synchrotron Radiation Laboratory 163

*H. Funke, T. Reich, G. Bernhard, V. Brendler, J. Claussner, G. Hüttig,
W. Matz, W. Neumann, W. Oehme*
The Radiochemistry Experimental Station at the Rossendorf Beamline 181

P. Berkvens, P. Colomp
Safety Considerations for Measurements of Radioactive Samples at the
European Synchrotron Radiation Facility 189

S. Tachimori
Synchrotron Radiation Facilities to Study Radioactive Materials at the Photon
Factory and SPring-8 199

C. Den Auwer, R. Revel
Actinide XAS on D44 at LURE..... 207

A.J. Dent
Radionuclide Facilities and Examples of Work at the Daresbury Synchrotron
Radiation Source 209

D.K. Shuh, K.H. Heinzelman
Safety Considerations for Experiments with Radioactive Materials
at the Advanced Light Source..... 211

Session IV: POSTER SESSION..... 213

M. Akabori, A. Itoh, Y. Okamoto, H. Motohashi, H. Shiwaku
X-Ray Absorption Spectra in Uranium Alloys: Uranium-Molybdenum Alloys 215

N. Baclet, D. Bazin
PuGa Alloys Structure Studied by X-Ray Absorption Spectroscopy 217

G. Bernhard, G. Geipel, V. Brendler, T. Reich, H. Nitsche
Validation of Complex Formation of Ca^{2+} , UO_2^{2+} and CO_3^{2-} 225

I. Bonhoure, C. Den Auwer, P. Moisy, C. Madic, C. Cartier dit Moulin
Structure and Electronic Structure of Actinide $\text{An/Fe}(\text{CN})_6$ Compounds 227

*D.L. Clark, S.D. Conradson, R.J. Donohoe, D.W. Keogh, D.E. Morris,
M.P. Neu, P.D. Palmer, W. Runde, B.L. Scott, C.D. Tait*
Co-ordination Chemistry of Heptavalent Neptunium under Highly Alkaline
Conditions 229

C. Den Auwer, M.G.B. Drew, M.J. Hudson, P.B. Iveson, M.L. Russell, C. Madic
XAS Investigation of the Mechanism by which Lanthanide(III) and
Actinide(III) Ions are Extracted from Solution by Malonamide Ligands 231

<i>C. Hennig, A. Roßberg, T. Reich, H. Nitsche, M.A. Denecke, G. Zahn</i> U _{LIII} Polarised XAFS Studies on Ba[<chem>UO2PO4</chem>] ₂ · 8H ₂ O	233
<i>C. Hennig, G. Nolze</i> Characterisation of the Preferred Orientation in EXAFS Samples Using Bragg-Brent and X-Ray Diffraction	235
<i>C. Hennig, T. Reich, T. Arnold, A. Roßberg, H. Nitsche</i> EXAFS Investigations of Uranyl Sorption on Ferrihydrite	245
<i>R. Jankowsky, S. Kirsch, M. Friebe, H. Spies, B. Johannsen</i> EXAFS Spectroscopy of Technetium and Rhenium Complexes Relevant to Nuclear Medicine.....	247
<i>J. Jolie, Th. Materna, B. Masschaele, W. Mondelaers, V. Honkimaki, A. Koch, Th. Tschentscher</i> Heavy Element Sensitive Tomography Using Synchrotron Radiation Above 100 keV	249
<i>D.W. Keogh, D.L. Clark, S.D. Conradson, R.J. Donohoe, D.E. Morris, M.P. Neu, P.D. Palmer, R.D. Rogers, W. Runde, B.L. Scott, C.D. Tait</i> Co-ordination Chemistry of Penta- and Hexavalent Actinide Ions (U, Np, Pu) Under Highly Alkaline Conditions	257
<i>Ph. Martin, A. Chevarier, N. Chevarier, G. Panczer, C. Den Auwer</i> EXAFS Characterisation of Europium Diffusion in Hydroxyapatite	259
<i>H. Moll, I. Farkas, F. Jalilehvand, M. Sandström, Z. Szabó, I. Grenthe, M.A. Denecke, U. Wahlgren</i> Structure of Uranium(VI), Uranium(IV) and Thorium(IV) Species in Solution	261
<i>J. Osán, B. Török, S. Török, K.W. Jones</i> Study of Chemical State of Toxic Metals During the Life Cycle of Fly Ash Using X-Ray Absorption Near-Edge Structure	269
<i>T. Reich, V. Brendler, M.A. Denecke, M. Bubner, S. Pompe, H. Nitsche, P.G. Allen</i> Structural Analysis of the Interaction of Uranium(VI) with Humic Acid and Simple Carboxylic Acids Using EXAFS	277
<i>A. Roßberg, T. Reich, C. Hennig, L. Baraniak, K.H. Heise, A. Günther, H. Nitsche, M.A. Denecke</i> Determination of Molecular-Level Structural Information of Uranium in Environmentally Relevant Samples by EXAFS	285
<i>Yu.A. Teterin, I.O. Utkin, I.V. Melnikov, A.Yu. Teterin, A.M. Lebedev, K.E. Ivanov, A.S. Nikitin, L. Vuckchevich</i> X-Ray Photoelectron Study of Synthetic and Natural Thorium Compounds	287
<i>Yu.A. Teterin, I.O. Utkin, A.M. Lebedev, A.Yu. Teterin, K.E. Ivanov, A.S. Nikitin</i> The Influence of Dynamic Effect on the Structure of X-Ray Photoelectron Spectra of Actinide Compounds	297

<i>Yu.A. Teterin, A.Yu. Teterin, A.M. Lebedev, A.P. Dementjev, I.O. Utkin, I.V. Melihov, V.I. Nefedov, D.G. Berdonosova, G.N. Bek-Uzarov, L. Vukchevich</i> XPS Study of Interactions of Uranyl Group UO_2^{2+} with Hydroxyl- and Fluorapatite in Water Solutions	307
<i>E. Welter, S. Mangold</i> Heavy Metal Speciation Analysis in Soils Using Synchrotron Radiation	315
<i>M.J. Wharton, B. Atkins, J.M. Charnock, F.R. Livens, R.A.D. Patrick, D. Collison</i> An X-Ray Absorption Study of the Reactions of Tc with Mackinawite (FeS).....	323
<i>T. Yaita, S. Suzuki, H. Narita, S. Tachimori, K. Takai, H. Motohashi, K. Kobayashi</i> XAFS Studies of Uranium(VI)-Amide Organophosphorous Compound Complexes in Ethanol	325
Annex 1. LIST OF PARTICIPANTS	331
Annex 2. ORGANISING COMMITTEE	343

EXECUTIVE SUMMARY

During recent years the interest in applying synchrotron radiation techniques to the investigation of radionuclides and actinides in particular has grown rapidly. Important research topics for which a molecular-level understanding is mandatory include the behaviour of radionuclides in the environment, nuclear waste management, radiopharmaceutical chemistry and general actinide chemistry and physics.

On 4-6 October 1998 the first Euroconference and NEA Workshop on Speciation, Techniques and Facilities for Radioactive Materials at Synchrotron Light Sources, Actinide-XAS-98, took place at the ESRF/ILL site. Over 90 scientists came from 13 European countries, the USA and Japan. Among them were 22 young scientists with an average age of 26 who benefited from travel awards provided by the European Commission. The main objectives of Actinide-XAS-98 were:

- To introduce the type of information that can be obtained from synchrotron-based techniques to environmental and nuclear scientists.
- To report the latest results on radionuclide/actinide work.
- To describe the protocols which are in place for actinide research at several synchrotron storage rings throughout the world.

The first day was tutorial in character and introduced several synchrotron radiation techniques. H. Nitsche described the sources of environmental contamination by radionuclides, the importance of understanding the chemical behaviour of radionuclides under environmental conditions, and the role X-ray absorption fine-structure (XAFS) spectroscopy plays in these investigations. D.C. Koningsberger, J. Goulon, and A. Filipponi presented the physical principles of XAFS and related experimental and theoretical aspects. V.I. Nefedov gave an introduction to X-ray photoelectron spectroscopy (XPS). D.K. Shuh described the complimentary application of XPS, near-edge X-ray absorption fine structure, and X-ray emission spectroscopy on actinide materials at energies below 2 keV. W. Matz and G.H. Lander gave tutorial lectures on X-ray diffraction and the application of X-ray scattering to the magnetism of actinides, respectively. U. Wahlgren covered molecular modelling of actinide complexes in aqueous solutions which is related to the information obtained from XAFS studies.

Representatives of nearly all laboratories known world-wide for using synchrotron radiation to study actinides reported on their latest results during the second day. Five invited lectures, 11 contributed lectures, and 22 poster presentations showed that important structural, chemical and physical information on technetium, uranium, neptunium and plutonium samples can be obtained using synchrotron radiation. The majority of presentations reported XAFS studies on actinide complexes in solution, crystalline samples and sorption of radionuclides on mineral surfaces. The discussion was focused both on basic and applied research, e.g. spatially-resolved XAFS measurements of contaminated soil samples. Other presentations described investigations on actinides using XPS, X-ray magnetic circular dichroism, and X-ray tomography.

On the last day, participants heard short presentations on experimental stations available for actinide experiments at synchrotron light sources, their experimental possibilities and the procedures and regulations for safe handling of radioactive materials. These reports included the following synchrotron light sources: SSRL (P.G. Allen), ESRF (P. Berkvens), ROBL-CRG at ESRF (H. Funke), APS (L. Soderholm), Photon Factory and SPring-8 (S. Tachimori), LURE (C. Den Auwer), Daresbury Synchrotron Radiation Source (A.J. Dent) and ALS (D.K. Shuh). The conference concluded with a tour of several ESRF beam lines including ID 20 (magnetic scattering), ID 21 (X-ray microscopy), ID 22 (X-ray fluorescence microprobe), and ID 24 (dispersive EXAFS). Of special interest to many participants was the new Rossendorf Beamline (ROBL, BM20) which had just completed its first XAFS measurements of radioactive samples. The participants asked for detailed explanations of the radiochemistry safety system, the sample handling in the specially designed glove box and the remote positioning of samples and detectors.

The meeting stressed the difficulty in handling radioactive materials at these facilities and the necessity of an international collaboration in this field. A follow-up meeting has been proposed to be held at ESRF, Grenoble, in the year 2000, and it has further been suggested that meetings should afterwards be convened every two years.

Session I

INTRODUCTION TO SYNCHROTRON RADIATION TECHNIQUES

*Chairs: N.M. Edelstein, C. Madic,
S. Tachimori, D.C. Koningsberger*

APPLICATION OF SYNCHROTRON RADIATION TECHNIQUES TO RADIONUCLIDE STUDIES

**H. Nitsche, T. Reich, C. Hennig, A. Roßberg, G. Geipel, M.A. Denecke,
L. Baraniak, P. Panak, A. Abraham, B. Mack, S. Selenska-Pobell, G. Bernhard**

Forschungszentrum Rossendorf E.V., Institute of Radiochemistry
P.O. Box 51 01 19, D-01314 Dresden, Germany

Abstract

We discuss the sources of radionuclides in the environment and summarise the level of radioactive contaminations world-wide. We delineate how X-ray absorption spectroscopy (XAS) can be used in molecular-level environmental radionuclide research and demonstrate the technique's application on the following three research topics related to contaminations from uranium mining:

1. The structure of a recently discovered aqueous species, $\text{Ca}_2\text{UO}_2(\text{CO}_3)_3(\text{aq})$ was studied by EXAFS and compared to the model systems $[\text{UO}_2(\text{CO}_3)_3]^{4-}(\text{aq})$ and $\text{Ca}_2\text{UO}_2(\text{CO}_3)_3 \cdot 10\text{H}_2\text{O}$.
2. EXAFS were used to study the aqueous complexes of U(VI) with a model substance, 3,4-dihydroxybenzoic acid (protocatechuic acid; PCS), and 2-hydroxyphenol (catechol; BCT). PCS is produced in flooded uranium mines by hydrothermal and microbial degradation of lignin, an initial wood degradation product. By comparing the results of the PCS complexation with those for BCT, it was established that the U(VI) is bound at low pH to the carboxylic group and at high pH to the hydroxy group(s).
3. A sulphate-reducing bacterial strain of the species *Desulfomicrobium baculatum* metabolises U(VI). The uranium oxidation state after metabolisation was determined by X-ray absorption near-edge fine structure (XANES) spectroscopy.

Introduction

In this paper we will describe the sources of radionuclides in the environment, summarise the level of radioactive contaminations world-wide, delineate how X-ray absorption spectroscopy (XAS) can be used in molecular-level environmental radionuclide research and illustrate the technique's application to selected research topics related to contaminations from uranium mining.

Sources and levels of radioactive environmental contaminations in the world

Contaminations were caused by nuclear weapons production and testing, nuclear reactor accidents, accidents during the transport of nuclear weapons, and by uranium mining and ore processing.

Above-ground testing of more than 420 nuclear weapons produced large amounts of radionuclides through fission and neutron activation products. More than four metric tonnes of plutonium were distributed on the earth's surface by global fallout [1].

The MAYAK plutonium production complex in the former Soviet Union (FSU) is located in the southern Urals, about 70 km north of Chelyabinsk and 15 km east of Kyshtym. Between 1949 and 1951 about 76 million cubic meters of liquid radioactive waste with a total activity of 100 PBq (2.7 MCi) were discharged into the Techa River [2,3]. To prevent further migration of the radionuclides, a series of reservoirs and bypass canals were constructed. Today, radioactive contaminated waters are seeping from the reservoirs and continue to contaminate the Techa River which is ultimately linked to the Arctic Sea through the rivers Iset, Tobol, Irtysh and Ob. Estimates between 1 and 10 PBq (27-270 kCi) of ^{90}Sr and ^{137}Cs and corresponding amounts of actinides may have been discharged into the ocean. About 2.5 million cubic meters of waste corresponding to 4.4 Ebq (120 MCi) were discharged into Lake Karachai near MAYAK. The discharges were mostly wastes from the organic/aqueous solvent extraction process separating plutonium from fission products and other actinides. Due to a severe drought in 1976, some of the lake's water evaporated and about 20 TBq (0.54 MCi) of radioactive materials, associated with the dust on the shore of the lake, was dispersed by a small tornado. An area of 1 800 km² extending up to 75 km was contaminated. As of 1995, the lake was filled with hollow concrete blocks in order to reduce its surface area from 36 to 16 hectares, thus suppressing wind-assisted dispersion of radioactive liquid aerosols from the water surface and dust from the shore. About 7.5 EBq (200 MCi) liquid high-level radioactive waste is stored in 257 surface tanks. One storage tank exploded in 1957 due to insufficient cooling. The liquid sludge was ejected to a height of 2 km into the atmosphere and the radioactive cloud dispersed between 74 and 740 PBq (2-20 MCi) into the environment. About 15 000 to 23 000 km² of land was contaminated reaching as far as 345 km north-east of the release point.

The reactor explosions in 1986 in Chernobyl released estimated amounts of 89 PBq (2.4 MCi) ^{137}Cs and 8 PBq (0.2 MCi) ^{90}Sr [2]. Twenty-three kilograms of plutonium isotopes totalling 6.5 PBq (0.18 MCi), 4.8 TBq (130 Ci) ^{241}Am , 1.1 PBq (30 kCi) ^{242}Cm and 6.2 TBq (168 Ci) ^{244}Cm were released. Within a 30-mile radius, the concentration of $^{239,240}\text{Pu}$ is between 3.7 and 185 GBq km⁻² (0.1-5 Ci km⁻²). Large areas in Byelorussia and the Ukraine were contaminated.

Severe contaminations occurred in the USA at many sites within the nuclear weapons complex. Hanford was the first industrial-scale plutonium production site. Between 1944 and 1981, approximately 220 000 cubic meters of liquid reprocessing waste, totalling 11.8 EBq (320 MCi), were produced and are stored in 149 single-shell and 28 double-shell steel tanks [4,5]. As much as 3 800 cubic meters of radioactive-contaminated liquid were released into the environment. During the earlier period of operation, some high-level wastes and other contaminated liquids were discharged

directly into the ground through trenches and shallow sub-surface drainage systems, so-called cribs. The released volume of more than one billion cubic meters contaminated around 500 km² with radionuclides and toxic chemicals. In Oak Ridge, 160 000 cubic meters of liquid waste containing fission products and transuranium elements were directly discharged into the ground, thus creating a radioactive burden of about 44.4 TBq (1.2 kCi). For the whole weapons complex in the United States, 5 700 contaminated groundwater plumes exist and estimates for the volume of contaminated soil range from 73 to 300 million cubic meters.

At Sellafield, the British nuclear fuel processing plant, between 1950-1992, discharges were made into the Irish Sea of 41 PBq (1.1 MCi) ¹³⁷Cs, 120 TBq (3.2 kCi) ²³⁸Pu, 600 TBq (16.2 kCi) ^{239,240}Pu and 540 TBq (14.6 kCi) ²⁴¹Am [6,7]. As of 1977, 280 TBq (7.6 kCi) ^{239,240}Pu and 340 TBq (9.2 kCi) ²⁴¹Am are strongly sorbed to the seabed sediments.

Uranium mining and ore processing has contaminated many areas that require restoration [8]. One impressive example is the legacy of 45 years of uranium mining in the southern parts of the former East Germany [9-12]. It has left the population exposed to an extensive number of mines, rock piles and mill tailings. Between 1946 and 1990, the WISMUT company mined about 220 000 metric tonnes of uranium, creating more than 800 mine tailing piles containing 500 million tonnes of rock. The successor company, now funded by the Federal Republic of Germany, assumed responsibility for an area of about 1 000-1 200 km² with 64 mine tailing piles. The mines have a total shaft length of 3 400 km and a depth of up to 1 800 m. Mill tailings comprise about 154 million cubic meters of residue that is contaminated with uranium and decay products. The defunct mines are being flooded by groundwater, and the flood waters, as well as the seepage waters from mine and mill tailing piles, constitute the primary source term of contamination. Uranium, radium, radon and their decay products are potential radioactive hazards to the biosphere.

Proposed disposal of high-level radioactive wastes and direct disposal of spent fuel in deep underground geologic repositories as well as the storage and disposal of plutonium from nuclear weapons dismantlement are further potential sources for actinide releases into the environment. Although much of the radioactivity of the contamination is caused by the relatively short-lived isotopes ⁹⁰Sr (29 y), ¹³⁷Cs (30.2 y) and other fission products, the potential long-term hazard comes from the following long-lived isotopes: ²³²Th (1.4 × 10¹⁰ y), ²³³U (1.59 × 10⁵ y), ²³⁵U (7.04 × 10⁸ y), ²³⁸U (4.47 × 10⁹ y) and some of their decay products: ²³⁸Pu (87.7 y), ²³⁹Pu (2.4 × 10⁴ y), ²⁴⁰Pu (6.4 × 10³ y), ²⁴¹Pu (14.4 y), ²³⁷Np (2.14 × 10⁶ y), ²⁴¹Am (432 y) and ²⁴³Am (7.4 × 10³ y).

It is essential to understand the behaviour of radionuclides in the environment in order to (a) develop efficient methods for the remediation and clean-up of contaminated sites; (b) predict their transport behaviour; (c) carry out performance assessment studies to determine if the repositories can safely contain them; and (d) engineer methods to retard their release and migration rates.

Excluding gaseous and airborne transport, radionuclides can migrate in the environment mostly via aqueous media such as groundwater and surface, river, lake and sea water. Models predicting the hydrological transport through the environment require as input a radionuclide concentration, the true amount that is actually available for transport. It is defined as the radionuclide source term and not as true solubility, because it may be a combination of dissolved and colloidal material. Three major processes define the radionuclide source term: (1) solubility; (2) organic interaction; and (3) sorption. They are dependent on each other and each individual process is the result of several sub-processes. Also, colloid formation plays a major role in the radionuclide source term, and it is common to each of the three main processes.

A basic molecular-level understanding is required to quantitatively describe the mechanisms of radionuclide transport in the environment. This microscopic information is used together with chemical/mathematical models to obtain macroscopic transport predictions.

XAS as a powerful tool in environmental radionuclide research

Many different methods are necessary to provide the microscopic information that is mandatory for making macroscopic predictions. XAS is a powerful technique to study many chemical elements in solids, liquids and gases. XAS spectroscopy can provide information on the speciation of metals and radionuclides and of speciation changes that result from changes of their chemical environment.

We are applying synchrotron-based X-ray absorption near edge structure spectroscopy (XANES) and extended X-ray absorption fine structure spectroscopy (EXAFS) for the following research areas:

- Speciation and complexation studies of radionuclides in aqueous and non-aqueous solutions pertinent to environmental contamination, pollution risk assessment and remediation strategies.
- Adsorption processes at the solid-water interface of radionuclide solutions with soils, minerals, mineral assemblies and uranium mill tailings.
- Adsorption and incorporation of radionuclides in biological materials in support of bioinorganic chemistry and bioremediation technologies.

Application of XAS to environmental uranium research

Uranium L-edges can be used for XAS with hard X-ray energies. EXAFS measurements were performed on beamline 4-1 at the Stanford Synchrotron Radiation Laboratory (SSRL) using a Si(220) double-crystal monochromator and at the HASYLAB beamline RÖMO II. At low UO_2^{2+} concentration, the fluorescence signal was measured with a four-pixel germanium detector, and ionisation chambers were used for high concentrations. For energy calibration, a UO_2 foil was used as a reference and measured simultaneously. The ionisation potentials of the uranium L_{II} and L_{III} edges were observed at 20 965 and 17 185 eV, respectively. The EXAFS spectra were analysed according to standard procedures using the suite of programs EXAFSPAK [13] and theoretical scattering phases and amplitudes calculated with the scattering code FEFF7 [14].

Structural investigations of the system $\text{Ca}^{2+}/\text{UO}_2^{2+}/\text{CO}_3^{2-}$

During recent studies of calcium-rich waters related to uranium mining, the existence of a neutral complex $\text{Ca}_2\text{UO}_2(\text{CO}_3)_3(\text{aq.})$ was established [15]. We performed extended X-ray absorption fine structure (EXAFS) measurements to validate the new species and to study its structure. EXAFS measurements were carried out on two solution samples. Solution 1 consisted of 0.5 mM UO_2^{2+} , 2 mM Ca^{2+} and 5 mM CO_3^{2-} at pH of 8.0. Solution 2 was calcium-free and contained 1 mM UO_2^{2+} and 20 mM CO_3^{2-} at pH 8.0. According to speciation calculations using the software package EQ3/6, the complex stability constant for the new complex, and the NEA database, Solutions 1 and 2 should contain nearly 82% of the $\text{Ca}_2\text{UO}_2(\text{CO}_3)_3(\text{aq.})$ complex and 99% of the $[\text{UO}_2(\text{CO}_3)_3]^{4-}(\text{aq.})$ species, respectively. For comparison, we measured two solid samples – Sample 3 and Sample 4 – which have

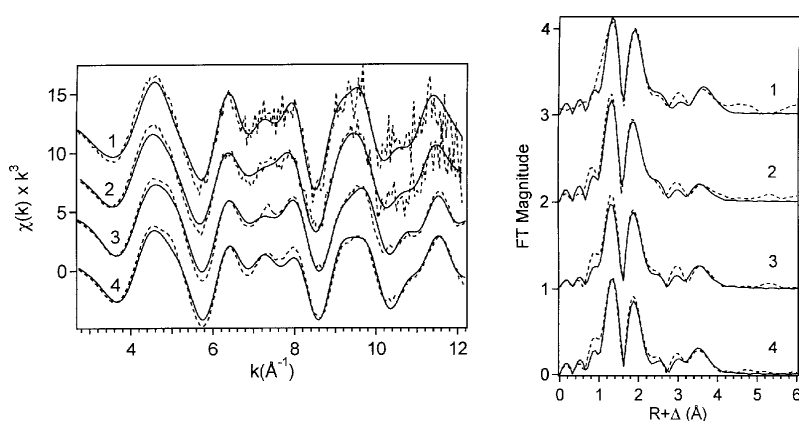
the same stoichiometric composition as solution complex 1. Sample 3 was a natural liebigite, $\text{Ca}_2\text{UO}_2(\text{CO}_3)_3 \cdot 11\text{H}_2\text{O}$, obtained from the Mineralogical Collection of Technische Universität Bergakademie Freiberg, Germany. Sample 4 was a synthetic liebigite prepared according to [16].

The uranium L_{II} edge EXAFS spectra of Samples 1 and 2 were measured in fluorescence mode. Due to higher concentrations, the uranium L_{III} edge EXAFS spectra of Samples 3 and 4 could be measured in transmission mode.

The k^3 -weighted uranium L_{II} and L_{III} edge EXAFS spectra of Samples 1-4 together with the best fits to the data are shown in Figure 1. Natural and synthetic liebigite samples show very similar EXAFS pattern up to $k = 12 \text{ \AA}^{-1}$. Due to the much lower uranium concentration in Solutions 1 and 2, the noise level of their EXAFS is higher than for Samples 3 and 4. Nevertheless, the solution samples show similar EXAFS oscillations as the liebigite mineral samples, indicating nearly identical uranium near-neighbour surrounding in all samples. This is also reflected by the observed similarities of the corresponding Fourier transforms (see Figure 1).

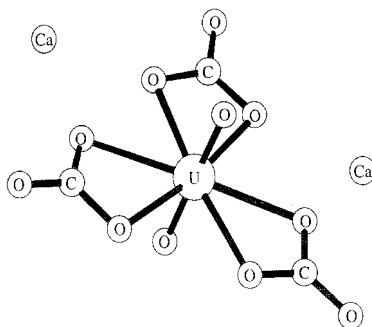
Figure 1. Left: k^3 -weighted EXAFS spectra of: (1) $\text{Ca}_2\text{UO}_2(\text{CO}_3)_3(\text{aq.})$, (2) $[\text{UO}_2(\text{CO}_3)_3]^{4-}(\text{aq.})$, (3) natural liebigite, and (4) synthetic liebigite, $\text{Ca}_2\text{UO}_2(\text{CO}_3)_3 \cdot 10\text{H}_2\text{O}$. Right: Corresponding Fourier transforms without phase corrections.

The dotted lines are the experimental data, and the solid line is the theoretical fit.



Based on the crystal structure of $\text{Ca}_2\text{UO}_2(\text{CO}_3)_3 \cdot 11\text{H}_2\text{O}$ [17], a fit to the experimental spectra of Samples 3 and 4 was performed using the structural model given in Figure 2.

Figure 2. Ball-and-stick drawing illustrating the structural model used for fitting the EXAFS spectra



The model consisted of four uranium co-ordination shells belonging to the $\text{UO}_2(\text{CO}_3)_3$ unit, i.e. U- O_{ax} , U- O_{eq} , U-C and U- O_{dis} . The U- O_{dis} co-ordination shell was modelled by the three-legged multiple-scattering interaction along the linear U-C- O_{dis} path. Since the $\text{UO}_2(\text{CO}_3)_3$ units are linked by several types of calcium polyhedra, an additional U-Ca shell was included in the fit. According to the crystal structure, the closest calcium atoms are located at 4.07 Å between neighbouring CO_3 units in the equatorial plane (see Figure 2). As can be seen from Table 1, the interatomic distances obtained by EXAFS are in good agreement with the crystallographic values. In spite of this agreement, it is difficult, if not impossible, to detect the presence of two calcium atoms at 4.07 Å unambiguously. The fit did not deteriorate significantly if the U-Ca shell was excluded from the fit since the missing U-Ca amplitude contribution was compensated by a small increase of the U- O_{dis} amplitude.

The EXAFS spectra of Samples 1 and 2 were fitted with the $\text{UO}_2(\text{CO}_3)_3$ unit as a structural model. As can be seen from the obtained structural parameters given in Table 1, the $\text{Ca}_2\text{UO}_2(\text{CO}_3)_3(\text{aq.})$ complex consists of the same $\text{UO}_2(\text{CO}_3)_3$ unit as in $[\text{UO}_2(\text{CO}_3)_3]^{4-}(\text{aq.})$ and solid liebigite. Although a somewhat better fit for Sample 1 was obtained by including the U-Ca shell than without, the location of the two calcium atoms in the aqueous complex cannot be derived from such small differences in the fit. However, the EXAFS results do not contradict the possibility that the calcium atoms in $\text{Ca}_2\text{UO}_2(\text{CO}_3)_3(\text{aq.})$ assume similar positions in the liebigite mineral (see Figure 2).

Table 1. EXAFS structural parameters for Samples 1-4 and comparison with XRD

Uncertainty of R is ± 0.02 Å

Sample	Description	2x(U- O_{ax})		6x(U- O_{eq})		3x(U-C)		3x(U- O_{dis})		2x(U-Ca)	
		R(Å)	$\sigma^2(\text{Å}^2)$	R(Å)	$\sigma^2(\text{Å}^2)$	R(Å)	$\sigma^2(\text{Å}^2)$	R(Å)	$\sigma^2(\text{Å}^2)$	R(Å)	$\sigma^2(\text{Å}^2)$
1	$\text{Ca}_2\text{UO}_2(\text{CO}_3)_3(\text{aq.})$	1.81	0.001	2.44	0.005	2.90	0.004	4.22	0.002	3.94	0.008
2	$[\text{UO}_2(\text{CO}_3)_3]^{4-}(\text{aq.})$	1.80	0.001	2.44	0.005	2.89	0.002	4.20	0.004	–	–
3	Liebigite (nat.)	1.80	0.002	2.43	0.006	2.88	0.003	4.17	0.002	4.04	0.014
4	Liebigite (synth.)	1.81	0.0009	2.43	0.006	2.89	0.004	4.18	0.007	4.00	0.005
XRD*	Liebigite (nat.)	1.78		2.43		2.86		4.12		4.07	

* Distances measured by XRD [17]

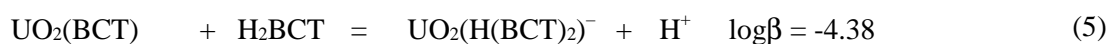
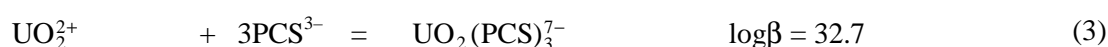
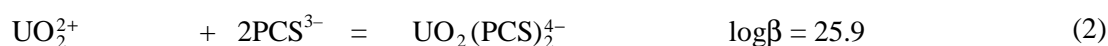
EXAFS investigations of the complexation behaviour of UO_2^{2+} with model compounds of phenolic wood degradation products

Several underground uranium mines in Saxony, Germany, are reinforced with spruce wood. Estimates for the largest mine range between 2.5 and 4 million cubic meters. During the mine's flooding the wood undergoes chemical and microbial degradation processes that are accelerated by the temperature and pressure at a depth of up to 80°C and 20 MPa. The above-mentioned amount of wood can produce about 0.3-0.5 million tonnes of lignin and 0.6 to 1 million tonnes of cellulose which degrade further in water-soluble chemical reactive components that can interact with the remaining uranium in the mine.

Spruce lignin degrades for example into ferulic acid (4-hydroxy-3-methoxy-cinnamic acid), vanillin (4-hydroxy-3-methoxy-benzaldehyde), vanillic acid (4-hydroxy-3-methoxy-benzoic acid) and protocatechuic acid (3,4,-dihydroxy-benzoic acid; PCS). Baraniak, *et al.* [18] determined the complex formation constants of uranium with these compounds with $\log \beta_{11}$ values of 6.88 ± 0.56 , 4.47 ± 0.09 , 7.16 ± 0.82 and 14.8 ± 0.74 , respectively. To investigate the interaction with uranyl(VI), the strongest

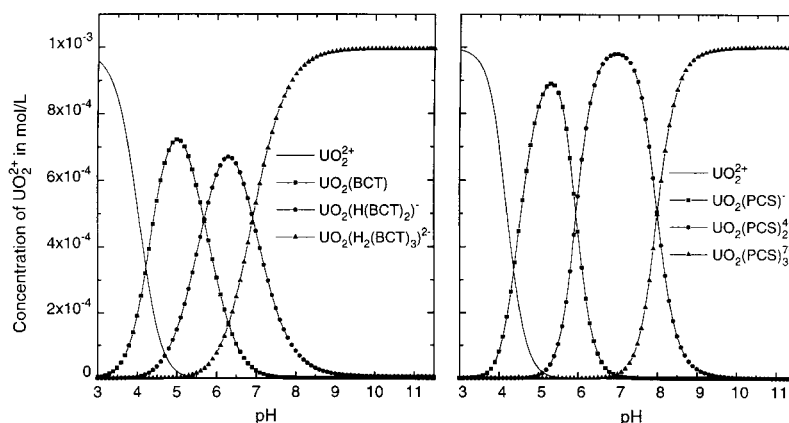
complexer, PCS, was investigated together with catechol (2-hydroxyphenol; BCT). The BCT, which can only bind to the U(VI) via the OH groups, was selected to clarify if binding of U(VI) to either the carboxylate or the hydroxy groups occurs for PCS with increasing pH.

Therefore, we calculated the aqueous speciation of the complexes in absence of CO₂ as a function of pH with the computer program RAMESES at 0.1 M ionic strength (NaClO₄) and at 25°C. The metal concentration was 1 mM UO₂(ClO₄)₂ and the ligand concentrations for PCS and BCT were 50 mM. UO₂²⁺ hydrolysis was considered in the calculations. The complexation equilibria for PCS (Eqs. 1-3) [18] and for BCT (Eqs. 4-6) [19] are:



The results of the speciation calculations are shown in Figure 3. For PCS and BCT the UO₂(PCS)⁻ complex (Eq. 1) and the UO₂(BCT) complex (Eq. 4) form at pH 5, respectively. The UO₂(PCS)₂⁴⁻ complex (Eq. 2) forms at pH 6.8. At pH 10, the UO₂(PCS)₃⁷⁻ complex (Eq. 3), and for BCT, the UO₂(H₂(BCT)₃)²⁻ complex (Eq. 6) is prevalent.

Figure 3. Calculated speciation of UO₂²⁺ complexes with BCT (left) and PCS (right); complex formation constants for PCS and BCT are from [18] and [19], respectively



It is supposed that PCS co-ordinates to the UO₂²⁺ ion as a five-membered chelate ring and that the carboxylic group is not involved in the complexation [20]. For BCT at pH 10, a 1:3 complex is expected. Our goal was to examine if the 1:3 complex with PCS also exists and to determine the role of the carboxylic group in the complexation behaviour of PCS.

To evaluate the EXAFS spectra, theoretical phases and amplitudes were calculated using the single scattering interface from OPT (FEFF7).

Table 2 shows the results of the EXAFS fits. The average of the radial distance is $1.80 \pm 0.02 \text{ \AA}$ between uranium and axial oxygens. This distance increased with increasing pH. The number of the oxygen atoms in the equatorial plane averages $5.5 \pm 20\%$. At pH 10, the spectra of the PCS and BCT complexes are identical (Figure 4, spectra *a* and *b*).

Table 2. Fit results for the first and second co-ordination shells

(Δ)*E* – energy shift, *N* – co-ordination number, *R* – radial distance in \AA
 σ^2 – Debye-Waller factor in \AA^2 , *MS* – measuring station (*S*: SSRL, *H*: HASYLAB)

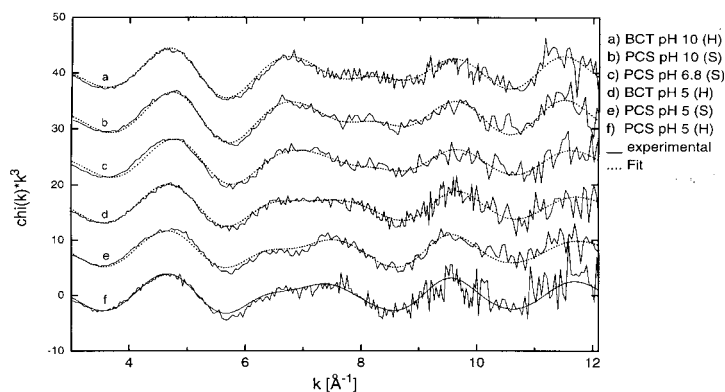
System	pH	MS	U-O axial			U-O equatorial			ΔE^*
			R	$\sigma^2 \cdot 10^{-3}$	N*	R	$\sigma^2 \cdot 10^{-3}$	N*	
PCS, UO_2^{2+}	5	H	1.80	1.1	2	2.42	10	5.7(4)	-13.8
PCS, UO_2^{2+}	5	S	1.79	2.0	2	2.44	8	4.9(4)	-13.0
BCT, UO_2^{2+}	5	H	1.78	2.4	2	2.39	8	5.6(2)	-15.7
PCS, UO_2^{2+}	6.8	S	1.81	2.4	2	2.37	9	5.5(4)	-13.0
PCS, UO_2^{2+}	10	S	1.81	1.5	2	2.38	6	5.4(3)	-13.0
BCT, UO_2^{2+}	10	H	1.81	1.5	2	2.37	6	5.7(3)	-15.7

* Constant during the fit procedure

That means that at pH 10 no differences arise from the additional carboxylic group. These complexes appear to co-ordinate UO_2^{2+} identically. The short U-O_{eq} distance of 2.37 \AA is characteristic for complexation of UO_2^{2+} with two neighbouring phenolic OH groups. The 1:2 PCS complex at pH 6.8 shows similar bonding. In contrast, differences in the radial distance of the equatorial oxygen atoms appear between PCS and BCT complexes (Table 2). Also, the EXAFS spectra *d*, *e* and *f* in Figure 4 show differences. The EXAFS spectra *e* and *f* in Figure 4 (PCS complexes, pH 5) are comparable with the EXAFS spectrum of uranyl triacetate [21]. In this compound three carboxylate groups, with a radial U-O_{eq} distance of 2.46 \AA , co-ordinate the UO_2^{2+} ion in a bidentate fashion.

Figure 4. Raw k^3 -weighted EXAFS spectra from PCS and BCT complexes

Measuring station – *S*: SSRL, *H*: HASYLAB



The average radial U-O_{eq} distance of 2.43 Å from the PCS complexes at pH 5 is significantly longer than the radial U-O_{eq} distance of 2.39 Å from the BCT complex at pH 5 (see Table 2). At pH 5, the PCS complexes the uranium through the carboxylic group and at pH 10 through the hydroxy group(s).

Determination of U(VI) reduction product after bacterial metabolisation by uranium L_{III} edge XANES spectroscopy

Certain microorganisms can reduce uranium(VI) to uranium(IV) under anaerobic conditions and thus reduce the mobility of uranium in the environment [22,23]. Therefore, the study of uranium interaction with heterotrophic anaerobic bacteria is important for the development of efficient and cost-effective remediation processes of uranium contaminated sites.

We applied uranium L_{III} edge XANES spectroscopy to determine the uranium oxidation state after metabolisation of uranium(VI) by a sulphate-reducing bacterial strain of the species *Desulfomicrobium baculatum*. After culturing the bacterial strain in 600 mL growth medium, the bacterial cells were obtained by centrifugation. Then they were suspended in 0.9% NaCl solution and the sample was incubated with 50 mL 10⁻⁴ M U(VI) solution at pH 5.0. After shaking the sample for two days under nitrogen atmosphere, the biomass was separated by centrifugation, washed with 5 mL 0.9% NaCl solution, and sealed in a polyethylene cuvette for XANES measurements. Two 0.04 M U(IV) and U(VI) solutions in 1 M HClO₄ served as reference samples for the uranium oxidation states. The U(VI) stock solution was obtained by dissolving Na₂U₂O₇ · 6H₂O in 7 M HClO₄. Part of this solution was reduced electrochemically to U(IV) at a mercury pool cathode. In addition, two samples with molar ratios of U(IV) to U(VI) of 3.0 and 0.33 were prepared by mixing U(IV) and U(VI) solutions under nitrogen atmosphere. Four mL of each solution was transferred into air-tight polyethylene cuvettes of 13 mm diameter. Uranium L_{III} edge spectra were measured at ambient temperature at HASYLAB at the experimental station RÖMO II, beamline X1.1, using the Si(311) double-crystal monochromator detuned 50% of the maximum incident flux. The bacteria sample was measured in fluorescence mode; all solution samples in transmission mode. The energy scale was calibrated against the first inflection point (defined as 17 165 eV) of a 0.04 M U(VI) solution sample, which was measured simultaneously. After background removal, the spectra were normalised to equal intensity at 17 250 eV. The U(IV)/U(VI) ratio of the aqueous mixtures was determined by fitting their XANES features as a linear combination of the experimental XANES of the single-component solutions. The same approach has been successfully applied to the determination of the As(III)/As(V) ratio in arsenic containing water samples [24].

Figure 5 shows the uranium L_{III} edge XANES spectra of the aqueous reference solutions and the mixtures containing both U(IV) and U(VI). Compared to U(VI), the white line (WL) intensity of the U(IV) XANES spectrum is increased and its energy is reduced. Additional changes occur also in the XANES above the WL. These observations agree with previous uranium L_{III} edge XANES measurements of UO₂ and UO₂(NO₃)₂ · 6H₂O [25]. The observed spectral changes allow to distinguish between U(IV) and U(VI) oxidation states and to determine their relative concentration as illustrated in Figure 5. The fitted XANEX of the mixtures in question coincide with the experimental spectra. The U(IV)/U(VI) ratios of 2.5 and 0.31 obtained are close to the corresponding values of 3.0 and 0.33 used for preparing these mixtures.

Figure 6 shows a comparison of the uranium L_{III} edge XANES spectra of the bacterial sample with the U(IV) reference solution. After metabolisation of hexavalent uranium by sulphate-reducing bacteria, uranium XANES shows almost identical spectral features as the U(IV) solution. Small

Figure 5. Top: Experimental U L_{III} edge XANES spectra of U(IV) and U(VI) reference solutions containing 0.04 M uranium in 1 M HClO₄. Bottom: Experimental U L_{III} edge XANES spectra of two 0.04 M uranium solution mixtures (dots) and the U(IV) (short-dashed curve) and U(VI) (long-dashed curve) constituents of the fit (solid curve)

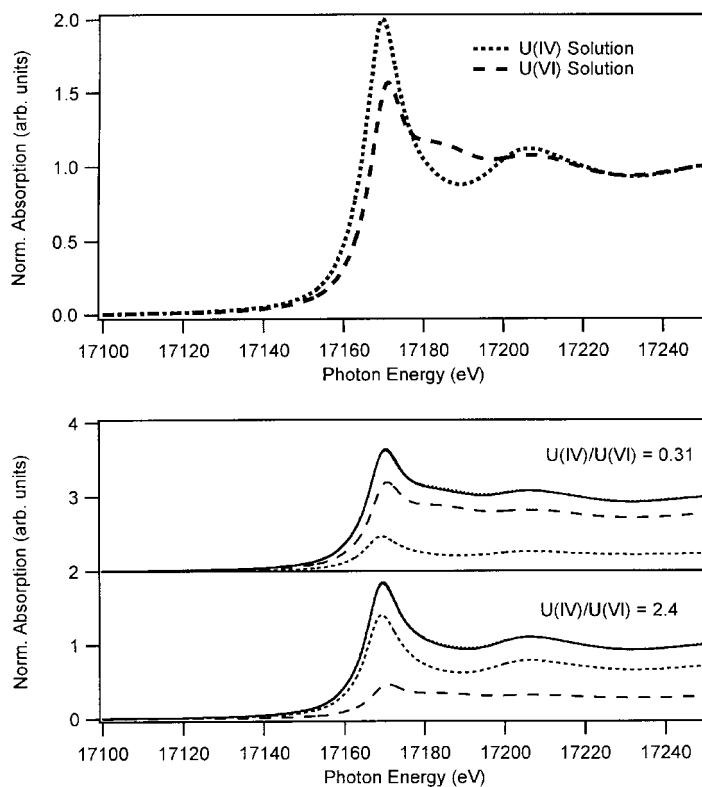
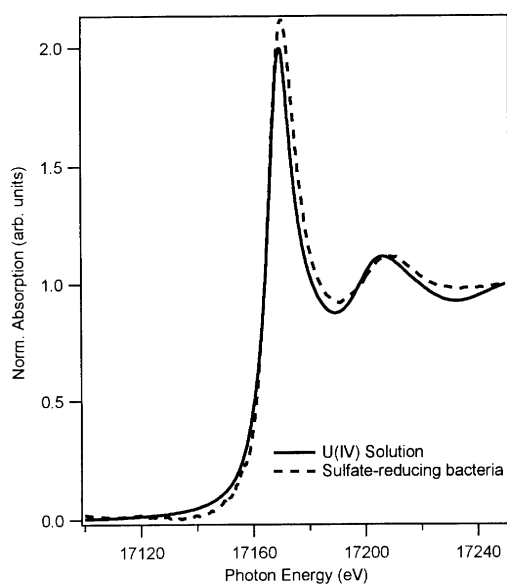


Figure 6. Experimental U L_{III} edge XANES spectra of 0.04 M U(IV) solution and uranium after bacterial metabolisation of U(VI)



deviations can indicate the different uranium near-neighbour surroundings between the bacterial sample and the reference solution. As in the case of the U(IV) reference solution, the energy of the WL maximum is shifted by 1.7 eV to lower energy relative to the U(VI) reference. It can be concluded that the bacteria sample contained only reduced tetravalent uranium.

Our measurements clearly demonstrate the analytical potential of uranium L_{III} edge XAS spectroscopy for the investigation of bacteria-uranium interactions. This process can be applied for the determination of U(IV) and U(VI) oxidation states and structural parameters of uranium near-neighbour surroundings.

Acknowledgements

We are indebted to D.K. Shuh, J.J. Bucher and N.M. Edelstein, Chemical Sciences Division, Lawrence Berkeley National Laboratory, and P.G. Allen, G.T. Seaborg Institute, Lawrence Livermore National Laboratory, USA, for their collaboration. EXAFS measurements were made at SSRL, Stanford, USA, which is operated by the US Department of Energy, and at HASYLAB, Deutsches Elektronen Synchrotron, Hamburg, Germany.

REFERENCES

- [1] H. Kiefer, W. Koelzer, *Strahlen und Strahlenschutz*, Springer-Verlag, Berlin, 74 (1987).
- [2] A. Aarkrog, Y. Tsaturov, G.G. Polikarpov, Sources to Environmental Radioactive Contamination in the Former USSR, European Commission Report XI-095/93, *Radiation Protection* 74 (1994).
- [3] B.F. Myasoedov, E.G. Drozhko, Up-to-Date Radioecological Situation Around the MAYAK Nuclear Facility, Actinides'97, International Conference, Session T4-B2, published in the *Journal of Alloys and Compounds*.
- [4] K.D. Crowley, Nuclear Waste Disposal: The Technical Challenges, *Physics Today*, Special Issue 32-39 (1997).
- [5] Linking Legacies – Connecting the Cold War Nuclear Weapons-Production Processes to Their Environmental Consequences, Report, US Department of Energy, Office of Environmental Management 36-37 (1997).
- [6] S.R. Jones, P. McDonald, Status of the Restoration of Contaminated Sites in Europe, European Commission Report 94-PR-014, *Radiation Protection* 90, T. Zeevaert, H. Vanmarcke, P. Govaerts, eds., 56 (1997).
- [7] S.R. Jones, P. McDonald, The Inventory of Long-Lived Artificial Radionuclides in the Irish Sea and Their Radiological Significance, European Commission Report, XI-5027/94, *Radiation Protection* 74, 1, 153-206 (1994).

- [8] J.P. Herbert, J.L. Daroussin, P. Michel, Ch. Perih, F. Lozano Martinez, A. Lopez Romero, J. Fietz, L. Langer, A. Kahn, V. Litvin, H. Nitsche, Decommissioning of Old Uranium Ore Extraction and Treatment Installations, European Commission Report EUR 16885 EN (1996).
- [9] R. Gatzweiler, D. Mager, Altlasten des Uranbergbaus. Der Sanierungsfall WISMUT, *Geowissenschaften* 11, 164-172 (1995).
- [10] R. Gatzweiler, A.T. Jakubick, F. Pelz, WISMUT-Sanierung. Konzepte und Technologien, *Geowissenschaften* 14, 448-451 (1996).
- [11] M. Hagen, G. Lange, Der Flutungsprozess ehemaliger Uranerzgruben in Ostdeutschland als Sanierungsschwerpunkt der WISMUT GmbH, *Erzmetall* 48, 779-804 (1995).
- [12] D. Mager, Das Sanierungsprojekt WISMUT: Internationale Einbindung, Ergebnisse und Perspektiven, *Geowissenschaften* 11, 443-447 (1996).
- [13] G.N. George, I.J. Pickering, EXAFSPAK, A Suite of Computer Programs for Analysis of X-Ray Absorption Spectra, Stanford Synchrotron Radiation Laboratory, USA (1995).
- [14] S.I. Zabinsky, J.J. Rehr, A. Ankudinov, R.C. Albers, M.J. Eller, *Phys. Rev. B* 52, 2995 (1995).
- [15] G. Bernhard, G. Geipel, V. Brendler, H. Nitsche, Speciation of Uranium in Seepage Waters of a Mine Tailing Pile Studied by Time-Resolved Laser-Induced Fluorescence Spectroscopy (TRLFS), *Radiochim. Acta* 74, 87 (1996).
- [16] R. Meyrowitz, D.R. Ross, A.D. Weeks, Synthesis of Liebigite, *US Geol. Survey Prof. Paper* 475-B, B 162 (1963).
- [17] K. Mereiter, The Crystal Structure of Liebigite, $\text{Ca}_2\text{UO}_2(\text{CO}_3)_3 \cdot 11\text{H}_2\text{O}$, *TMPM Tschermaks Min. Petr. Mitt.* 30, 277 (1982).
- [18] L. Baraniak, M. Schmidt, G. Bernhard, H. Nitsche, Complex Formation of Hexavalent Uranium with Lignin Degradation Products, in Report FZR-180, Institute of Radiochemistry, Annual Report 1996, p. 28 (1997).
- [19] A.E. Martell, R.M. Smith, R.J. Motekaitis, Critically Selected Stability Constants of Metal Complexes, Database Version 2.0, Texas A&M University (1995).
- [20] E.S. Jayadevadappa, S. Renukarani, P.B. Hukkeri, Studies of Chelate Formation of 4-Carboxycatechol with Some Metal Ions, *J. Karnatak Univ., Science* 14, 64-71 (1969).
- [21] M.A. Denecke, T. Reich, S. Pompe, M. Bubner, K.H. Heise, H. Nitsche, P.G. Allen, J.J. Bucher, N.M. Edelstein, D.K. Shuh, Differentiating Between Monodentate and Bidentate Carboxylate Ligands Co-ordinated to Uranyl Ions Using EXAFS, *J. Phys. IV France* 7, C2-637 (1997).
- [22] D.R. Lovley, E.J.P. Phillips, Y.A. Gorby, E.R. Landa, Microbial Reduction of Uranium, *Nature* 350, 413 (1991).
- [23] D.R. Lovley, Dissimilatory Metal Reduction, *Ann. Rev. Microbiol.* 47, 263 (1993).

- [24] M.A. Denecke, H. Friedrich, T. Reich, G. Bernhard, T. Kneiß, D. Rettig, T. Zorn, H. Nitsche, Determination of Relative Arsenite and Arsenate Concentrations in Aqueous Mixtures by XANES, *HASYLAB Annual Report 1996* 1, 751 (1997).
- [25] J. Petiau, G. Calas, D. Petitmaire, Delocalization Versus Localized Unoccupied 5f States and the Uranium Site Structure in Uranium Oxides and Glasses Probed by X-Ray Absorption Near-Edge Structure, *Phys. Rev. B* 34, 7350 (1986).

XAFS SPECTROSCOPY: A POWERFUL TOOL TO INVESTIGATE LOCAL STRUCTURE AND ELECTRONIC PROPERTIES

D.C. Koningsberger

Department of Inorganic Chemistry and Catalysis
Debye Institute, Utrecht University
P.O. Box 80083, 3508 TB Utrecht, The Netherlands

Abstract

The structural and electronic characterisation of a material provides a basic understanding of its properties. Traditionally, diffraction techniques (XRD, neutron diffraction, LEED) have been used for most of the structural investigations and reliable structures can be determined for materials that exhibit a long-range structural order (like single crystals or polycrystalline material). X-ray Absorption Fine Structure (XAFS) spectroscopy is a powerful technique to characterise all forms of matter irrespective of their degree of crystallinity. In this lecture the physical principles of XAFS will be given.

EXAFS (Extended X-ray Absorption Fine Structure) spectroscopy probes the local structure of a material. The local structure of highly disordered solids, amorphous materials and liquids can be unravelled with EXAFS. The EXAFS equation forms the basis of the data analysis. It will be shown how to obtain co-ordination parameters (N = co-ordination number, R = co-ordination distance and $\Delta\sigma^2$ = disorder) from the experimental EXAFS data.

In addition, the chemical state and the electronic properties can be determined from the X-ray Absorption Near Edge Structure (XANES) which extends within 40 eV of the X-ray absorption edge. It will be explained how the near edge structure can be used to derive the local symmetry of the X-ray excited atom.

Recently it has been shown that Atomical X-ray Absorption Fine Structure (AXAFS) forms part of the total X-ray absorption spectrum. The study of AXAFS is extremely powerful to derive information of interatomic potentials. AXAFS is determined by the “Through Coulomb Field” and the “Through Bond Inductive” effects. Examples will be given showing how nearest and next nearest neighbours can influence the interatomic potential of the X-ray absorbing atom.

EXPERIMENTAL ASPECTS OF X-RAY ABSORPTION SPECTROSCOPY

José Goulon

European Synchrotron Radiation Facility (ESRF)
Boite Postale 220, 38043 Grenoble, Cedex, France

Abstract

The information content of X-ray absorption spectra of actinides is expected to be particularly rich because, in such high Z elements, the very large core hole spin-orbit coupling results in a fairly long multiplet series of well separated absorption edges: K, L_I, L_{II}, L_{III}, M_I, M_{II}, M_{III}, M_{IV}, M_V, N_I, N_{II}, N_{III}, N_{IV}, N_V, N_{VI}, N_{VII}, O_I, O_{II}, O_{III}, O_{IV}, O_V. K and L edges are indeed most suitable for EXAFS studies, even in heavily absorbing matrices, whereas M, N, etc., edges are of remarkable interest for magnetic studies combining XMCD and RIXS spectra. From the experimental point of view, the spectral range to be investigated is huge since it starts from the very soft X-ray range to end up in the fairly hard X-ray domain ($E > 100$ keV). It is then becomes quite obvious that a wide variety of specific instrumentation needs to be developed if one wishes to take full advantage of the potential of third generation synchrotron radiation sources which are ideal for such experiments. The presentation will start with elementary recommendations on how to record high quality EXAFS spectra: design of stable optical components, rejection of unwanted harmonics by at least four orders of magnitude, careful preparation of homogeneous samples for transmission experiments, problems arising with radiation damages, etc. On the other hand, taking benefit of the long experience gained at the five ESRF public beamlines which are now operational and open to the users, I would like to emphasise the new technical opportunities which are offered by a 6 GeV third generation storage ring: access to the high energy K edges of high Z elements (e.g. at the ESRF bending magnet beamline BM29), exploitation of undulator sources to obtain a full control of the polarisation and perform very accurate XMCD experiments at the M_{IV-V} edges of actinides (ESRF beamline ID12A), optimisation of an undulator beamline to record EXAFS spectra on highly dilute samples or sample containing ppm trace amounts of absorbing elements (ESRF beamline ID26) with a possible extension towards the exploitation of microfocus beams, optimisation of time resolved experiments using an energy-dispersive optics (ESRF beamline ID24). New possibilities associated with the design of high resolution fluorescence spectrometers will also be illustrated.

THEORETICAL FRAMEWORK FOR DATA AND ERROR ANALYSIS AS APPLIED TO X-RAY ABSORPTION SPECTROSCOPY

Adriano Filipponi

Dipartimento di Fisica – Università dell' Aquila
Via Vetoio 67010, L' Aquila, Italy

Abstract

Modern X-ray absorption fine structure data analysis methods are based on theoretical calculations of the interference signals associated with clusters of atoms surrounding the selected photo-absorber species. The final state photoelectron wave-function is evaluated as a scattering state in a muffin-tin effective potential. Many body effects are included in the exchange and correlation part of the potential which has an imaginary component accounting for loss effects and in an empirical amplitude rescaling factor. The presence of multi-electron excitation thresholds can be taken into account using an empirical background shape.

The agreement between observed and calculated signals in the case of simple molecules of known structure is excellent, indicating the validity of the present theoretical framework. Multiple scattering effects, usually associated with triplets of atoms in nearly collinear configurations, are often observed and correctly accounted for by the present formalism. The XAFS signals can be calculated for the widest variety of structures including molecules, clusters, crystalline solids, both in the harmonic and non-harmonic vibrational state, but also for liquid systems where the structure is described by a set of partial radial distribution functions among the different atomic species.

In the case of unknown structures model spectra can be fitted to the experimental data refining unknown structural parameters. A rigorous statistical evaluation of the fitting results can be performed and, in favourable cases, the errors associated with the noise in the experimental data can be estimated.

The recent improvements in the experimental facilities and the adoption of an advanced method for data analysis have increased the potential of the X-ray absorption spectroscopy as a tool for structural investigations in physics, chemistry, biology and environmental science.

**INTRODUCTION TO X-RAY PHOTOELECTRON SPECTROSCOPY:
A COMPLEMENTARY TECHNIQUE TO X-RAY ABSORPTION SPECTROSCOPY**

V.I. Nefedov

Institute of General and Inorganic Chemistry
Russian Academy of Science
Moscow, Leninski pr. 31

Abstract

The general description of the XPS possibilities to investigate chemical compounds – particularly actinide compounds – is given. The binding energy of inner electrons is proportional to effective charge and oxidation number of actinides. The binding energy of valence levels gives a general picture of the electron structure. The estimation of 5f-electron numbers in actinide compounds and the determination of interatomic distances in uranyl compounds are possible using XPS data. The intensity of inner levels lines is proportional to the concentration of the elements and can be used for the quantitative analysis of actinides reactions with some minerals and the humic acid. The reaction products of uranyl with minerals are present mainly on the surface and contain uranyl group attached to the hydroxides and anions of mineral.

The humic acid reacts as a particle but not as a molecule, therefore the concentration of the ion under the investigation in bulk and on the surface depends on the nature of this ion. The Fe(III) ion inhibits the complex formation between uranyl and humic acid.

INTRODUCTION TO ACTINIDE INVESTIGATIONS WITH X-RAY TECHNIQUES BELOW 2 KEV

David K. Shuh

Actinide Chemistry Group, Chemical Sciences Division
MS 70A-1150, 1 Cyclotron Road
Lawrence Berkeley National Laboratory, Berkeley, CA 94720 USA

Abstract

The vacuum ultraviolet (VUV)/soft X-ray region of the synchrotron radiation spectrum has tremendous potential for the investigation of both fundamental and applied actinide science. Over the past decade, several workshops have recognised the scientific opportunities that would be made possible by the capability to investigate actinides in this energy region. However, technical difficulties related to safely handling radioactive materials and performing meaningful experiments with existing VUV/soft X-ray storage ring end stations have prevented such activities. Third-generation VUV/soft X-ray source characteristics of high brightness and flux, coupled with improved detectors and vacuum techniques, now provide extraordinary opportunities to exploit techniques in this energy region for the investigation of actinide materials. The synchrotron radiation methods in this energy region also have matured, permitting more complicated investigations and enabling new spectroscopic approaches. Of particular importance are the microspectroscopy and spectromicroscopy capabilities that will provide spatial information in addition to the high resolution spectroscopic data.

The primary methods to study actinide materials will be the complementary application of photoelectron spectroscopies, near-edge X-ray absorption fine structure (NEXAFS), and X-ray emission spectroscopy (XES). Resonant photoemission techniques capable of resolving the 5f electron contributions to actinide bonding along with angle-resolving measurements for band structure and surface structure determinations, have immediate applications. Furthermore, venerable angle-integrating core and valence band photoelectron spectroscopy will prove invaluable. Combined with results from NEXAFS measurements, this will provide the information needed to understand the electronic structure of actinide materials and their surface chemistries. The NEXAFS studies will also provide opportunities to extend theoretical modelling methods to the low-energy edges of the actinides. A new and useful consequence of third generation source development is the renaissance of XES techniques. XES is an atom specific probe, complementary to both photoemission and absorption, that is especially amenable to studies of buried and disordered materials systems. Thus, from a comprehensive multi-technique approach in this energy region, a significant understanding of actinide materials chemistry and physics may be obtained. Examples from each of the aforementioned techniques, as applied to actinide materials when available, will be presented. Future directions for the study of actinide science in this energy region will be discussed.

This work is supported by the Director, US Department of Energy, Energy Research, Office of Basic Energy Sciences, Chemical Sciences Division and Materials Sciences Division under Contract No. DE-AC03-76SF00098.

INTRODUCTION TO X-RAY DIFFRACTION AT SYNCHROTRON LIGHT SOURCES

Wolfgang Matz

Forschungszentrum Rossendorf
Institute of Ion Beam Physics and Materials Research
P.O.B. 51 01 19, D-01314 Dresden, Germany
E-mail: W.Matz@fz-rossendorf.de

Abstract

The physical basis of X-ray diffraction with synchrotron radiation is the same as for laboratory experiments with X-rays from conventional tube sources. The advantages and qualitatively new possibilities for X-ray diffraction at synchrotron light sources result mainly from the source quality (high intensity, broad, continuous wavelength distribution of radiation) and the radiation properties (low divergence, polarisation).

The lecture will give a general introduction to the information one can extract from diffraction patterns. An overview of the advantages from the use of synchrotron radiation in the fields of single crystal diffraction, energy dispersive powder diffraction, time resolved diffraction and magnetic diffraction will be given. In more detail the following topics will be discussed: high resolution powder diffraction, use of anomalous scattering in powder diffraction, diffraction studies on small samples (especially thin films) and diffraction on non-crystalline materials.

Introduction

The availability of dedicated synchrotron light sources for structural investigations over the last three decades has brought many new applications for X-ray diffraction. In 1995 the 100th anniversary of the discovery of X-rays by W.C. Röntgen was celebrated. It was only about 20 years after this discovery that the first application to structural studies was successfully performed by Laue. The theory of X-ray diffraction was quite well developed when synchrotron radiation became available as a research tool. In the field of X-ray diffraction the new sources allowed quantitative progress based on the brightness of the sources as well as on the specific properties of the radiation.

Principles of X-ray diffraction

For diffraction experiments with synchrotron radiation the same theory applies as when laboratory tube sources are used. The diffraction pattern results from the interference of the elastic scattering of the photons by individual atoms. The scattering centres are the electrons in the solid. Since the atomic arrangement is studied with detectors some centimetres away from the scatterers, and the wavelength as well as the interatomic distance are in the order of 0.1 nm, the observed intensity may be dealt with in the plane wave approximation. For the most frequent case of a crystalline powder sample the interference condition is given by the Bragg equation:

$$n\lambda = 2d \sin\vartheta$$

where λ is the wavelength of radiation, d is the net plane distance in the crystal and ϑ is the half scattering angle. The Bragg equation is a special case of the more general Laue equations. In the powder diffraction experiment the scattered intensity is recorded as function of the angle 2ϑ . According to the Bragg equation maxima are observed at distinct values of 2ϑ . The intensity of these maxima is determined by the crystal structure of the substance under investigation according to the following formula:

$$I(\vartheta) \propto LP \frac{j}{V_{EZ}^2} |F_{hkl}(\vec{\kappa})|^2 A(\vartheta) * \delta(\vec{\kappa} - \vec{\tau})$$

LP stands for polarisation and Lorentz factor, V_{EZ} is the volume of the unit cell, j is the multiplicity of the net planes, $A(\vartheta)$ is an absorption correction, and the delta-function represents the interference condition in more general vector form applicable also for single crystals. $\vec{\kappa}$ is the scattering vector and $\vec{\tau}$ the reciprocal lattice vector.

The structure amplitude F_{hkl} contains the main crystallographic information:

$$F_{hkl} = \sum_i f_i(\kappa, \lambda) e^{-W_i} \exp(-2\pi i(hx_i + ky_i + lz_i))$$

$f_i(\kappa, \lambda)$ is the atomic scattering factor of the individual atoms in the unit cell, x_i, y_i, z_i are the atomic positions, h, k, l the Miller indices of the reflecting plane, and W_i stands for a thermal factor which reduces the intensity due to thermal motion of the atoms. The sum runs over all atoms of the unit cell.

Diffraction peaks are observed at $\vec{\kappa} = \vec{\tau}$ and if $F_{hkl} \neq 0$. From the systematics of the peak positions the lattice type and the lattice constants are deduced. One gets a three-dimensional structure information from a two-dimensional record. The intensity of the peaks allows to determine the distribution of atoms within the unit cell.

Specific application fields of synchrotron radiation

Comparison of laboratory X-ray tube and synchrotron light

The new fields of application for X-ray diffraction using synchrotron radiation result mainly from the different source quality compared to a laboratory tube source.

The spectrum of the X-ray tube is composed of a bremsstrahlung continuum mainly determined by the acceleration voltage, and the emission line characteristic for the anode element. Mostly the intense K_{α} emission line is used. The brilliance of the line is about a factor of 100 higher than the maximum of the continuum and so only this line is used in the most diffractometers. The brilliance is the number of photons per second, unit area, unit space angle square, and 0.1% bandwidth of radiation. Only some metallic elements can be used technically for X-ray tubes and consequently the available wavelengths are quite limited. The X-ray tube is a source with high divergence that may reduce intensity at the sample significantly.

In contrast the spectra from bending magnets and wigglers at synchrotron radiation sources are smooth distributions of intensity at approximately the same brilliance of nearly three orders of energy. Undulator sources have some ripples in the spectrum but an intensity gain of up to five orders of magnitude compared to bending magnets. The brilliance of the light emission from an ESRF bending magnet is about seven orders of magnitude higher than the $Cu-K_{\alpha}$ line of a rotating anode source [1]. This high intensity is available in the broad range from 1-100 keV and not only at selected energies. Besides the broad spectral distribution and the much higher brilliance of the radiation the small divergence of the beam and the high polarisation are important properties for the X-ray diffraction. When comparing intensities from both source types incident on the sample one should be aware that the gain in brilliance from the source is partly lost because of the much greater distances between source and sample in the case of the use of synchrotron radiation.

White beam diffraction

The broad energy distribution of the synchrotron radiation and the high intensity make it attractive for white beam X-ray diffraction. The classical field of this technique is Laue photographs from *single crystals* allowing to fully solve the structure. The experimental set-up uses transmission geometry for the sample and an area detector (e.g. image plate). The diffraction spots originating from the different net planes by appropriate combinations of variable wavelength *and* variable scattering vector give a symmetric point pattern. The application field is mainly biology or life sciences (e.g. structure of proteins) and organic chemistry (structure of macromolecules). Today the evaluation of data can be automated so that similar structures can be solved rapidly. This development results in the project to install a “structure factory” at the synchrotron radiation source BESSY II for the human genome project.

Also in the field of *powder diffraction* the use of the white beam had made new research possible. The experimental arrangement uses an energy dispersive detector. In a polycrystalline

sample the Bragg equation is fulfilled for one fixed scattering angle with different wavelengths for the different net planes. High pressure experiments are a significant field of application. Here the very small sample is surrounded by a big chamber for generating pressures up to 100 GPa. Investigations of structures under high pressure are necessary to understand the materials behaviour in the earth's interior or to investigate phase diagrams under extreme conditions (e.g. crystallisation of gaseous elements). Another important field is time resolved diffraction. For the study of structural changes during phase transitions or chemical reactions it is possible to take series of diffraction patterns from powder samples with time steps below 10 seconds. This technique has been used for very practical problems, for example to study the hardening process in Portland cement [2].

Monochromatic beam diffraction

Most of the synchrotron beamlines use monochromatic radiation for the diffraction experiment. A crystal monochromator selects a wavelength (or energy) from the broad spectrum. Any desired wavelength can be selected, as the monochromator is tuneable. Typical energy resolutions of monochromators at synchrotron beamlines are $\Delta E/E \approx 10^{-3} \dots 10^{-4}$. Restricting to structural studies of crystalline samples the most important fields of application of synchrotron light are:

- Magnetic X-ray scattering.
- High resolution X-ray diffraction.
- Use of anomalous scattering.
- Thin film studies.

The scattering of X-rays from the atoms results from the electron cloud and is predominately charge scattering. The magnetic scattering amplitude is weaker by a factor $\hbar\omega/mc^2$, which results in an intensity drop of about 10^{-6} [3]. Thus the study of magnetic scattering apart from resonance effects became possible only at synchrotron sources. For applications of magnetic X-ray scattering we refer to other contributions at this conference. Examples for the other three above-mentioned fields will be given in the next section.

Powder diffraction with synchrotron radiation

High resolution powder diffraction

At synchrotron light sources of the third generation high resolution for powder diffraction is inherent because of the *low beam divergence* from the source. For this technique the instrumental resolution is defined by:

$$\frac{\Delta d}{d} = \frac{\Delta\lambda}{\lambda} + \Delta\vartheta \cot\vartheta$$

Here d is the net plane distance of the sample to be determined. The resolution depends on the wavelength sharpness and on an angular term in which ϑ is the Bragg angle for the scattering at the sample. $\Delta\vartheta$ is the beam divergence in the scattering plane which is small for synchrotron sources having a low divergence. The wavelength term is given by:

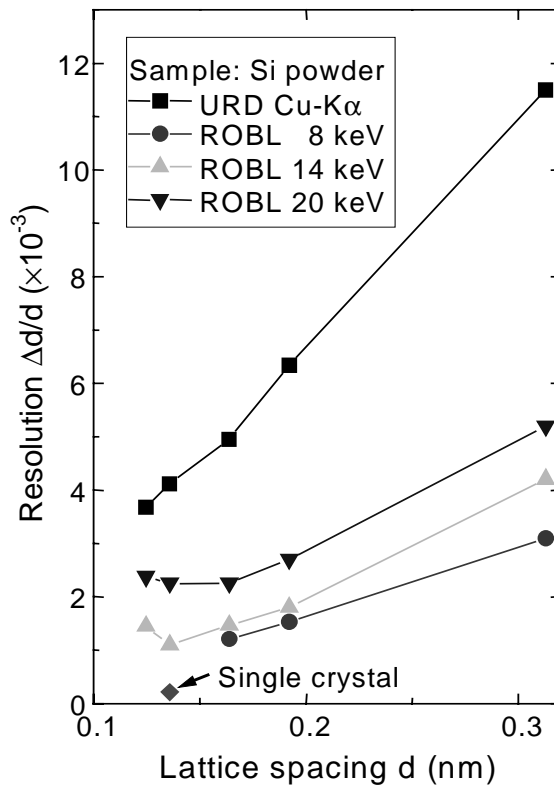
$$\frac{\Delta\lambda}{\lambda} = \cot\vartheta_M \sqrt{(\alpha^2 + \omega_M^2)}$$

where α is the source divergence (e.g. 50 μ rad at the ESRF bending magnet) and ω_M the intrinsic width of the reflection curve for the monochromator crystal (e.g. 40 μ rad for Si(111) planes at 8 keV).

The angular term is the dominating one as well for laboratory as for synchrotron diffractometers. As an example Figure 1 shows the resolution curves for the ROBL-MRH diffractometer. The curves are experimentally determined with silicon powder but they do not directly reflect the instrumental resolution. Measurements with a silicon single crystal show diffraction line width of 0.008° FWHM or slightly better. From this result it can be seen that the powder profile is already broadened by the sample crystallite size and that the instrumental contribution to the resolution is negligible for powder experiments. It should be mentioned that no special arrangements for high resolution have been made. A comparison to a standard laboratory X-ray diffractometer arranged for good resolution in Figure 1 shows the significant gain of synchrotron based diffractometers.

Figure 1. Experimentally determined diffraction resolution $\Delta d/d$ in dependence of the net plane distance d for different energies of the primary beam at ROBL MRH [4]

The most broadening comes from the crystallite size effects of the silicon powder samples as can be seen from the significantly lower resolution value obtained with a single crystal sample. For comparison the curve for a laboratory X-ray diffractometer URD-6, using Cu-K α radiation is given (detector slit 0.22).



The higher experimental resolution for diffraction expressed in a smaller FWHM of the Bragg peaks gives significantly better conditions at least in three fields:

- Structures with big unit cells: Separation of the many nearly overlapping peaks.
- Diffraction with short wavelength: The angular distance of peaks becomes smaller, however the higher resolution of the instrument allows good identification of a large number of different peaks.
- Conditions for Rietveld (structure) refinement are significantly improved. Here also the more symmetric line shape at the synchrotron is helpful.

In many cases the very high resolution of the instrument is not necessary and could be relaxed to get higher intensity. Then it is favourable to make use of the parallel beam experimental arrangement in which the small receiving slit positioned in front of the detector is replaced by soller slits receiving nearly all intensity scattered from an extended sample. The FWHM is now determined by the opening angle of the soller slits. Values of 0.1° are easily achievable. This is good resolution as compared to standard laboratory diffractometers and the technique is very well suited for thin film studies [5].

Use of anomalous scattering

Far away from absorption edges the scattering factor of an atom is proportional to the total number of electrons Z . The scattered intensity is then correlated with Z^2 . The smooth dependence of scattering power through the periodic table is often problematic for structure solutions. The most interesting cases are substances combined from neighbouring elements in the periodic table and substances containing light and very heavy elements. Many mathematical techniques have been developed for structure solution in the mentioned cases. The easy *tunability of the wavelength* of radiation at a synchrotron source opens an experimental access to study such structures by the use of anomalous scattering. Anomalous scattering denotes the fact that the scattering factor is composed from a scattering part f_1 and an absorption part f_2 .

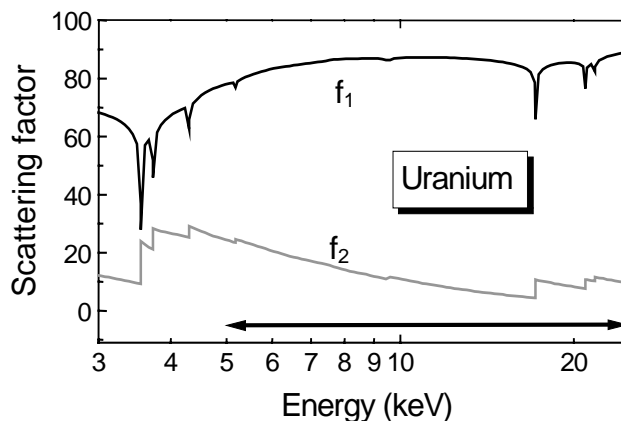
$$f = f_1 + if_2$$

Figure 2 shows the scattering factor for uranium as a function of the energy of X-rays. Near the absorption edges marked by steps in f_2 (L-edges above 17 keV; M-edges below 6 keV) the f_1 part shows a significant drop. By diffraction experiments with wavelengths (energies) at the absorption edge and away from the edge it is possible to realise a contrast variation technique. The scattering factor of uranium for example drops from 92 far from the edges to less than 70 at the L_{III} -edge (17.15 keV).

In order to illustrate the effect of contrast variation the diffractogram of CaUO_4 was calculated for an energy of 16 keV (0.0773 nm) away from absorption edges and for an energy of 17.15 keV (0.0722 nm) at the uranium L_{III} -edge. Since the scattering at the heavy uranium dominates the intensity of the diffractogram all intensities drop for the energy at the absorption edge. This means that the contributions of the light atoms O and Ca become more significant and it will be easier to determine their positions in the unit cell accurately. The different atomic species contribute dissimilarly to the reflections and so it is possible to extract the additional structure information when

Figure 2. Energy dependence of the two components f_1 and f_2 of the scattering factor of uranium [6]

The bar in the lower part indicates the energy range of ROBL [4]



using anomalous scattering. The table below gives the reduction of the structure factor (proportional to measurable intensity) for selected reflections in CaUO_4 when going from 16 keV to 17.15 keV in the diffraction experiment. This drop is only due to the reduction of uranium scattering while the contributions from Ca and O remain unchanged but are more significant for the anomalous scattering experiment.

Miller indices (hkl) for CaUO_4	(111)	(110)	(221)	(1-10)
Structure factor ratio (16 keV/17.15 keV)	0.52	0.65	0.48	0.705

For structure determination of actinide compounds by diffraction the use of thermal neutrons may be favourable. In this case the atomic scattering factor f is replaced by the scattering length b . The values of b have a variation range of $(0.2-1.4) \times 10^{-12}$ cm [7] which is much smaller than the variation range for f between 1 and 95 over the periodic table of elements. In addition the neutron scattering lengths are not correlated with the atomic number. Hence light and heavy elements may give nearly the same scattering contribution. For the above example of CaUO_4 the neutron scattering lengths (all in 10^{-12} cm) $b_o = 0.58$, $b_{ca} = 0.49$, and $b_u = 0.84$ are to be compared to the relation between the atomic scattering factor of the elements O, Ca, and U which are 8, 20 and 92, respectively. The structure factor of the (1-10) reflection is the sum of the scattering power of all atoms in the unit cell. To this peak the uranium contributes only 41% of the intensity for the neutron case while it contributes 87% and 81% for the X-ray cases at 16 keV and 17.5 keV, respectively. How much the use of neutron diffraction is significantly favourable compared to anomalous X-ray diffraction depends on the composition and structure of the substance under investigation.

It should be noted that besides the possibility of tuning the energy (wavelength) with synchrotron radiation the given high resolution is another prerequisite for using anomalous scattering with actinide compounds. The absorption edges are in the region of 15-20 keV, which results in smaller Bragg angles and hence smaller distances between the peaks in the diffractogram. The clear separation of reflections is needful for good structural information.

Thin film studies

Thin layers on a surface or directly beneath it (buried layers) are now widespread in technologically relevant materials. Applications fields are coatings (e.g. against corrosion, for hardening), surface modifications by energetic beams (e.g. formation of non-equilibrium compounds), nanostructures (e.g. in microelectronics or micromechanics). Also the reaction regions on surfaces during chemical processes are thin films in many cases. For the structural investigation of thin films by X-ray diffraction one has to deal with the problem to study the scattering from a small volume, and to separate it from the substrate scattering. Often depth gradients within the thin film play a role. The standard experimental technique is grazing incidence diffraction. The incident angle of the radiation is fixed to a low value in order to have penetration depths of the X-rays similar to the film thickness. In this case the substrate effects are significantly suppressed. Typical incidence angles are between 0.2° and 5° . If for example the sample has a length of 10 mm it accepts only a beam height of $175\ \mu\text{m}$ for an incidence angle of 1° . That means that from the primary intensity only a small fraction can be used for geometrical reasons. To realise this in the laboratory experiment one has to use a (quasi) parallel beam technique and to refrain from the focusing geometries normally used in powder diffraction on the X-ray tube. To get enough intensity the resolution is also poor. The gain of synchrotron radiation experiments for thin film studies consists in the following points:

- Nearly parallel beam.
- High intensity.
- Energy variation (to match the penetration depth to the film thickness).

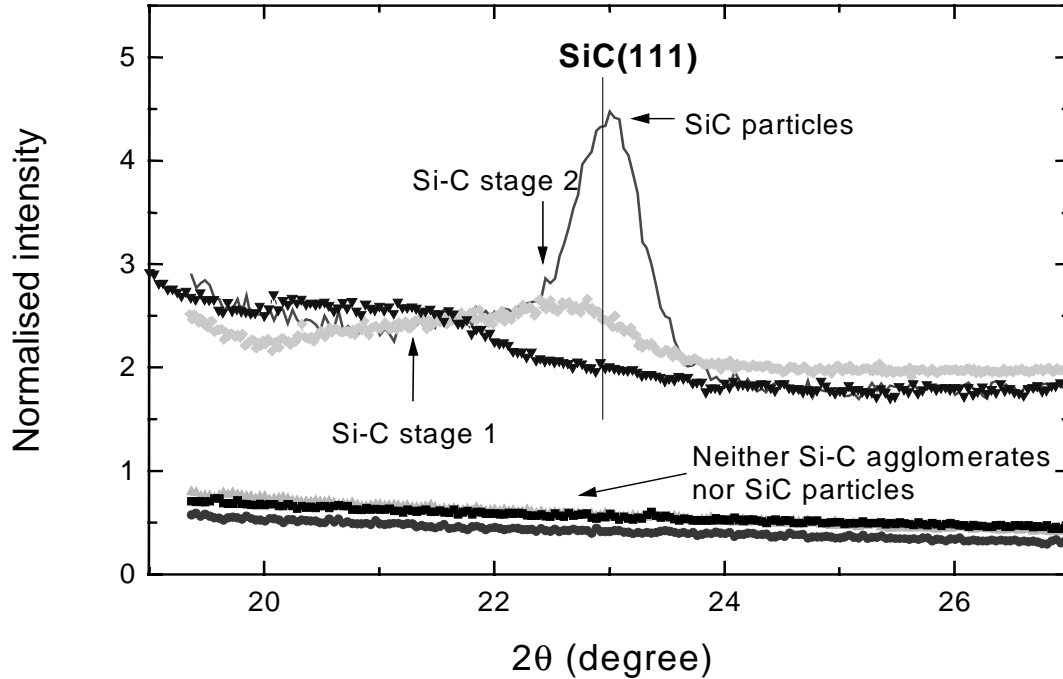
The two typical experiments with thin films are diffraction and reflectometry. In the diffraction experiment the information about the phase composition, atomic structure and possible phase changes with depth can be extracted. The set-up uses a constant incidence angle and a variation of the scattering angle 2ϑ in a wide range. It is an asymmetric arrangement. The reflectometry experiment in contrast has a symmetric beam path, the angles of incident and outgoing beams are identical and in the range of 0° to 5° . The reflectometry experiments yields information about layer thickness, atomic density of the layer and interface roughness.

In the diffraction experiment with synchrotron radiation the one possibility for a depth resolution is the variation of the incidence angle. The additional tunability of the energy allows the change of penetration depth at the same incidence angle. Because of the existence of absorption edges from the elements it is possible to combine depth selectivity partially with element selectivity.

As an example the results of a diffraction study of silicon single crystals implanted with C are presented. Carbon can act as a gettering centre in silicon in order to prevent the penetration of metallic impurities into the active volume of microelectronic devices. Additionally, there are efforts to produce single crystalline SiC layers in Si for the use of SiC as microelectronic component. By ion implantation of C into Si one can study the structural mechanisms of the gettering effect as well as the conditions of SiC phase formation. In the study [8] C ions with energies of 195 keV were implanted in Si(001) wafers. The implantation dose varied between 5×10^{15} ions/cm² and 4×10^{17} ion/cm² and the implantation temperature was between room temperature and 800°C . Figure 3 shows the diffraction curves in the vicinity of the most intense 3C-SiC(111) reflection obtained at ROBL-MRH [4]. In addition to the SiC Bragg peak the diffraction curves of the Si(400) were

Figure 3. Diffraction curves ($\vartheta:2\vartheta$ scans) in the vicinity of the most intense 3C-SiC(111) reflection indicating the formation of Si-C prestages and crystalline SiC particles.

Curves correspond to different implantation conditions. The line marks the position of the SiC(111) diffraction line according to the JCPDS-PDF data. For clarity the curves are shifted vertically in two groups. The lower group corresponds to $5 \cdot 10^{15}$ C ions/cm² at room temperature, 500°C, and 800°C. In the upper group the symbols denote: ∇ $5 \cdot 10^{16}$ ions/cm² (500°C), \diamond $4 \cdot 10^{17}$ ions/cm² (500°C), and $-$ $4 \cdot 10^{17}$ ions/cm² (800°C).



recorded. They reveal the lattice strain component perpendicular to the sample surface. Moreover, oscillations on both sides of the interference maximum, which are observable through the high resolution of the instrument, give information on the layer structure of the implanted region.

No intensity from SiC was detected in all the samples implanted with the lowest dose of 5×10^{15} ions/cm² in Figure 3. With increasing implantation dose (5×10^{16} ions/cm² to 4×10^{17} ions/cm²) and temperature (500-800°C) a diffraction line occurs starting with small intensity at the low-angle side and grows up to a true crystalline peak at the expected line position. The early form of Si-C Stage 1 agglomerates (5×10^{16} ions/cm²; 500°C) with an enhanced lattice spacing ($\Delta a/a = 0.07$ in comparison to the value of 3C-SiC) gives the wide peak in the SiC diagram. Such Si-C agglomerates with a diameter of 2 nm were suggested by TEM studies [9]. In the next stage (4×10^{17} ions/cm²; 500°C) one observes a relaxation of Si-C agglomerates in the Si lattice, the Stage 2 of the Si-C particle formation with an increased lattice spacing $\Delta a/a = 0.02$. Finally, crystalline 3C-SiC particles are found for a fluence of 4×10^{17} C ions/cm² at 800°C. They are aligned to the Si host lattice and surrounded by an expanded Si lattice. The SiC lattice itself is strained only negligible if the phase formation occurs during the high-temperature implantation process. This in contrast to the strained SiC particles ($\Delta a/a \approx 0.01$) which are formed only in the thermal treatment following the implantation [10].

Structure of non-crystalline materials

X-ray diffraction studies into the structure of non-crystalline materials can also profit from the use of synchrotron radiation. The experimental result is a structure factor $S(Q)$ measured for an interval Q_{min} to Q_{max} . Here Q is the modulus of the scattering vector ($Q = 4\pi\sin\vartheta/\lambda$). The radial distribution function of atoms is then calculated by a Fourier transform:

$$G(r) = \frac{2}{\pi} \int_0^{\infty} Q[S(Q) - 1] \sin(Qr) dQ$$

The function $G(r)$ gives the distance of neighbouring atomic shells and the number of atoms therein. It corresponds to the information gained by EXAFS, but is not connected with a specific atom at $r = 0$ as the EXAFS result measured at a specific absorption edge. The crucial point is the upper limit of the experiment Q_{max} which is far from infinity. The half width of the maxima in $G(r)$, which determines the resolution of peaks, depends on Q_{max} : $\Delta r \propto 1/Q_{max}$. With an Ag X-ray tube the laboratory experiment is limited to Q_{max} about 120 nm^{-1} while with 25 keV synchrotron radiation one reaches 160 nm^{-1} and with 35 keV radiation about 220 nm^{-1} if a maximum scattering angle of 140° is assumed. In addition to the significantly enhanced resolution in the radial distribution function the use of anomalous scattering at the synchrotron source offers the possibility to determine partial structure factors in multi-component systems by contrast variation [11].

Summary

For X-ray diffraction the synchrotron sources give new possibilities for investigation of atomic structure of condensed matter. Many new experiments are a quantitative advance of earlier work because of the higher brightness of the source (high intensity, low divergence) which allows work with higher resolution and on smaller sample volumes. Qualitatively new possibilities are opened by the tunability of the energy (wavelength) which allows anomalous scattering and thus a much higher degree of element specificity. In the meantime the experimental possibilities at laboratory X-ray diffractometers have improved significantly with technical developments. Thus, X-ray diffraction experiments on synchrotron sources should concentrate on problems where at least one of the superior qualities of the source apart from intensity is necessary. The beam time at synchrotron sources is severely limited, and in the laboratory there is independence over experimental schedule.

Acknowledgements

The author thanks his colleagues F. Prokert, F. Eichhorn, N. Schell and J. Claußner for supporting the preparation of the lecture with experimental data and figures.

REFERENCES

- [1] ESRF Highlights 1995/1996, p. 64, Grenoble, 1996.
- [2] P. Barnes, A.C. Lewis, X. Turillas, C. Hall, *et al.*, ESRF Annual Report 1994/95, p. 15.
- [3] M. Alterelli, in Neutron and Synchrotron Radiation for Condensed Matter Studies, Vol. I, J. Baruchel, J.L. Hodeau, M.S. Lehmann, J.R. Regnard, C. Schlenker, eds., Springer, Berlin, 1993, p. 263.
- [4] W. Matz, F. Prokert, R. Schlenk, J. Claußner, N. Schell, F. Eichhorn, G. Bernhard, The Rossendorf Beamline at the ESRF (Project ROBL), Internal Report FZR-158, Forschungszentrum Rossendorf, November 1996.
See also: http://www.fz-rossendorf.de/FWE/project_group.html
- [5] C.R.A. Catlow, in Applications of Synchrotron Radiation, C.R.A. Catlow and G.N. Greaves, eds., Blackie, Glasgow and London, 1990, p. 39.
- [6] Centre of X-Ray Optics Database: <http://www-cxro.lbl.gov>.
- [7] Int. Tables for Crystallography, A.J.C. Wilson, ed., Vol. C, pp. 384-391, Kluwer, Dordrecht 1992.
- [8] F. Eichhorn, N. Schell, W. Matz, R. Kögler, submitted to *Appl. Phys. Letts.*
- [9] P. Werner, S. Eichler, G. Mariani, R. Kögler, W. Skorupa, *Appl. Phys. Letts.* 70 (1997) 252.
- [10] U. Preckwinkel, J.K.N. Lindner, B. Stritzker, B. Rauschenbach, *Nucl. Instrum. Methods Phys. Res. B* 120 (1996) 125.
- [11] W. Matz, W. Hoyer, in Amorphous Structures, Methods and Results, D. Schulze, ed., Physical Research, Vol. 12, Akademie-Verlag, Berlin, 1990, p. 63.

X-RAY SCATTERING APPLIED TO MAGNETISM OF THE ACTINIDES

G.H. Lander

European Commission, JRC, Institute for Transuranium Elements
Postfach 2340, D-76125 Karlsruhe, Germany

Abstract

Photons are scattered only very weakly by magnetic moments (some 10^{-6} less on average than they are scattered by the electron charge) so the observation of magnetism with photon beams always resembles a tour-de-force experiment, and is difficult even with today's new synchrotron sources. On the other hand, what has been discovered is that this small cross-section becomes appreciably, and in some cases enormously, enhanced when the photon energy is tuned to a particular absorption edge of the magnetic element in the material. This, and the development of the related theories, has led to a large number of experiments in dichroism and scattering at synchrotrons using photons tuned to the resonances. Obviously, the information is element specific, but it also gives new information about magnetic materials that was not previously available. For scattering experiments, in particular, the information is complementary to that obtained by neutron scattering.

The enhancement of the resonant scattering for f electron systems is particularly marked at the M edges. In the lanthanides these edges are at too low an energy (below 2 keV) to be useful for conventional scattering experiments (which must obey Bragg's law), but these requirements are satisfied for the actinides (3.5 to 5 keV). Thus many pioneer experiments have been performed with actinide samples that are simply not possible with magnetic elements in other parts of the periodic table.

This report will explain the effects and give a number of examples, mostly from the ID20 beamline at the ESRF, at which some of the forefront experiments are being performed.

Acknowledgements

Many collaborators are involved in this study. I would like to acknowledge, N. Bernhoeft (ILL), D. Gibbs (BNL), W. Stirling (U. of Liverpool), C. Vettier (ESRF) and G. Watson (U. of Maryland).

MOLECULAR MODELLING OF ACTINIDE COMPLEXES

U. Wahlgren, B. Schimmelpfennig, L. Maron, V. Vallet

Institute of Physics, Stockholm University
P.O. Box 6730 S-113 85 Stockholm, Sweden

I. Grenthe

Department of Chemistry, Inorganic Chemistry
The Royal Institute of Technology
Teknikringen 30, 10044 Stockholm, Sweden

O. Gropen

Institute of Mathematical and Physical Science
University of Tromsø
N-9037 Tromsø, Norway

Abstract

Actinides present a new challenge to theoretical chemistry for two reasons: the large relativistic effects and the active role of the 5f-orbitals in molecular bonds. In the present contribution we first focus on the methods, using the reduction of uranyl(VI) by the addition of hydrogen as an example. Several methods were used in this work, including both the regular MO schemes including correlation and the Density Functional Theory (DFT) method. A model reaction where the hydrogen is provided by water is found to be only slightly endothermic. Spin-orbit effects on reduced UO_2^{2+} have been calculated. The effect on the energetic of the reaction is substantial.

The second part of the study concerns the structure of dioxouranium(VI) in strongly alkaline surroundings. The results are compared with newly obtained EXAFS data. We find that although our computed bond lengths are too long, observed experimental trends are reproduced.

Introduction

The chemistry of the 5f elements is in many aspects very different from that of the 4f elements and of the other transition elements; examples being the large number of chemically accessible oxidation states for the pre-curium elements and the formation of linear dioxo-actinoid (V or VI) ions. It is reasonably easy to obtain quantitative chemical information on thorium and uranium, while special experimental facilities are required to obtain such information for the other elements. The chemical properties for the other actinide elements for a given oxidation state are often found to vary in a predictable way, making it possible to use correlations of various types to obtain estimates of the chemical properties of all these elements based on experimental data from a few of them. The chemistry of those elements represents a challenge for both experimental and theoretical chemists. In this paper we will describe the extension of current quantum chemical methods to some particular chemical problem for actinides, including a comparison between experimental and theoretical data. The theoretical calculations are not straightforward, but the way has been partly paved by a number of previous investigations.

It is well known that actinide chemistry is an area with many important applications, for example reprocessing and nuclear waste management. To take the latter area as an example; understanding of the interactions between spent nuclear fuel and intruding ground water, including radiolysis products, is necessary for the analyses of the function and safety of repositories for high-level radioactive waste. This requires prediction of the chemical behaviour of actinides, which must have a sound theoretical basis.

Theoretically, there are a number of difficulties that are particular to the actinides. They are very heavy, which means that relativistic effects are important, if not dominant, and must be accurately accounted for. The electronic structure involves a partly filled f-shell, which means that all complexes except the simplest ones will have highly complex electronic structures. Furthermore, the 5f shell is more diffuse than the 4f shell, and can participate actively in the bonding. Another property specific for the actinides is, as pointed out by Pyykkö [1], that what in lighter elements normally is considered the outer core (i.e. the 6s and the 6p atomic orbitals in the actinides) is highly polarisable and must be treated as valence orbitals in calculations. The number of electrons, which have to be included in a calculation thus, becomes quite large, which makes accurate calculations using standard correlation methods difficult.

The 5f participation in the actinide bonding is nicely illustrated by the actinyl(VI) ions, which are doubly charged, stable, symmetric, linear di-oxygen ions with a VI-valent actinide at the centre. Stable actinyls of this kind exist in the sequence uranium to americium. The increased nuclear charge stabilises the 5f orbital along the actinide series. The electronic configuration for the atomic ground state in this sequence is for U $5f^3 6d^1 7s^2$, for Np $5f^4 6d^1 7s^2$, for Pu $5f^6 6d^0 7s^2$ and for Am $5f^7 6d^0 7s^2$, showing the gradual stabilisation of the 5f orbital as we move to the right along the actinide series. As the 5f orbital starts to compete with the 6d orbital it mixes into the molecular bonds and participates actively in the bond formation, giving rise to the characteristic doubly charged dioxo ions for U-Am. After Am the 5f orbitals have become so stabilised that no more such ions can be formed. The stabilisation of the 5f orbital is also demonstrated by the oxidising properties. Uranyl(VI) is very stable while it is easier to reduce plutonyl(VI) than uranyl(VI), a fact that is used in the nuclear waste separation process. The AmO_2^{2+} ion is strongly oxidising and only stable in a reducing environment. It is thus very important to be able to describe the f-orbitals in a satisfactory manner in theoretical calculations on the actinides.

The bonding in actinide complexes differs in more respects from the usual bonding in lighter systems. Due to the relativistic effects, the 7s orbitals in the actinides tend to become stabilised and the high angular momentum orbitals destabilised compared to less relativistic systems, which affects the binding properties. In ThO, for example, the bonding takes place primarily between the Th d and the O p_z orbitals while the Th 7s orbital becomes a diffuse lone pair [2]

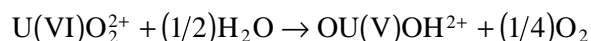
The unusual polarisability of the outer core orbitals mentioned above gives rise to difficulties in theoretical calculations, at least at the conventional MO-level, in that the outer core electrons must be included in CI calculations. As an example, at least 24 electrons (the oxygen 2s and 2p and the uranium 6s, and 6p orbitals) have to be correlated in UO₂²⁺, and 26 electrons in PuO₂²⁺.

Two conclusions emerge from this list of difficulties and unusual properties. The first is the need for simplifications, such as local density methods, and the second is the need to assess the accuracy of necessary approximations. For example, the MP2 and CASPT2 [3,4] methods are fast and easy to apply, but there is hitherto little experience as to how accurate these methods are for actinide complexes. Certainly, the MP2 and CASPT2 methods suffer from the same drawbacks as ordinary Hartree-Fock methods in that they are limited by the need to calculate all two-electron integrals.

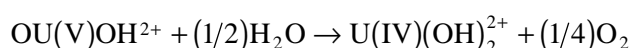
Local density methods have been used in calculations on UO₂²⁺ complexes, but again it is difficult to assess their accuracy [5]. In an investigation by Ismail, *et al.* [6] it is concluded that for uranyl(VI) the hybrid method B3LYP seems to give reasonable results for spectroscopic constants on uranyl(VI) and plutonyl(VI), while the pure DFT functional BP86 gives a bent uranyl(VI). However, in view of the large number of electrons and the problems encountered with perturbation methods (MP2 and CASPT2; in the study quoted above uranyl(VI) became bent with the supposedly more accurate MP4 method), DFT-type methods will probably prove to be a necessity. Results published by Gagliardi, *et al.* [7] appear to be promising.

In this communication we will describe the use of theory in two areas of “practical” importance. The first area deals with the redox transformation between uranium(VI) and uranium(V) and (IV), which is important for the integrity of spent nuclear fuel in contact with ground water, and for the mobility of other actinides in ground water systems. The reason is that actinide(IV) compounds are very insoluble while most actinide(VI) systems are soluble. The theoretical problem is difficult and our model calculations represent only the very first step required for the understanding of such redox reactions.

The model reaction we chose to study was the reduction of uranium(VI) in uranyl by water first to U(V) and then to U(IV):



and



During the first reaction, the uranyl ion is reduced from VI to V by adding one electron into an open f-shell, and during the second uranium is further reduced to IV by adding a second f-electron. This type of reduction is known to take place in photochemical reactions, although no reduction has been observed in neutral water. The two reactions studied are of interest since they represent the

initial and final states in the photochemical reduction and also serve as a very simple model for actinide reduction by hydrogen transfer. It is also well known that dioxo ions after uranium are more easily reduced than uranyl(VI), and we have also calculated the corresponding reaction energies for PuO_2^{2+} . Our results clearly show the plutonyl reactions to be energetically much more favourable than the uranyl reactions, in agreement with experiment. However, in the present study we concentrate on the methodological aspects of the two reactions, and the plutonyl reduction process will be presented elsewhere.

The second area deals with predictions of the co-ordination of actinide complexes. This is important because all reprocessing technologies are based on selective complex formation. The mobility of actinides in nature is also strongly influenced by the type of complex formed in ground water systems. Chemical information on the structure and bonding of such compounds is therefore extremely useful. By comparing experimental data and theoretical predictions, one might be able to replace difficult and costly experiments by calculations. We will exemplify this by a theoretical and experimental study of complexes formed by uranium(VI) in strongly alkaline solutions.

Initially, the problem concerned the structure of $\text{UO}_2(\text{OH})_4^{2-}(\text{aq})$, with the hypothesis that uranyl(VI) could, due to the stabilising effect of the uranium f-orbitals, co-ordinate two hydroxide ions and one “oxo” type oxygen in a trigonal bi-pyramid configuration. In this study, we investigated the possible conformations of the complex in the trigonal bi-pyramid configuration stabilised by two water molecules, and co-ordinated by four hydroxide ions and a water molecule. The two systems are iso-electronic, which minimises errors associated with the computational procedures used. We also made calculations on $\text{UO}_2^{2+}(\text{aq})$ in a neutral solution, using $\text{UO}_2(5\text{H}_2\text{O})^{2+}$ as a model. Uranyl complexes with nitrate and sulphate ligands have been studied previously using ECP, MP2 and DFT [5].

The structure of $\text{UO}_2(5\text{H}_2\text{O})^{2+}$ was known at the time this study was started, but no structural information of the complexes formed in strongly alkaline solutions was available. Later EXAFS experiments were successfully carried out also in strongly alkaline solutions, resulting in structural information. These results are presented in a separate report [8].

The calculations were carried out on isolated ions, without any stabilising external medium representing the bulk of the solution. This is, of course, a rather crude model of the complex in solution, but the relative energies should nevertheless provide a solid guideline to the relative stability of the complexes. However, one should not put too much emphasis on absolute numbers. Although all calculated bond distances are too long by up to 0.1 Å, observed trends are well reproduced by the theoretical calculations. The error in the experimental determination of co-ordination numbers is fairly large. Hence, theoretical calculations may provide important additional information when selecting the “best” mode. Bond distances determined by EXAFS are much more precise and will thus be important for model validation. The most stable configuration obtained from the theoretical calculations is a four co-ordinated uranyl with one water molecule at long distance.

Technical details

All molecular orbital-based calculations presented in this report were done using the MOLCAS4 [9] program package. Scalar relativistic effects (i.e. all relativistic effects except for spin-orbit coupling) were described using the no-pair equation deduced from the Douglas-Kroll transformation [10]. The implementation of the no-pair DK equation was done using the procedure outlined by Hess [11].

The molecular orbital calculations were done using a variety of methods: SCF/RASSCF, the approximately size-consistent ACPF method [12] and CCSD(T). At the all-electron level, we used the primitive 24s, 19p, 14d and 11f functions by Faegri [13], contracted to 9s, 8p, 7d and 5f-functions using Rafenetti's general contraction scheme [14]. For oxygen, we used the primitive 9s, 5p basis set suggested by Huzinaga [15], augmented by one diffuse p-function and one d-function, contracted to 3s, 4p and 1d using the Rafenetti scheme. Hydrogen, finally, was described by Huzinaga's 5s, basis contracted to 3s, with one diffuse p-function.

In order to reduce the size of the problem, the calculations on the uranyl(VI) complexes in solution were done using the AIMP method suggested by Huzinaga, Seijo and Barandarian [16,17]. The core used in the AIMP on uranium consisted of the 1s, 2s, 3s, 4s, 2p, 3p, 4p, 3d, 4d and 4f atomic orbitals, leaving 32 valence electrons in neutral uranium. The AIMP basis set was constructed by a least square fit to the all-electron atomic orbitals, using 15s, 12p, 10d and 7f, contracted to 5s, 5p, 4d and 3f using the Rafenetti scheme. Oxygen and hydrogen were described at the all-electron level. The AIMP was determined for the ground state of the neutral uranium atom.

The geometry optimisations were done at the SCF level using gradient techniques, with symmetry constraints, and relativistic effects were included at the full DK level. The final energies for the various configurations were calculated at the MP2 level at the optimised SCF geometries. The CI effects on the internal dioxouranium bond distance is quite large, a lengthening of 0.05-0.07 Å, but test calculations at the MP2 level showed only small effects on the properties of the complexes (except of course for the expected lengthening of the internal dioxouranium bond).

Results and discussion

Reduction of uranium(VI)

Optimised geometries for UO_2^{2+} various levels of approximation are shown in Table 1.

Table 1. Optimised UO_2^{2+} geometries. Distances in Å.

Method	Level	g-functions	re(Ångström)
AE	SCF	No	1.6518
AE	SCF	Yes	1.6471
AE	ACPF	No	1.7162
AE	ACPF	Yes	1.7116
AE	CCSD(T)	Yes	1.7059
AE	CASPT2	Yes	1.7276
AIMP	SCF	Yes	1.6269

If we first consider the all-electron results, it is clear that the sensitivity to the inclusion of two g-functions at the correlated is relatively small, a shortening of 0.005 Å. However, it is surprising that the effect at the SCF level is of the same magnitude, since the effect of basis functions with higher l quantum numbers usually is much larger at the correlated level than at the SCF level. The g-functions cannot, for parity reasons, mix with the f-functions in the bond, and the effect must thus largely be hybridisation of the d-functions. This conclusion is consistent with the previous results on ThO [2], where the bond was the result of an interaction between Th(d) with O(p) orbitals, with the Th(7s) function forming a non-interacting lone-pair orbital.

The effect of correlation on the bond is significant, resulting in a bond lengthening of 0.06-0.08 Å. For lighter elements, this would be a strong indication of near-degeneracy effects (a large static correlation contribution), which normally are manifested in strong interaction between bonding and (empty) anti-bonding orbitals. No local effects of this type, however, could be seen in uranyl(VI).

The agreement between the ACPF and the more accurate CCSD(T) calculations is quite satisfactory, showing that ACPF gives good results even though the number of correlated electrons is large. The CASPT2 calculation is done using a single, closed shell reference state, and bearing this fact in mind the CASPT2 result is more than satisfactory.

The bond distance obtained at the AIMP level is 0.02 Å too short, which is a satisfactory result.

The reduced species OUOH^{2+} is linear, which shows that the binding is ionic. In Table 2 we can see that the differences between the different levels of calculation are larger than in the case of uranyl(VI).

Table 2. Calculated geometries for OUOH^{2+} . Distances in Å.

Method	Level	g-functions	r(O1-U)	r(O2-U)	r(O2-H)
AE	SCF	No	1.6828	1.8992	0.9206
AE	SCF	Yes	1.6768	1.8892	0.9705
AE	ACPF	No	1.7527	1.9388	0.9937
AE	ACPF	Yes	1.7344	1.9236	0.9902
AE	CASPT2	Yes	1.7475	1.8918	1.0040

While the ground state of UO_2^{2+} is a closed shell $^1\Sigma^+$, both reduced species have open shells. When the first hydrogen approaches uranyl and the O-H bond forms, an electron is transferred into an essentially atomic 5f orbital with a magnetic quantum number of 3 on uranium, giving rise to a $^2\phi$ state for OUOH^{2+} . Since the open orbital has atomic character, this result follows the expectations from Hund's rules.

The geometry trends resemble those of UO_2^{2+} . The effect of the g-functions is similar and correlation lengthens the bond between the uranium and the oxygens, although not as much as for UO_2^{2+} . The geometry obtained using CASPT2 shows rather large deviations for the hydroxide ion compared to ACPF. However, the bond is long and rather weak, and considering the low level of the CASPT2 (one reference state) the result is still satisfactory.

The final case, U(IV) in $\text{U}(\text{OH})_2^{2+}$, is shown in Table 3.

Table 3. Calculated geometries for $\text{U}(\text{OH})_2^{2+}$. Distances in Å.

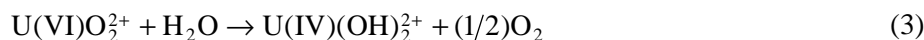
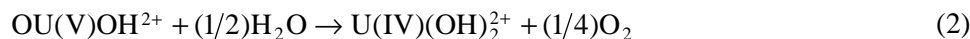
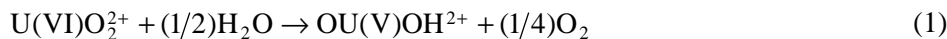
Method	Level	g-function	r(U-O)	r(O-H)
AE	SCF	No	1.9715	0.9603
AE	SCF	Yes	1.9623	0.9605
AE	ACPF	No	1.9823	0.9817
AE	ACPF	Yes	1.9652	0.9832
AE	CASPT2	Yes	1.9457	0.9907

The ground state of the $\text{U}(\text{OH})_2^{2+}$ ion is ${}^3\text{H}_g$, with the two unpaired electrons occupying f-orbitals with magnetic quantum number 3 and 2. This result is again as expected from Hund's rules. As in the case of OUOH^{2+} , the open shells are predominantly atomic f-functions and the ground state of the atom is, as expected, ${}^3\text{H}$. Ismail, *et al.* [6] obtained the same ground state for the iso-electronic plutonyl ion, while Craw, *et al.* find a ${}^3\Sigma^-$ ground state. In an all-electron calculation on plutonyl, PuO_2^{2+} , we find the same ground state as for $\text{U}(\text{OH})_2^{2+}$, in agreement with the result of Ismail, *et al.* This result supports our assignment for $\text{U}(\text{OH})_2^{2+}$.

It should be mentioned that since we use real basis functions, our ground state consists of two configurations with equal weight.

In $\text{U}(\text{OH})_2^{2+}$ the U-O distance becomes further lengthened when compared to UO_2^{2+} and the uranium-hydroxide bond in OUOH^{2+} . As in the case of OUOH^{2+} the CASPT2 gives a somewhat shorter U-O distance and a somewhat longer O-H distance.

The reaction energies for the reactions:



are shown in Tables 4-6.

The most important result from the tables is that the CASPT2 calculations, using a single reference state (in fact the reference state for $\text{U}(\text{OH})_2^{2+}$ consists of two determinants, but only for technical reasons; in a complex basis the reference state is described by one determinant), are satisfactory compared to the ACPF and, when applicable, the CCSD(T) results. This is an important result since it is impossible to use anything more complicated than CASPT2 with a very small reference space for larger systems. In the subsequent section, which deals with the structure and relative stability of uranyl(VI) complexes in solution, the energies have been calculated at the MP2 (which in that case is equivalent to CASPT2) level.

Table 4. Reaction energies for the reaction $\text{U(VI)}\text{O}_2^{2+} + (1/2)\text{H}_2\text{O} \rightarrow \text{OU(V)}\text{OH}^{2+} + (1/4)\text{O}_2$

The energy is calculated as (RHS)-(LHS) in the reactions, i.e. a positive ΔE means that the reaction is endothermic. Energies in kcal/mol.

Level	g-function	ΔE	Reaction
SCF	No	-7.04	Exoth.
SCF	Yes	-5.02	Exoth.
ACPF	No	9.90	Endoth.
ACPF	Yes	9.71	Endoth.
CCSD(T)	Yes	11.36	Endoth.
CASPT2	Yes	13.68	Endoth.

Table 5. Reaction energies for the reaction $\text{U(V)OH}_2^{2+} + (1/2)\text{H}_2\text{O} \rightarrow \text{U(IV)(OH)}_2^{2+} + (1/4)\text{O}_2$

The energy is calculated as (RHS)-(LHS) in the reactions, i.e. a positive ΔE means that the reaction is endothermic. Energies in kcal/mol.

Level	g-function	ΔE	Reaction
SCF	No	-33.17	Exoth.
SCF	Yes	-27.95	Exoth.
ACPF	No	1.93	Endoth.
ACPF	Yes	5.66	Endoth.
CASPT2	Yes	1.10	Endoth.

Table 6. Reaction energies for the reaction $\text{U(VI)O}_2^{2+} + \text{H}_2\text{O} \rightarrow \text{U(IV)(OH)}_2^{2+} + (1/2)\text{O}_2$

The energy is calculated as (RHS)-(LHS) in the reactions, i.e. a positive ΔE means that the reaction is endothermic. Energies in kcal/mol.

Level	g-function	ΔE	Reaction
SCF	No	-40.21	Exoth.
SCF	Yes	-32.97	Exoth.
ACPF	No	11.83	Endoth.
ACPF	Yes	15.37	Endoth.
CASPT2	Yes	14.25	Endoth.

One remarkable feature emerging from Tables 4-6 is that correlation destabilises the reactions substantially, by nearly 50 kcal/mol for the reaction $\text{UO}_2^{2+} + \text{H}_2\text{O} \rightarrow \text{U(OH)}_2^{2+} + (1/2)\text{O}_2$. This amount of correlation energy is much larger than the difference in correlation between H_2O and $(1/2)\text{O}_2$, which is only about 10 kcal/mol. Looking at only the uranium system, the total correlation energy in UO_2^{2+} is 523 kcal/mol while it is only 487 kcal/mol in U(OH)_2^{2+} , at the correlated equilibrium geometry, a difference of 36 kcal/mol favouring UO_2^{2+} . This is an unexpected result since there are two more electrons in U(OH)_2^{2+} compared to UO_2^{2+} . This effect can be explained by the binding properties of these systems. The U-O bond in UO_2^{2+} can be described as a triple bond, mainly between uranium d-orbitals and oxygen p-orbitals, strongly stabilised by the uranium f-orbitals. From the population analyses it follows that the 6d and 5f orbitals contribute 1.6 and 2.4 electrons to the bonding in UO_2^{2+} , while the corresponding numbers in U(OH)_2^{2+} are 0.8 and 0.7. The correlation contribution from d- and f-contribution in the bonds is large, and can, together with the fact that two triple bonds are broken and replaced by single bonds, balance the increased correlation from the negative hydroxides and the two unpaired f-electrons.

We have calculated the effect of spin-orbit interaction for the reaction:



The spin-orbit effect on $\text{U}(\text{OH})_2^{2+}$ lowers the energy of the ground state by of 13 kcal/mol, making the global reaction essentially thermoneutral (endothermic by 2 kcal/mol). Since UO_2^{2+} has a closed shell ground state, there is only a small second order spin-orbit effect affecting the initial state in the reaction.

The UO_2^{2+} ion in a strongly alkaline solution

The present study was undertaken prior to the experimental EXAFS work on UO_2^{2+} in strongly alkaline solutions had been done by Moll, *et al.* [8]. The problem initially posed was if UO_2^{2+} in a strongly alkaline solution can co-ordinate four hydroxide ions and one water molecule in an essentially pentagonal bi-pyramid structure or if an oxo-oxygen and two hydroxide ions in an essentially trigonal bi-pyramid structure is more stable.

Our model of the UO_2^{2+} complexes is a doubly negative complex, $[\text{UO}_2(\text{OH})_4 \cdot \text{H}_2\text{O}]^{2-}$ for the pentagonal bi-pyramid structure and $\text{UO}_2\text{O}(\text{OH})_2^{2-} \cdot 2\text{H}_2\text{O}$ for the trigonal bi-pyramid structure, without any additional stabilising counter-ions or water molecules. This is a rather crude model considering the fact that the complex is charged and surrounded by a solvent.

The reason for using the complex $\text{UO}_2\text{O}(\text{OH})_2^{2-} \cdot 2\text{H}_2\text{O}$ rather than just $\text{UO}_2\text{O}(\text{OH})_2^{2-}$ as the model for the trigonal case is that $\text{UO}_2\text{O}(\text{OH})_2^{2-} \cdot 2\text{H}_2\text{O}$ and $[\text{UO}_2(\text{OH})_4 \cdot \text{H}_2\text{O}]^{2-}$ are isomers, which makes the comparison of energies straightforward.

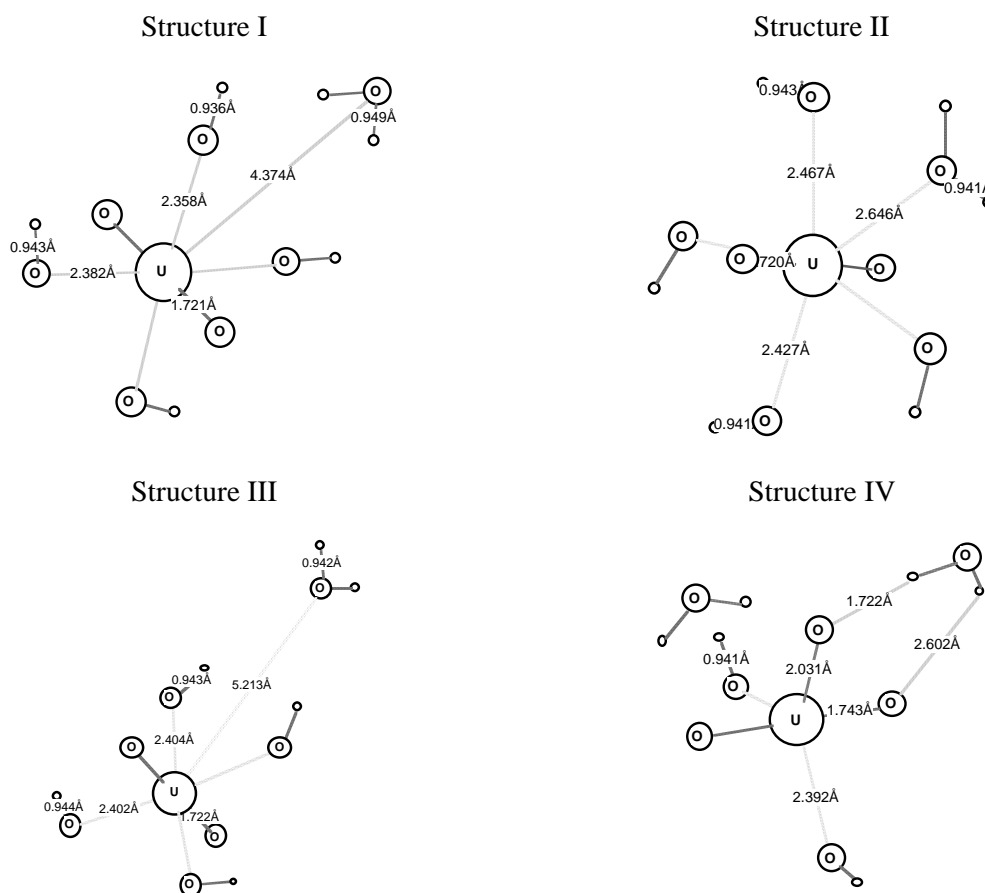
All geometries were optimised using gradient techniques. The overall symmetry was in all cases constrained to C_{2v} , and the geometries were optimised at the self-consistent field (SCF) level of approximation using an AIMP description of the uranium atom and a full Douglas-Kroll formalism to include scalar relativistic effects. The hydroxide hydrogens were, in all cases, constrained to lie in the equatorial plane. We did not investigate any other orientation of the hydrogens, as the distances make it very likely that the rotational barrier of the co-ordinated hydroxide ions should be low. Considering that our model is rather crude, these approximations and restrictions are reasonable. In particular, a complete unrestricted geometry optimisation does not seem meaningful. The optimised geometries are shown in Figure 1.

Our assumption that the barrier to internal rotation of the hydroxide hydrogens is small has been confirmed in a very recent DFT study on $[\text{UO}_2(\text{OH})_4]^{2-}$ by Schreckenbach, *et al.* [18].

Three different structures of the $[\text{UO}_2(\text{OH})_4 \cdot \text{H}_2\text{O}]^{2-}$ were investigated, one with the hydrogens of the water molecules pointing toward the dioxouranium oxygens (Structure I), one with the water molecule perpendicular to the equatorial plane with the oxygen pointing towards the uranium (Structure II) and the last one with the water molecule in the equatorial plane with the hydrogens pointing towards the neighbouring hydroxide ions (Structure III). The trigonal bi-pyramid complex is also shown in Figure 1 (Structure IV).

Structures I and III are clearly four co-ordinated, with one water molecule at very long distance, while Structure II is penta co-ordinated in the equatorial plane. Comparing the energies of these three structures, Structure I is the lowest, followed by Structure II (Table 6). The fact that the most stable

Figure 1



$[\text{UO}_2(\text{OH})_4 \cdot \text{H}_2\text{O}]^{2-}$ cluster is four co-ordinated actually suggests that even more stable configurations might be obtained if the water molecule would be allowed to co-ordinate to a dioxouranium oxygen and allowing the hydroxide hydrogens to bend out of plane. This possibility has not yet been investigated.

Table 6. Relative energies in kcal/mol

Complex	Relative energy (SCF)	Relative energy (MP2)
I	0.00	0.00
II	11.83	6.87
III	16.40	17.55
IV	5.43	-9.23

Experimentally a UO_2^{2+} ion in a strongly alkaline solution has four co-ordinated hydroxide ions and possibly an additional co-ordinated water molecule. It is difficult to decide between these two possibilities using EXAFS data alone. At the most sophisticated level, the calculations predict the lowest structure to be a trigonal bi-pyramid with two water molecules which bind to the dioxouranium and the oxy-oxygens.

The two water molecules in $\text{UO}_2\text{O}(\text{OH})_2^{2-} \cdot 2\text{H}_2\text{O}$ stabilise the system by about 50 kcal/mol, compared to $\text{UO}_2\text{O}(\text{OH})_2^{2-} + 2\text{H}_2\text{O}$ at large distance. In $\text{UO}_2\text{O}(\text{OH})_2^{2-} \cdot 2\text{H}_2\text{O}$, there are four hydrogen bonds (see Figure 1), giving an energy contribution of 12-13 kcal/mol per hydrogen bond. This is a very strong stabilisation induced by the two water molecules. The reason for the unusually large stabilisation is that H_2O is a dipole, and the cluster is negatively charged, which gives rise to a large Coulomb attraction. This indicates that our model is too small to reliably describe the difference in hydration energy for $[\text{UO}_2(\text{OH})_4]^{2-}$ and $\text{UO}_2\text{O}(\text{OH})_2^{2-}$. Inclusion of more water molecules in the model would certainly improve the model, making the stabilisation less dominant for $\text{UO}_2\text{O}(\text{OH})_2^{2-}$ compared to the structures with four hydroxide ions. However, the calculations show that the most stable configuration for $[\text{UO}_2(\text{OH})_4 \cdot \text{H}_2\text{O}]^{2-}$ is a square pyramid, and this fact allows us to conclude that an octahedral geometry for $[\text{UO}_2(\text{OH})_4]^{2-}$ is preferred rather than a pentagonal bi-pyramid $[\text{UO}_2(\text{OH})_4 \cdot \text{H}_2\text{O}]^{2-}$. Both these structures are in fact consistent with the experimental EXAFS data.

Experimental and theoretical geometries for $[\text{UO}_2(\text{OH})_4 \cdot \text{H}_2\text{O}]^{2-}$ and for $[\text{UO}_2 \cdot 5\text{H}_2\text{O}]^{2+}$ are shown in Tables 7 and 8.

Table 7. Calculated and experimental bond distances in $[\text{UO}_2(\text{OH})_4 \cdot \text{H}_2\text{O}]^{2-}$

Distances in Å. Optimisation at the SCF level. The $U\text{-O}_{\text{uranyl}}$ bond distances have been corrected for the lack of correlation and (within parenthesis) for the error in the AIMP.

	$r(\text{U-O}_{\text{uranyl}})$	$r(\text{U-O}_{\text{hydr.}})$	$r(\text{U-O}_{\text{water}})$	$r(\text{O-H})_{\text{hydr.}}$
Structure I	1.78 (1.80)	2.36-2.38	4.37	0.94
Structure II	1.78 (1.80)	2.43-2.47	2.65	0.94
Structure III	1.78 (1.80)	2.40	5.21	0.94
Ref. [18]	1.84-1.85	2.33-2.34	–	–
Experiment [8]	1.82	2.24	–	–
Experiment [19]	1.80	2.21	–	–

Table 8. Calculated and experimental bond distances in $[\text{UO}_2 \cdot 5\text{H}_2\text{O}]^{2+}$

Distances in Å. Optimisation at the SCF level. The $U\text{-O}_{\text{uranyl}}$ bond distances have been corrected for the lack of correlation and (within parenthesis) for the error in the AIMP.

	$r(\text{U-O}_{\text{uranyl}})$	$r(\text{U-O}_{\text{water}})$
This work	1.73 (1.75)	2.57
Experiment [8]	1.78	2.41
Experiment [19]	1.70	2.42

All geometries were optimised at the SCF level. The bond distance in an isolated uranyl(VI) is 1.65 Å at the SCF level and 1.71 Å when correlation energy is accounted for (Table 1). Assuming the correlation effect to be approximately the same in an isolated and a hydrated uranyl(VI) ion 0.06 Å should be added the dioxouranium bond distances for Structures I-III. The SCF optimised bond distances were 1.72 Å for all three $[\text{UO}_2(\text{OH})_4 \cdot \text{H}_2\text{O}]^{2-}$ complexes and 1.67 Å for $[\text{UO}_2 \cdot 5\text{H}_2\text{O}]^{2+}$. Correcting for the lack of correlation changes the internal dioxouranium bond distances in $[\text{UO}_2(\text{OH})_4 \cdot \text{H}_2\text{O}]^{2-}$ to 1.78 Å and in $[\text{UO}_2 \cdot 5\text{H}_2\text{O}]^{2+}$ to 1.73 Å. Only the corrected dioxouranium bond distances are shown in Tables 7 and 8.

Furthermore, the AIMP approximation gives a dioxouranium bond distance, which is too short by 0.002 Å. Correcting also for this known error gives the values shown in parenthesis in Tables 7 and 8.

The agreement between the calculated bond distances and experiment is satisfactory for UO_2^{2+} (using the corrected values), where the uranium-oxygen bond distances are too short compared with experiment (Ref. [8]) by 0.04 Å. The calculated distances to the equatorial oxygens are too long by .12-.15 Å, probably due to an oversimplified model of hydrated UO_2^{2+} . However, comparing UO_2^{2+} in a near neutral surrounding $[\text{UO}_2 \cdot 5\text{H}_2\text{O}]^{2+}$ with UO_2^{2+} in a strongly alkaline surrounding (in $[\text{UO}_2(\text{OH})_4 \cdot \text{H}_2\text{O}]^{2-}$) the calculated uranium-oxygen bond distance in the uranyl unit increases by 0.05 Å, in excellent agreement with experiment, 0.04 Å. Likewise, the calculated bond distance between uranium and the equatorial oxygens decreases by 0.20 Å, in reasonable agreement with experiment, 0.17 Å.

Conclusions

We have presented theoretical results obtained for a number of uranium(VI) complexes and redox reactions.

One of the obstacles with theoretical calculations of properties of actinide compounds is the large number of electrons, which have to be explicitly considered in the calculations, another is the occurrence of unpaired f-electrons. In the first section, we have investigated the accuracy of different methods. An important result of the method investigation is that quite simple calculations using perturbation techniques (CASPT2, MBPT2) appear to work very well.

In the second section, we have studied the structure of the uranyl(VI) ion in strongly alkaline and nearly neutral solutions, using a very simplified model comprising only (conceivable) nearest neighbours. The structure of dioxouranium(VI) in strongly alkaline and neutral solutions was studied, comparing several different structures in the former case. The model appears to be too crude to properly describe situations where the number of water molecules varies, but reasonable when complexes with only one water molecule are compared. The calculations confirm that uranyl(VI) ion should be four co-ordinated in a strongly alkaline solution. The shifts in bond distances between a neutral and an alkaline solution is reproduced by the calculations, although the absolute values of the bond distances differ significantly (by up to 0.15 Å) from experiment. In our opinion, this is due to the simplified model used in this study, and a better description of the interaction with the surrounding is needed for quantitative agreement with experiment.

REFERENCES

- [1] P. Pyykkö, *Inorg. Chim. Acta*, 139 (1987), 989.
- [2] C.M. Marian, U. Wahlgren, O. Gropen and P. Pyykkö, *J. Mol. Struct. (Theochem.)* (1988), 339.
- [3] K. Andersson, P.-Å. Malmqvist, B.O. Roos, A.J. Sadlej and K. Wolinski, *Phys. Chem.*, 94 (1990), 5483.
- [4] K. Andersson, P.-Å. Malmqvist, B.O. Roos, A.J. Sadlej and K. Wolinski, *Phys. Chem.*, 94 (1990), 5483.
- [5] J.S. Craw, M.A. Vincent, I.H. Hillier and A.L. Wallwork, *Phys. Chem.*, 99 (1995), 10181.
- [6] N. Ismail, J.-L. Heully, T. Saue, J.-P. Daudey and C.J. Marsden, *Chem. Phys. Lett.*, to be published.
- [7] L. Gagliardi, A. Willets, C.-K. Skylaris, N.C. Handy, S. Spencer, A.G. Ioannou and A.M. Simper, *Chem. Phys. Lett.*, to be published.
- [8] H. Moll, M.A. Denecke I. Farkas, F. Jalilehvand, M. Sandström, Z. Szabo, U. Wahlgren and I. Grenthe, contribution at ACTINIDE XAS 98.
- [9] MOLCAS-4 Program Package, Lund University, Sweden, 1997. Contributors: K. Andersson, M.R.A. Blomberg, M.P. Fielcher, G. Karlström, R. Lindh, P.-Å. Malmqvist, P. Neogady, J. Olsen, B.O. Roos, A.J. Sadlej, M. Schütz, L. Seijo, L. Serrano-Andres, P.E.M. Siegbahn and P.-O. Widmark.
- [10] M. Douglas and N.M. Kroll, *Ann. Phys. (NY)*, 82 (1974), 89.
- [11] B.A. Hess, *Phys. Rev.*, A 33 (1986), 3742.
- [12] R.J. Gdanitz and R. Ahlrichs, *Chem. Phys. Lett.*, 143 (1988), 413.
- [13] K. Faegri, Oslo University, personal communication.
- [14] R.C. Raffinetti, *J. Chem. Phys.*, 58 (1973), 4452.
- [15] S. Huzinaga, *J. Chem. Phys.*, 42 (1965), 1293.
- [16] S. Huzinaga, L. Seijo, Z. Barandarian and M. Klubokowski, *J. Chem. Phys.*, 86 (1987), 2132.
- [17] S. Huzinaga, L. Seijo and Z. Barandarian, *J. Chem. Phys.*, 91 (1989), 7011.

[18] Schreckenbach, P.J. Hay and R.L. Martin, *Inorg. Chem.*, 37 (1998), 4442.

[19] M. Åberg, D. Ferri, J. Glaser and I. Grenthe, *Inorg. Chem.*, 22 (1983), 3986-3989.

Session II

APPLICATIONS OF SYNCHROTRON TECHNIQUES

*Chairs: P.G. Allen, F.R. Livens,
A.M. Scheidegger, N. Baclet, D.K. Smith*

APPLICATION OF X-RAY ABSORPTION SPECTROSCOPY (XAS) TO ACTINIDE SOLUTION CHEMISTRY

Charles Madic

DCC, CEA/Saclay (France)
madic@amandin.cea.fr

Christophe Den Auwer

DCC, CEA/Valrhô-Marcoule (France)

Robert Guillaumont

IPN-Orsay (France)

Abstract

Actinide (An) solution chemistry, in aqueous, organic or fused salt media, has been the subject of a considerable amount of work in the past in connection with applied goals such as: (i) the production of nuclear materials for defence needs, (ii) electricity production, (iii) waste treatment. In the 80s and 90s, new applied fields such as: (i) design of nuclear waste underground repository, (ii) contaminated site remediation, (iii) dismantling of old nuclear facilities and (iv) partitioning of actinides, appeared requiring more precise or new data related to actinide solutions. X-ray absorption spectroscopy methods (XANES and EXAFS) can provide answers to numerous questions which remain pendant in this field, and particularly in the identification of the An oxidation state in complex liquid systems and of the co-ordination polyhedra of the An ions.

The aim of this article is: (i) to present a brief overview on An chemistry in aqueous and organic solutions, highlighting the various oxidation states of An and their redox reactions; An complex formation with inorganic and organic ligands; An compounds formed during liquid-liquid extraction and, finally, the missing information, (ii) to tell the usefulness of XAS to obtain some important missing information, (iii) to give examples of recent achievements of XAS in An solution chemistry and (iv) to describe future developments in An XAS chemistry.

Introduction

Actinide (An) solution chemistry in water, organic liquids and fused salts has been the subject of a tremendous amount of work in the past, essentially in connection with applied goals such as the production of nuclear materials for defence needs and electricity production, or waste treatment. These goals were reached according to hydrometallurgical processes using:

- i) Liquid-liquid extraction or ion-exchange chromatography. Examples are: uranium refining from ores, reprocessing of used fuel for U and Pu recycling, according to the PUREX process, and production of transuranium elements (TRU) for defence and civilian applications.
- ii) Pyrometallurgical processes, such as liquid-liquid extraction between fused salts and liquid metals and electrorefining, for recycling of weapons-grade Pu and reprocessing of used nuclear used fuel (at the pilot scale).

In the 80s and 90s, new applied fields appeared requiring more precise or new data related to aqueous, organic and fused salt solutions of An. Among these, one can cite:

- i) The design of nuclear waste underground repository.
- ii) The remediation and dismantling of nuclear contaminated sites.
- iii) The TRU partitioning for their transmutation (P&T strategy).

Even if the knowledge related to An solution chemistry increased a lot during that period of time, important information is still missing, especially concerning the precise speciation of An in these various complicated liquid media. This is particularly the case for the knowledge of the co-ordination polyhedra of the An species.

The aim of this article is:

- i) To present a brief overview on An chemistry in aqueous and organic solutions highlighting the various oxidation states of An and their redox reactions; An complex formation with inorganic and organic ligands; An compounds formed during liquid-liquid extraction and, finally, the missing information.
- ii) To tell the usefulness of XAS for obtaining some important missing information.
- iii) To give examples of recent achievements of XAS in An solution chemistry.
- iv) To describe future developments in An XAS chemistry.

Brief overview of An solution chemistry

A choice was made here to focus the interest of the reader mainly on An solution chemistry in water and organic solvents, after liquid-liquid extraction of An species.

An aqueous solution

Aqua ions

The actinide family of elements, starting with actinium ($Z = 89$) and ending with lawrencium ($Z = 103$) possesses a very rich aqueous chemistry, owing to the numerous oxidation states they can exhibit in solution (see Table 1), in particular for the elements uranium (U) to americium (Am) from the first half of the series. The most stable oxidation state of these elements first increases from III (Ac) to VI (U), then decreases to III (Am) which remains the most important, or sometimes the only, oxidation state of the following elements of this series, except for nobelium (No). Oxidation state VII, which was discovered in 1967 by Krot, *et al.* at Moscow (Russia) for neptunium (Np) in alkali solutions, is also observed for plutonium (Pu) and Am. These An(VII) species are highly unstable in acidic solution.

The formula of the aqua ions (in acidic non-complexing media) of An depends on the oxidation states. M(III) and M(IV) ions are composed of aqua species with formula: $M(H_2O)_x^{3+}$ and $M(H_2O)_x^{4+}$. The numbers of water molecules, x , bound to the metal centre in the inner co-ordination sphere are still a subject of controversy. The values $x = 8$ to 11 have been proposed. Moreover, it is known that the water molecules bound to the M(III) and M(IV) metal centres are in rapid exchange with bulk water molecules.

M(V) and M(VI) species are oxo-aqua complexes with the following formulas: $MO_2(H_2O)_x^{+or2+}$. The main characteristics of these species are:

- i) The existence of a linear moiety $O = M = O$, named actinyl, where two oxygens are firmly doubly bound to the metal centre making the exchange of oxygens with bulk water oxygen not so rapid (M(V) species) or very slow (M(VI) species). The existence of such linear actinyl moieties was proven by vibrational Raman spectroscopy: a single Raman peak was observed for each M(V) or M(VI) aqua species in the frequency range 750 to 870 cm^{-1} . These single peaks correspond to the ν_1 stretching vibrations of the linear actinyl moieties.
- ii) The presence of water molecules bound to the metal centre in the equatorial plane of the actinyl moiety. For M(VI) species, a general agreement exists for the value $x = 5$. For M(V) species, it is not clear yet whether x equals also 5 or 6. Water molecules bound to M(V) and M(VI) actinyl ions are in rapid exchange with bulk water. The co-ordination chemistry of M(V) and M(VI) species corresponds to the exchange of ligands in the equatorial plane of the actinyl moieties.

The nature of M(VII) species in acidic non-complexing media was only studied for Np(VII) by Krot, *et al.* and by Musikas, *et al.* in the 70s. Contrary to the proposal of the Russian discoverers of Np(VII), Musikas, *et al.* proposed the following formula: $NpO_3(H_2O)_x^+$, which was then agreed by the Russians. Nevertheless, based on quantum mechanics calculations, Ionova proposed in the 80s the formula: $NpO_2(OH)_2(H_2O)_x^+$. The question of the nature of Np(VII) species in acidic (or alkaline) media cannot yet be considered as solved. One of the difficulties here relies in the high instability of Np(VII) in acidic solution: Np(VII) is rapidly reduced to Np(VI) species by water.

Redox potentials and electrochemistry

The redox potentials of the various An (An = U to Am) redox couples in acidic non-complexing media at 298 K are highly valuable to predict the stability of An species vs. redox reactions with water or vs. disproportionation. Note that the redox “window” of water lies in 1 mol/L proton at 298 K between 0 V (reduction of H⁺ in hydrogen gas) and 1.23 V/NHE (oxidation of water into oxygen gas).

From known data [1a] one can make the following comments:

- i) For U, the only oxidation states which are thermodynamically stable in 1 mol/L H⁺ are U(IV) and U(VI). U(V), while stable vs. water, disproportionates into a mixture of U(IV) and U(VI). U(III) is unstable vs. its oxidation by the proton or water. Nevertheless, aqueous U(III) chemistry can be studied owing to the slowness of U(III) oxidation by the medium. No U(II) species have ever been observed in water.
- ii) For Np, the species Np(III), Np(IV), Np(V) and Np(VI) are thermodynamically stable in acidic water solutions at 298 K. Np(II) was never observed and Np(VII), while observed and studied (see above), is unstable vs. water reduction.
- iii) The plutonium case is very special. If Pu(III) to Pu(VI) species can exist in the “redox window” of water, the redox potentials of the various Pu couples are so close to each other that one can observe a property which is unique among all the elements of the Periodic Table: the coexistence of four oxidation states at equilibrium in the same acidic solution, Pu(III) + Pu(IV) + Pu(V) + Pu(VI).
- iv) Am(III) is the only thermodynamically stable species of americium in acidic water solutions. If the oxidation of Am(III) into Am(IV) is quite impossible (Am(IV) was only observed as a transient species during the irradiation of Am(III) solution saturated by N₂O gas by an intense electron beam), it is possible to observe and study Am(V) and Am(VI) species, even if these species are unstable vs. water reduction, owing to the relative slowness of their reduction reactions. Like Am(IV), the Am(II) species has only been observed as transient and highly unstable species during electron beam irradiation of Am(III) solution in the presence of alcohol.

The transformation of an An(x) species into another An species with higher or lower oxidation states can be carried out electrochemically. The results obtained so far permit to make a link between electrochemical and structural properties of the different An species. As an example, one can discuss the case of plutonium. The voltammogrammes of Pu solutions at different oxidation states exhibit reversible waves for Pu(III)/Pu(IV) and Pu(V)/Pu(VI) systems. Half-wave potentials were found close to the thermodynamic potential values [1a]. These are direct proofs that only slight modifications occur during redox reactions within the Pu(III)/Pu(IV) and Pu(V)/Pu(VI) pairs. On the contrary, to oxidise Pu(IV) into Pu(V), or to reduce Pu(V) into Pu(IV), it is necessary to use over-potentials of about 0.8 V (positive for the oxidation of Pu(IV) into Pu(V) and negative for the reduction of Pu(V) into Pu(IV)), in comparison to the thermodynamic redox potential. The existence of such over-potentials for these redox reactions are direct proofs of the deep modifications which occur within the structures of the Pu species of the Pu(IV)/Pu(V) redox pair when one species is converted into the other.

Redox reactions

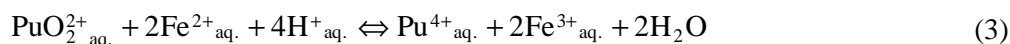
The redox reactions of An species in aqueous solutions can be divided into two categories.

- *Category 1:* These reactions correspond to *simple exchange of electrons*. Consequently, they are *very rapid*. This is the case when An(III)/An(IV) and An(V)/An(VI) couples are involved. Following is an example of such a rapid electron exchange reaction between Pu(III)/Pu(IV) and Fe(II)/Fe(III) redox pairs:

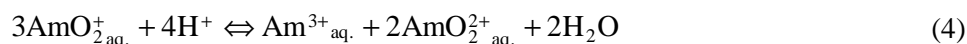


- *Category 2:* These reactions occur with exchange of electron *and creation or rupture of M=O actinyl bonds*. These reactions are generally *slow*.

As examples one can cite redox reactions between U or Pu species and Fe ones:



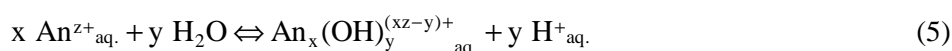
In this second category, one can cite also some An disproportionation reactions, such as that of Am(V):



The half-time period of this reaction is about 25 minutes for a $3 \cdot 10^{-2}$ mol/L Am(V) in 6 mol/L HClO₄ solution at 298 K.

Hydrolysis of An ions

The hydrolysis of a $\text{M}^{z+}_{\text{aq}}$ can be written as follows:



The ability of An ions for hydrolysis depends on the An oxidation state. When possible, the following sequence is observed for any An element: IV > VI > III > V.

As an example, one can mention the pH for which hydrolysis begins for 0.1 mol/L Pu aqua ions aqueous solutions at room temperature: 0.5, 4, 7 and 9 for Pu(IV), Pu(VI), Pu(III) and Pu(V), respectively.

The knowledge of x and y in An/OH⁻ oligomers is still a subject of debate. Moreover, the knowledge about the formation and structures of these oligomers are most often poor.

Potential-pH diagrams

It is well known, since Pourbaix, that a simple way to represent the redox and hydrolytic properties of the species of one element in aqueous solution is to draw a potential-pH (E/pH) diagram. This permits in a simple way to visualise the stability domains of each species.

Complex formation of An ions with inorganic and organic ligands

Like the lanthanide ions, An ions can be considered as “hard acids”, according to the Pearson hard and soft acid-base theory (HSAB). Hard acids and bases react essentially by ionic interaction, while soft acids and bases react covalently.

As a consequence of this property, An ions react with hard bases, preferably O and F donor ligands. Except F⁻, few F bearing ligands are known to react with An ions. At the reverse, O-bearing ligands reacting with An ions are very numerous. Most often, the higher the An^{z+} “ionic potential”, expressed as the ratio of the formal charge of the ion by the crystal radius r of the metal ion (z/r), the stronger the affinity of An ions for a particular O-bearing ligand. The higher the number of donor atoms of the ligands, the more stable the corresponding An complexes. In the case of An(V) and An(VI) species, the binding of the ligand occurs only in the equatorial plane of the actinyl moiety.

Numerous questions are still unresolved. For example: (i) the inner vs. outer sphere complexation of An species, (ii) the number of co-ordinating atoms of the ligands bound to the An ion, (iii) the number of water molecules still remaining in the An first co-ordination sphere after complexation by the ligand.

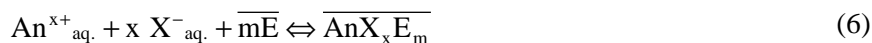
An solvent extraction chemistry

Some general rules can be listed for the solvent extraction of An metal ions or salts. Among them the most important rules are the following:

- i) An ions or salts are extracted preferably by O-bearing extractants.
- ii) The affinity order of An ions or salts vs. a peculiar O-bearing extractant is often proportional to the ionic potential z/r of the An ion, also mentioned above for complex formation in homogeneous aqueous solution.
- iii) The affinity order of An(x) species for an extractant depends on the atomic number Z of the An. Sometimes the affinity increases with Z, and sometimes it decreases.
- iv) Like in the case of complex formation, polydentate extracting ligands exhibit stronger affinities for An ions and salts than the corresponding monodentate extractants.

Among the important extraction systems for An chemistry one can cite:

- i) Monodentate neutral extractants: organophosphates, phosphonates, phosphinates, phosphine oxides (TRPO), monoamides. In this case the extraction reaction can be written as follows:



For example: Am(NO₃)₃E₃ or UO₂(NO₃)₂E₂ solvates are formed with most of the extractant E listed above.

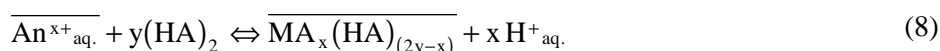
- ii) Polyfunctional neutral extractants, such as: carbamoylmethylphosphonates (CMPs), oxides of carbamoylmethylphosphine (CMPOs), or diamides. In this case, the extraction reactions can be written essentially as Eq. (6). The question of the denticity of the extractants vs. the

An ion is sometimes not so obvious. If CMPs and CMPOs are often considered monodentately bound to the metal centre through their phosphoryl oxygens (P = O), in some cases, both the carbonyl and phosphoryl oxygens are bound to the An ion. For diamide extractants, it seems that most often the extractants are bidentately bound to the An ion.

- iii) Tertiary and quaternary ammonium salts, such as those of *tri-n*-octylamine (TOA), *tri-n*-laurylamine (TLA), or Aliquat 336. For example, in the case of *tetra*-alkylammonium salt, An ion-pairs are formed in the solvent according to the following equation:



- iv) Organophosphoric acids, such as *di*-2-ethylhexylphosphoric acid (HDEHP) and *di*-isodecylphosphoric acid (DIDPA), or organophosphinic acid like CYANEX 301. In these cases when an An^{x+} is extracted, $x \text{H}^+$ are released into the aqueous phase. The An ion extraction reaction for moderate solvent loading can be written according to the following equation:



with $(\text{HA})_2$ the dimeric form of the extractants, as often observed in numerous diluents, such as aliphatic or benzenic ones. Note that for high An ion solvent loading, the nature of the extracted complex is sometimes different, as in the case of HDEHP and DIDPA; An polymers are formed which are difficult to destroy.

Importance of XAS for An solution chemistry

As mentioned above, a large amount of information is still missing for a precise understanding of actinide solution chemistry, whatever the nature of the solvent: water, organics, fused salts or liquid metals.

X-ray absorption spectroscopy (XAS) is a powerful method that can provide useful information about the co-ordination polyhedron of any An ions in any type of liquid media, such as those mentioned above. Among the information, which can be obtained by XAS methods (XANES and EXAFS) for An solutions, one must cite:

- i) The oxidation state of An, using the XANES part of the XAS spectra.
- ii) The nature of the neighbours of An atom in the first and second co-ordination shells of the complexes (EXAFS).
- iii) The number of such neighbours with a ± 10 to 15% uncertainty (EXAFS).
- iv) The distance of the atoms co-ordinated to the An centre, with ± 0.002 nm uncertainty (EXAFS).

Nevertheless, to obtain the above mentioned information it is necessary to be prudent:

- i) Model compounds with known structures (crystalline An compounds) must be studied before the corresponding An solutions.
- ii) When processing the data.
- iii) There is an urgent need to use an efficient computer model to process the data.

But, if great care is taken when performing XAS experiments and data processing, the XAS method can be considered as an unique tool to study An ions and compounds in miscellaneous solutions.

Examples of recent achievement in An XAS solution chemistry

As noted above, XAS methods (XANES and EXAFS) can provide very useful information in the various aspects of An solution chemistry. Below, some highly interesting recent work which concerns aqueous and organic actinide solution chemistry has been selected.

Aqueous solutions

- *Example 1.* This example concerns the identification of the oxidation state of Pu aqua ions. Conradson, *et al.* [2] studied the XANES part of the XAS spectra of Pu(III), Pu(IV), Pu(V) and Pu(VI) aqua ions. They showed that the position of the Pu L_{III} white line depends on the oxidation state of the Pu species. The higher the Pu oxidation state, the higher the energy of the maximum of the white line. Moreover, for Pu(V) and Pu(VI) aqua ions, the existence of a slight inflexion on the right hand-side of the white line peak is a “signature” of the presence of actinyl moieties within these complex aqua ions.
- *Example 2.* Allen, *et al.* [3] provide answers to the question: inner-sphere vs. outer-sphere for the complexation of some An(x) aqua ions by the chloride ligand using An EXAFS. It is well known that Cl^- is a weak ligand for An ions. For U(VI), Cl^- ligand competes with water in the first co-ordination sphere for chloride ion concentration higher than 4 mol/L. At the reverse, for Pu(III), even for chloride ion concentration as high as 12.3 mol/L, no Cl^- enters the inner co-ordination sphere of Pu(III). In this case, the Pu(III) chloro complexes are outer-sphere.
- *Example 3.* Among the hydroxo complexes of actinide ions, the hydroxo colloid of Pu(IV) has great importance in Pu process chemistry and in Pu-bearing waste treatment. Conradson *et al.* [4] studied the EXAFS spectra of Pu(IV) hydroxo colloids, and related compounds, such as PuO_2 or anionic ion-exchange resin residue. EXAFS study of Pu(IV) colloid reveals its structure where Pu centres are linked together in the polymeric network by ol and oxo bridges. Pu found in resin residue was found similar to Pu(IV) colloid.
- *Example 4.* Speciation of Np(V) carbonato complexes was achieved by Clark *et al.* [5] using EXAFS. Three Np(V) carbonato complexes were identified with stoichiometries 1/1, 1/2 and 1/3. The carbonate ligands are bound to Np(V) through its actinyl equatorial plane.

- *Example 5.* An speciation in natural environmental conditions is an important prerequisite in view of remediation actions. U(VI) binding mode to natural and synthetic humic acids complexing agents was studied by EXAFS by Denecke *et al.* [6]. This permits to identify the binding mode of the carboxylato groups born by the humic acids towards U(VI).

Organic solutions

Only two examples are chosen here.

- *Example 6.* The inclusion of U(VI) in the cavity of crown ethers in acetonitrile solutions was evidenced by EXAFS, in a study by Deshayes *et al.* [7]. The linear O = U = O moiety was found at the centre of the cavity of each crown ether studied, the six ether oxygens being bound to U centre in the equatorial plane of the U(VI) actinyl moiety.
- *Example 7.* The question of the co-ordination polyhedra of An(x) ions and salts when extracted by the different type of extractants (see above) is most often still open. In this field, Den Auwer, *et al.* [8] studied by EXAFS the U co-ordination polyhedron when U(VI) is extracted as a nitrate salt by organophosphates, like *tri-n*-butylphosphate (TBP), or by monoamides. For TBP it was found that the two extractant molecules are bound to U(VI) through its actinyl equatorial plane, where two bidendate nitrate ions are also present. In case of U(VI) monoamide extraction from nitrate medium, it was shown that U(VI) nitrate solvated by two monoamide molecules is formed when LiNO₃ solution is used while U(VI) is extracted as an *tri*-nitrate ion-pair with protonated monoamide when U(VI) is extracted from highly concentrated nitric acid aqueous media.

Conclusions

For actinide aqueous and organic solutions chemistry a rapidly growing interest is observed world-wide for the XAS methods. This can provide quite unique information about: An speciation and reactivity, molecular engineering for complexants and extractants for An separation (e.g. An(III) vs. Ln(III)), and wastes treatment and site remediation.

One can forecast the usefulness of XAS methods for An fused salts and liquid metal solutions. These fields are concerned with An separation from wastes but also for the development of new nuclear concepts involving pyrochemical methods, as in the case of the so-called hybrid systems, for example.

The challenge for the future in this field will be to study *in-situ* An samples with access to the dynamics of the reactions.

Of course, XAS methods alone cannot give answers to all the unresolved questions in An solution chemistry. Nevertheless, XAS methods if employed jointly with other methods like NMR, IR and Raman spectroscopies can provide “clearer pictures” of An solution chemistry.

In conclusion, one can say that XAS methods have a brilliant future in the field of basic An solution chemistry.

REFERENCES

- [1] Most of the information presented in the first two sections can be found in major books such as:
- a/ J.J. Katz, G.T. Seaborg and L.R. Morss, "The Chemistry of the Actinide Elements", second edition, Vol. 2, Chapman and Hall (1986).
 - b/ J. Fuger and F.L. Oetting, "The Chemical Thermodynamics of Actinide Elements and Compounds, Part 2, The Actinide Aqueous Ions", International Atomic Energy Agency, Vienna (1976).
 - c/ J. Fuger, *et al.*, "The Chemical Thermodynamics of Actinide Elements and Compounds, Part 12, The Actinide Aqueous Inorganic Complexes", International Atomic Energy Agency, Vienna (1992).
 - d/ H. Wanner, *et al.*, "Chemical Thermodynamics of Uranium", published by the OECD/NEA and North Holland, distributed by Elsevier (1992).
 - e/ R.J. Silva, *et al.*, "Chemical Thermodynamics of Americium", published by the OECD/NEA and North Holland, distributed by Elsevier (1995).
- [2] S.D. Conradson, *et al.*, *Polyhedron*, 17, 4, 599 (1998).
- [3] P.G. Allen, *et al.*, *Inorg. Chem.*, 36, 4676 (1997).
- [4] S.D. Conradson, *Applied Spectroscopy*, 52, 7, 252 A (1998).
- [5] D.L. Clark, *et al.*, *J. Am. Chem. Soc.*, 118, 2089 (1996).
- [6] M.A. Denecke, *et al.*, *Radiochim. Acta*, 79/3, 151 (1997).
- [7] L. Deshayes *et al.*, *Polyhedron*, 13/11, 1725 (1994).
- [8] C. Den Auwer, *et al.*, in the Proceedings of the OECD/NEA Workshop on Long-Lived Radionuclide Chemistry in Nuclear Waste Treatment, Villeneuve-lès-Avignon, France, 18-20 June 1997.

Table 1. Oxidation states of actinide elements observed in aqueous solutions

(The most stable oxidation state of each element is in bold)

Z	89	90	91	92	93	94	95	96	97	98	99	100	101	102	103
Symbol	Ac	Th	Pa	U	Np	Pu	Am	Cm	Bk	Cf	Es	Fm	Md	No	Lw
Oxidation states													I		
	III			III	III	III	III	III	III						
		IV	IV	IV	IV	IV	IV	IV	IV						
			V	V	V	V	V								
				VI	VI	VI	VI								
					VII	VII	VII								

**MICRO/SPATIALLY RESOLVED XRF AND XAFS
FOR THE IN SITU INTERROGATION OF RADIONUCLIDE
DISTRIBUTION AND SPECIATION IN ENVIRONMENTAL SAMPLES**

Paul M. Bertsch, Douglas B. Hunter and Martine Duff

Advanced Analytical Center for Environmental Sciences
The University of Georgia, SREL, Drawer E
Aiken, South Carolina USA

Abstract

It is now widely accepted that information on chemical speciation and species transformations is prerequisite to the development of a comprehensive understanding of toxic element behaviour in the environment. A major obstacle in developing realistic environmental risk assessments or in designing environmentally sound, yet cost effective chemical and biological remediation strategies has been the inability to properly characterise the chemical speciation of contaminants in an environmental sample or waste form. Over the past decade there has been an explosion in applications of synchrotron-based X-ray techniques in the environmental sciences. Much of the emphasis has been on using XAFS spectroscopy to provide molecular-level information on sorption processes of contaminants with well characterised homogeneous model mineral sorbates. While the information generated in these studies has been useful for evaluating and revising accepted conceptual models of surface complexation, it has been difficult to translate this molecular level information in a meaningful way to critical environmental processes occurring heterogeneously over large length scales.

Using a dedicated microprobe beamline (X-26A National Synchrotron Light Source) we have been conducting spatially resolved XRF and XAS studies on a variety of environmental samples and on samples produced in waste isolation and processing activities. XANES spectroscopy has provided detailed information on the oxidation states of U, Pu, Cr, Se, As, and other metals and metalloids in contaminated soils, waste forms, and biota on regions as small as 12 μm , with minimal sample manipulation. Qualitative information on bonding environments of many of these contaminants has been deduced based upon elemental associations generated at 6 μm spatial resolution on identical regions where complete XANES spectra were collected and also on the “fingerprint” or multiple scattering regions of the XANES spectra. Methods have been developed for rapid determination of oxidation states by selecting strategic regions in the XANES spectrum to collect data, thus allowing spatially resolved XANES to be used as a powerful analytical technique for conducting contaminant source term characterisation or for evaluating the efficacy of chemical and biological intervention technologies used to remediate contaminated soil. Recent installation of Kirkpatrick-Baez X-ray focusing mirrors have increased the effective flux in micro-regions by $\sim 10^3$, thus reducing the time required for analyses and greatly enhancing both the spatial resolution and sensitivity of these techniques. The Geo/Soil/Enviro CARS undulator beamline at Sector 13 of the APS, which also employs Kirkpatrick-Baez optics, has increased the effective flux in defined micro-regions by an additional $\sim 10^3$. These recent enhancements allow for the collection of XAFS spectra in $\sim 1 \mu\text{m}$

regions, at much lower concentrations, and in a fraction of the time required at X-26A. Recent experiments using the Geo/Soil/Enviro CARS sector at the APS have included studies on the sorption of Pu to mineral aggregates in rock thin sections, where highly selective localisation of Pu with Mn-oxide phases and spatially resolved oxidation states and co-ordination environments have been delineated.

EXAFS STUDIES OF URANIUM(VI) SORPTION ON MINERAL SURFACES

T. Reich*, H. Moll, M.A. Denecke, C. Hennig, G. Geipel, G. Bernhard, H. Nitsche

Forschungszentrum Rossendorf e.V.

Institute of Radiochemistry

P.O. Box 510119, D-01314 Dresden, Germany

P.G. Allen, J.J. Bucher, N.M. Edelstein, D.K. Shuh

Lawrence Berkeley National Laboratory

Chemical Sciences Division

MS 70A-1150, Berkeley, CA 94720, USA

Abstract

Structural parameters of the near-neighbour surrounding of uranium(VI) sorbed onto silica gel and ferrihydrite surfaces have been determined by U L_{III} edge extended X-ray absorption fine structure (EXAFS) analysis. The sorption on silica gel was studied at pH 4 with uranium(VI) concentrations in the range of 5×10^{-2} - 2×10^{-5} Mol/L. Sorption experiments with ferrihydrite have been performed at pH 5.8 with uranium(VI) concentrations of 10^{-4} and 10^{-5} Mol/L and at pH 7.8 with 10^{-5} Mol/L uranium(VI). The structural parameters for the uranium co-ordination shells (U-O_{ax}, U-O_{eq} and U-Si/Fe) indicate formation of inner-sphere, mononuclear uranyl complexes at the silica gel and ferrihydrite surfaces.

* Corresponding author: T. Reich@fz-rossendorf.de

Introduction

An important factor which determines the mobility of radionuclides in the environment is their interaction with mineral-water interfaces [1]. To predict radionuclide mobility, it is necessary to understand fundamental processes such as surface precipitation and surface complexation [2]. Studies of uranium sorption onto mineral surfaces have great practical importance for risk assessment and development of effective remediation strategies for areas exposed to intensive uranium mining and processing in the past, for example, parts of the Erzgebirge in Germany and the neighbouring Czech Republic.

This study is a continuation of previous investigations of uranium(VI) sorption onto silica gel [3,4] and ferrihydrite [5,6] by uranium L_{III} edge extended X-ray absorption fine structure (EXAFS) analysis. Silica gel has been used as a model for silicate surfaces in studies of uranium(VI) sorption for several years [7-11]. In nature silicates may be coated by a thin layer of iron oxides and hydroxides. Ferrihydrite is a hydrous ferric oxide which easily precipitates from iron(III) solution near pH 6 and is characterised by poor structural order and small particle size [12]. The study of uranium sorption on ferrihydrite can serve as a first step toward the understanding of the influence of microscopic iron-containing coatings on the sorption behaviour of uranium(VI).

Experimental

Sample preparation

Silica gel samples

Five sorption samples labelled Si1-Si5 were prepared in air at room temperature using silica gel 60 (for chromatography) from Merck and uranyl perchlorate solutions with uranium concentrations ranging from $0.05\text{-}2 \times 10^{-5}$ Mol/L (see Table 1). Samples Si1-Si3 were prepared by shaking 1 g of sorbent with 20 mL uranyl perchlorate solution of the corresponding concentration for 50 hours. The pH of the mixtures was adjusted once at the start to 4. For samples Si4 and Si5, the exposure time was 100 hours and the ratio of solid to solution volume 10 g/L at an ionic strength of 0.1 M NaClO₄. The pH of the mixture was adjusted at the beginning of the exposure and after 24 hours to 4. Table 1 shows the pH of all samples measured at the end of the exposure and the amount of uranium sorbed onto the silica.

Ferrihydrite samples

Ferrihydrite was precipitated in air from 1×10^{-3} Mol/L iron(III) nitrate solution by slowly raising the pH to 7 [12]. This suspension was aged for about 30-60 minutes before the pH was lowered to 5 and the ionic strength adjusted to 0.1 M NaNO₃. Afterwards, the ageing of the ferrihydrite proceeded by continuously stirring at room temperature for 65 hours. To analyse the precipitate, it was separated by centrifugation, washed several times with MILLIQ water, and air-dried. Based on powder X-ray diffraction using a Co K α -source, the solid phase was identified as six-line ferrihydrite.

Three samples labelled Fe1-Fe3 were prepared in air at room temperature from 2 L suspensions of aged ferrihydrite (10^{-3} M as Fe). Samples Fe1 and Fe2 were obtained at pH = 5.8 and sample Fe3 at pH = 7.8. To speed up the equilibration period and achieve equilibrium with atmospheric CO₂,

a certain amount of NaHCO_3 , calculated with the equilibrium speciation computer code HYDRAQL [13], was added to the suspension Fe3. Afterwards, the uranium(VI) concentration in suspension Fe1 was adjusted to 10^{-4} Mol/L. For suspensions Fe2 and Fe3, the uranium(VI) concentration was 10^{-5} Mol/L. Before and after adding uranyl nitrate stock solution to the suspensions, the pH was adjusted to the desired values. After 50 hours of continuous stirring, the pH of the suspension had not changed. Previous sorption experiments under identical conditions showed that $95\pm 5\%$ of the uranium is sorbed onto samples Fe1, Fe2 and Fe3 [14,15].

EXAFS measurements

For the EXAFS measurements, the samples were separated by centrifugation and transferred as a wet paste into polyethylene cuvettes of 3 mm diameter. The cuvettes were hermetically sealed to prevent the pastes from drying. Uranium L_{III} edge X-ray absorption (XAS) spectra of all samples were collected simultaneously in transmission and fluorescence mode at room temperature at the Stanford Synchrotron Radiation Laboratory (SSRL) using the Si(220) double-crystal monochromators on beamlines 2-3 and 4-1. Transmission spectra were collected using argon-filled gas ionisation chambers. The fluorescence was measured using a four pixel Ge fluorescence detector [16]. The uranium L_{III} edge measurements of samples Fe1 and Fe2 were repeated with a new batch of samples at Hamburger Synchrotronstrahlungslabor (HASYLAB) on beamline X1.1 using a Si(311) double-crystal monochromator. The energy scale of each spectrum was calibrated by simultaneously measuring the XAS spectra of a yttrium foil or a 0.2 Mol/L UO_2Cl_2 solution. The threshold energy, E_0 , of the uranium L_{III} edge was arbitrarily defined 20 eV above the first inflection point of the corresponding absorption edge of 17 166 eV [17].

Data analysis was performed according to standard procedures [18] using the EXAFSPAK software developed by G. George and I. Pickering at SSRL. Theoretical scattering amplitudes and phases for each pair of atoms were calculated with the program FEFF7 [19]. During the least-squares fitting of the k^3 -weighted EXAFS data, the co-ordination number of the axial oxygen atoms, O_{ax} , in the uranyl group, UO_2^{2+} , was fixed at two. The contribution of multiple scattering (MS) interaction within the uranyl unit to the EXAFS signal was taken into account as described in [20]. A single value of the shift in threshold energy, ΔE_0 , was allowed to vary for all co-ordination shells of a given sample.

Results and discussion

Silica gel samples

The results of the curve fitting to the k^3 -weighted EXAFS data are shown in Figure 1 and summarised in Table 2. For samples Si1-Si4, the best fit to the data was obtained with a structural model consisting of three oxygen co-ordination shells. The first shell consists of two axial oxygen atoms (O_{ax}) of the uranyl group, UO_2^{2+} , at a distance of 1.79 ± 0.02 Å. The second and third shells are the equatorial ligands of the uranyl group. At distances of 2.26-2.29 Å, the uranium atom is surrounded by 2-3 oxygen atoms O_{eq1} . The third shell of oxygen atoms (O_{eq2}) at 2.51 ± 0.02 Å has a co-ordination number between 2-4. The main characteristic of the surface species of samples Si1-Si4 is that the best fit to the data is obtained using two oxygen co-ordination shells in the equatorial uranyl plane separated by approximately 0.24 Å. This confirms our previous studies of uranium(VI) sorption onto silicic acid and silica gel [4].

A similar splitting of the oxygen shell was also observed by uranium L_{III} edge EXAFS analysis of schoepite and U(VI) oxide precipitates at pH \approx 7 [21]. The U-U interaction from oxygen bridging between neighbouring uranyl units was clearly observed in the FTs as a pronounced peak around 3.5 Å (see Figure 2 in Ref. [21]). The FTs of samples Si1-Si3 in Figure 1 do not show any significant intensity above 3 Å. This indicates that even at the highest uranyl loading, we do not detect any U-U interaction indicative of sorption of multinuclear uranyl complexes such as $\text{SiO}(\text{UO}_2)_3(\text{OH})_5^+$. This polynuclear species was taken into account in the surface complexation model for uranium(VI) sorption from 1.5×10^{-6} Mol/L solution onto amorphous silica in the pH range of 4-7 [11]. Although the noise level above 3 Å is higher in the FTs of samples Si4 and Si5, we do not observe any distinct peak which could be attributed to backscattering from uranium neighbours. Therefore, the observed splitting indicates that one group of oxygen atoms forms bonds with the silanol groups of the silica surface and another group is co-ordinated by free hydrate or hydroxo groups.

A different structural model had to be used to fit to the experimental data of sample Si5. Instead of a split equatorial oxygen shell, we used only one O_{eq} shell and included a U-Si co-ordination shell as the third shell. The structural parameters of sample Si5 (Table 2) has the uranium atom surrounded by two axial oxygen atoms at 1.79 ± 0.02 Å and approximately three oxygen atoms at 2.26 ± 0.02 Å in the equatorial plane. Not more than one silicon atom ($N = 0.5 \pm 0.4$) is located 2.72 ± 0.02 Å from the uranium atom. This U-Si distance is much smaller than observed in silicon containing uranium(VI) minerals such as soddyite and uranophane. In these minerals, silicate tetrahedra are linked to uranium via two oxygen atoms. The corresponding U- O_{eq} and U-Si distance for soddyite (uranophane) as detected by EXAFS were 2.38 (2.32) and 3.16 (3.17) Å [4,22]. The short U-Si distance of 2.71 Å observed for the surface species of sample Si5 can be rationalised by a model where one silica tetrahedron is linked via two of its oxygen atoms to the uranyl group (edge-sharing co-ordination; bidentate complex). Assuming typical values for the O-Si-O tetrahedron angle (109°), Si-O bond length (1.64 Å), and taking the U- O_{eq} distance as 2.26 Å, the calculated U-Si distance is 2.77 Å. This is in close agreement with the EXAFS result given in Table 2. Attempts to fit the spectra of samples Si1-Si4 using the edge-sharing structural model as for sample Si5 and vice versa were not successful. Either the co-ordination number, N , for O_{eq} or the uncertainties of N and the bond distance, R , were beyond reasonable limits.

Based on the splitting of the equatorial shell and the lack of U-U interaction, the surface species at uranium loadings greater than 1 mg U/g can be described as a mononuclear inner-sphere surface complex. However at a uranyl loading below 1 mg U/g, the U- O_{eq} and U-Si distances are consistent with a bidentate surface complex of UO_2^{2+} characterised by edge-sharing with the silica tetrahedra. Since we did not detect U-Si interaction at uranium loadings greater than 1 mg U/g, it is suggestive that the surface species has a different structure compared to the low loading region. One such structure could be a bridging bidentate configuration with the uranium binding to two surface sites as proposed in [7]. At high uranium loadings, the EXAFS signal may represent a superposition of several inner-sphere mononuclear surface species. For example two mononuclear species were included in the surface complexation modelling mentioned previously [11].

Ferrihydrite samples

The k^3 -weighted uranium L_{III} edge EXAFS data and the corresponding FTs of samples Fe1-Fe3 are shown in Figure 2. Except for a somewhat more pronounced shoulder at 6.5 \AA^{-1} in the EXAFS spectrum of sample Fe3, the EXAFS and FTs of the samples are quite similar. To obtain the structural

parameters given in Table 3, a four-shell fit to the experimental EXAFS data was utilised. Samples Fe1-Fe3 all have uranium surrounded by two O_{ax} atoms at 1.81 ± 0.02 Å. Approximately five O_{eq} atoms are co-ordinated to the uranyl group at 2.36-2.39 Å in the equatorial plane. The large Debye-Waller (DW) factor observed for this shell indicates a rather broad distribution of $U-O_{eq}$ distances. The observation of a single, although broad, O_{eq} shell contradicts the detection of O_{eq1} and $O_{sorbing}$ shells at 2.35 and 2.52 Å, respectively, for ferrihydrite sample UF 4 [6]. Sample UF 4 was prepared under similar conditions as sample Fe1, e.g. 2 L batch of ferrihydrite (10^{-3} M as Fe) and 10^{-4} uranium(VI) at pH = 5.5. This difference can not be explained by the longer data range of up to $k = 16$ Å⁻¹ of that study. The weighted average of the $U-O_{eq1}$ and $U-O_{sorbing}$ distances is 2.42 Å. This is 0.03-0.06 Å longer than the $U-O_{eq}$ distance obtained in the present work.

For sample Fe3, one iron atom is detected at a U-Fe distance of 3.42 Å. This distance agrees with the corresponding value of sample UF 4 (see Table 3). For samples Fe1 and Fe2, the co-ordination number of the U-Fe shell was held constant at unity to obtain a stable fit. Note that the $U-O_{ax}$ MS interaction at 3.6 Å, which was accounted for in all fits, interferes with the U-Fe interaction. As Table 3 shows, the U-Fe DW factor for samples Fe1 and Fe2 is twice that of sample Fe3. Since the U-Fe co-ordination number was the same in all fits, one can argue that the disorder in the U-Fe shell of samples Fe1 and Fe2 results from the presence of more than one surface species. However, the observation of U-Fe interaction for all samples indicates the formation of an inner-sphere surface complex. Since attempts to fit this shell as U-U interaction instead of U-Fe were unsuccessful, we conclude that multinuclear uranyl species are not sorbed at the surface.

The theoretical fits to the data improved when uranium interaction with a light scatterer like oxygen or carbon was included. The U-O/C distance of about 2.9 Å found in this study is too large for a direct bond between uranium and oxygen or carbon. In case of carbon, 2.93 ± 0.02 Å matches the U-C distance observed for a bidentate co-ordination of the CO_3^{2-} group to UO_2^{2+} [23]. Detection of the U-C interaction may indicate the formation of a ternary complex such as $(\equiv FeO_2)UO_2CO_3^{2-}$ [6]. The presence of a ternary species at the ferrihydrite surface can be verified by repeating the EXAFS measurements on samples prepared under an inert gas atmosphere, e.g. without CO_2 present.

Based on the U-Fe interaction and the absence of a U-U interaction, we conclude that a mononuclear inner-sphere complex is formed at the ferrihydrite surface. Additionally, the EXAFS results show evidence of U-C/O interaction at 2.9 Å. Future studies will determine if this interaction results from the formation of ternary surface complexes involving CO_3^{2-} .

Conclusions

This investigation shows that uranium L_{III} edge EXAFS spectroscopy is a valuable tool for determining structural parameters for the uranium near-neighbour environment at water-solid interfaces. In this study, the uranium(VI) species on the ferrihydrite surface has been identified as a mononuclear, inner-sphere complex. This is based on the absence of a U-U interaction and the presence of a U-Fe interaction near 3.46 Å. This distance is in accord with an edge-sharing, bidentate surface complex. Splitting of the equatorial oxygen shell into two distances was observed for the uranium(VI) species on the surface of silica gel at pH 4. At low uranyl loading onto the surface, a U-Si interaction indicative of polyhedral edge-sharing at 2.72 Å was found. Furthermore, no U-U interaction was detected. The uranium(VI) species on the silica gel surface is also inner-sphere and mononuclear.

Acknowledgements

We thank G. Grambole for her help during the preparation of the silica gel sorption samples and W. Wiesener and G. Schuster for performing the ICP-MS and BET measurements, respectively. We gratefully acknowledge the XRD measurement of ferrihydrite by Josef Friedl at Technische Universität München-Weihenstephan. The majority of the EXAFS experiments were done at SSRL which is operated by the Department of Energy, Office of Basic Energy Sciences. We thank also HASYLAB for its support of the EXAFS experiments.

REFERENCES

- [1] R.J. Silva, H. Nitsche, *Radiochimica Acta*, 70/71 (1995), 377.
- [2] K.V. Ticknor, *Radiochim. Acta*, 64 (1994), 229.
- [3] A.J. Dent, J.D.F. Ramsay, S.W. Swanton, *J. Colloid Interface Sci.*, 150 (1992), 45.
- [4] T. Reich, H. Moll, M.A. Denecke, G. Geipel, G. Bernhard, H. Nitsche, P.G. Allen, J.J. Bucher, N. Kaltsoyannis, N.M. Edelstein, D.K. Shuh, *Radiochim. Acta*, 74 (1996), 219.
- [5] A. Manceau, L. Charlet, M.C. Boisset, B. Didier, L. Spadini, *Appl. Clay Sci.*, 7 (1992), 201.
- [6] T.D. Waite, J.A. Davis, T.E. Payne, G.A. Waychunas, N. Xu, *Geochim. Cosmochim. Acta*, 58 (1994), 5465.
- [7] J. Stanton, R.W. Maatman, *J. Colloid Sci.*, 18 (1963), 132.
- [8] L. Maya, *Radiochim. Acta*, 31 (1982), 147.
- [9] K.H. Lieser, S. Quandt-Klenk, B. Thybusch, *Radiochim. Acta*, 57 (1992), 45.
- [10] P. Michard, E. Guibal, T. Vincent, P. Le Cloirec, *Microporous Mat.*, 5 (1996), 309.
- [11] N. Labonne-Wall, V. Moulin, J.P. Vilarem, *Radiochim. Acta*, 79 (1997), 37.
- [12] R.M. Cornell, U. Schwertmann, *The Iron Oxides*, VCH, Weinheim, 1996.
- [13] C. Papelis, K.F. Hayes, L.O. Leckie, Department of Civil Engineering, Stanford University, HYDRAQL: A Program for the Computation of Chemical Equilibrium Composition of Aqueous Batch Systems Including Surface-Complexation Modeling of Ion Adsorption at the Oxide/Solution Interface (1988).

- [14] T. Arnold, M. Kohler, G. Bernhard, H. Nitsche, Institute of Radiochemistry, Annual Report 1995, FZR-123 (1996), 18.
- [15] T. Arnold, G. Geipel, G. Bernhard, H. Nitsche, Institute of Radiochemistry, Annual Report 1996, FZR-180 (1997), 4.
- [16] J.J. Bucher, P.G. Allen, N.M. Edelstein, D.K. Shuh, N.W. Madden, C. Cork, P. Luke, D. Pehl, D. Malone, *Rev. Sci. Instrum.*, 67 (1996), 1.
- [17] J.A. Bearden, A.F. Burr, *Rev. Mod. Phys.*, 39 (1967), 125.
- [18] D.C. Koningsberger, R. Prins, X-Ray Absorption. Principles, Applications, Techniques of EXAFS, SEXAFS and XANES, John Wiley and Sons, Inc., New York, 1988.
- [19] S.I. Zabinsky, J.J. Rehr, A. Ankudinov, R.C. Albers, M.J. Eller, *Phys. Rev. B*, 52 (1995), 2995.
- [20] E.A. Hudson, P.G. Allen, L.J. Terminello, M.A. Denecke, T. Reich, *Phys. Rev. B*, 54 (1996) 156.
- [21] P.G. Allen, D.K. Shuh, J.J. Bucher, N.M. Edelstein, C.E.A. Palmer, R.J. Silva, S.N. Nguyen, L.N. Marquez, E.A. Hudson, *Radiochim. Acta*, 75 (1996), 47.
- [22] H.A. Thompson, G.E. Brown Jr., G.A. Parks, *Am. Mineralogist*, 82 (1997), 483.
- [23] P.G. Allen, J.J. Bucher, D.L. Clark, N.M. Edelstein, S.A. Ekberg, J.W. Gohdes, E.A. Hudson, N. Kaltsoyannis, W.W. Lukens, M.P. Neu, P.D. Palmer, T. Reich, D.K. Shuh, C.D. Tait, B.D. Zwick, *Inorg. Chem.*, 34 (1995), 4797.

Figure 1. Left panel: Experimental (solid line) and fitted (dashed line) uranium L_{III} edge k^3 -weighted EXAFS spectra of samples Si1-Si5. Right panel: Corresponding Fourier transformed EXAFS of spectra Si1-Si5.

Note: Due to their lower signal statistics, the EXAFS spectra of samples Si4 and Si5 have been analysed in a shorter k range than the other samples.

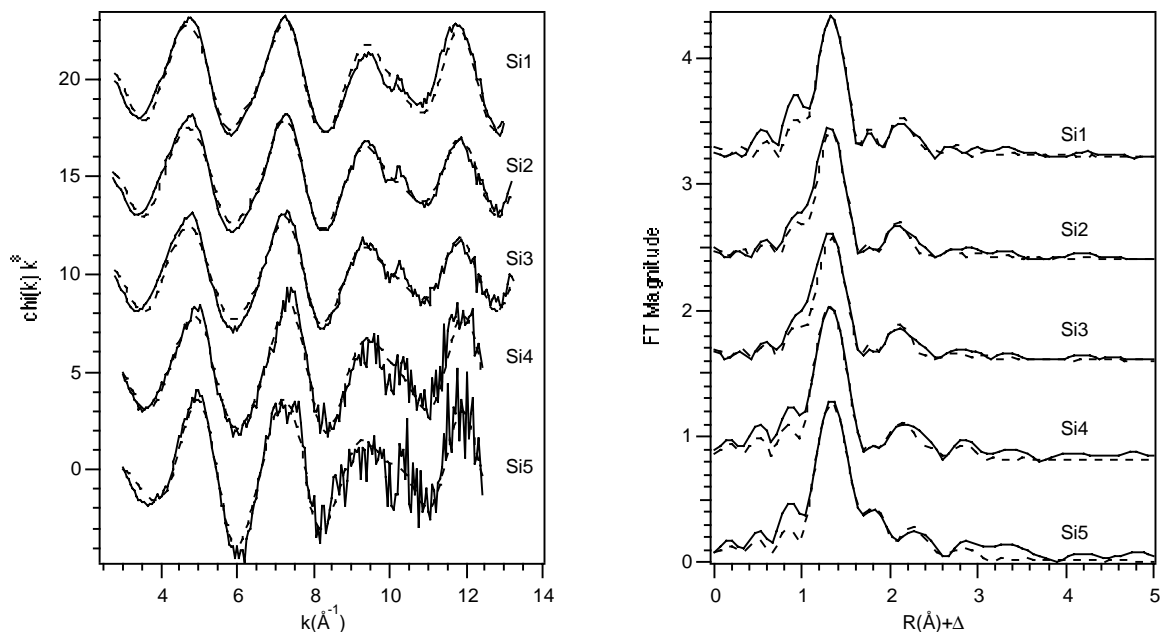


Figure 2. Left panel: Experimental (solid line) and fitted (dashed line) uranium L_{III} edge k^3 -weighted EXAFS spectra of samples Fe1-Fe3. Right panel: Corresponding Fourier transformed EXAFS of spectra Fe1-Fe3.

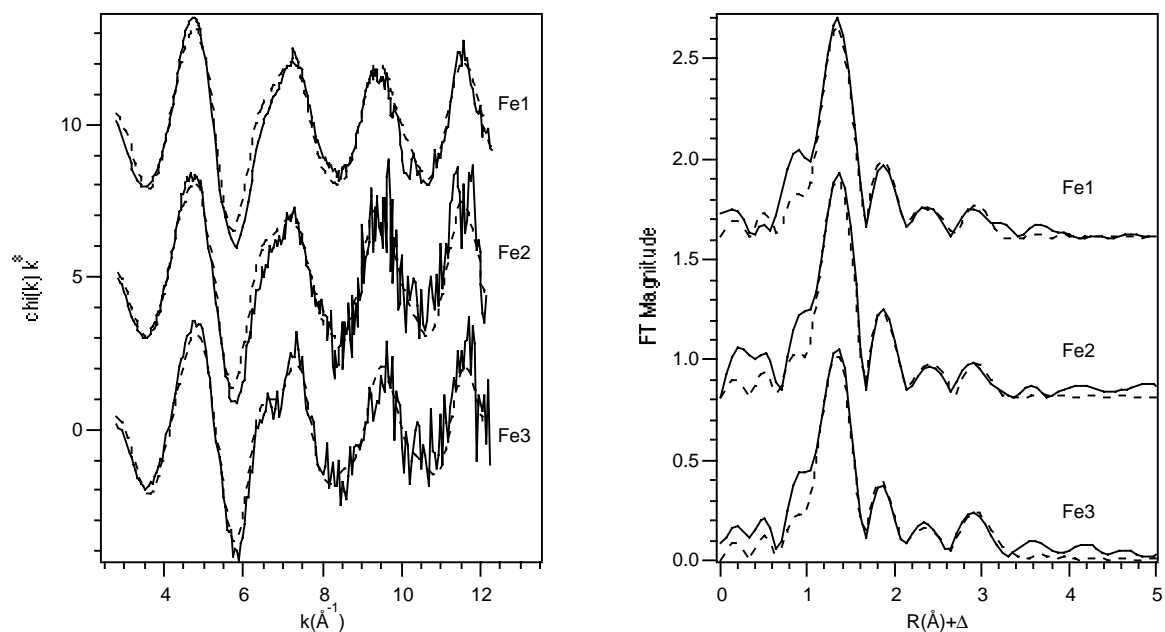


Table 1. Initial uranium(VI) concentration in solution, pH at the end of the exposure, amount of uranium sorbed onto silica gel, and percentage of uranium retained on silica gel*

Sample	UO ₂ ²⁺ (Mol/L)	pH	U loading (mg U/g)	U retained on silica (%)
Si1	5×10^{-2}	4.0	59	28
Si2	1×10^{-2}	3.5	19	36
Si3	5×10^{-3}	3.5	12	45
Si4	3×10^{-4}	4.5	7	94
Si5	2×10^{-5}	4.5	0.5	99

* Silica Gel 60 (for chromatography) from Merck, particle size of 5-65 μ m, proton exchange capacity 0.87 ± 0.01 meq/g, surface area 490 ± 49 m²/g. The uranium uptake was calculated from the amount of uranium left in the supernatant solutions as measured by ICP-MS.

Table 2. EXAFS structural parameters for uranyl sorbed onto silica gel at pH 4

Sample	Shell	R (\AA)	N	σ^2 (\AA^2)	ΔE_0 (eV)
Si1 (59 mg U/g)	U-O _{ax}	1.80	2	0.015	-14
	U-O _{eq1}	2.29	2.2(5)	0.0057	
	U-O _{eq2}	2.51	3.0(6)	0.0070	
Si2 (19 mg U/g)	U-O _{ax}	1.79	2	0.0023	-14
	U-O _{eq1}	2.26	1.7(2)	0.0042	
	U-O _{eq2}	2.50	3.6(6)	0.0111	
Si3 (12 mg U/g)	U-O _{ax}	1.80	2	0.0026	-14
	U-O _{eq1}	2.27	2.2(3)	0.0060	
	U-O _{eq2}	2.52	3.2(6)	0.0091	
Si4 (7 mg U/g)	U-O _{ax}	1.78	2	0.0013	-13
	U-O _{eq1}	2.26	2.5(6)	0.0058	
	U-O _{eq2}	2.51	2.0(7)	0.0045	
Si5 (0.5 mg U/g)	U-O _{ax}	1.79	2	0.0013	-13
	U-O _{eq}	2.26	2.6(4)	0.0035	
	U-Si	2.72	0.5(4)	0.0034	

Table 3. EXAFS structural parameters for uranyl sorbed onto ferrihydrite

Sample	Shell	R (Å)	N	σ^2 (Å ²)	ΔE_0 (eV)
Fe1	U-O _{ax}	1.81	2	0.0022	-13
	U-O _{eq}	2.39	6(1)	0.019	
	U-C	2.93	1*	0.002	
	U-Fe	3.48	1	0.013	
Fe2	U-O _{ax}	1.81	2	0.0018	-13
	U-O _{eq}	2.39	4.4(6)	0.014	
	U-C	2.93	1*	0.002	
	U-Fe	3.47	1	0.013	
Fe3	U-O _{ax}	1.80	2	0.0028	-14
	U-O _{eq}	2.36	5.9(8)	0.018	
	U-C	2.93	1*	0.001	
	U-Fe	3.42	1.0(5)	0.0063	
UF 4 [6]	U-O _{ax}	1.80	2.0	0.0028	-0.9
	U-O _{eq1}	2.35	3.0	0.0081	-0.9
	U-O _{sorbing}	2.52	2.0	0.0084	-0.9
	U-Fe	3.41	1.08	0.009	-4.2

* *N* was held constant at the closest integer value determined in a fit to the k^2 -weighted data.

X-RAY ABSORPTION SPECTROSCOPY STUDIES OF PLUTONIUM NITRATE SPECIES IN SOLUTION AND ON ION EXCHANGE RESINS

D. Kirk Veirs

Los Alamos National Laboratory
Los Alamos, NM 87545

Abstract

Plutonium nitrate complexes are fundamental to the separation techniques presently employed to process nuclear materials (solvent extraction and anion exchange) and have only recently been studied in detail. Nitrate speciation behaviour in acid has been recently studied using UV/VIS absorption spectroscopy and extended X-ray absorption fine structure (EXAFS) at ionic strengths up to nineteen molal. Details of the structure of plutonium nitrate complexes in solution have been determined using EXAFS and compared with the plutonium hexanitrate structure found in solid compounds that have been characterised by X-ray diffraction. This structural information has been used to develop novel anion exchange materials with improved performance. Molecular models of the interaction of the plutonium nitrate complex with the anion exchange site guide the design of these improved materials. Such molecular models require reliable experimental structural information. Used ion exchange resin that is now waste retains some plutonium even after extensive washing. Surprisingly detailed information about the chemical form of plutonium in these complex materials can be obtained using X-ray absorption spectroscopy. The plutonium in these materials is difficult to characterise because the materials are radioactive, opaque to visible light, and the plutonium concentration is often quite low. The oxidation state of plutonium can be deduced using X-ray absorption near edge spectroscopy (XANES), and in many cases the speciation of the plutonium can be deduced from the EXAFS spectrum. X-ray absorption spectroscopy has been shown to be a valuable tool when combined with other characterisation methods for studying speciation, determining structures in solution, and for characterising plutonium species in complex materials.

**AQUO IONS OF SOME TRIVALENT ACTINIDES:
EXAFS DATA AND THERMODYNAMIC CONSEQUENCES**

F. David, B. Fourest, S. Hubert, J.F. Le Du
IPN, 91406 Orsay Cedex, France (CNRS/IN2P3)

R. Revel, C. Den Auwer, C. Madic
CEA Marcoule, DCC/DRRV/SEMP, 30207 Bagnols sur Cèze Cedex, France

L.R. Morss
Argonne National Lab., Chem. Technology Division, Argonne, IL 60439, USA

G. Ionova, V. Mikhalko, V. Vokhmin, M. Nikonov
Institute of Physical Chemistry, Moscow 117915, Russia

J.C. Berthet, M. Ephritikhine
CEA, DSM/DRECAM/SCM, CNRS URA 331, 91191 Gif-sur-Yvette, France

Abstract

We have achieved a systematic study to obtain cation-oxygen bond distances d_{exp} and co-ordination numbers N for the trivalent actinide series U^{3+} , Np^{3+} , Pu^{3+} , Am^{3+} and Cf^{3+} in 1 M HCl solution. The distance d_{exp} values are 2.56, 2.52, 2.51, 2.51 and 2.44 Å respectively, and N values are between 9 and 10 for U^{3+} , Np^{3+} , Pu^{3+} , Am^{3+} and 8.5 for Cf^{3+} . The comparison of d_{exp} to those which can be evaluated from an ionic model, d_i , show a decreasing difference $\Delta d = d_i - d_{\text{exp}}$, as the atomic number of the actinide increases. This result is consistent with the more covalent character of the light actinide elements in comparison with the heavy ones. The Δd value for californium confirms our evaluation of the size of the water molecule in the vicinity of the cation and the dominant ionic character of the Cf^{3+} ion. As expected, the Δd values are correlated with the difference between +3 and the calculated effective charge of the cations (Δq). Finally, we have calculated the free energies of hydration of the cations on the basis of a model that takes into account the Born term, the influence of dipole, induced dipole and quadrupole interactions, the dispersion effect, the formation of a cavity, the influence of water molecules in the second hydration sphere, the electrostriction effect, and the packing factor for water molecules.

Introduction

The main task of the present work is to describe the structure of the aqua actinide ion in order to build a general and realistic model, which could describe the ion-solvent interactions and could be applied to slight covalent species such as actinides.

To be useful for experimental chemists the model has to fulfil two conditions:

- Firstly, the thermodynamic function should reproduce the available experimental data related to the aqua ion (such as free energy of hydration $\Delta G(\text{hyd})$), with a sufficient accuracy (around 1%).
- Secondly, in order to give the possibility to predict new data, the model should involve parameters that characterise the ion and have physical meaning.

For the modelling, we have chosen to retain five parameters which are: (i) the number of water molecules in the primary hydration sphere (N); and (ii) in the second hydration shell (H); (iii) the M^{3+} ion crystallographic radius $R_c(N)$; (iv) the charge of the ion q ; and (v) the size of the water molecule R_w . The distance d , between the ion and the closest oxygen atom, is $R_c(N) + R_w$. We will see that these parameters are not all independent.

The proposed Eq. [1] that gives the Gibbs hydration energy, $\Delta G(\text{hyd})$, is the following:

$$\begin{aligned} \Delta G(\text{hyd}) = & a q^2 (R_c + R_w)^{-1} + b q N (R_c + R_w)^{-2} + c q N (R_c + R_w)^{-3} \\ & + d q^2 N (R_c + R_w)^{-4} + e H + w (R_c + R_w)^3 + \text{disp} \end{aligned} \quad (1)$$

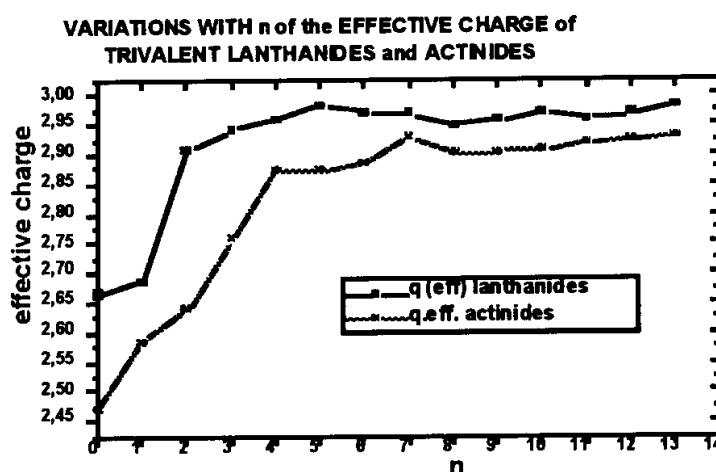
$\Delta G(\text{hyd})$ is a function $f(q, N, R_c, R_w, H)$ and depends on seven different terms: successively, the Born term, the influence of dipole, quadrupole and induced dipole interactions, the influence of water molecules in the second hydration sphere, the cavity formation and the dispersion effect. Most of these terms have been discussed during decades by theoreticians of the aqueous ions and recent books or reviews have been published [2,3,4].

The improvements of the proposed solvation model and Eq. (1) in comparison with previous models are essentially based on three considerations. Firstly, the size of the water molecule (R_w) should not to be considered as a constant (generally taken as the radius of the water molecule in the bulk: 1.38 Å), but depends on the distance to the central ion [5]. Secondly, the effect of the second hydration sphere should not to be neglected and H is a monotonous function of the charge density on the primary sphere [5]. Finally, since the medium has discontinuous properties in the vicinity of the central ion due to electrostriction phenomena, the parameters a , b , c , etc., which are algebraic functions of the characteristics of the medium, cannot be calculated assuming a dielectric constant equal to the value observed in the bulk. Therefore, these parameters have been evaluated [1] using 27 experimental data of $\Delta G(\text{hyd})$. Under these conditions, the calculated values of $\Delta G(\text{hyd})$ are in perfect agreement with experimental data corresponding to ionic species such as halides, alkalis, alkalino-earths and trivalent lanthanides (standard deviation are less than 0.2%). Since this model could be applied successfully to all monatomic ionic species, the question is now to see if it could be adapted to slightly covalent actinide or lanthanide species.

Hydration of trivalent actinides

It is now necessary to consider the effective charge of the covalent actinide aqua ions and to evaluate the transfer of s and p electrons of oxygen to the lanthanide or actinide orbitals. The overlap integral, S, corresponding to different electron transfers has been computed recently [6]. Based on these data, the effective charge q_{eff} of the cations has been deduced for the members of the two trivalent series (Figure 1). Consequently, a larger covalent effect of the light actinides is observed in comparison with homologous lanthanides. Even if the absolute determination of the effective charge should be re-evaluated more accurately, the general trend in the two series seems realistic. The evaluation of the effective charge has several consequences. First, we have accepted the hypothesis that $(3-q_{\text{eff}})/3$ quantifies the covalent effect, and, consequently, we can calculate $\Delta G(\text{hyd})_{\text{cov}}$ as the product $\Delta G(\text{hyd})_{\text{exp}} * \Delta q/q$. Then, in the case of lanthanides, $\Delta G(\text{hyd})_{\text{(ionic)}}$ is obtained as the difference $\Delta G(\text{hyd})_{\text{exp}} - \Delta G(\text{hyd})_{\text{cov}}$.

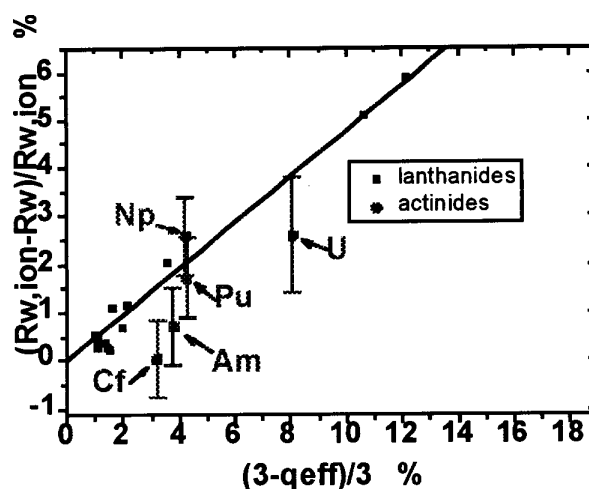
Figure 1. Variations of the calculated effective charge with the number of f electrons for the trivalent lanthanides and actinides



We can also, however, evaluate the covalent contribution in another manner. From the previous ionic model we can replace the charge in Eq. (1) by the calculated effective charge and then obtain a first approximation of the ionic contribution. By subtracting calculated and experimental data we have deduced the covalent contribution in the trivalent lanthanide series. The two evaluations of the covalent effect show a disagreement at the beginning of the lanthanide series. This apparent discrepancy could be interpreted by the fact that the latter data were obtained with the hydration model using the calculated effective charge when all other parameters and distances were kept identical as for ionic species. In fact it is well known that the distance cation-oxygen should also be affected by the covalent effect. Therefore, we can adjust that distance in such a way that Eq. (1) fits the previous $\Delta G(\text{hyd})_{\text{(ionic)}}$ computation. This new distance imposes to decrease the radius R_w of the water molecule: for a given $\Delta q/q$ value we can evaluate $\Delta R_w/R_w$.

The results of the evaluation of $\Delta q/q$ and $\Delta R_w/R_w$ in the lanthanide series show that the two quantities are linearly correlated (Figure 2). In order to verify and test this correlation in the case of trivalent actinide ions, which is based on the hypothesis of a linear correlation between the covalent effect and the decrease of the effective charge, it is necessary to determine experimentally the distance cation-oxygen for trivalent aqua actinide ions.

Figure 2. Correlation of $\Delta q/q$ with $\Delta R_w/R_{w,ion}$ for lanthanides (squares) and actinides (circles); the line corresponds to the calculated correlation with lanthanide data



EXAFS data

EXAFS appears as the appropriate tool to determine the cation-oxygen distances. Up to now only data on Pu^{3+} aquo ion have been published [7]. Experiments on other trivalent actinide ions have been carried out at LURE (Orsay, France): U^{3+} , Np^{3+} , Pu^{3+} , Am^{3+} and Cf^{3+} in 1 M HCl solutions. U^{3+} , Np^{3+} and Pu^{3+} were prepared from the tetravalent state using Zn amalgam. We have verified by UV absorption spectroscopy and XAS [8] that, in the presence of Zn amalgam, the totality of the actinides is reduced and that no re-oxidation occurs. Since we have no oxide reference such as M_2O_3 we have adopted the following procedure to process the XAS data: the $\text{UO}_{2.0}$ spectrum was acquired as reference. Simulation by FEFF702 gives the electronic parameters and FEFF allows to calculate these parameters for $Z > 92$. Then, these electronic parameters were adopted for the treatment of the An^{3+} aqua ion XAS spectra and the structural parameters were extracted: co-ordination numbers N , distances R , the Debye-Waller terms σ and ΔE . These main EXAFS data are reported in Table 1. Since N is measured with insufficient accuracy, we have focused our effort on the determination of R and accepted the co-ordination of 9.0 for AM and 8.5 for Cf which were the values reported earlier [9]. Co-ordination of 9 has also been reported for light actinides [10] and we chose, in a first step, this co-ordination value for the light trivalent actinide ions. Table 2 summarises the distance determinations and the main deductions. By subtracting the crystallographic radius R_c at the co-ordination number under consideration, we have deduced the experimental value of the radius, R_w , of the water molecule. These R_w data are compared to the radii that are deduced from the ionic model [5], $R_{w,ion}$. The two radii corresponding to californium ion are in perfect agreement; that is consistent with the ionicity of this element. It confirms our evaluation of the water molecule radius $R_{w,ion}$. As expected, we observe that the difference ΔR_w is significantly increasing when the element is more and more covalent. Surprisingly, U^{3+} appears as an exception. Since chemical observations and effective charge calculations lead to larger covalent effect in the case of light actinide ions in comparison with heavier ions, we have to admit that the crystallographic radius of U^{3+} should be larger than 1.226 Å. In other words, it should correspond to a larger co-ordination number than the value of 9 which was initially assumed. This hypothesis seems consistent with the generally observed trend: an increasing of N when the crystallographic radius is increasing.

Table 1. Experimental values of the co-ordination number N, the distance R (in Å), σ (in Å) and ΔE (in eV). Values in parenthesis are calculated errors on the last digit.

	N	R	σ	ΔE (eV)
UO _{2.0}	8.0	2.373(9)	0.09(1)	1.6(6)
U ³⁺ _{aq}	8.7(9)	2.56(1)	0.10(1)	2.1(6)
Np ³⁺ _{aq}	9.8(9)	2.52(1)	0.10(1)	3.8(7)
Pu ³⁺ _{aq}	9.9(9)	2.51(1)	0.10(1)	2.3(6)
Am ³⁺ _{aq}	9.5(9)	2.51(1)	0.10(1)	1.0(7)
Cf ³⁺ _{aq}	9.5(9)	2.44(1)	0.10(1)	2.5(9)

Table 2. Evaluation (in Å) of the cation-water molecule distance R, crystallographic radius R_c(N) of the cation, experimental R_w and calculated radius R_{w,ion} of the water molecule and difference $\Delta R_w = R_{w,ion} - R_w$

	R	R _c (N)	R _w	R _{w,ion}	ΔR_w
U ³⁺	2.56 ₀	1.226 (N = 9)	1.33 ₄	1.35 ₄	0.02 ₀
U ³⁺	2.56 ₀	1.259 (N = 9.5)	1.30 ₁	1.35	0.05
Np ³⁺	2.52 ₃	1.206 (N = 9)	1.31 ₇	1.35 ₂	0.03 ₅
Pu ³⁺	2.51 ₄	1.187 (N = 9)	1.32 ₇	1.35 ₀	0.02 ₃
Am ³⁺	2.50 ₈	1.169 (N = 9)	1.33 ₉	1.34 ₉	0.01 ₀
Cf ³⁺	2.43 ₅	1.094 (N = 8.5)	1.34 ₁	1.34 ₂	0.00 ₁

Finally, if we accept our experimental value of the distance, d_{exp} , the smaller value of ΔR_w could be interpreted by assuming that the co-ordination of the trivalent ion is larger than 9. For instance, if N is assumed to be equal to 9.5, then $\Delta R_w = 0.05$ Å (Table 2).

We can now introduce these data in the correlation between effective charge and distance ($\Delta q/q$ and $\Delta R_w/R_{w,ion}$) (Figure 2). It is shown that covalency is correlated with a decrease of ΔR_w . However, the calculated effective charges seem systematically smaller than those we can deduce from the expected correlation.

Conclusions

In conclusion, we have shown that the fundamental equation proposed for aqua ions having ionic character can be applied for slight covalent aqua ions such as actinides by taking into account their effective charge and the real distance between central ion and water. The computation of the effective charge of the actinide ions allows the evaluation of the cation-water molecule distances. Inversely, the experimental determination of the distances could be used to evaluate the real effective charges of the covalent ions. Moreover, several thermodynamic functions and the size of the aqua ions could be evaluated. Free hydration energy has been determined and the absolute covalent effect is quantified. By derivation versus temperature, Eq. (1) allows to elaborate a first realistic model of the entropy of any monatomic aqua ions. Therefore, the entropy of trivalent aqua actinide ions that has not been measured experimentally could be determined. Finally, the knowledge of the effective charge, size of the aqua ions and the number of water molecules involved could also be used to evaluate the activity coefficients of actinide ions with the Specific Interaction Theory or with determination of water activity [11].

Acknowledgements

We thank H. Noël of Rennes 1 University, CSIM for providing the UO_{2.0} sample. We are indebted for the loan of ²⁴⁹Cf through the heavy isotopes production programme of the US Department of Energy, specifically the High Flux Isotope Reactor and Radioelement Development Centre of Oak Ridge National Laboratory.

REFERENCES

- [1] F. David, V. Vokhmin, B. Fourest, P. David, to be published, see also F. David, B. Fourest, J. Duplessis, *J. Nucl. Materials*, 130 (1985), 273.
- [2] J.O'M. Bockris, A.K.N. Reddy, "Modern Electrochemistry", 2nd ed., Plenum Press, 1998.
- [3] Y. Marcus, "Ion Solvation", J. Wiley, ed., 1985.
- [4] Y. Marcus, *Chem. Rev.*, 88 (1988), 1475.
- [5] F. David, B. Fourest, *New J. of Chemistry*, 21 (1997), 167.
- [6] V. Mikhalko, G. Ionova, F. David., Proceedings of the NRC4 Conference, CP10, Saint Malo, 8-13 Sept. 1996.
- [7] P.G. Allen, J.J. Bucher, D.K. Shuh, N.M. Edelstein, T. Reich, *Inorg. Chem.*, 36 (1997), 467.
- [8] S.D. Conradson, I.A. Mahamid, D.L. Clark, N.J. Hess, E.A. Hudson, M.P. Neu, P.D. Palmer, W.H. Runde, C.D. Tait, *Polyhedron*, 17, No. 4 (1998), 599.
- [9] B. Fourest, G. Blain, F. David, L. Morss, *Radiochim. Acta*, 69 (1995), 215.
- [10] T. Kimura, Y. Kato, *J. Alloys and Compounds*, 271-273 (1998), 867.
- [11] M. Vdovenko, M.A. Ryazanov, *Zh. Fiz. Khim.*, 42 (1968), 1936.

APPLICATIONS OF XAFS SPECTROSCOPY TO SPECIATION PROBLEMS IN ENVIRONMENTAL RADIOCHEMISTRY

Patrick G. Allen

Glenn T. Seaborg Institute for Transactinium Science, LLNL
Livermore, CA 94551

D.K. Shuh, J.J. Bucher, N.M. Edelstein

Actinide Chemistry Group, Chemical Sciences Division, LBNL
Berkeley, CA 94720

T. Reich

Forschungszentrum Rossendorf, Inst. f. Radiochemie
D-01314 Dresden, Germany

Abstract

Radionuclide speciation information is essential for assessing and developing long-term strategies addressing issues such as migration in nuclear waste repositories or improvements in the processing of nuclear waste and materials. X-ray absorption fine structure (XAFS) spectroscopy utilising synchrotron radiation is an element specific structural technique which determines the average local structure around almost any atom, regardless of its speciation. The information is similar to crystallography (i.e. bond lengths and co-ordination numbers) with the important exception that XAFS does not require crystalline samples and can be performed on amorphous solids or species in solution. This is a key point for environmental systems where the element of interest often exists either in a surface adsorbed complex, aqueous solution or colloidal suspension. XAFS is becoming vital to characterising nuclear waste (i.e. site remediation) and to studying solution complexation processes (i.e. migration modelling).

We will present several XAFS examples in this paper, including results obtained for the aquo and chloro complexes of U(VI) (uranyl), Np(V) (neptunyl), Np(IV) and Pu(III) formed in concentrated chloride solutions. With the exception of Pu(III), the results demonstrate the trends of increasing chloride ligation and decreasing water ligation as a function of increasing chloride concentration. The numbers of co-ordinated chlorides are consistent with the formation of mono-, di-, and higher inner sphere chloro complexes. Along with uranyl carbonate and nitrate complexes, we have studied the solution structure of uranyl complexed with tartaric, malic and citric acids. The data for these mixtures at pH = 3 show the characteristic short U-O interactions of the uranyl ion, UO_2^{2+} , at 1.80 Å along with ~5 oxygen near neighbours around the uranyl equator at 2.40 Å. The XAFS of these solutions reveal a U-U interaction at 3.92 Å, indicating the presence of a dimeric structure which was proposed in earlier potentiometric titration experiments. The structure-solubility relationship for U(VI) oxide precipitates produced as a function of pH has been investigated. A structural trend is observed whereby the axial oxygen bond lengths increase from 1.80 Å at pH = 7 to 1.90 Å at pH = 11.

A concomitant decrease in the U-U nearest neighbour distance occurs with increasing pH. We will also present investigations on the mechanism of Tc immobilisation in cement waste forms which have shown that blast furnace slag and other sulphide-containing additives effectively reduce Tc(VII) to Tc(IV), a less soluble form.

**PROBING ACTINIDE ATOMS IN VARIOUS LIQUID
PHASE U, Np and Pu CO-ORDINATION COMPOUNDS**

C. Den Auwer*, R. Revel*, M.C. Charbonnel, M.T. Presson

CEA Marcoule, DCC/DRRV/SEMP Valrho

BP 171 30207 Bagnols-sur-Cèze, France

* *LURE* associate member

C. Madic

CEA Saclay, DCC, 91191 Gif-sur-Yvette, France

S.D. Conradson

Materials Science and Technology Division

Los Alamos National Laboratory

Los Alamos, NM 87545, USA

E. Simoni, J.F. Le Du

IPN, Bâtiment 100

Centre Universitaire Paris Sud

91407 Orsay Cedex, France

Abstract

Waste management of nuclear fuel represents a major environmental concern of this decade. To recycle fissile valuable materials, intimate knowledge of complexation mechanisms involved in the solvent extraction processes is indispensable. As a consequence, species occurring in the so-called PUREX process, such as $\text{UO}_2(\text{NO}_3)_2(\text{tributylphosphate})_2$ were at the starting point of these studies. Evolution of the actinide co-ordination sphere with the extracting ligand (i.e. organophosphorous, monoamide or diamide donor ligands), and with the actinide valence state were probed by XAS at the metal L_{III} edge.

Firstly, co-ordination sphere changes have been noticed when L is varied in the complexes of type $\text{UO}_2(\text{NO}_3)_2\text{L}_2$, L being either an organophosphorous oxygen donor ligand. Secondly, L being the tributylphosphate ligand, dramatic changes in the actinide co-ordination sphere appeared when the actinyl(VI) rod is replaced by An(IV). However, no significant evolution in the actinide environment has been noticed across the series UO_2^{2+} , NpO_2^{2+} and PuO_2^{2+} .

In all cases, molecular modelling, in addition with multiple scattering data analysis was used in order to fine tune the structural models that account for the evolution observed.

Introduction

The chemical species involved in the PUREX liquid-liquid extraction process of the back-end of the nuclear fuel cycle are still poorly identified, particularly concerning the co-ordination polyhedra of the complexes of actinide ions (e.g. U(VI), Pu(IV)) present in the solvent phase. In order to fine-tune the design of selective extractants for better actinide/less hazardous waste separation, macroscopic extraction parameters (such as kinetics, thermodynamics) must be understood. This task might be achieved by a better understanding of the molecular interactions between the chelating extracting ligand and the metal salt to be extracted in the solvent phase. Thus, molecular structural parameters have to be determined in the solvent phase. XAS is a particularly useful probe for both structural and electronic characterisation for non-isotropic systems. In this work, we present measurements at the L_{III} edges of actinide ions U, Np and Pu in series of various liquid phase co-ordination complexes involving organophosphate $OPOR_3$ (R = isobutyl, butyl and methyl group) ligands [1,2]. This type of ligand is used in liquid extraction processes such as the so-called PUREX process involving tributylphosphate (TBP) for U and Pu recovery [3].

The solid state compound $UO_2(NO_3)_2(TiBP)_2$ (TiBP = tri-*iso*-butylphosphate) of known crystallographic structure [4] was taken as a reference compound by extensive use of *ab initio* XAS calculation code FEFF702 [5].

Experimental

Synthesis of the U, Np and Pu complexes are described in both Refs. [1,2]. Data were acquired on both D44 beam line of the DCI (1.85 GeV, 300 mA) ring (LURE, France) and 4-2 beam line of the SPEAR (3 GeV, 100 mA) ring (SSRL, USA). Details on the data acquisition and the data treatment are given in [2].

Results and discussion

$UO_2(NO_3)_2(OPOR_3)_2$ liquid phase complexes

Figure 1 shows the schematic structure of these types of complexes. In order to evaluate the modifications of the uranyl nitrate co-ordination spheres, for R = isobutyl (ligand = TiBP), butyl (ligand = TBP) and methyl (ligand = TMP) ligands, a detailed analysis of the uranium photoelectron scattering paths was undertaken. Based on a previous study of the uranium co-ordination sphere [6] in the solid state compound $UO_2(NO_3)_2(TiBP)_2$, path enumeration was fully accomplished on these complexes using FEFF7 code. According to this, quantitative adjustments of the filtered FT were carried out in two times for all four complexes.

Figure 2 shows the Fourier transform (FT) of the calculated (FEFF7) EXAFS spectrum of solid state $UO_2(NO_3)_2(TiBP)_2$ at 77 K. All the 540 scattering paths that contribute to the total EXAFS spectrum for more than 0.1% were included (path amplitudes are normalised with respect to the amplitude of the most intense path over the entire k range, set to 100%). However, only paths that contribute more than 10% were isolated and presented in Figure 2 for the purpose of clarity. Each path contributes constructively or destructively to the total EXAFS spectrum, depending on its phase. It is also to be noted that multiple scattering paths that involve forward scattering are

Figure 1. Schematic representation of $\text{UO}_2(\text{NO}_3)_2(\text{TBP})_2$ complex

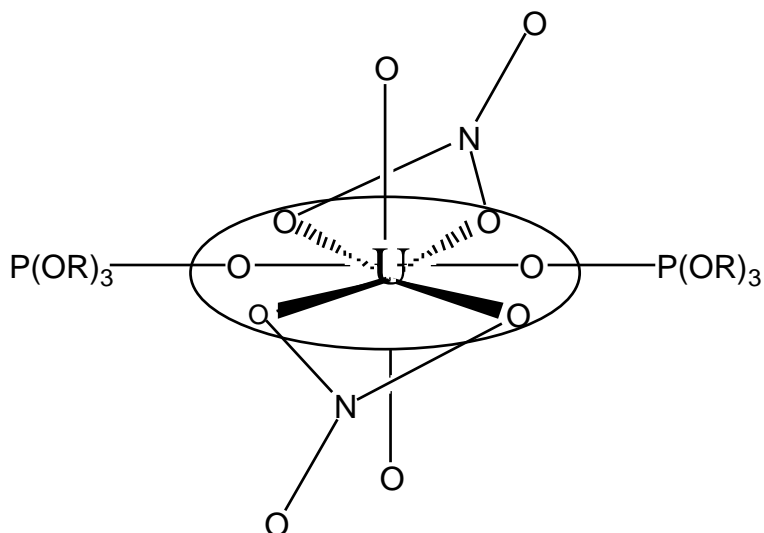
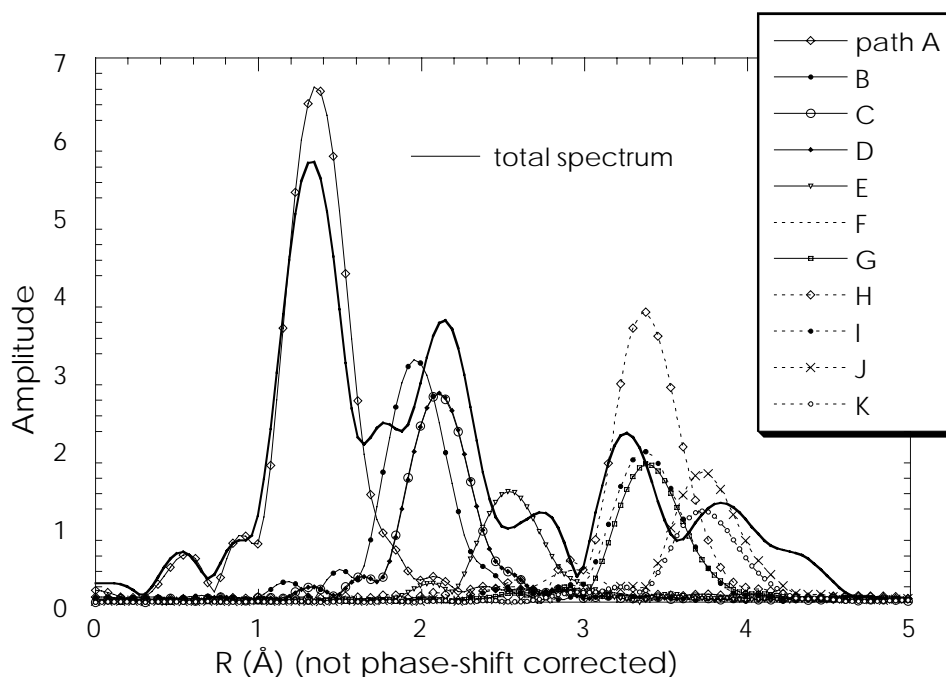


Figure 2. Modulus of the Fourier transform of the calculated EXAFS spectrum (FEFF7) of $\text{UO}_2(\text{NO}_3)_2(\text{TiBP})_2$ complex. Moduli of the Fts of the main photoelectron scattering paths are also represented [1].



particularly intense, as for example paths F and I. All multiple paths that do not include forward scattering are less than 10% intense. The path enumeration also shows that single scattering paths that involve all the oxygen first neighbours as well as the two nitrogen atoms of the two nitrate groups can be isolated within a filter window between 0.7 and 2.9 Å (not phase-shift corrected). Taking this window and neglecting the small part of multiple scattering paths that is included in it, a pure single scattering approach is a reasonable approximation to fit the contributions that occur in this range.

The five first paths were therefore included in the fitting procedure of the filtered EXAFS spectra of compounds $\text{UO}_2(\text{NO}_3)_2(\text{TiBP})_2$, $\text{UO}_2(\text{NO}_3)_2(\text{TBP})_2$, and $\text{UO}_2(\text{NO}_3)_2(\text{TMP})_2$. Structural parameters (i.e. U-X (X = O, N atoms) distances and their corresponding Debye-Waller factors) that were obtained are displayed in Table 1. In the case of $\text{UO}_2(\text{NO}_3)_2(\text{TiBP})_2$ at 77 K, bond distances compare satisfactorily within the error of ± 0.02 Å with the U-O structural data given by X-ray diffraction at 77 K for this solid state complex. It is however not surprising that path E is less accurately determined (within the error of $+0.04$ Å) since it does not correspond to a chemical bond between the central atom and the backscattering atom. Considering the TBP solution complex, it was previously shown [6] that there is no significant differences in r_p when the isobutyl groups in the solid state complex are replaced by the butyl ones in the liquid phase complex, both at 298 K. On the other hand, the significant shortening of r_p from $\text{UO}_2(\text{NO}_3)_2(\text{TBP})_2$ to $\text{UO}_2(\text{NO}_3)_2(\text{TMP})_2$ (-0.05 Å), both measured at room temperature in the liquid phase, seems to be caused by the replacement of the butyl groups by the methyl groups. Our assumption is that the steric hindrance of the phosphate ligand plays the main role in the structure modification. In fact, it has been shown using relativistic molecular orbital calculations that a decrease of the electronic donor effect of the alkyl group (in the order TBP > TMP) leads to a decrease of the strength of the covalent U-O(P) bond in the order TBP > TMP and thus must result in a decrease of r_p from TMP to TBP [7]. The opposite phenomenon is observed here. We think that the size of the TMP ligand allows it to approach the UO_2^{2+} co-ordination plane closer than the TBP ligand does, thus leading to a smaller value of r_p for TMP complex.

Table 1. Best fit parameters (U to neighbour distances, r ; Debye-Waller factors, σ) of the single scattering adjustment of the filtered EXAFS spectra of $\text{UO}_2(\text{NO}_3)_2(\text{TiBP})_2$, $\text{UO}_2(\text{NO}_3)_2(\text{TBP})_2$ and $\text{UO}_2(\text{NO}_3)_2(\text{TMP})_2$

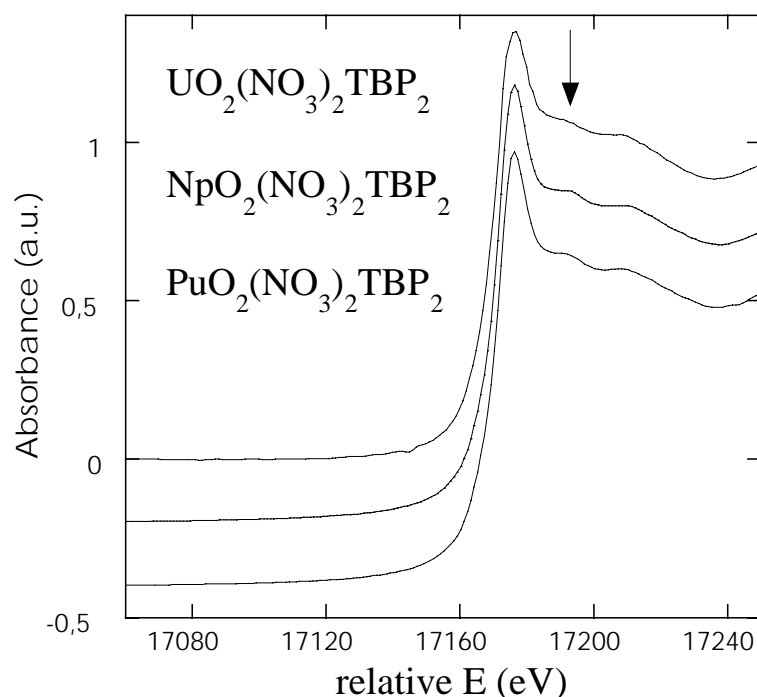
Path	Crystallographic value at 77 K ¹	TiBP (solid) 77 K	TiBP (solid) 298 K	TBP (liquid) 298 K	TMP (liquid) 298 K
A: U-O	$r = 1.757$ Å	$r = 1.78 \pm 0.01$ Å $\sigma = 0.032$ Å	$r = 1.78 \pm 0.01$ Å $\sigma = 0.045$ Å	$r = 1.77 \pm 0.01$ Å $\sigma = 0.046$ Å	$r = 1.78 \pm 0.01$ Å $\sigma = 0.050$ Å
B: U-O(P)	$r = 2.372$ Å	$r = 2.37 \pm 0.02$ Å $\sigma = 0.064$ Å	$r = 2.38 \pm 0.02$ Å $\sigma = 0.045$ Å	$r = 2.41 \pm 0.01$ Å $\sigma = 0.067$ Å	$r = 2.36 \pm 0.02$ Å $\sigma = 0.051$ Å
C: U-O(N)	$r = 2.509$ Å	$r = 2.53 \pm 0.01$ Å $\sigma = 0.057$ Å	$r = 2.54 \pm 0.01$ Å $\sigma = 0.056$ Å	$r = 2.54 \pm 0.01$ Å $\sigma = 0.077$ Å	$r = 2.53 \pm 0.02$ Å $\sigma = 0.086$ Å
D: U-O'(N)	$r = 2.510$ Å	$r = 2.53 \pm 0.01$ Å $\sigma = 0.057$ Å	$r = 2.54 \pm 0.01$ Å $\sigma = 0.056$ Å	$r = 2.54 \pm 0.01$ Å $\sigma = 0.077$ Å	$r = 2.53 \pm 0.02$ Å $\sigma = 0.086$ Å
E: U...N	$r = 2.960$ Å	$r = 3.00 \pm 0.01$ Å $\sigma = 0.009$ Å	$r = 2.98 \pm 0.02$ Å $\sigma = 0.036$ Å	$r = 2.99 \pm 0.03$ Å $\sigma = 0.072$ Å	$r = 2.96 \pm 0.08$ Å $\sigma = 0.090$ Å
r factor		0.03	0.04	0.03	0.05

¹ Structural parameters of $\text{UO}_2(\text{NO}_3)_2(\text{TiBP})_2$ solid state complex [4]

AnO₂(NO₃)₂(TBP)₂ liquid phase complexes

The series of U, Np and Pu complexes with general formula $\text{AnO}_2(\text{NO}_3)_2(\text{TBP})_2$ (An = U, Np, Pu) in TBP solution has been considered here. Figure 3 shows the L_{III} edges of all three complexes. All edges exhibit the characteristic resonance feature (underlined by an arrow on the Figure) that

Figure 3. L_{III} edges of the $AnO_2(NO_3)_2(TBP)_2$ solution complexes (An = U, Np, Pu). Edge energies are renormalised versus the white line maximum of the An(VI) species [2].



accounts for multiple scattering within the actinyl rod. This resonance has been shown to be attributed to triple and quadruple multiple scattering paths along the rod [1,5]. In the EXAFS spectra, the same five scattering paths as mentioned above have been taken into account in the fitting procedure. Table 2 shows that no significant bond length evolution occurs across the series. Recent calculation studies have shown a slight decrease in covalency from U to Pu adducts [8]. However, An-O(phosphate) distances are very unlikely to be affected by such a small overlap density variation, as confirmed by the present results.

Table 2. Best fit parameters (r and σ) of the EXAFS spectra of $AnO_2(NO_3)_2(TBP)_2$ (An = U, Np, Pu) solution complexes at room temperature

Neighbours	U	Np	Pu
An-O N = 2	$r = 1.77 \pm 0.01 \text{ \AA}$ $\sigma = 0.04 \pm 0.02 \text{ \AA}$	$r = 1.75 \pm 0.01 \text{ \AA}$ $\sigma = 0.04 \text{ \AA}$	$r = 1.75 \pm 0.01 \text{ \AA}$ $\sigma = 0.04 \text{ \AA}$
An-O(P) N = 2	$r = 2.41 \pm 0.01 \text{ \AA}$ $\sigma = 0.06 \pm 0.04 \text{ \AA}$	$r = 2.38 \pm 0.02 \text{ \AA}$ $\sigma = 0.06 \text{ \AA}$	$r = 2.40 \pm 0.02 \text{ \AA}$ $\sigma = 0.06 \text{ \AA}$
An-O(N) N = 2	$r = 2.54 \pm 0.01 \text{ \AA}$ $\sigma = 0.07 \pm 0.04 \text{ \AA}$	$r = 2.51 \pm 0.01 \text{ \AA}$ $\sigma = 0.07 \text{ \AA}$	$r = 2.50 \pm 0.01 \text{ \AA}$ $\sigma = 0.07 \text{ \AA}$
An-O'(N) N = 2	$r = 2.54 \pm 0.01 \text{ \AA}$ $\sigma = 0.07 \pm 0.04 \text{ \AA}$	$r = 2.51 \pm 0.01 \text{ \AA}$ $\sigma = 0.07 \text{ \AA}$	$r = 2.50 \pm 0.01 \text{ \AA}$ $\sigma = 0.07 \text{ \AA}$
An...N N = 2	$r = 2.98 \pm 0.03 \text{ \AA}$ $\sigma = 0.06 \pm 0.05 \text{ \AA}$	$r = 2.90 \pm 0.03 \text{ \AA}$ $\sigma = 0.06 \text{ \AA}$	$r = 2.91 \pm 0.03 \text{ \AA}$ $\sigma = 0.06 \text{ \AA}$
r factor	0.02	0.03	0.03

An(NO₃)₄(TBP)₂ liquid phase complexes

EXAFS spectra of the Pu and Np adducts with formal oxidation states equal to IV have been recorded (the U(IV) nitrate complex is not stable). In Figure 4, as an example, the FT of the EXAFS spectra of both Pu(VI) and Pu(IV) complexes show the disappearance of the axial oxygen upon reduction of Pu(VI) into Pu(IV). Contribution A, related to the 1.75 Å Pu-O axial bond is absent of the Pu(IV) spectrum. In both complexes, Contribution B accounts for the Pu-O(nitrate) and Pu-O(phosphate) bonds. As identified in previous studies, Contribution C is attributed to backscattering of the two phosphorous atoms, showing that the Pu-O(phosphate) bond length is not dramatically changed upon reduction of the Pu oxidation state. Two structural models may be considered for the Np(IV) and Pu(IV) species. The first one (Model 1) consists of two oxygen bridged TBP ligands and four monodentate nitrates; Model 2 consists of the two oxygen bridged TBP ligands and four bidentate nitrates. Fitting procedure according to both models for the Pu and Np adducts leads us to unambiguously discard Model 1. Table 3 compares the best fit parameters obtained for both Pu and Np adducts according to Model 2. Comparable bond distances are found in both Np and Pu cases, confirming the similarity of these complexes as in the case of AnO₂(NO₃)₂TBP₂ complexes (Table 2). Going from AnO₂(NO₃)₂TBP₂ complexes (An = Np, Pu) to An(NO₃)₄TBP₂ complexes, the An-O bond distances seem to be slightly decreasing (even if the difference stays within the error bars). This would be in agreement with an increase of the electrostatic charge going from the AnO₂²⁺ species to the An⁴⁺ ions and/or a decrease of the steric effect of the axial oxygen around the An atom and resulting in an increase of the An-O interaction.

Figure 4. Fourier transform (modulus and imaginary part) of the EXAFS spectra of solution complexes PuO₂(NO₃)₂(TBP)₂ and Pu(NO₃)₄(TBP)₂ [2]

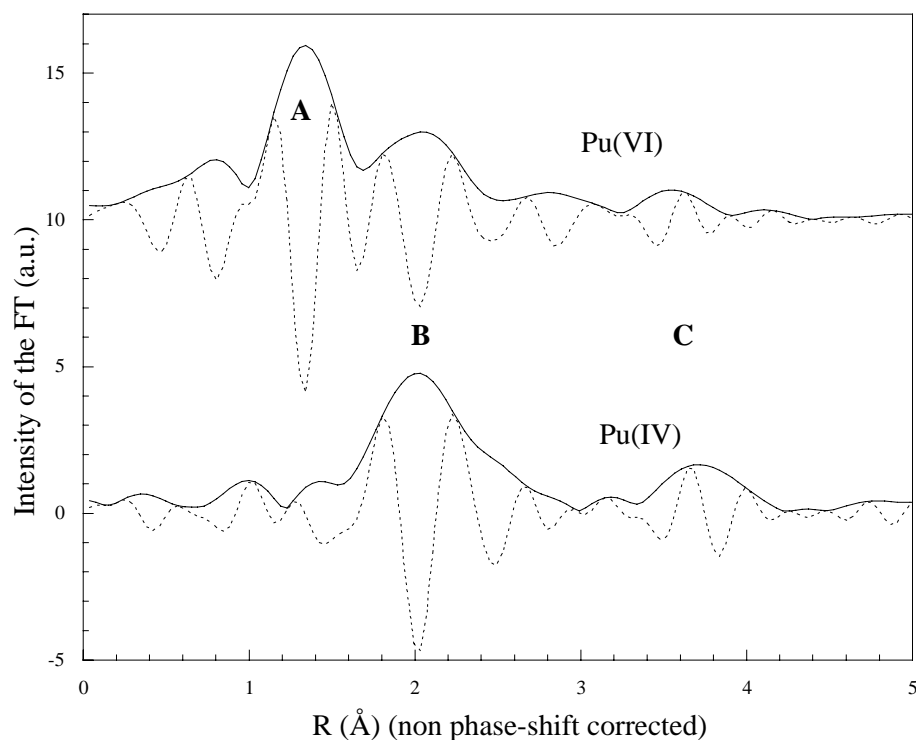


Table 3. Best fit parameters of the EXAFS spectra of both Pu(VI) and Pu(IV) TBP solution species at room temperature

Neighbours	Np (IV)	Pu (IV)
An-O(P) N = 2	$r = 2.35 \pm 0.02 \text{ \AA}$ $\sigma = 0.07 \pm 0.04 \text{ \AA}$	$r = 2.38 \pm 0.01 \text{ \AA}$ $\sigma = 0.07 \text{ \AA}$
An-O(N) N = 8	$r = 2.50 \pm 0.01 \text{ \AA}$ $\sigma = 0.08 \pm 0.03 \text{ \AA}$	$r = 2.48 \pm 0.01 \text{ \AA}$ $\sigma = 0.08 \text{ \AA}$
An...N N = 4	$r = 2.96 \pm 0.02 \text{ \AA}$ $\sigma = 0.07 \pm 0.04 \text{ \AA}$	$r = 2.95 \pm 0.01 \text{ \AA}$ $\sigma = 0.07 \text{ \AA}$
r factor	0.02	0.02

Conclusion

In this work, $\text{An(VI)O}_2(\text{NO}_3)_2(\text{TBP})_2$ solution complexes are shown to be isostructural across the U, Np and Pu series. No significant An-O bond length change has been observed at the An L_{III} edge. Upon reduction of the An oxidation state (An = Pu, Np) from VI to IV, evidence of the disappearance of the axial O atoms is given by both EXAFS and XANES investigation, while adjustment of the structural EXAFS parameters account for the Pu-O(nitrate) and Pu-O(phosphate) co-ordination sphere evolution.

Acknowledgements

We would like to thank Dr. J.P. Dognon for fruitful discussions and advice on An synthesis and model cluster construction. We would like to acknowledge COGEMA for funding.

REFERENCES

- [1] C. Den Auwer, M.C. Charbonnel, C., Madic, R Guillaumont, *Polyhedron* 17, 4507 (1998).
- [2] C. Den Auwer, R. Revel, M.C. Charbonnel, M.T. Presson, S.D. Conradson, E. Simoni, J.F. Le Du, C. Madic, *J. Synch. Rad.* 6, 101 (1999).
- [3] W.W. Shulz, L.L. Burger, J.D. Navratil, Science and Technology of Tributylphosphate, Vol. III, CRC-Press Inc., Boca Raton, Florida (1990).
- [4] J.H. Burns, G.M. Brown, *Acta Cryst. C*, 41 (1985), 1446.

- [5] A.L. Ankudinov, S.D. Conradson, *Phys. Rev. B* 57 (1998), 7518-7525.
- [6] C. Den Auwer, C. Lecouteux, M.C. Charbonnel, C. Madic, R. Guillaumont, *Polyhedron*, 16 (1997), 2233.
- [7] Y. Oda, H. Funasaka, H. Adachi, in proceedings of the GLOBAL Conference, Yokohama (Japan), 5-10 October 1997, p. 1478.
- [8] M. Hirata, R. Sekine, J. Onoe, H. Nakamatsu, T. Mukoyama, K. Takeuchi, S. Tachimori, *J. Al. Comp.* 271 (1998), 128-132.

EXAFS STUDY OF URANIUM(VI) SORBED TO HEMATITE

S.W. Swanton, G. Baston and M.M. Cowper

AEA Technology plc
424.4 Harwell, Didcot, Oxon, OX11 0RA, UK

J.M. Charnock

Daresbury Research Services, Daresbury Laboratory
Warrington, Cheshire, WA4 4AD, UK

Abstract

EXAFS spectroscopy has been used to study the structure of uranium(VI) species sorbed onto colloidal hematite under near-neutral conditions: at pH 5 and pH 7 in equilibrium with air, and at pH 7 in equilibrium with a 2% CO₂ atmosphere. The EXAFS spectra for all three samples are similar, showing a split U-O equatorial shell with short U-O distances of 2.18 Å and 2.36 Å. A shell at ~3.7 Å which is strongest at pH 5 and rather weak at high carbonate concentration is assigned to a surface iron atom. The U-Fe distance is significantly longer than measured for uranium(VI) sorbed onto ferrihydrite (3.44 Å, Waite *et al. Geochim. Cosmochim. Acta* 58, 5465, 1984) and suggests that the sorption site is monodentate rather than bidentate. The results also suggest that the sorbed species at pH 5 and pH 7 in equilibrium with air may retain some carbonate, which requires confirmation by other techniques. At pH 7 and 2% CO₂, the predominant uranium species appears to be an outer-sphere carbonate complex.

Introduction

Under near-neutral pH conditions characteristic of natural waters, there is little information available concerning the structure of sorbed actinide species upon mineral surfaces. An understanding of sorption processes is important for the interpretation of macroscopic measurements (e.g. batch sorption data) and the development of models for the speciation and distribution of radionuclides in the geosphere. Previous studies have demonstrated the potential of the EXAFS technique for studying the structure of sorbed species including uranium(VI) [1-5] on mineral surfaces. An important criterion for applying the EXAFS technique is that samples contain sufficient concentrations of the element of interest so that data of suitable quality for structural analysis can be obtained. However, at the pH of natural waters, the solubilities of actinide elements are low and, although sorption distribution coefficients may be very high, the preparation of samples suitable for EXAFS analysis may be difficult. For this reason, published EXAFS studies on uranium(VI) sorption have focused on samples prepared at low pH (< 5) where the solubility of uranium(VI) is high.

This paper describes a feasibility study to investigate the structure of uranium(VI) sorbed onto hematite under near-neutral conditions. Uranium is a key element to the safety case for the deep disposal of radioactive wastes; iron oxides are important contributors to sorption in natural rock systems. In previous studies of uranium sorbed onto ferrihydrite at pH 5 [2,3], the EXAFS spectra were interpreted as indicating that the uranyl ion is sorbed as an inner sphere bidentate surface complex of the type $(\equiv \text{FeO}_2)\text{UO}_2$, i.e. by sharing edges with $\text{Fe}(\text{O},\text{OH})_6$ octahedra. Furthermore, adsorption data in the alkaline pH range [3] suggested the existence of a second surface species, modelled as a surface complex of UO_2CO_3^0 , which on the basis of an ionic strength dependence of the sorption may be outer sphere. In this study, EXAFS data have been recorded for samples prepared at higher pH and using colloidal hematite rather than ferrihydrite as the substrate. Uranium(VI) was sorbed onto hematite at concentrations below the solubility limit at pH 5 (to repeat the conditions of [2,3]), pH 7 in equilibrium with air and at pH 7 in equilibrium with a 2% CO_2 atmosphere, where carbonate species are predicted to dominate the uranium(VI) speciation [3]. To aid the interpretation of the sorbed uranium data, spectra were also recorded for schoepite, $\text{UO}_2(\text{OH})_2 \cdot \text{H}_2\text{O}$, the thermodynamically most stable uranyl hydroxide phase, the potassium salt of the uranyl tricarbonate complex, $\text{K}_4\text{UO}_2(\text{CO}_3)_3$, and the ion $[\text{UO}_2(\text{CO}_3)_3]^{4-}$ in solution.

Experimental

Dilute dispersions ($0.15\text{-}0.3 \text{ g dm}^{-3}$) of colloidal hematite, prepared according to the method of Matijevic *et al.* [6] (particle size $\sim 100 \text{ nm}$), were used as the substrates. Samples of hematite were loaded with uranium(VI) under three conditions: pH ~ 5 (in equilibrium with air), designated HEM-U1; pH 7.0 in air, designated HEM-U2; and pH 6.95 in a 2% CO_2 atmosphere, designated HEM-U3. For sample HEM-U3, the hematite was contacted with a $10^{-4} \text{ mol dm}^{-3}$ uranium solution for several weeks. For HEM-U1 and HEM-U2, the uranium(VI) sorptive was added in increments, with additions designed to maintain the solution phase concentration of uranium(VI) below its solubility limit at the appropriate pH. In parallel with the preparation of samples for the EXAFS measurements using natural uranium, experiments were performed with ^{233}U to monitor the uptake of uranium onto the hematite. For EXAFS measurements, samples of the uranium-loaded hematites were collected by ultrafiltration onto 50 000 MWCO membranes, which were then sealed into plastic bags for mounting into the X-ray beam. The uranium to iron mole ratios in the samples were: 0.0032 for HEM-U1, 0.0033 for HEM-U2 and 0.0133 for HEM-U3. Coverages are estimated to be about 15%, 15% and 60% respectively assuming that each uranium atom is bound to a bidentate site.

A 0.3 mol dm⁻³ solution of [UO₂(CO₃)₃]⁴⁻ was prepared by dissolving schoepite in saturated NaHCO₃ solution (~1.2 mol dm⁻³).

EXAFS measurements were performed at the uranium-L_{III} X-ray absorption edge on station 9.2 of the Synchrotron Radiation Source at Daresbury Laboratory (2.0 GeV, 200 mA). The X-ray absorption spectra from the three solid samples and the [UO₂(CO₃)₃]⁴⁻ solution were measured in transmission. The uranium-loaded hematite samples were studied by fluorescence detection with multiple scans. The analysis was performed as described previously [1], except that the program EXCURV97 [7] was used instead of EXCURV88, and the phaseshifts were calculated using Hedin-Lundqvist potentials [8] and von Barth ground state rather than Xalpha potentials. Amplitude and inelastic loss factors were refined on the model compound uranyl nitrate hexahydrate and were transferred to the other samples without further refinement.

Results

The EXAFS data and the Fourier transforms (FTs) with model fits are compared in Figures 1 and 2 respectively. The results of the data analyses are presented in Table 1. The EXAFS spectra of uranium(VI) compounds are dominated by backscattering from the two axial oxygen atoms (O_{ax}) of the uranyl group, which give rise to a strong peak at ~1.8 Å in the FTs of all the samples studied. A second shell arises from oxygen atoms in the equatorial plane of the uranyl group. For UO₂(NO₃)₂ · 6H₂O and K₄UO₂(CO₃)₃, six equatorial oxygen atoms (O_{eq}) are fitted at ~2.45 Å; there are also significant contributions from the nitrogen or carbon atoms at ~2.9 Å and terminal oxygen atoms ~4.2 Å of the bidentate nitrate (2) or carbonate (3) ligands, respectively. Owing to the linear configuration of the uranium atom with the N-O or C-O bond there is a significant multiple scattering (MS) contribution to the amplitude of the terminal oxygen shell. This MS contribution was included in the simulations.

Figure 1. EXAFS (full line) and model fit (dashed line), for (a) UO₂(NO₃)₂ · 6H₂O, (b) 0.3 M [UO₂(CO₃)₃]⁴⁻_(aq), (c) UO₂(OH)₂₂ · H₂O, (d) HEM-U1, (e) HEM-U2, (f) HEM-U3

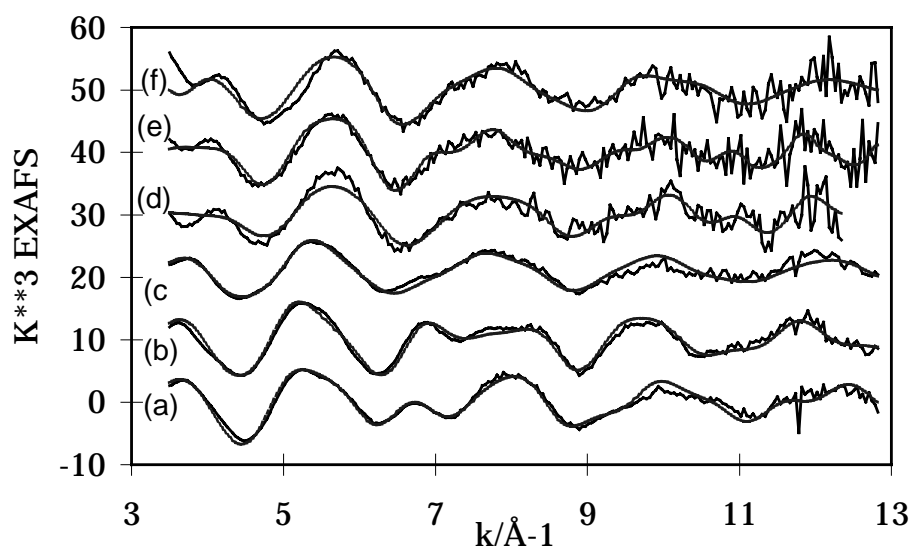


Figure 2. Amplitudes of the Fourier transforms of EXAFS (full line) and model fits (dashed line) for (a) $\text{UO}_2(\text{NO}_3)_2 \cdot 6\text{H}_2\text{O}$, (b) $0.3 \text{ M } [\text{UO}_2(\text{CO}_3)_3]^{4+}$, (c) $\text{UO}_2(\text{OH})_2 \cdot \text{H}_2\text{O}$, (d) HEM-U1, (e) HEM-U2, (f) HEM-U3

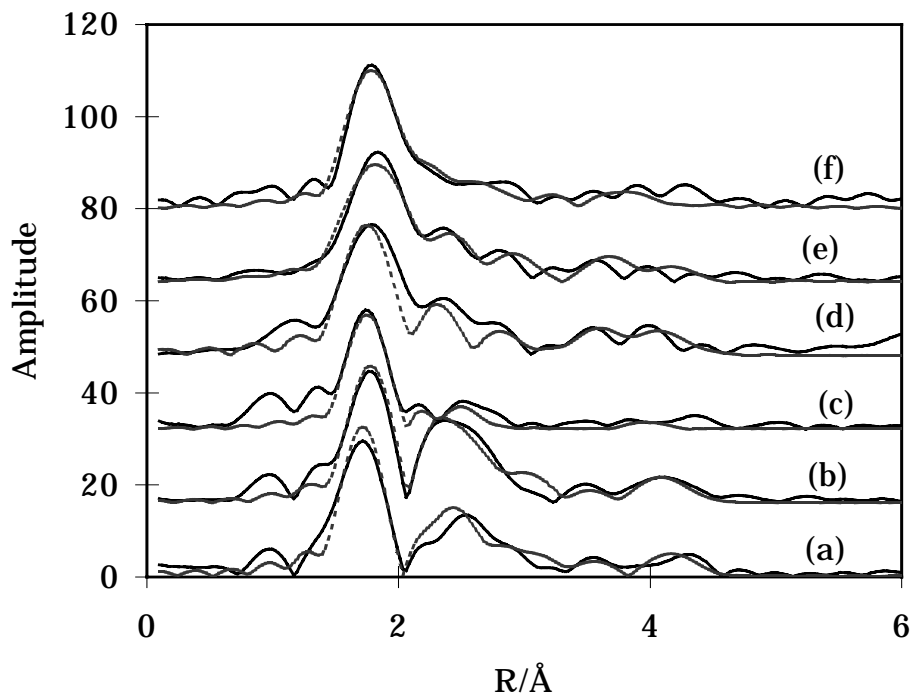


Table 1. Results of model fitting to EXAFS data

Sample	Atom type	N	R (Å)	$2\sigma^2$ (Å ²)
$\text{UO}_2(\text{NO}_3)_2 \cdot 6\text{H}_2\text{O}$	O_{ax}	2	1.77	0.004
	O_{eq}	6	2.48	0.015
	N^\dagger	2	2.98	0.005
	O^\dagger	2	4.24	0.008
$\text{K}_4\text{UO}_2(\text{CO}_3)_3$	O_{ax}	2	1.82	0.003
	O_{eq}	6	2.44	0.012
	C^\dagger	3	2.89	0.008
	O^\dagger	3	4.13	0.013
	K	6	3.78	0.039
0.3 mol dm ⁻³ [$\text{UO}_2(\text{CO}_3)_3$] ⁴⁺ solution	O_{ax}	2	1.81	0.002
	O_{eq}	6	2.44	0.012
	C^\dagger	3	2.91	0.003
	O^\dagger	3	4.17	0.010
schoepite ($\text{UO}_2(\text{OH})_2 \cdot \text{H}_2\text{O}$)	O_{ax}	2	1.78	0.003
	O_{eq}	2	2.29	0.014
	O_{eq}	3	2.46	0.015
	U	2	3.93	0.023

[†] Multiple scattering was included in the simulation from these pairs of carbonate C (or nitrate N) and O atoms.

Table 1. Results of model fitting to EXAFS data (cont.)

Sample	Atom type	N	R (Å)	2σ ² (Å ²)
HEM-U1	O _{ax}	2	1.78	0.007
	O _{eq}	2	2.17	0.003
	O _{eq}	3	2.35	0.005
	C [†]	1	2.89	0.004
	Fe	1	3.70	0.004
	O [†]	1	4.14	0.010
HEM-U2	O _{ax}	2	1.79	0.009
	O _{eq}	2	2.18	0.003
	O _{eq}	3	2.36	0.005
	C [†]	1	2.89	0.002
	Fe	1	3.72	0.008
	O [†]	1	4.15	0.007
HEM-U3	O _{ax}	2	1.78	0.003
	O _{eq}	2	2.19	0.004
	O _{eq}	3	2.35	0.007
	C [†]	2	2.90	0.004
	Fe	1	3.73	0.021
	O [†]	2	4.12	0.008

[†] Multiple scattering was included in the simulation from these pairs of carbonate C (or nitrate N) and O atoms.

An additional feature is observed ~ 3.6 Å in the FT for the nitrate and carbonate salts. This feature is understood to arise from multiple scattering along the linear uranyl group (O = U = O) through the central atom [9], and corresponds to twice the U-O_{ax} distance. A correct understanding of this feature is important for the analysis of the EXAFS from sorbed uranium(VI) species, because it appears at a distance that would be appropriate for a U-Fe interaction in a uranium surface complex. EXCURV97 enables full cluster multiple scattering through the central atom to be calculated and this contribution was included in those analyses where a peak was observed at ~ 3.6 Å.

The structural parameters fitted to the solid K₄UO₂(CO₃)₃ are in close agreement with those reported elsewhere in the literature [10]. The spectra for the [UO₂(CO₃)₃]⁴⁻ solution (Figure 1(b)) is very similar to that of the solid except that the potassium counter ions are no longer detected.

The EXAFS of schoepite are distinctly different from that of the uranyl nitrate and carbonate salts. The amplitude of the oxygen equatorial shell contribution is markedly reduced. This can be accounted for by splitting of the U-O_{eq} distances. A similar split is observed in the crystal structure of UO₂(OH)₂ [11]. The best integral fit of co-ordination number was obtained with two oxygen atoms at 2.29 Å and three oxygens at 2.46 Å. The peak at 4 Å in the FT can be attributed to uranium atoms. Two uraniums were fitted at 3.93 Å consistent with doubly bridged UO₂U units. It was noted that the uranyl MS peak at 3.6 Å is absent from the EXAFS of schoepite and it was not necessary to include this contribution in the fit. Multiple scattering is highly dependent on the geometry and the absence of this peak indicates that the uranyl unit is not perfectly linear in the disordered structure of schoepite.

The three uranium-loaded hematite samples gave similar spectra, which resemble qualitatively that of schoepite at high k values but are significantly different from schoepite at lower k. The spectra of HEM-U1 and HEM-U2 are very similar and could be fitted with similar models; the spectrum of

HEM-U3 shows some small differences at 4.5-5.5 Å⁻¹, 8 Å⁻¹ and 10 Å⁻¹ and differences in the FT. In each case, the inner co-ordination sphere of the uranium was best fitted with the two axial oxygens at ~1.8 Å, with four or five equatorial oxygens. As in schoepite, the contribution from the equatorial oxygen shell was very weak, and to obtain a good fit it was necessary to split the shell into two groups, with two oxygens at ~2.18 Å and three oxygens at ~2.36 Å. There is also a peak at ~3.7 Å in all three spectra which was strongest for HEM-U1 and weakest for HEM-U3. The best fit (integral co-ordination number) was obtained with a shell of one iron atom in each case with increasing Debye-Waller factor as pH and pCO₂ increased. Fits to this shell using full cluster multiple scattering from the linear O = U = O group instead of an iron atom, though reasonable, did not give as good a fit as the iron. Omitting the MS resonance is supported by the absence of this feature from the EXAFS of schoepite.

Owing to the similarity of the sorbed uranium spectra to that of schoepite at high k, an attempt was made to fit an outer shell of uranium atoms instead of an iron shell to the spectra of HEM-U2 and HEM-U3. However, in neither case did this shell fit. The Debye-Waller factors iterated to very high numbers indicating that if there is a surface precipitate it is not well ordered. For HEM-U3, there was a slight improvement to the fit if both an iron shell at 3.73 Å and a uranium shell at 3.93 Å were included. However, the improvement was not good enough to justify the extra parameters.

There is evidence in all three spectra for bidentate carbonate co-ordination to the uranium. An improvement in the fit was obtained by including a carbon atom shell at ~2.9 Å. A terminal oxygen atom at ~4.1 Å could also be included. The best fits (for integral values of co-ordination number) were obtained by including one carbonate for the HEM-U1 and HEM-U2 spectra and two for the HEM-U3 spectrum.

Discussion

The results indicate that the predominant surface species for uranium sorbed onto hematite at pH 5 and pH 7 in equilibrium with air is an inner-sphere complex. However, the U-Fe distance of ~3.7 Å measured here is significantly longer than that reported for uranium(VI) sorbed onto ferrihydrite (3.44 Å in) [3] and the U-O_{eq} distances are rather shorter at 2.18 Å and 2.36 Å compared to 2.36 Å and 2.52 Å in [3]. These results suggest that there is a change in the mode of co-ordination of uranyl ion to the surface from bidentate binding on ferrihydrite to monodentate binding on hematite. The fitted co-ordination number for the iron shell of about one suggests that each uranyl group is linked to a single iron atom via a single oxygen bridge. This change in the type of co-ordination site may result from the condensed crystal structure of hematite which is characterised by face-sharing between adjacent pairs of octahedral sheets [12]. Corner sharing rather than edge sharing sites may predominate at the hematite surface.

The two U-O_{eq} distances fitted for the sorbed uranium species are also smaller than the values fitted for schoepite in which U atoms are linked via dihydroxy bridges with a U-U distance of 3.93 Å. In the crystal structure of UO₂ · H₂O [11], the uranyl groups (U-U distance ~4.2 Å) are linked to four others via single equatorial oxygen bridges with two shorter oxygen atoms at 2.24±0.06 Å and two at 2.43±0.06 Å. Tightening of the U-O_{eq} bonds for the sorbed uranium species bonds may indicate a reduction in the co-ordination number to four and would be consistent with a change in the type of oxygen bridge. It is possible that steric constraints imposed upon the equatorial atoms around the uranyl group due to the monodentate binding to the surface may cause a reduction in co-ordination number from five to four.

The small contribution of the iron peak for HEM-U3 and the presence of carbonate ligands is consistent with the formation of predominantly outer-sphere carbonate complex(es) at pH 7 in equilibrium with 2% CO₂ atmosphere. Although the best fit is obtained by including two carbonate ligands, there is significant uncertainty in this co-ordination number. The presence of carbonate in the sorbed species on hematite at pH 5 and pH 7 in equilibrium with air is not predicted by thermodynamic modelling [13], however. The results presented here suggest that carbonate may bind to sorbed uranium on hematite at lower pH than predicted. Ho and Miller [14] observed charge-reversal of hematite sols on sorption of uranium(VI) in the presence of bicarbonate at pH < 7.6 which was ascribed to the sorption of the negatively charged hemicarbonate complex [(UO₂)₂CO₃(OH)₃]⁻. Reich, *et al.* [15] have also observed a light atom at ~2.9 Å, assigned as a carbonato-carbon atom, in the EXAFS of uranium(VI) sorbed onto ferrihydrite at pH 5.8 and pH 7.8. Other techniques need to be applied to investigate this observation further.

Conclusions

This feasibility study has shown that it is possible to collect EXAFS data of suitable quality for structural analysis from colloidal mineral samples loaded with relatively low levels of an actinide. The U/Fe ratios studied here are over an order of magnitude lower than those studied by Waite, *et al.* [3]. The value of comparative EXAFS measurements on samples of known or related structure (in this case the [UO₂(CO₃)₃]⁺ ion and schoepite) to build confidence in the interpretation of the EXAFS data from unknown samples has been demonstrated. This study has provided novel data on the structure of the uranium species sorbed onto the surface of hematite at near-neutral pH values and indicates that the mode of inner-sphere surface complexation may be different from that found on ferrihydrite. The EXAFS technique has significant potential for studying the structure of sorbed actinide species, data that is not available from any other technique and which can provide fundamental understanding of sorption processes, an important topic in environmental actinide chemistry and in safety assessment studies for the deep disposal of radioactive waste.

Acknowledgements

This work was undertaken as part of the Nirex Safety Assessment Research Programme. Keeley Bond and Claire Linklater are thanked for preliminary thermodynamic modelling calculations. We thank Daresbury Laboratory for the provision of beam time and experimental facilities.

REFERENCES

- [1] A.J. Dent, J.D.F. Ramsay and S.W. Swanton, *J. Colloid Interface Sci.* 150, 45-60, 1992.
- [2] A. Manceau, *et al.*, *Appl. Clay Sci.* 7, 201-223, 1992.
- [3] T.D. Waite, *et al.*, *Geochim. Cosmochim. Acta* 58, 5465-5478, 1994.
- [4] C. Chisholm-Brause, *et al.*, *Geochim. Cosmochim. Acta* 58, 3625-3631, 1994.
- [5] T. Reich, *et al.*, *Radiochim. Acta* 74, 219-223, 1996.
- [6] E. Matijevic, *Ann. Rev. Mater. Sci.*, 483-516, 1985.
- [7] N. Binsted, *et al.*, Daresbury Laboratory EXCURV97 Program, 1997.
- [8] L. Hedin and S. Lundqvist, *Solid State Physics* 23, 1-181, 1969.
- [9] P.G. Allen, *et al.*, *Inorg. Chem.* 34, 4797-4807, 1995.
- [10] A. Anderson, C. Chieh, D.E. Irish and J.P. Tong, *Can. J. Chem.* 58, 1651 (1980).
- [11] R.B. Roof, D.T. Cromer and A.C. Larsen, *Acta Cryst.* 17, 701-705, 1964.
- [12] R.L. Blake, R.E. Hessewick, T. Zoltai and L.W. Finger, *Amer. Mineral.* 51, 123-129, 1966.
- [13] C.M. Linklater, personal communication.
- [14] C.H. Ho and N.H. Miller, *J. Colloid Interface Sci.* 110, 165-171, 1986.
- [15] T. Reich, *et al.*, *J. Electron Spectrosc. Rel. Phenom.* 96, 237-243, 1998.

X-RAY MAGNETIC CIRCULAR DICHROISM OF URANIUM COMPOUNDS

A. Rogalev, M. Finazzi, J. Goulon, C. Neumann
European Synchrotron Radiation Facility (ESRF)
B.P. 220, 38043 Grenoble Cedex, France

W. Grange, J.-P. Kappler
IPCMS-GEMME
23 rue du Loess, 67037 Strasbourg, France

J.-P. Sanchez, P. Dalmas, A. Yaouanc
CEA
Département de Recherche Fondamentale sur la Matière Condensée, SPSMS
38054 Grenoble Cedex 9, France

Ph. Sainctavit
Laboratoire de Minéralogie et Cristallographie de Paris
CNRS URA9, Universités de Paris 6 et 7
75252 Paris, France

Abstract

Actinide compounds, which are straddling the magnetic properties of rare earths and transition metals, are attracting much interest. The fact that the 5f states are involved in both the chemical bonding and the magnetism leads to a wide variety of magnetic behaviours, such as Pauli paramagnetism, localised and itinerant magnetism, and heavy fermions [1].

We review the results of X-ray magnetic circular dichroism (XMCD) experiments performed at the $M_{IV,V}$ absorption edges of uranium in a wide variety of compounds including localised and itinerant ferromagnets and heavy fermion superconductors. It has been shown [2] that valuable information about the localised vs. itinerant character of 5f states can be obtained from the ratio of the orbital to spin moment. Since the magneto-optical sum rules relate directly the $M_{IV,V}$ edge dichroic signal and the projected orbital L_z and spin S_z component of the magnetic moment in the ground state as well as their ratio, XMCD appears to be an experimental measure of 5f states delocalisation.

Experimental results are presented in comparison with available polarised neutron scattering data. Rather good agreement is found for strongly localised (US, USbTe) and fully itinerant (UFe₂, UNi₂) systems, which proves the validity of the sum rules for U $M_{IV,V}$ edges and the reliability and the great potentialities of the XMCD technique. The failure of pure J multiplet calculations to reproduce the shape of the M_V -dichroic signal and strong discrepancies between experiments and the results of the band structure calculations clearly indicate that the proper theoretical description of the magnetic properties of uranium compounds has to be revised.

REFERENCES

- [1] Handbook on the Physics and Chemistry of the Actinides, Vols. 1, 2 and 5, A.J. Freeman and G.H. Lander, eds., North Holland (1989).
- [2] G.H. Lander, M.S.S. Brooks and B. Johansson, *Phys. Rev.* B43, 13672 (1991).

**X-RAY ABSORPTION AND DIFFRACTION STUDIES OF MONOMERIC
ACTINIDE TETRA-, PENTA-, AND HEXAVALENT CARBONATO COMPLEXES**

**David L. Clark^a, Steven D. Conradson^b, D. Webster Keogh^c, Mary P. Neu^c,
Phillip D. Palmer^c, Wolfgang Runde^d, Brian L. Scott^d, and C. Drew Tait^c**

^aChemical Science and Technology Division

^bMaterials Science and Technology Division

^cNuclear Materials and Technology Division

G.T. Seaborg Institute for Transactinium Science

Los Alamos National Laboratory, Los Alamos, NM 87545, USA

Abstract

Structural similarities between solid state and solution carbonato complexes for the light actinide elements (U, Np and Pu) are discussed. For hexa- and pentavalent complexes, linear trans-dioxo bonds and bidentate carbonate complexation are common themes, with bond lengths changing only slightly between solid and solution state. While bidentate carbonate complexation can accommodate a co-ordination number of 6 in the equatorial bonding plane, a decrease to a co-ordination number of 5 occurs as carbonate ligands are successively replaced by water. For the tetravalent Pu, a pseudo equatorial carbonato complexation can be seen, with approximately trans-bidentate carbonates to form a pentacarbonato Pu(IV) complex. As with the other oxidation states, the bond distances and structure vary little between solid and solution states. When combined, the data provide a consistent and compelling argument as to the solution molecular structures of actinide carbonato complexes.

Introduction

Carbonate and bicarbonate are common anions present in significant concentrations in many natural water environments, and are exceptionally strong complexing agents for actinide ions [2-8]. Actinide ions that normally exhibit quite low solubilities in near-neutral solutions can be complexed by carbonate ligands and form solutions of higher actinide ion concentrations through formation of anionic carbonato complexes [2]. Therefore, carbonato complexes of the actinide ions may play an important role in migration from a nuclear waste repository or in accidental site contamination. The environmental behaviour of actinide carbonato complexes will ultimately depend on their molecular scale structure and properties, thus it is of intrinsic interest to determine the co-ordination chemistry and molecular structures of actinide carbonato complexes both in solution and in the solid state. X-ray diffraction and spectroscopic methods are among the most useful for providing molecular-scale information, and in this report we provide a brief overview of our most recent molecular-level structural studies of anionic carbonato complexes of actinide ions using X-ray absorption and X-ray diffraction techniques.

Tetravalent actinide carbonato complexes

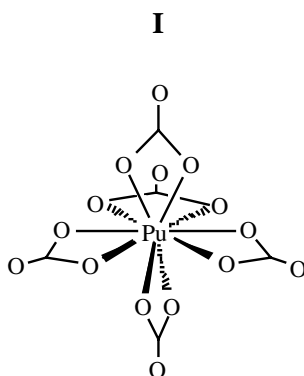
Over the last decade, there have been many studies focused on determination of the identities of the chemical species present in the plutonium(IV) carbonate system, resulting in essentially two interpretations of Pu(IV) carbonate thermodynamic data put forth in the literature. One interpretation favours the simple stepwise formation of $[\text{Pu}(\text{CO}_3)_n]^{4-2n}$ complexes ($n = 0 - 5$) [5,6,9-11], while the other [12-14] favours the formation of mixed hydroxo-carbonato complexes of general formula $[\text{Pu}(\text{OH})_m(\text{CO}_3)_n]^{4-m-2n}$. The difficulty in interpreting the data arises from the fact that the hydrolysis and carbonate formation constants are similar in magnitude, making it difficult to distinguish between the various models. As a result, it is important to unequivocally identify the nature of the limiting complex in the plutonium-carbonate system to provide a starting point for identifying other complexes formed in the system. We employed X-ray diffraction and absorption to unequivocally determine the structures of the limiting complex both in solution and the solid state [15].

Solid state X-ray diffraction

Single crystals of $[\text{Na}_6\text{Pu}(\text{CO}_3)_5]_2 \cdot \text{Na}_2\text{CO}_3 \cdot 33\text{H}_2\text{O}$ were prepared by slow evaporation a 0.15 M solution of Pu(IV) in 2.6 M Na_2CO_3 . The asymmetric unit contains a complex network consisting of $[\text{Pu}(\text{CO}_3)_5]^{6-}$ anions and Na^+ cations which are linked through interactions with CO_3^{2-} and H_2O ligands. The full details of the three-dimensional structure have been reported [15]. In the $\text{Pu}(\text{CO}_3)_5^{6-}$ anion (I) the central Pu atom is co-ordinated to ten O atoms of five bidentate carbonato ligands, in a structural unit that is very similar to the related $\text{Th}(\text{CO}_3)_5^{6-}$ anion [16]. For the purpose of comparison, it is useful to view this complex structure as a modification of the hexagonal bi-pyramidal co-ordination polyhedron seen in $[\text{AnO}_2(\text{CO}_3)_3]^{n-}$ complexes, with three CO_3^{2-} ligands in a pseudo equatorial plane, and two in axial positions, and is illustrated qualitatively in Figure 1. The ten Pu-O distances to the carbonate ligands average 2.415(7) Å, and the five nonbonding Pu--C and distal Pu--O distances average 2.874(9) and 4.117(10) Å. Bond distances are compared in Table 1.

Solution EXAFS studies

We employed extended X-ray absorption fine structure (EXAFS) spectroscopy for structural details of the limiting plutonium(IV) ion in 2.5 M Na_2CO_3 solution. Under these conditions, the



limiting Pu(IV) species is characterised by a strong electronic absorption band at 485.5 nm [9,10]. Electronic absorption spectra of the solution from which the EXAFS sample was taken were examined both before and after EXAFS analysis, and indicated that the same limiting Pu(IV) species was present in excess of 99%. X-ray absorption measurements were performed at the plutonium L_{III} edge. The Fourier transform and theoretical fit (without phase corrections) of the k^3 -weighted EXAFS data are shown in Figure 2.

Backscattering phases and amplitudes of the individual neighbouring atoms, using mono- and bidentate ligation models were calculated using FEFF7 [17]. The fitting parameters found for the Pu solution structure are listed in Table 1 [15]. The limiting species in high carbonate solution for Pu(IV) is best fit using five carbonate ligands and hence is consistent with the $[Pu(CO_3)_5]^{6-}$ formulation found in the solid state. The first shell contains ten O atoms with Pu-O = 2.42(2) Å; the second shell was fit with five C atoms with Pu-C = 2.89(2) Å, and a third shell was fit with five O atoms with Pu-O = 4.17(2) Å. These distances and co-ordination numbers correspond well with the average Pu-O, nonbonding Pu-C and distal Pu-O distances of 2.415(7), 2.874(9), and 4.117(10) Å found in the $[Pu(CO_3)_5]^{6-}$ ion in the solid-state structure of $[Na_6Pu(CO_3)_5]_2 \cdot Na_2CO_3 \cdot 33H_2O$.

The three single shell contributions to the total EXAFS fit are shown with negative fit amplitudes in Figure 2. The close spacing of Pu-O and Pu-C shells generates the appearance of a single peak in the EXAFS Fourier transform. Despite its greater distance from the Pu atom, the nonbonding distal O shell of the carbonate ligand derives its intensity from multiple scattering effects which are important when atoms are arranged in an approximately collinear fashion. In such cases, the photoelectron is strongly focused by the intervening atom, resulting in significant amplitude enhancement. The focusing effect occurs for bidentate carbonate ligands, where Pu, C, and the distal O atom are all collinear [18,19].

The UV-Vis diffuse reflectance spectrum of a single crystal of $[Na_6Pu(CO_3)_5]_2 \cdot Na_2CO_3 \cdot 33H_2O$ ground into a powder is nearly identical to the solution absorption spectrum of the limiting Pu(IV) carbonate complex in 2.5 M Na_2CO_3 solution. The peak by peak correspondence by position and relative absorption strengths, along with solution EXAFS data, suggest that the Pu(IV) chromophore is the same in both cases, and confirms that the $[Pu(CO_3)_5]^{6-}$ ion is the limiting species in high carbonate solutions [15].

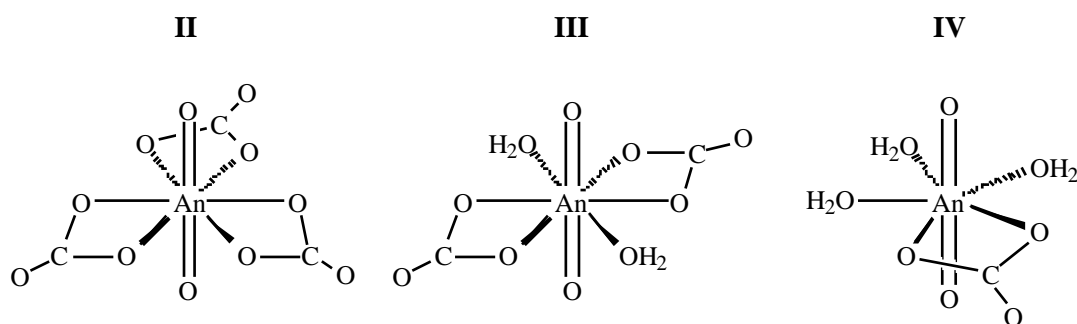
Pentavalent actinide carbonato complexes

The pentavalent state of U and Pu are generally unstable with respect to disproportionation under the relatively high solution concentrations needed for XAFS studies, so we focused our initial efforts on Np(V) [20]. Neptunium(V) solubility in carbonate solutions is controlled by the formation of

solids of general formula $M_{(2n-1)}\text{NpO}_2(\text{CO}_3)_n$ [2]. The limited solubilities (10^{-4} - 10^{-4} M) [21,22] of these phases make the solution species in equilibrium with the solids very difficult to study using common structural probes. We found that alkali metal-free synthesis, employing the tetrabutylammonium (TBA) cation provides 10^{-4} M solutions of $\text{NpO}_2(\text{CO}_2)^-$, and $\text{NpO}_2(\text{CO}_3)_2^{3-}$ [20], and afforded the opportunity to determine the molecular structures of these environmentally important complexes employing EXAFS spectroscopy. Known thermodynamic constants were used to prepare single component solutions [22], and NIR spectroscopy was used both before and after EXAFS analysis to confirm that each solution sample contained an essentially single, pure neptunyl carbonato species.

Solution XAFS studies

X-ray absorption measurements of 0.001 M Np solutions were performed at the Np L_{III} edge, and calibrated against a Zr foil [20]. EXAFS Fourier transforms (not phase shift corrected) for $\text{NpO}_2(\text{CO}_3)_3^{5-}$ (II), $\text{NpO}_2(\text{CO}_3)_2^{3-}$ (III), and $\text{NpO}_2(\text{CO}_3)^-$ (IV) are shown in Figure 3. Curve-fitting was complicated by noise resulting from measuring dilute solutions enclosed in several layers of radiological containment, and the proximity of the equatorial and distal O and C shells to the O = Np = O multiple scattering (ms) shell.



For the tris complex, $\text{NpO}_2(\text{CO}_3)_3^{5-}$ (II) assignment of shells corresponding to a hexagonal bi-pyramidal co-ordination of the NpO_2^+ ion is straightforward. The first shell at 1.86 Å corresponds to two trans neptunyl O atoms (Table 1), while the second shell at 2.53 Å arises from six O atoms in the equatorial plane. The three C and distal O atoms give rise to the third and fourth shells at 2.98 and 4.23 Å. Inclusion of a O = Np = O ms shell (3.7 Å) was essential to the fit as observed in uranyl systems [23]. The EXAFS data show unequivocally that the carbonate ligands must be co-ordinated in a bidentate fashion based on the combination of six Np-O and three Np-C distances of 2.53 and 2.98 Å, respectively. The Np = O distance of 1.86 Å is in agreement with that observed (1.85 Å) in EXAFS studies of the NpO_2^+ aquo ion [24]. The Np-O, Np-C, and Np-O distances (Table 2) compare favourably to 2.55, 2.97, and 4.29 Å seen in the solid state structure of $\text{K}_3\text{NpO}_2(\text{CO}_3)_3$, where hexagonal bi-pyramidal co-ordination and bidentate carbonate ligation were observed [25]. Fitting the bis- and mono-carbonato complexes proved more difficult. Np = O shells at 1.85 and 1.84 Å were observed along with equatorial Np-O shells of 2.48 and 2.49 Å (Table 1). Of significance is a distinct change in co-ordination geometry about the neptunyl ion, from six O atoms in the tris- and bis-carbonato complexes, to five O atoms in the mono-carbonato complex (Table 1).

Thermodynamic data establishes the stoichiometry of II-IV [22], NIR spectra verified that individual EXAFS solutions of II-IV contain a single species, and EXAFS spectra provide the molecular level structural details. The change in co-ordination number in the equatorial plane in IV relative to III and II is not expected, yet reasonable. Bidentate carbonate ligation is indicated by the

Np--C distances of 2.93-2.99 Å (Table 1). Finally, with two O per bidentate carbonate ligand, the remainder of O atoms in the equatorial plane of Np must correspond to H₂O molecules, yielding our proposed molecular structures for II-IV above.

Hexavalent actinide carbonato complexes

Compounds containing the hexavalent actinyl (AnO_2^{2+}) group were among the first actinide complexes to be studied by X-ray diffraction techniques. While the most precise studies have dealt with complexes of U, a few single crystal structures and many powder diffraction studies have been performed on transuranic actinyl compounds [26]. In solution, the actinyl(VI) carbonate systems can be quite complicated in that they may consist of several different complex ions in rapid equilibria with one another [7] and with the aquo ion or hydrolysed species depending on solution conditions. To avoid this complication in our studies, we focused our efforts on solution conditions that will favour the limiting anionic $\text{AnO}_2(\text{CO}_3)_3^{4-}$ complex. All the relevant data on the Np(VI) and Pu(VI) complexes point to the same limiting monomeric species of general formula $\text{AnO}_2(\text{CO}_3)_3^{4-}$ [27-34].

Solid-state X-ray diffraction studies

Single crystal X-ray diffraction studies have been reported for a large number of uranyl complexes and a few of the neptunyl analogues of general formula $\text{M}_4\text{AnO}_2(\text{CO}_3)_3$ (An = U, Np; M = monovalent cation). The unit cell parameters have been reported for a variety of Pu(VI) analogues, but to the best of our knowledge, no refinement to give structural parameters has been performed. In order to provide a realistic comparison of identical structures across the light actinide series, we employed the well-known hydrogen-bonding ability of the guanidinium counter cation [23] [$\text{C}(\text{NH}_2)_3^+$] to obtain single crystals suitable for X-ray diffraction analysis.

Cooling of guanidinium carbonate solutions of AnO_2^{2+} ions produced single crystals of formula $[\text{C}(\text{NH}_2)_3]_4[\text{AnO}_2(\text{CO}_3)_4]$ (An = U, Np, Pu) which crystallise in rhombohedral space group R3 [35]. In the solid state, all monomeric $[\text{C}(\text{NH}_2)_3]_4[\text{AnO}_2(\text{CO}_3)_4]$ complexes are isostructural and show the same basic structural features. A ball-and-stick drawing of the repeat unit is shown in Figure 4. The central $\text{AnO}_2(\text{CO}_3)_3^{4-}$ ion displays a hexagonal bi-pyramidal co-ordination geometry where three bidentate carbonate ligands lie approximately in a hexagonal plane, and two *trans* oxo ligands occupy co-ordination sites above and below the plane. The complex anion displays approximately D_{3h} symmetry as shown qualitatively in II. Guanidinium cations form hydrogen bonds with the CO_3^{2-} ligands, and produce an extensive H-bonding network. For the axial An = O bonds, one can observe a relatively smooth decrease in bond distance from 1.79(1) to 1.77(1) to 1.75(1) Å for U, Np, and Pu compounds, respectively. Although the differences are not statistically significant, we observe the trend of decreasing bond length with increasing atomic number as expected from the actinide contraction. For the equatorial An-O distances to the carbonate ligand, the distances are essentially identical at 2.45(1) Å for U, and 2.44(1) Å for Np and Pu. Bond distances are compared in Table 1.

Solution XAFS studies

Solution EXAFS measurements were performed at the actinide L_{III} edge for 0.01 M solutions of $\text{AnO}_2(\text{CO}_3)_3^{4-}$ (An = Np, Pu) ions in 0.03 M Na_2CO_3 solution and $9 < \text{pH} < 10$. Samples were characterised with electronic absorption and ¹³C NMR spectroscopy to confirm the sample

composition prior to XAFS analysis [35]. The EXAFS Fourier transforms (FT) show four well-resolved peaks whose qualitative assignment based on the monomeric structure observed in the solid-state is straightforward, and a representative solution FT spectrum of $\text{AnO}_2(\text{CO}_3)_3^{4-}$ is shown in Figure 5. Curve-fitting revealed peaks at 1.75(1), 2.44(1), 2.89(1), and 4.19(3) Å which may be identified as distances from the actinide to the actinyl oxygens, the six carbonate oxygens in the equatorial plane, the carbonate carbon and distal oxygen atoms, respectively. A well-established actinyl ion ($\text{O} = \text{An} = \text{O}$) multiple scattering peak is seen at 3.51 Å in both spectra [18,19]. The close spacing of Pu-O and Pu-C shells generates the appearance of a single peak in the EXAFS Fourier transform shown in Figure 5.

Concluding remarks

In this overview we have attempted to show that X-ray absorption and diffraction techniques can be combined to give detailed molecular structure information about actinide carbonate complexes in solution and in the solid state. For carbonate complexes, where multiple species can coexist, known thermodynamic formation constants can be combined with conventional spectroscopies (UV-Vis-NIR, NMR, etc.) to prepare (and verify) solutions that contain predominantly a single component. From such solutions one can obtain single crystals for X-ray diffraction, and the resulting molecular structure can serve as a model for fitting EXAFS data in solution. Favourable comparisons between molecular structures determined by EXAFS and diffraction gives us some calibration as to the necessity of EXAFS fitting parameters such as multiple scattering and focusing effects, that can be subsequently used for more complicated systems.

For the hexa- and pentavalent actinide carbonate complexes, we have shown that linear trans-dioxo bonds and bidentate carbonate ligand co-ordination are common structural themes, with bond lengths changing only subtly between solid and solution state. While bidentate carbonate bonding can force a co-ordination number of 6 in the equatorial plane, relaxation to a co-ordination number of 5 can occur as enough carbonate ligands are replaced by water *vis-à-vis* $\text{NpO}_2(\text{CO}_3)(\text{OH}_2)_3$. For tetravalent plutonium, one can view the structural motif of $\text{Pu}(\text{CO}_3)_5^{6-}$ as one which contains equatorial carbonate ligands, and two carbonate ligands occupy trans positions in a pseudo hexagonal bi-pyramid. As with the other oxidation states, the bond distances and structure vary little between the solid state and solution.

Experimental conditions for XAFS measurements on radioactive samples

All operations were carried out inside HEPA-filtered fume hoods or negative-pressure glove boxes designed for containment of radioactive materials. Standard radiochemical procedures were used throughout. The EXAFS sample cells were designed to enable EXAFS studies of radioactive Pu at a non-nuclear facility. The primary sample cell consisted of a Teflon body with a Kapton (high-strength polyimide film, DuPont) window which had been pressure tested to 28.8 psi. The sample was loaded and tested for contamination and placed inside a secondary container of the same design, which was subsequently placed inside a third container with Kapton windows and mounted inside the X-ray experimental hutch. The experimental hutch was modified for radiochemical experiments by using a portable experimental tent within the hutch. This allowed for maintenance of three zones of negative pressure, and the vacuum system passed through 0.3 micron HEPA filters. The hutch was equipped with continuous air monitors and radiation sampling safety equipment and monitored continuously throughout the course of the experiment.

Actinide L_{III} edge X-ray absorption spectra were collected at the Stanford Synchrotron Radiation Laboratory on wiggler beamline 4-2 (unfocused) with an electron beam energy of 3.0 GeV and maximum stored beam currents between 60-100 mA. A Si (220) double-crystal monochromator was used. Rejection of higher harmonic content in the X-ray beam was achieved by employing a flat Rh-coated quartz mirror tuned at a critical angle for the rejection of photons having energies above 24 000 eV. Having rejected greater than 95% of the higher order harmonics with the mirror, the monochromator was operated fully tuned with respect to θ , the orientation between the two crystals. Spectra were collected simultaneously both in transmission mode using three N_2 -filled ionisation chamber detectors, and in fluorescence mode using a 13-element Ge detector (Canberra). For the Ge detector, the count rate was controlled by adjusting the hutch entrance slits or by moving the detector closer to, or farther from, the sample windows. Data reduction and analysis were performed using techniques described elsewhere [19]. The summed data for each detector (transmission or fluorescence) were then inspected, and only those channels that gave high-quality signal-to-noise ratios were included in the final weighted average. Three EXAFS scans were collected on the solution at ambient temperature (ca 25°C). The spectra were energy calibrated by simultaneously measuring the spectrum of a Zr foil placed between the second and third ion chambers, defining the first inflection point at the Zr K edge as 17 999.35 eV. In any series of scans, the measured energy of the first inflection of the Zr foil spectrum varied by less than 1 eV. Averaged EXAFS data were referenced to the Zr calibration of the first scan of a series, since the energy drift in any series of scans was too small to perturb the EXAFS oscillations. The data were manipulated and analysed using either WinXAS 97 [36] or in-house data analysis packages. The data were normalised by setting the edge jump equal to unity above the ionisation threshold ($k = 0$), defined as 18 064 eV (Pu) and 17 616 eV (Np). A five-region cubic spline function was used to fit the background over the EXAFS region which extended out to $k = 11.864 \text{ \AA}^{-1}$. Fourier transforms of the k^3 -weighted data were calculated over the range $k = 2.288-11.864 \text{ \AA}^{-1}$ with a Gaussian window parameter of 30. Theoretical phases and amplitudes were derived from the program FEFF7 [17] to fit the backscattering contributions from the O and C neighbours of oxo or carbonato ligands. For the distal O shell, the single path as well as two multiple scattering paths, one three-legged and one four-legged, were included in the analysis. The parameters refined in the fit were ΔE_0 , the photoelectron energy threshold; R_i , the distance from An to atom i ; n_i the number of i atoms; and σ_i^2 , the Debye-Waller term for atom i . The co-ordination numbers for the C shell and the distal O shell could be correlated to be half the co-ordination number of the first O shell as required by the stoichiometry of a bidentate carbonate ligand. The quality of the fit was determined by the residuum between the fit and k -space data.

Acknowledgements

This research was supported by the US DOE Office of Basic Energy Sciences, under Contract W-7405-ENG-36 with the University of California. XAS experiments were performed at the Stanford Synchrotron Radiation Laboratory, which is supported by the US DOE Office of Basic Energy Sciences.

Table 1. Summary of X-ray diffraction and k^3 -weighted EXAFS results for actinide carbonato complexes

Compound	An = O	An-O	An--C	An—O	Ref.
Pu^{IV}(CO₃)₅⁶⁻ XRD (solid) EXAFS (solution)	– –	2.415(7) 2.42(1)	2.874(9) 2.88(2)	4.117(10) 4.16(2)	15 15
Np^VO₂(CO₃)₃⁵⁻ EXAFS (solution)	1.86(2)	2.53(3)	2.98(3)	4.22(3)	20
Np^VO₂(CO₃)₂³⁻ EXAFS (solution)	1.85(2)	2.48(3)	2.93(3)	4.18(3)	20
Np^VO₂(CO₃)⁻ EXAFS (solution)	1.84(2)	2.49(3)	2.94(3)	4.24(3)	20
U^{VI}O₂(CO₃)₃⁴⁻ XRD (solid) EXAFS (solid)	1.79(2) 1.79	2.44(2) 2.42	2.896(10) 2.89	4.139(13) 4.12	35 23
Np^{VI}O₂(CO₃)₃⁴⁻ XRD (solid) EXAFS (solution)	1.770(12) 1.78(2)	2.438(10) 2.42(3)	2.883(4) 2.87(3)	4.129(6) 4.15(3)	35 35
Pu^{VI}O₂(CO₃)₃⁴⁻ XRD (solid) EXAFS (solution)	1.75(2) 1.75(2)	2.442(9) 2.46(3)	2.893(4) 2.91(3)	4.140(5) 4.19(3)	35 35

Figure 1. Ball-and-stick drawing of the central $[\text{Pu}(\text{CO}_3)_3]^{6-}$ ion and emphasising the pseudo hexagonal bi-pyramidal co-ordination geometry about the central plutonium metal centre [15]

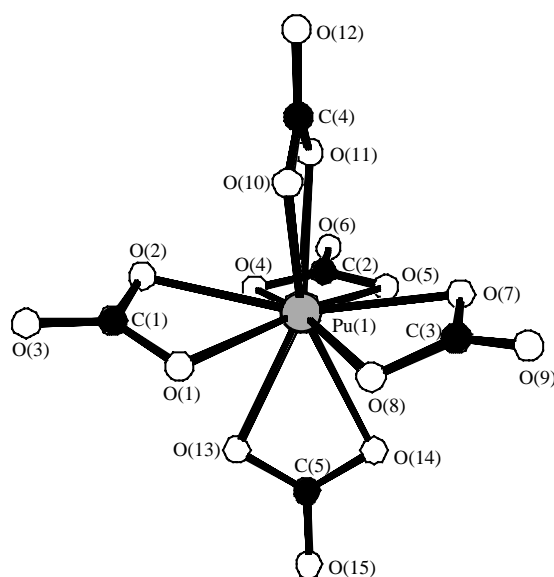


Figure 2. Fourier transform (without phase corrections) of the k^3 -weighted EXAFS spectra of the limiting Pu(IV) complex in 2.5 M Na_2CO_3 solution [15]. The solid line is the experimental data, and the dashed line is the theoretical fit. Shown with negative FT amplitudes are the single shell contributions to the fit.

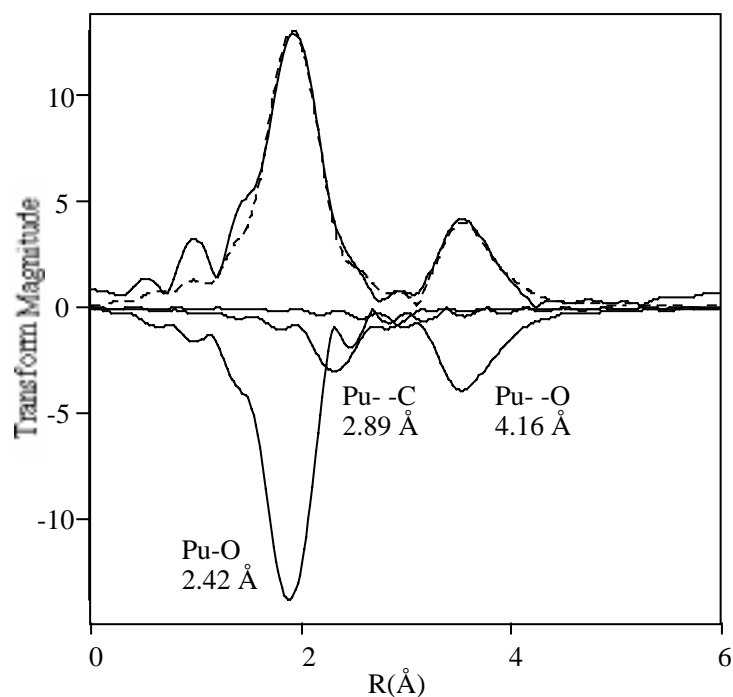


Figure 3. Comparison of the Fourier transforms of the experimental data (solid line) with those of the theoretical signal (dashed line) for $\text{NpO}_2(\text{CO}_3)^-$, $\text{NpO}_2(\text{CO}_3)_2^{3-}$, in $\text{TBA}_2(\text{CO}_3)$ solution; and $\text{NpO}_2(\text{CO}_3)_3^{5-}$ in $\text{Na}_2(\text{CO}_3)$ solution [20]

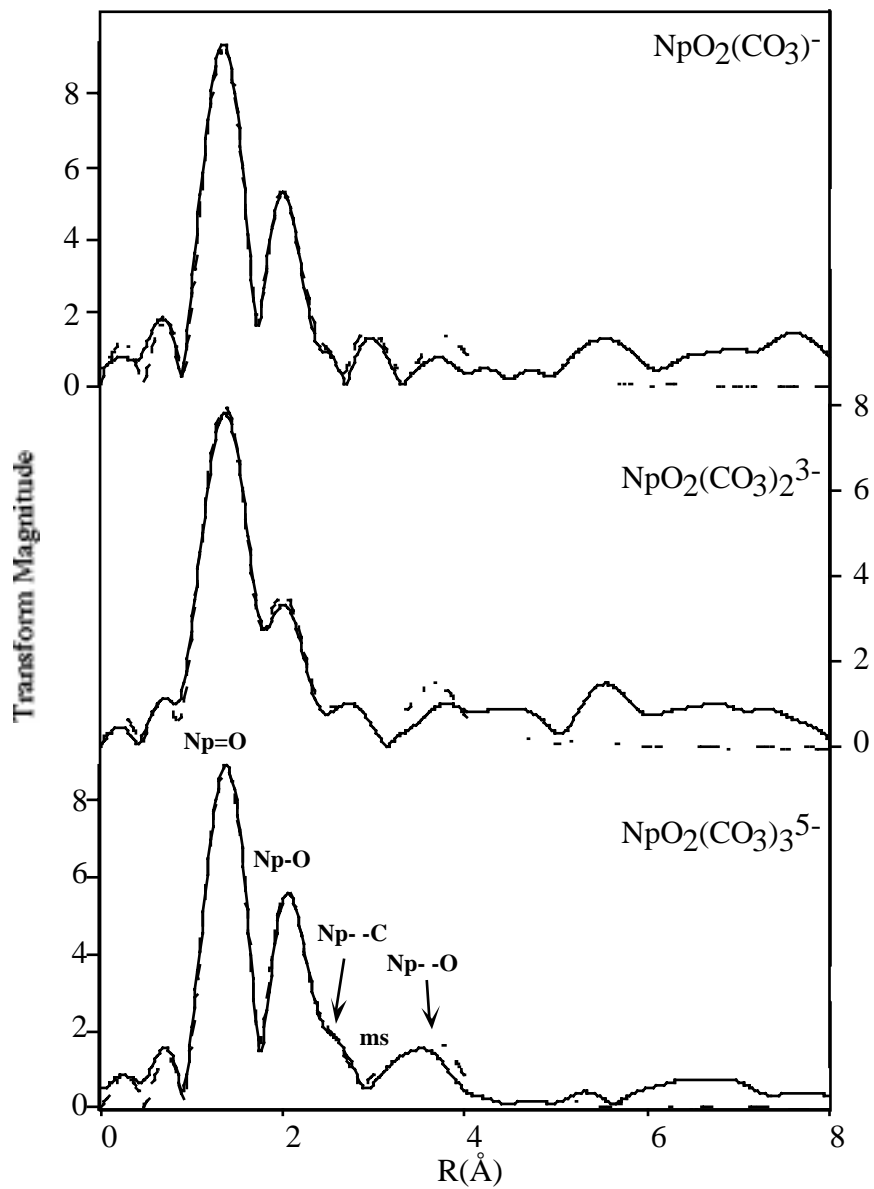


Figure 4. Ball-and-stick drawing of the repeat unit in $[\text{C}(\text{NH}_2)_3]_4[\text{AnO}_2(\text{CO}_3)_3]$ and emphasising the hexagonal bi-pyramidal co-ordination geometry about the central actinide atom [35]

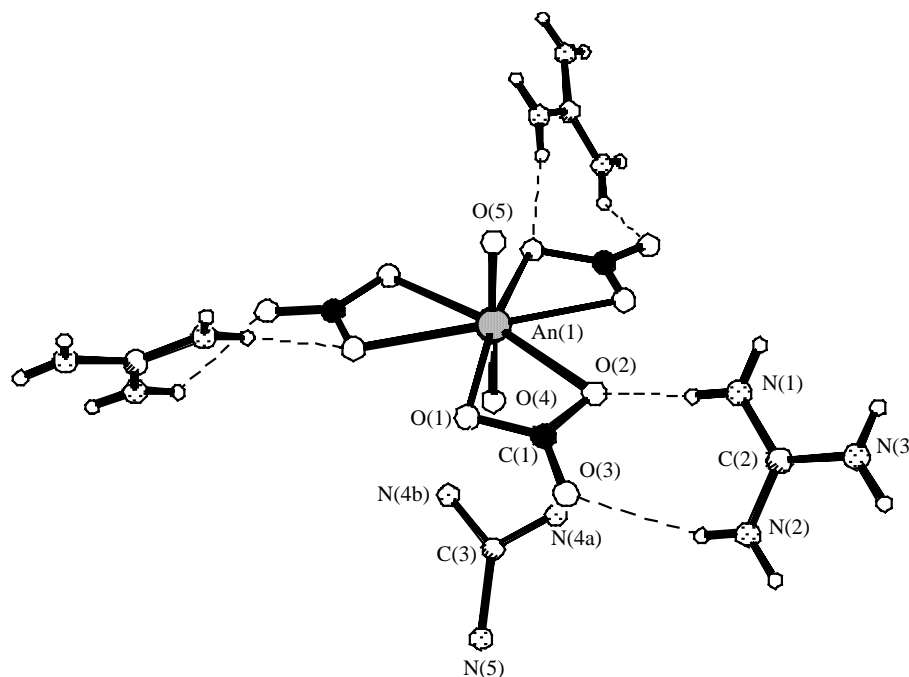
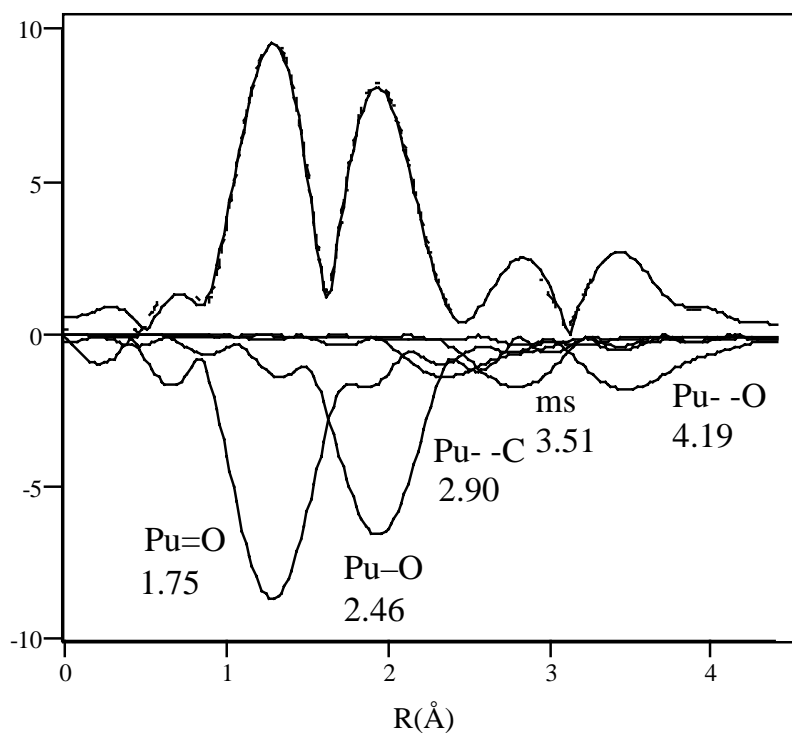


Figure 5. EXAFS Fourier transform and fit (without phase corrections) of the k^3 -weighted EXAFS spectra of the limiting $\text{PuO}_2(\text{CO}_3)_3^{4-}$ complex (0.01 M) in 0.3 M Na_2CO_3 solution at pH 9.5 and $\rho = 2.0$ m [35]. The solid line is the experimental data, and the dashed line is the theoretical fit. Shown with negative FT amplitudes are the single shell contributions to the fit.



REFERENCES

- [1] (a) Mail Stop E500, (b) Mail Stop D429, (c) Mail Stop G739, (d) Mail Stop J514.
- [2] D.L. Clark, D.E. Hobart, M.P. Neu, *Chem. Rev.* 1995, 95, 25.
- [3] J. Fuger, *Radiochim. Acta* 1992, 59, 81.
- [4] M. Dozol, R. Hagemann, *Pure and Appl. Chem.* 1993, 65, 1081.
- [5] J.I. Kim, C. Lierse, F. Baumgartner, in *ACS Symposium Series No. 216*; American Chemical Society: Washington, DC, 1983, p. 317.
- [6] R.J. Silva, H. Nitsche, *Radiochimica Acta* 1995, 70/71, 3776.
- [7] I. Grenthe, J. Fuger, R.J.M. Konigs, R. J. Lemire, A.B. Muller, C. Nguyen-Trung, H. Wanner, *Chemical Thermodynamics of Uranium*, Elsevier Science Publishing Company, Inc.: New York, 1992, Vol. 1.
- [8] R.J. Silva, G. Bidoglio, M.H. Rad, P. Robouch, H. Waner, I. Puigdomenech, *NEA-TDB Chemical Thermodynamics of Americium*, Elsevier Science Publishers, 1995.
- [9] M. Eiswirth, J.I. Kim, C. Lierse, *Radiochimica Acta* 1985, 38, 1971.
- [10] H. Capdevila, P. Vitorge, E. Giffaut, L. Delmau, *Radiochim. Acta* 1996, 93.
- [11] C. Lierse, J.I. Kim, Institut fur Radiochemie, TU Munchen, RCM 02286, 1986.
- [12] D.E. Hobart, P.D. Palmer, T.W. Newton, "The Carbonate Complexation of Plutonium(IV)", Los Alamos National Laboratory, LA-UR-86-968, 1986.
- [13] C.D. Tait, S.A. Ekberg, P.D. Palmer, D.E. Morris, "Plutonium Carbonate Speciation Changes as Measured in Dilute Solutions with Photoacoustic Spectroscopy", Los Alamos National Laboratory, LA-12886-MS, 1995.
- [14] T. Yamaguchi, Y. Sakamoto, T. Ohnuki, *Radiochim. Acta* 1994, 66/67, 9.
- [15] D.L. Clark, S.D. Conradson, D.W. Keogh, P.D. Palmer, B.L. Scott, C.D. Tait, *Inorg. Chem.* 1998, 37, 2893.
- [16] P.S. Voliotis and E.A. Rimsky, *Acta Crystallogr.* 1975, B31, 2612, and R.E. Marsh, F.H. Herbstein, *Acta Crystallogr.* 1988, B44, 77.
- [17] A.L. Ankudinov, J.J. Rehr, *Phys. Rev. B* 1997, 56, R1712.

- [18] B.K. Teo, *EXAFS; Basic Principles and Data Analysis*; Springer-Verlag: Berlin, 1986.
- [19] R. Prins, D.C. Koningsberger, *X-Ray Absorption: Principles, Applications, Techniques for EXAFS, SEXAFS and XANES*, Wiley: New York, 1988.
- [20] D.L. Clark, S.D. Conradson, S.A. Ekberg, N.J. Hess, M.P. Neu, P.D. Palmer, C.D. Tait, *J. Am. Chem. Soc.* 1996, 118, 2089.
- [21] H. Nitsche, *Radiochim. Acta.* 1991, 52/53, 3.
- [22] V. Neck, W. Runde, J.I. Kim, B. Kanelakopoulos, *Radiochim. Acta* 1994, 65, 29.
- [23] P.G. Allen, J.J. Bucher, D.L. Clark, N.M. Edelstein, S.A. Ekberg, J.W. Gohdes, E.A. Hudson, N. Kaltsoyannis, W.W. Lukens, M.P. Neu, P.D. Palmer, T. Reich, D.K. Shuh, C.D. Tait, B.D. Zwick, *Inorg. Chem.* 1995, 34, 4797.
- [24] J.-M. Combes, C.J. Chisholm-Brause, G.E. Brown, Jr., G.A. Parks, S.D. Conradson, P.G. Eller, I.R. Triay, D.E. Hobart, A. Meijer, *Environ. Sci. Technol.* 1992, 26, 376.
- [25] Y.F. Volkov, G.I. Visyashcheva, S.V. Tomilin, I.I. Kapshukov, A.G. Rykov, *Radiokhimiya* 1981, 23, 248.
- [26] C. Musikas, J.H. Burns, In *Transplutonium 1975*, W. Müller, R. Linder, eds., North-Holland Publishing Company: Amsterdam, 1975.
- [27] I. Grenthe, C. Riglet, P. Vitorge, *Inorg. Chem.* 1986, 25, 1679.
- [28] I. Grenthe, P. Robouch, P. Vitorge, *J. Less-Common Met.* 1986, 122, 225.
- [29] W.J. Ullman, F. Schreiner, *Radiochim. Acta* 1988, 43, 37.
- [30] L. Maya, *Inorg. Chem.* 1984, 23, 3926.
- [31] P. Robouch, P. Vitorge, *Inorg. Chim. Acta* 1987, 140, 239.
- [32] C. Nguyen-Trung, G.M. Begun, D.A. Palmer, *Inorg. Chem.* 1992, 31, 5280.
- [33] C. Madic, D.E. Hobart, G.M. Begun, *Inorg. Chem.* 1983, 22, 1494.
- [34] L.J. Basile, J.R. Ferraro, M.L. Mitchell, J.C. Sullivan, *Appl. Spectrosc.* 1978, 32, 535.
- [35] D.L. Clark, S.D. Conradson, M.P. Neu, P.D. Palmer, B.L. Scott, C.D. Tait, manuscript in preparation.
- [36] T. Ressler, *J. Physique IV* 1997, 7, C2.

METAL-OXYGEN BOND DISTANCE DETERMINATION FROM XANES SPECTRA

Melissa A. Denecke

Forschungszentrum Karlsruhe
Institut für Nukleare Entsorgungstechnik
Postfach 3640, 76021 Karlsruhe, Germany

Abstract

Experimental results showing energy shifts of XANES features associated with MS pathways involving uranyl oxygen atoms and co-ordinating atoms as a function of bond distance are presented. The energy (E) position of multiple scattering (MS) features in XANES spectra are dependent on bond length (R). The dependency generally follows the formula $\Delta E * R^2 = C$ or $k * R = C'$, where k is the wave vector and C' is a constant. An increase in R for atoms involved in MS events associated with a XANES peak leads to a shift of that peak to lower energy and vice versa. By measuring energy positions of the U L3 edge XANES feature at ~35 eV above the white line for a series of uranyl carboxylate compounds with known R, the constant C is experimentally determined as $197 \pm 8 \text{ eV}\text{\AA}^2$. From this information, the equatorial oxygen bond distance of a dilute uranyl system is ascertained from its XANES. Finally, an example is presented using energy shifts in the white line shoulder observed in U L3 XANES spectra to corroborate EXAFS results showing small changes in axial oxygen bond distances.

Introduction

Bond distance determinations from peak energies in X-ray absorption near-edge structure (XANES) spectra, as an alternative to determinations from extended X-ray absorption fine structure (EXAFS) data, can be of great importance. Although R determinations from XANES spectra are not as precise as EXAFS analysis, this method is useful, for example, for studies of samples with low concentrations, where measuring good-quality EXAFS data is not possible. Furthermore, obtaining bond distance information from XANES data is sometimes necessary when the measurable energy range is limited, such as in time-resolved dispersive-XAFS and piezo-XAFS experiments. Finally, spatially resolved micro-XAS experiments are only possible on a feasible time-scale when such fast data recording techniques are used. This makes the estimation of bond distances from XANES spectra necessary in micro-XAS experiments.

It has long been known that the energy position of multiple scattering (MS) features (also called resonances) in XANES spectra are dependent on bond length (R) [1]. The dependency generally follows the formula $k * R = C'$ or $\Delta E * R^2 = C$, where C' and C are constants, k is the wave vector, and ΔE is the energy difference between the MS resonance and the average potential of the interstitial region, V_0 [2]. An increase in R for atoms involved in MS events associated with a XANES peak leads to a shift of that peak to lower energy and vice versa. By measuring energy positions of XANES features with known R, it is possible to experimentally determine C. From this information, R of an unknown system can be ascertained from its XANES. Likewise, systematic changes in bond distances as a function of a given parameter (e.g. dopant concentration [3], co-ordination sphere distortion [4], etc.) can be estimated from shifts of XANES features. Numerous studies using XANES for bond length determination have been reported [5-9] and have been successfully applied to a wide range of scientific disciplines such as materials science [10,11], biology [12], mineralogy [13,14], and inorganic [2] as well as organic chemistries [15,16].

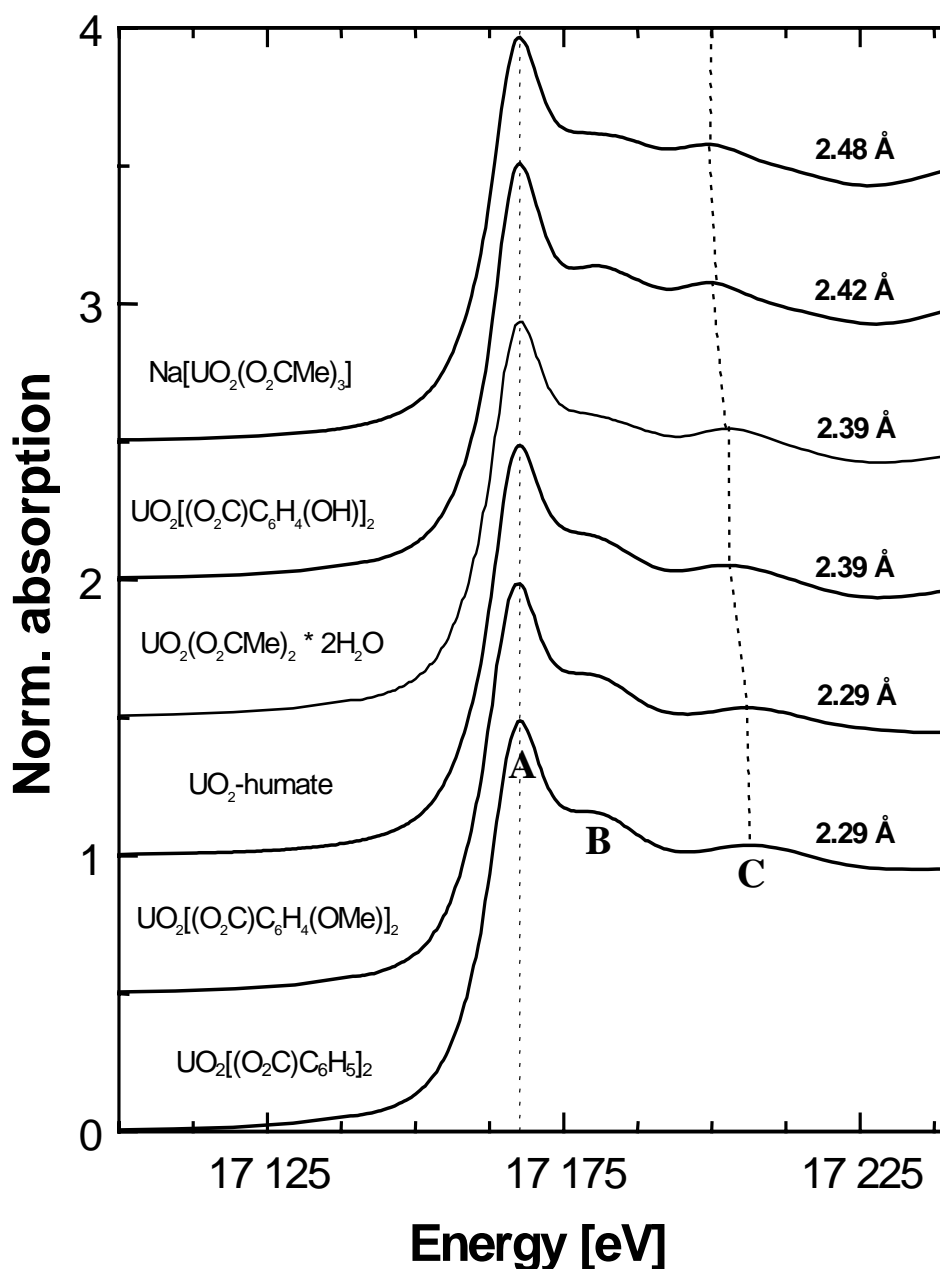
In the present paper, experimental results demonstrating the use of energy shifts of XANES features associated with MS pathways involving uranyl oxygen atoms and co-ordinating equatorial atoms to determine U-O bond distances will be presented.

Prerequisite to using XANES features for determining bond distance are the following:

- A) Certainty that the XANES feature used in the determination actually results from scattering on the co-ordination shell of interest.
- B) Knowledge of V_0 between the atoms [2].
- C) Energy independence of the phase shift.

In the case of uranyl compounds, these prerequisites can be fulfilled. The origin of XANES features in U L3 edge spectra of uranyl compounds are understood. Uranyl U L3 edge XANES spectra all exhibit three features, marked A, B, and C in Figure 1. The absorption maximum, A, is referred to as a white line, WL, and results from a dipole-allowed transition of the excited 2p electron to final states of 6d character. The shoulder B at about 10 eV above the WL results from constructive interference of MS paths between the absorber and the axial oxygen atoms, O_{ax} , of the linear uranyl unit [17,18]. The origin of feature C located at about 35 eV above the WL as scattering on atoms in the equatorial plane surrounding the UO_2^{2+} cation (denoted O_{eq} , for oxygen ligands) has been experimentally verified [17]. Because B and C result from scattering on O_{ax} and O_{eq} , respectively, shifts in their energies can be used for bond length determinations of these atoms. The lack of

Figure 1. U L3 edge XANES spectra for the uranyl carboxylate compounds indicated. The U-O_{eq} bond lengths are given at right. Dotted lines are to aid the eye, showing the alignment of the white lines and the shift of the feature C to higher energy with decreasing bond length. A, B and C mark U L3 edge XANES features common to uranyl compounds and described in the text.



knowledge of V_0 can be circumvented by determining ΔE as the energy difference between resonance B or C and feature A. This is possible because A is a bound molecular (atomic-like) XANES feature. This has been successfully applied in a similar manner using the $1s \rightarrow 3d$ pre-peak in K edge XANES of 3-D transition metals having tetrahedral co-ordination [9]. The last prerequisite, energy independence of the phase shift in the region of interest, is fulfilled in our case by using compounds of similar symmetry, without extreme differences in bond length.

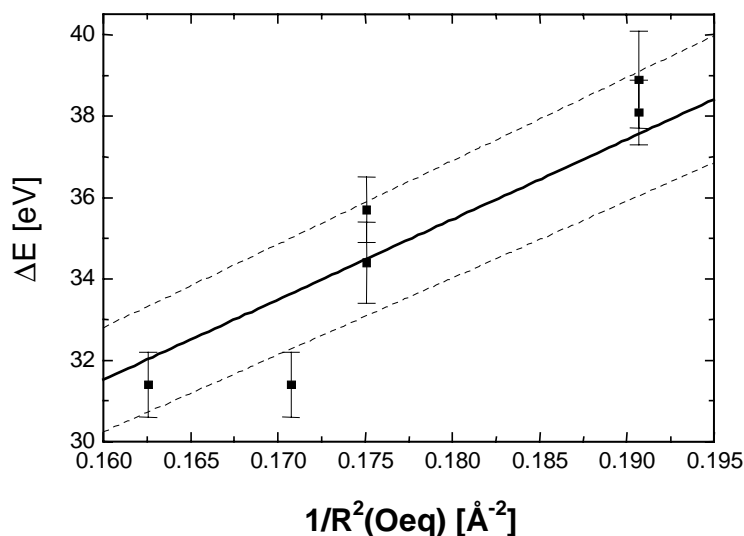
Examples

Equatorial oxygen bond distances

The U L3 edge XANES spectra for six different uranyl carboxylate samples are shown in Figure 1. The carboxylate ligands are composed of either acetate (I = Na[UO₂(O₂CMe)₃] and III = UO₂(O₂CMe)₂ * 2H₂O), salicylate (II = UO₂[(O₂C)C₆H₄(OH)]₂), humate (IV = UO₂²⁺-humate), o-methoxybenzoate (V = UO₂[(O₂C)C₆H₄(OMe)]₂), or benzoate (VI = UO₂[(O₂C)C₆H₅]₂). The spectra are ordered from the compound with the longest U-O_{eq} bond length, R(U-O_{eq}), (I) at the top to that with the shortest (VI) at the bottom and are aligned so that the WL energies are the same in all spectra. The bond distances given in the figure were determined from U L3 edge EXAFS data [19]. Upon inspection of Figure 1, it is clearly evident that the feature C shifts towards higher energies with decreasing bond length.

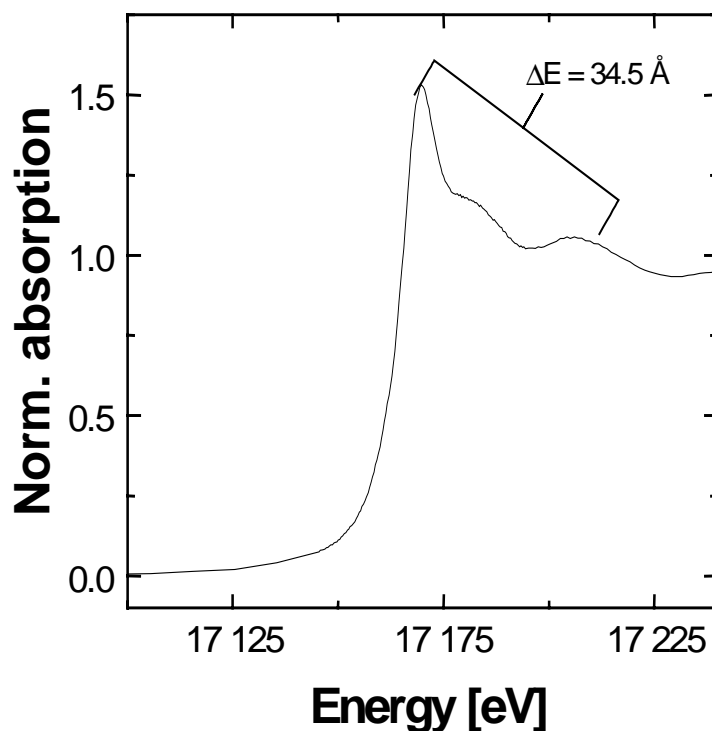
The correlation of ΔE in the spectra versus $1/R(U - O_{eq})^2$ is depicted as squares in Figure 2. The error bars result from the step-width between data points in the spectra, which defines the precision of determining maxima. The lines in Figure 2 give the range for determining bond distances graphically from this plot. The solid line was calculated from the average value for $\Delta E * R^2$, which was $197 \pm 8 \text{ eV}\text{\AA}^2$. The dotted lines represent the range falling within the standard deviation of the average.

Figure 2. ΔE as the difference between the WL (A) and feature C in the spectra of Figure 1 (points with bars). The lines depict $\Delta E = (197 \pm 8)/R^2$.



To demonstrate the usefulness of the correlation in Figure 2, we have determined the bond distance in a solution of 28 mg natural humic acid and 4 mL aqueous $5 * 10^{-4}$ M U(VI) at pH = 3.9. The U L3 edge XANES spectrum of this uranyl humate sample is shown in Figure 3. From this figure, ΔE is determined and the corresponding value of R(U - O_{eq}) either calculated as $(197 \pm 8/\Delta E)^{1/2}$ or determined graphically from Figure 2. R(U - O_{eq}) = $2.39 \pm 0.05 \text{ \AA}$ was obtained for this sample. This result is the same as that obtained from the analysis of the EXAFS data for the same sample, $2.39 \pm 0.02 \text{ \AA}$ [20]. Although the XANES determination is less precise, the amount of time for recording the XANES spectrum for this dilute sample (~0.25 h) required about 1/25 of the time as that for recording the EXAFS data (~6 h). This is a considerable time advantage.

Figure 3. UL 3 edge XANES of an aqueous solution of 28 mg humic acid and $5 \cdot 10^{-4}$ M U(VI), pH = 3.9. ΔE is indicated.



Axial oxygen bond distances

It is difficult to develop a calibration curve, similar to that in Figure 2, for determining U - Oax bond lengths, $R(\text{U} - \text{Oax})$, utilising the energy difference between XANES features A and B. This is simply because $R(\text{U} - \text{Oax})$ tends to always have values near 1.8 Å. For example, $R(\text{U} - \text{Oax})$ for samples I through VI were found to all be 1.78 ± 0.02 Å. However, energy shifts of the feature B can be used to corroborate $R(\text{U} - \text{Oax})$ values from the analysis of EXAFS data. Although not quantitatively evaluated in the original publication, the shift of feature B reported for a series of uranyl precipitates is a linear function of $R(\text{U} - \text{Oax})$ [21].

A second difficulty in making $R(\text{U} - \text{Oax})$ determinations from U L3 edge XANES spectra is the problem of determining its true energy position, because feature B appears as a high energy shoulder on the WL. We have performed fits to the experimental data, in order to deconvolute the spectra and thereby accurately determine the position of feature B. Fits were done using the `edge_fit` program of EXAFSPAK software package [22]. As an example, fit results to U L3 edge XANES for three solution samples containing 0.05 M of UO_2^{2+} and desferrioxamine B (DFO), at pH 4.6, 7.0 and 10.3, are listed in Table 1. The spectra were modelled using a step function, a Lorentzian function to model the WL (peak A), and two Gaussian functions to model features B and C. The step function parameters were held constant as follows. The step function was set to the natural linewidth of the U $2p_{3/2}$ core hole (7.4 eV) [23], the amplitude constant at one to account for normalisation of the spectra, and the energy position set to 17 166 eV, which was the position of the inflection point of the rising edge of all spectra. The half-widths of the Lorentzian and Gaussian functions were set at 5 and 7 eV, respectively.

Table 1. Peak positions and peak amplitudes obtained from XANES fits to spectra of uranyl-DFO solutions at indicated pH values

pH	Lorentzian function		1 st Gaussian function		2 nd Gaussian function		$\Delta\Delta E^*$	R(U-Oax)
	E [eV]	Amplitude	E [eV]	Amplitude	E [eV]	Amplitude		
4.6	17 170.8	0.72	17 183.8	0.24	17 207.3	0.11	0	1.80
7.0	17 170.9	0.71	17 183.4	0.25	17 207.4	0.10	-0.4	1.81
10.3	17 170.8	0.71	17 183.0	0.25	17 206.5	0.10	-0.8	1.82

* $\Delta\Delta E$ = Energy difference {E (Lorentzian) - E (1st Gaussian)} relative to the pH = 4.6 sample.

Only the amplitude and energy position of these three functions were varied. Also included in Table 1 are the R(U - Oax) values extracted from the EXAFS data. The changes in these distances are small, lying within the range generally considered to be the error in EXAFS analysis. However, the shifts in the peak position of the first Gaussian, which simulates feature B, also indicate a change in R(U - Oax). The increase in R(U - Oax) from 1.80 Å, at pH 4.6, to 1.82 Å, at pH 10.3, is accompanied by a relative shift of 0.8 eV to lower energy.

Conclusion

The purpose of this paper is to introduce the method of extracting bond distance information from XANES data for actinide systems. These principles can be applied to a variety of systems. Especially where dilute samples are to be studied, for example, in environmentally or biologically relevant systems, can this method be of great assistance. In addition, the added timesaving advantage this method offers for newer spatially resolved techniques should prove to be profitable.

REFERENCES

- [1] C.R. Natoli, in *EXAFS and Near Edge Structure*, Vol. 27 of the Springer Series in Chemical Physics, A. Bianconi, L. Incoccia, S. Stipcich, eds., Springer Verlag, Berlin (1984).
- [2] H. Nkamatsu, *Chem. Phys.* 200 (1995), 49-62.
- [3] D.-K. Kim, J.-H. Choy, M. Osada, M. Kakihana, M. Yoshimura, *Solid State Ionics* 108 (1998), 291-5.
- [4] G. Onori, A. Santucci, A. Scafati, M. Belli, S. Della Longa, A. Bianconi, L. Palladino, *Chem. Phys. Lett.* 149 (1988), 289-94.
- [5] Z.Y. Wu, S. Gota, F. Jollet, M. Pollak, M. Gautier-Soyer, C.R. Natoli, *Phys. Rev. B* 55 (1997), 2570-7.
- [6] M. Kasrai, M.E. Fleet, G.M. Bancroft, K.H. Tan, J.M. Chen, *Phys. Rev. B* 43 (1991), 1763-72.

- [7] S.K. Pandey, A.R. Chetal, P.R. Sarode, *Physica B* 172 (1991), 324-8.
- [8] F.W. Lytle, *Berichte der Bunsengesellschaft für Physikalische Chemie* 91 (1987), 1251-7.
- [9] A. Bianconi, E. Fritsch, G. Calas, J. Petiau, *Phys. Rev. B* 32 (1985), 4292-5.
- [10] F.W. Lytle, R.B. Gregor, A.J. Panson, *Phys. Rev. B* 37 (1988), 1550-62.
- [11] A. Bianconi, Chenxi Li, F. Campanella, S. Della Longa, I. Pettiti, M. Pompa, S. Turtu, D. Udron, *Phys. Rev B* 44 (1991), 4560-9.
- [12] L. Palladino, S. Della Longa, A. Reale, M. Belli, A. Scafati, G. Onori, A. Santucci, *Chem. Phys.* 98 (1993), 2720-6.
- [13] A.K. Chakraborty, A.R. Chetal, P.R. Sarode, *Phys. Status Sol. A* 130 (1992), 19-23.
- [14] M. Kasrai, M.E. Fleet, T.K. Sham, G.M. Bancroft, K.H. Tan, J.R. Brown, *Solid State Commun.* 68 (1988), 507-11.
- [15] J. Stöhr, F. Sette and A.L. Johnson, *Phys. Rev. Lett.* 53 (1984), 1684.
- [16] F. Sette, J. Stöhr, A.P. Hitchcock, *Chem. Phys. Lett.* 110 (1984), 517-520.
- [17] E.A. Hudson, P.G. Allen, L.J. Terminello, M.A. Denecke, T. Reich, *Phys. Rev. B* 54 (1996), 156.
- [18] A.L. Ankudinov, S.D. Conradson, J. Mustre de Leon, J.J. Rehr, *Phys. Rev. B* 57 (1998), 7518.
- [19] M.A. Denecke, T. Reich, M. Bubner, S. Pompe, K.H. Heise, H. Nitsche, P.G. Allen, J.J. Bucher, N.M. Edelstein, D.K. Shuh, *J. Alloys Comp.* 271-273 (1998), 123-7.
M.A. Denecke, S. Pompe, T. Reich, H. Moll, M. Bubner, K.H. Heise, R. Nicolai, H. Nitsche, *Radiochim. Acta* 79 (1997), 151-9.
- [20] M.A. Denecke, S. Pompe, T. Reich, unpublished results.
- [21] P.G. Allen, D.K. Shuh, J.J. Bucher, N.M. Edelstein, T. Reich, M.A. Denecke, *J. Physique IV* 7 (1997), C2-789-92.
- [22] G.N. George, I.J. Pickering, "EXAFSPAK: A Suite of Computer Programs for Analysis of X-Ray Absorption Spectra", Stanford Synchrotron Radiation Laboratory, Stanford, CA, USA (1995).
- [23] M.O. Krause, J.H. Oliver, *J. Phys. Chem., Ref. Data* 8, 329 (1979).

X-RAY ABSORPTION SPECTROSCOPY OF CARBONATE AND CATECHOLATE COMPLEXES OF URANIUM(V) IN AQUEOUS SOLUTION

T.I. Doerat

Research & Technology, BNFL Springfields
Preston PR4 0XJ, England

J.F.W. Mosselmans, J.M. Charnock*

CLRC Daresbury Laboratory
Warrington WA4 4AD, England

**Also at University of Manchester*

M.W. Whiteley, D. Collison, F.R. Livens

Department of Chemistry, The University of Manchester
Manchester M13 9PL, England

C. Jones, M.J. Edmiston

Research & Technology, BNFL Sellafield
Seascale, Cumbria CA20 1PG, England

Abstract

Little is known of the co-ordination chemistry of U(V) in aqueous solution since it readily disproportionates. As part of a wider study of the chemistry of penta- and hexavalent U and Np, UO_2^+ has been generated electrochemically in aqueous solution and its complexes with carbonate and a range of substituted catecholate ligands characterised by X-ray absorption spectroscopy. Uranium L(III) edge X-ray absorption spectra were collected on Station 9.3 at the CLRC Daresbury Synchrotron Radiation Source in fluorescence mode, using a 13-element Ge detector. The spectral data were calibrated and background subtracted using the Daresbury Laboratory programs EXCALIB and EXBACK, then analysed using EXCURV97, including full cluster multiple scattering calculations.

Edge positions, calculated co-ordination numbers and distances for $[\text{UO}_2(\text{CO}_3)_3]^{5-}$ and, for comparison, $[\text{UO}_2(\text{CO}_3)_3]^{4-}$ are given in Table 1. The one-electron reduction of $[\text{UO}_2(\text{CO}_3)_3]^{4-}$ to $[\text{UO}_2(\text{CO}_3)_3]^{5-}$ causes the U L(III) edge position to shift by 2.4 eV. The axial U-O distances increase by 0.11 Å on reduction and the distances of all ligand atoms from the U centre increase by about 0.10 Å, suggesting that the geometry of the CO_3^{2-} ligands is not substantially changed.

Calculated co-ordination numbers and interatomic distances for U(V) and U(VI) catecholate complexes are given in Table 2. The results for the U(VI) species are consistent with a monomeric complex, with three catecholate ligands in the equatorial plane. The two different equatorial U-O distances may arise from crowding of the relatively bulky ligands. The results for the U(V) complex

are more difficult to interpret. The edge position is consistent with U(V), but data fitting suggests a dimeric complex, with bridging catecholate ligands. Although examples of such species are known from the d-transition elements, they are not well known in the actinides, so this proposed structure cannot be viewed as definitive. Additional experiments (^{17}O nmr) are in progress to define the nature of this species more fully.

Table 1. Summary of EXAFS data fits for tricarbonato complexes of dioxouranate(VI) and dioxouranate(V)

C.N. – co-ordination number, *r* – interatomic distance, $2\sigma^2$ – Debye-Waller factor

Shell	$[\text{UO}_2(\text{CO}_3)_3]^{4-}$			$[\text{UO}_2(\text{CO}_3)_3]^{5-}$		
	C.N.	<i>r</i> (Å)	$2\sigma^2$ (Å ²)	C.N.	<i>r</i> (Å)	$2\sigma^2$ (Å ²)
1	2 O	1.81±0.02	0.004	2 O	1.91±0.02	0.010
2	6 O	2.44±0.02	0.014	6 O	2.50±0.02	0.019
3	3 C	2.90±0.04	0.006	3 C	2.96±0.04	0.008
4	3 O	4.15±0.04	0.009	3 O	4.22±0.04	0.014
Edge position (eV)		17 165.7		17 163.3		

Table 2. Summary of EXAFS data fits for catecholato complexes of dioxouranate(VI) and dioxouranate(V)

C.N. – co-ordination number, *r* – interatomic distance, $2\sigma^2$ – Debye-Waller factor

Shell	$[\text{UO}_2(\text{C}_6\text{H}_4\text{O}_2)_3]^{4-}$			“ $[(\text{UO})_2(\text{C}_6\text{H}_4\text{O}_2)_4]^{2-}$ ”		
	C.N.	<i>r</i> (Å)	$2\sigma^2$ (Å ²)	C.N.	<i>r</i> (Å)	$2\sigma^2$ (Å ²)
1	2 O	1.83±0.02	0.005	1 O	1.83±0.02	0.019
2	4 O	2.37±0.02	0.008	3 O	2.34±0.02	0.005
3	2 O	2.55±0.04	0.005	2 O	2.50±0.04	0.005
4	6 C	3.23±0.04	0.047	1 U	3.80±0.04	0.009

Acknowledgements

We are grateful to BNFL for financial support and to CLRC Daresbury Laboratory for provision of beam time.

**USE OF X-RAY ABSORPTION FINE STRUCTURE (XAFS) SPECTROSCOPY
AT THE NUCLEAR WASTE MANAGEMENT LABORATORY, PSI**

A.M. Scheidegger, R. Dähn, B. Baeyens, M.H. Bradbury

Waste Management Laboratory
Paul Scherrer Institute
Switzerland

D.L. Sparks

Department of Plant and Soil Sciences
University of Delaware
Newark, Delaware, 19717-1303, USA

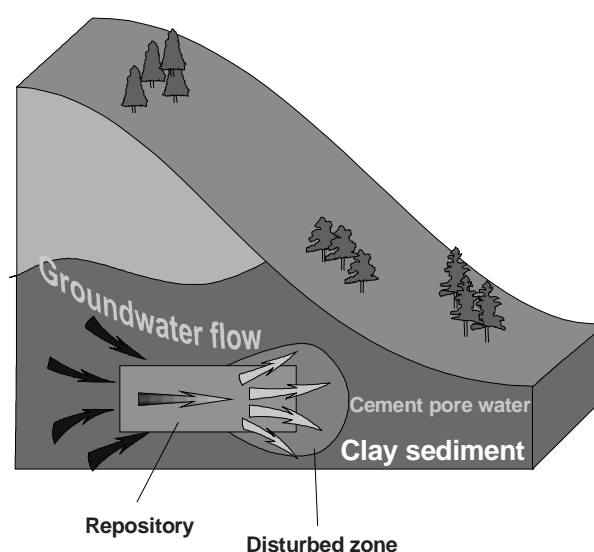
Abstract

The work at the Waste Management Laboratory, PSI, concentrates on the understanding of safety relevant mechanisms and processes that govern the release of radionuclides from waste matrices and their transport through engineered barrier systems and the surrounding geosphere. For this reason, detailed sorption studies of radionuclides (Cs, Sr, Ni, Zn, Eu, Am, Th and Se) in clay and cement systems are conducted. The sorption studies are combined with kinetic investigations and advanced spectroscopic and microscopic methods in order to understand the sorption mechanisms on an atomic/molecular level. In this paper a case study of Ni sorption on clay minerals is presented to illustrate how XAFS can successfully be used to determine sorption processes of radionuclides in nuclear waste repository systems.

Introduction

The aim of the activities at the Waste Management Laboratory are to develop and test models, and to acquire selected data in support of the performance assessments of Swiss nuclear waste repositories. Figure 1 represents a schematic drawing of a possible future nuclear waste repository. The figure illustrates the flow of ground water through a repository. This process can potentially result in the release of radionuclides from waste matrices. The released radionuclides can then be transported through engineered barrier systems (near-field) and the surrounding geosphere (far-field). The release of radionuclides can be considerably retarded due to interactions with solid phases. Thus, a detailed understanding of sorption mechanisms of radionuclides in cement and clay systems is of great importance for safety assessment.

Figure 1. A schematic drawing of a possible future nuclear waste repository



Research in the engineered near-field

The work in the near-field experimental programme focuses on the interactions of radionuclides (Ni, Sr, Eu, Th, I) with cement and cement phases (calcium silicate hydrates, calcium aluminium silicate hydrates, and portlandite) under highly alkaline conditions. Approx. 95 wt.% of the near-field material of the planned Swiss disposal cavern for low and intermediate level waste consists of cement and cementitious backfill materials. Hence, a detailed understanding of the chemical processes which govern the retention of radionuclides is a prerequisite for predicting the long-term behaviour of radionuclides in a repository. XAFS studies are used complementary to sorption studies to gain information on the speciation of elements in cementitious pore waters with respect to the oxidation state and chemical form as well as on the sorption mechanisms occurring at the solid-liquid interface.

Research in the geological far-field

The work in the far-field experimental programme focuses on the determination of distribution coefficients of radionuclides on repository components and rock materials in order to compile specific and consistent sorption databases [1-3]. For this reason, sorption studies of radionuclides

(Ni, Zn, Am, Sr, Cs, Se, Th and Eu) on sedimentary rock systems and clays have been investigated in great detail [1-5]. The clay materials of interest are predominantly montmorillonite, illite, kaolinite, Marl and Opalinus clay. Montmorillonite is a 2:1 clay material with substantial isomorphic substitution. The clay material is a major component in backfill for a high-level waste repository and an important mineral responsible for the retention of metals in the geosphere. Marl and Opalinus clay are potential host rock formation for Swiss high-level nuclear waste. The argillaceous formations are composed of sheet silicates (approx. 50-80%) such as illite, illite/smectite mixed layers, chlorite and kaolinite. Thus, the interactions of radionuclides with the individual components of such rock materials are also studied.

Ni sorption on clay minerals: A case study

Initial research with Co/clay mineral systems demonstrated the formation of polynuclear metal complexes using XAFS spectroscopy, but the polynuclear structure was not strictly identified and referred to as a Co-hydroxide like structure [6-7]. Thus, the exact mechanism for “surface precipitate” formation remained unknown. Recent research suggests that during sorption of Ni and Co metal ions, dissolution of the clay mineral or aluminium oxide surface leads to precipitation of mixed Ni/Al and Co/Al hydroxide phases at the mineral/water interface [8-13]. This is illustrated in Figure 2. The figure shows a comparison of k^2 -weighted XAFS functions for the Fourier back-transformed spectra of pyrophyllite, a 2:1 model clay without isomorphic substitution, to the theoretical spectra derived with parameters from analysis of the isolated shells. The clay material (surface area: $97 \text{ m}^2 \text{ g}^{-1}$) has been reacted with Ni at pH = 7.5 (resulting sorption density: $3.1 \text{ } \mu\text{mol m}^{-2}$). The spectra of crystalline Ni(OH)_2 , takovite (a natural mixed Ni/Al hydroxide phase) and nepouite (a natural mixed Ni/Si hydroxide phase) are shown for comparison. The figure and data analysis demonstrates that there is an obvious similarity between the spectrum of the Ni/pyrophyllite sample and the spectrum of takovite, suggesting the presence of Ni phases of similar structure [8,11].

Figure 2. k^2 -weighted, Fourier-filtered and back-transformed XAFS spectra of Ni on pyrophyllite, takovite, Ni(OH)_2 , and nepouite (solid lines) in comparison with the fits derived from data analysis (dashed lines)

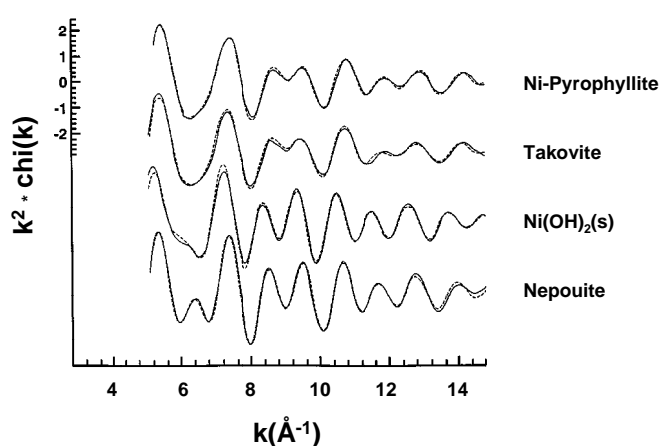
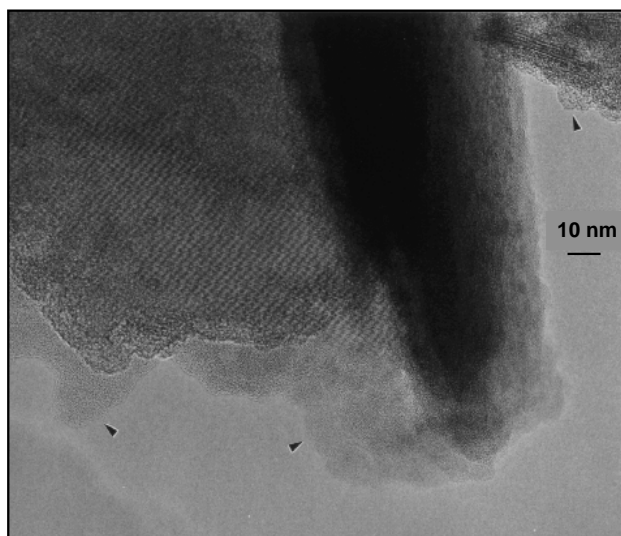


Figure 3 shows a HRTEM image of a Ni treated pyrophyllite sample at high magnification [14]. The image illustrates how the surface deposits grow. Rather than a homogenous precipitate, we observe clustered structures that protrude from the surface. Their widths vary considerably, ranging

Figure 3. HRTEM image of a Ni-treated pyrophyllite surface. The image shows surface deposited material with a rough, scalloped, “cauliflower-like” appearance along the particle edge.



from a few nm up to 30 nm. Surface deposits seem to occur preferentially along the edges of the particle. The bottom and top faces of the particle have not noticeably changed upon Ni sorption; the lattice fringes of pyrophyllite are still clearly visible. This finding fully agrees with the XAFS findings and supports the current understanding that edge surface sites are of great importance for metal removal from solution by natural clay mineral surfaces.

Mixed-cation hydroxide phases have structures in which divalent and trivalent metal ions are distributed within the same brucite-like octahedral hydroxide layer. The general chemical formula for the compounds is $[\text{Me}_{1-x}^{2+}\text{Me}_x^{3+}(\text{OH})_2]^{+x} \cdot (x/n)\text{A}^{-n} \cdot m\text{H}_2\text{O}$, where, for example, Me^{2+} is Mg(II), Ni(II), Co(II), Zn(II), Mn(II), and Fe(II), and Me^{3+} is Al(III), Fe(III), and Cr(III). The compounds exhibit a net positive charge x per formula unit which is balanced by an equal negative charge from interlayer anions A^{-n} such as Cl^- , Br^- , I^- , NO_3^- , OH^- , ClO_4^- , and CO_3^{2-} ; water molecules occupy the remaining interlayer space [15-19]. Minerals with the chemical formula given above are classified as the pyroaurite-sjoegrenite group [19]. The minerals takovite, $\text{Ni}_6\text{Al}_2(\text{OH})_{16}\text{CO}_3 \cdot \text{H}_2\text{O}$ and hydrotaalcite, $\text{Mg}_6\text{Al}_2(\text{OH})_{16}\text{CO}_3 \cdot \text{H}_2\text{O}$ are among the most common natural mixed-cation hydroxide compounds containing Al [15]. A detailed review on the synthesis, characterisation, natural occurrence and catalytic properties of mixed-cation hydroxide phases can be found elsewhere [20].

The following discussion will focus on some of the recent research on the formation kinetics of mixed cation hydroxide phases upon Ni sorption on montmorillonite. The sorption system has been studied in our laboratory over a wide range of reaction conditions (pH, ionic strength, initial metal concentration, and reaction time). Based on the sorption data and the macroscopic surface properties of the clay a mechanistic surface complexation model was developed [4-5]. We will present a combined macroscopic and spectroscopic approach. A combination of kinetic and spectroscopic data can provide a better understanding of what chemically happens on an atomic/molecular level over time and thus, can be important in assessing the mobility of metals in the mineral systems over extended time periods. To date there are only a few examples in the literature of studies where mechanisms of metalloid sorption reactions on natural components have been proposed via kinetic experiments and verified in separate XAFS studies (see e.g. [21-22]).

Figure 4 illustrates the kinetics of Ni sorption on montmorillonite (surface area: $697 \text{ m}^2 \text{ g}^{-1}$) at a fairly high Ni concentration [11]. The initial Ni concentration (3 mM), the solid/solution ratio (10 g L^{-1}) and the reaction pH (pH = 7.5) were selected to achieve sufficient sorption densities for the XAFS measurements and to ensure that the bulk solutions were undersaturated with respect to crystalline $\text{Ni}(\text{OH})_2$. A constant Ni sorption rate was observed following a first fast sorption step (approx. 35% or $0.152 \mu\text{mol m}^{-2}$ sorbed within the first 40 minutes). After approximately six weeks 91% of the initial Ni was sorbed.

Figure 4. Kinetics of Ni sorption [%] on montmorillonite from a 3 mM Ni solution at pH = 7.5 and an ionic strength $I = 0.1 \text{ M}$ (NaNO_3). Relative Ni removal (%) and the amount of sorbed Ni (mol m^{-2}) are shown as function of reaction time (h). The full symbols (●) denote samples which were used for XAFS measurements.

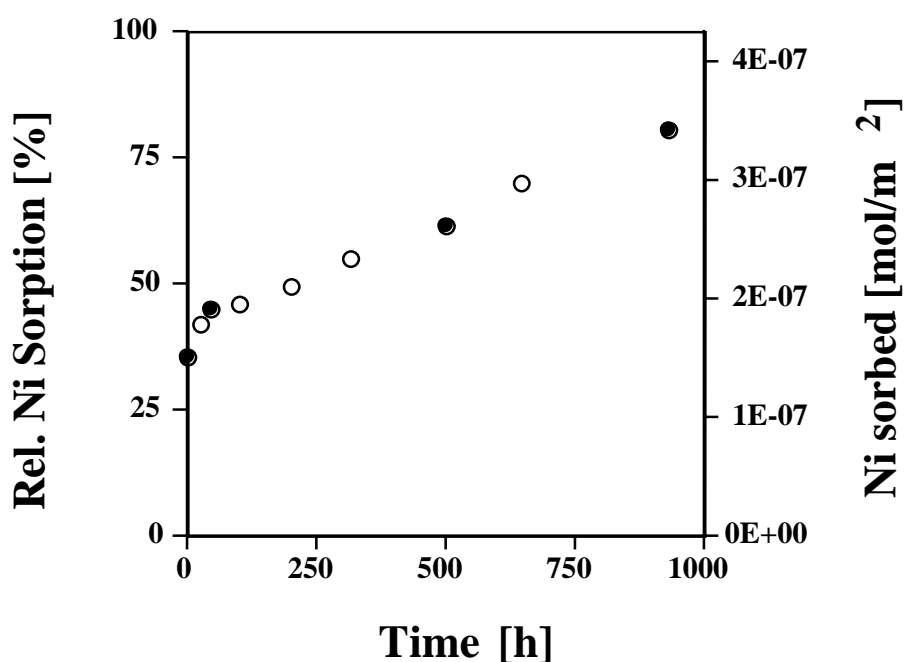
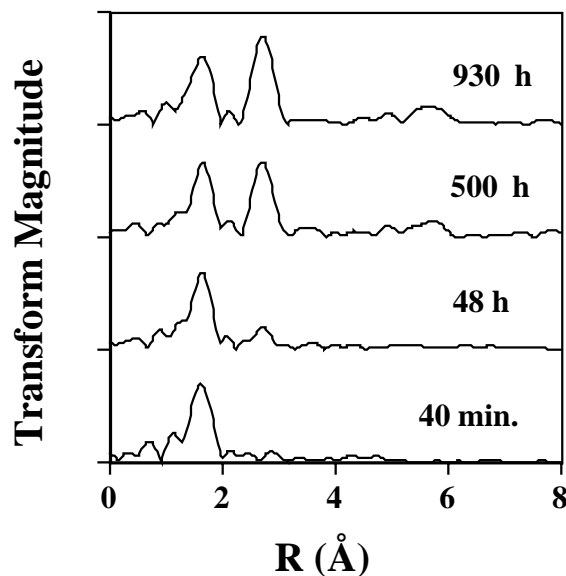


Figure 5 illustrates radial structure functions (RSFs) of montmorillonite treated with Ni for different reaction times (40 minutes, 48 h, 500 h and 930 h) [11]. The spectra are uncorrected for phase shift. All spectra show a peak at distance R of $\approx 1.8 \text{ \AA}$ which represents the first co-ordination shell of Ni. The structural parameters derived from data analysis suggest that Ni is surrounded by six O atoms. This behaviour indicated that Ni is in an octahedral environment. The Ni-O bond distance ($\approx 2.05 \text{ \AA}$) and numbers were not affected by the reaction time. A second peak representing the second Ni co-ordination shell can be observed at $R \approx 2.8 \text{ \AA}$ in the spectra of all Ni sorption samples except for the Ni/montmorillonite sample treated with Ni for 40 min. This peak reflects the presence of a mixed Ni/Al hydroxide phase. As reaction time progressed, and relative Ni removal from solution increased, the peak at $R \approx 2.8 \text{ \AA}$ in the RSFs increased in intensity. Data analysis revealed that the number of Ni second-neighbour (N) atoms at a distance of $3.06\text{-}3.07 \text{ \AA}$ increased from an N of about 2 to an N of about 6, indicating the continuous growth of a Ni/Al hydroxide phase with progressing reaction time [11].

Figure 5. Radial structure functions (RSFs) of Ni treated montmorillonite. The spectra are uncorrected for phase shift. Note the growth of a peak at an R of about 2.7 Å with increasing reaction time.



REFERENCES

- [1] M.H. Bradbury and L.R. van Loon, Cementitious Near-Field Sorption Databases for Performance Assessment of a L/ILW Repository in a Palfris Marl Host Rock, PSI-Bericht 98-01, Paul Scherrer Institute, Villigen, Switzerland (1998).
- [2] M.H. Bradbury and B. Baeyens, Far-Field Sorption Data Bases for Performance Assessment of a L/ILW Repository in an Undisturbed Palfris Marl Host Rock, PSI-Bericht 97-15, Paul Scherrer Institute, Villigen, Switzerland (1997).
- [3] M.H. Bradbury and B. Baeyens, Far-Field Sorption Data Bases for Performance Assessment of a L/ILW Repository in a Disturbed/Altered Palfris Marl Host Rock. PSI-Bericht 97-16, Paul Scherrer Institute, Villigen, Switzerland (1997).
- [4] B. Baeyens and M.H. Bradbury, A Mechanistic Description of Ni and Zn Sorption on Na-Montmorillonite. Part I: Titration and Sorption Measurements, *J. Contam. Hydrol.* 27, 199-222 (1997).
- [5] M.H. Bradbury and B. Baeyens, A Mechanistic Description of Ni and Zn Sorption on Na-Montmorillonite. Part II: Modelling, *J. Contam. Hydrol.* 27, 223-248 (1997).

- [6] P.A. O'Day, G.E. Brown, Jr. and G.A. Parks, X-Ray Absorption Spectroscopy of Cobalt (II) Multinuclear Surface Complexes and Surface Precipitates on Kaolinite, *J. Colloid Interface Sci.* 165, 269-289 (1994a).
- [7] P.A. O'Day, G.A. Parks, and G.E. Brown, Jr., Molecular Structure and Binding Sites of Cobalt (II) Surface Complexes on Kaolinite from X-Ray Absorption Spectroscopy, *Clay Clay Miner.* 42:337-355 (1994b).
- [8] A.M. Scheidegger G.M. Lamble and D.L. Sparks, Spectroscopic Evidence for the Formation of Mixed-Cation Hydroxide Phases upon Metal Sorption on Clays and Aluminium Oxides, *J. Colloid Interface Sci.* 186, 118-128 (1997).
- [9] A.M. Scheidegger, G.M. Lamble and D.L. Sparks, The Kinetics of Nickel Sorption on Pyrophyllite as Monitored by X-Ray Absorption Fine Structure (XAFS) Spectroscopy, *J. de Physique IV*, 7 (C2), 773-775 (1997).
- [10] A.M. Scheidegger, G.M. Lamble and D.L. Sparks, Investigation of Ni Adsorption on Pyrophyllite: An XAFS Study, *Environ. Sci. Technol.* 30, 548-554 (1996).
- [11] A.M. Scheidegger, D.G. Strawn, G.M. Lamble and D.L. Sparks, The Kinetics of Mixed Ni-Al Hydroxide Formation on Clay and Aluminum Oxide Minerals: A Time-Resolved XAFS Study, *Geochim. Cosmochim. Acta.* 62, 2233-2245 (1998).
- [12] J.B. d'Espinose de la Caillerie, M. Kermarec and O. Clause, Impregnation of γ -Alumina with Ni(II) and Co(II) Ions at Neutral pH: Hydrotalcite-Type Coprecipitate Formation and Characterization, *J. Am. Chem. Soc.* 117, 11471-11481 (1995).
- [13] S.N. Towle, J.R. Bargar, G.E. Brown, Jr. and G.A. Parks, Surface Precipitation of Co(II) on Al_2O_3 , *J. Colloid Interface Sci.* 187, 62-82 (1997).
- [14] A.M. Scheidegger, M. Fendorf and D.L. Sparks, Mechanisms of Nickel Sorption on Pyrophyllite: Macroscopic and Microscopic Approaches, *Soil. Sci. Soc. Am. J.* 60, 1763-1777 (1996).
- [15] R.M. Taylor, The Rapid Formation of Crystalline Double Hydroxy Salts and other Compounds by Controlled Hydrolysis, *Clay Miner.* 19, 591-603 (1984).
- [16] R. Allmann, Doppelschichtstrukturen mit brucitaehnlchen Schichtionen $[Me(II)_{1-x}Me(III)_x(OH)_2]^{x+}$, *Chimia* 24, 99-108 (1970).
- [17] D.L. Bish and G.W. Brindley, A Reinvestigation of Takovite, a Nickel Aluminum Hydroxy-Carbonate of the Pyroaurite Group, *Am. Mineral.* 62, 458-464 (1977).
- [18] G.W. Brindley, and S. Kikkawa, A Crystal-Chemical Study of Mg,Al and Ni,Al Hydroxy-Perchlorates and Hydroxy-Carbonates, *Am. Mineral.* 64, 836-843 (1979).
- [19] K. Hashi, S. Kikkawa and M. Koizumi, Preparation and Properties of Pyroaurite-Like Hydroxy Minerals, *Clays Clay Miner.* 31, 152-154 (1983).

- [20] F. Cavani, F. Trifiro and A. Vaccari, Hydrotalcite-Type Anionic Clays: Preparation, Properties and Applications, *Catalysis Today* 11, 173-301 (1991).
- [21] C.C. Fuller, J.A. Davis and G.A. Waychunas, Surface Chemistry of Ferrihydrite: Part 2. Kinetics of Arsenate Adsorption and Coprecipitation, *Geochim. Cosmochim. Acta* 57, 2271-2282 (1993).
- [22] G.A. Waychunas, B.A. Rea, C.C. Fuller and J.A. Davis, Surface Chemistry of Ferrihydrite: Part 1. EXAFS Studies of the Geometry of Coprecipitated and Adsorbed Arsenate, *Geochim. Cosmochim. Acta* 57, 2251-2270 (1993).

SYNCHROTRON RADIATION STUDIES ON NUCLEAR FUELS

L. Desgranges¹, M. Ripert², M. Beauvy³, T. Petit⁴

CEA – Direction des Réacteurs Nucléaires – Département d'Etudes des Combustibles

¹SDC/LEC Centre d'Etudes de Cadarache 13108 St. Paul-lez-Durance, France

²SDC/LMC Centre d'Etudes de Cadarache 13108 St. Paul-lez-Durance, France

³SPU Centre d'Etudes de Cadarache 13108 St. Paul-lez-Durance, France

⁴SECC/LA3C, 17 rue des Martyrs, 38054 Grenoble Cedex 9, France

Abstract

A renewed interest in nuclear fuel research has developed because of the necessity to decrease the cost of nuclear energy and the possibility to incinerate the actinides produced in irradiated fuel.

The aim of this paper is to present some of the work performed within CEA topics on nuclear fuel characterisation through the use of synchrotron radiation.

Fundamental aspects concerning the electronic structure and thermal vibration of atoms in uranium dioxide will be presented. Ongoing work on unirradiated fuels will be discussed in terms of phase determination and chemical state. Irradiated fuels and their requirements will be also presented. A list of information that can be obtained with synchrotron radiation will be discussed, and specific problems related to irradiated fuel handling will also be alluded to.

Introduction

Since the sixties, uranium dioxide has been the chemical compound chosen for nuclear fuel in pressurised water reactors (PWRs). It has thus been extensively characterised and can be considered as the third most studied material after silicon and iron. New trends in nuclear industry, however, have lent to a renewed interest in fuel research and modelling. Among them, increase of fuel burn-up, decrease of plutonium inventory and waste management have a major influence. This evolution leads to the design of optimised or new nuclear fuels that need to be studied in manufacturing and operating phase before any commercial application.

Up to now synchrotron radiation has been little used for nuclear fuel studies. However requirements for new fuel characterisation will need it for general reasons. New nuclear fuels will indeed be composed with several actinide elements that cannot be distinguished by classical X-ray diffraction. This implies that more powerful methods will have to be used to gain structural information on each actinide element: obviously EXAFS and anomalous X-ray diffraction shall be considered. During operation of nuclear fuel, fission products are created, some of them at very low concentration. In order to quantify and locate these fission products, very sensitive methods are necessary: X-ray fluorescence is of course appropriate, especially with microfocus. Fission products also segregate forming clusters of nanometric and then micrometric dimensions. Small angle scattering could help to understand this segregation.

After a brief recall of the main nuclear fuel research objectives, a selection of established results, going on research and prospective work will be presented, giving an overview of this fascinating field.

Objectives in nuclear fuel research

Nuclear fuel research is ruled by economic and safety aspects. The fuel designer must establish that nuclear fuel elements will not release any radioactive isotope under any operating condition, considering that power plant operations are optimised to increase their profitability. A nuclear fuel element contains sintered UO_2 pellets, the nuclear fuel itself, which are stacked into an airtight zirconium based cladding. During operation, the fuel behaviour must never induce a failure of the cladding which is the first containment barrier. That is the reason why a lot of experimental and theoretical work has been performed in the following directions:

- The thermo-mechanical properties of UO_2 were determined as a function of temperature in order to prove that the strains created in fuel pellets by power production do not induce stresses in the cladding that could fracture it. Thermo-mechanical properties are, however, linked to a lot of solid state physical variables. Thus a great effort was also made for nuclear fuel characterisation and fundamental physics.
- The chemical evolution of fuel must not induce an unacceptable corrosion of the cladding. That is the reason why a lot of experimental work was performed to locate all the chemical elements in irradiated fuel, and why some theoretical work has led to the prediction of their chemical evolution.
- Fission gas production can lead to an increase of pressure in fuel elements. A huge amount of experimental and theoretical work has been devoted to gas production, migration and escape from fuel.

UO₂ characterisation

Structural properties

Uranium dioxide crystallises in the fluorite structure (Fm3m space group), i.e. the uranium atoms form a face centred cubic sublattice in which the oxygen atoms occupy all the tetrahedral sites. Although UO₂ has a simple crystallographic structure, the thermal motion of uranium and oxygen atoms still requires a better understanding. The U-O distance calculated using EXAFS data is shorter than the one calculated using neutron diffraction data, while the U-U distance is the same for both methods [1]. Anharmonic vibrations of oxygen atoms were suggested to explain this feature. This hypothesis is consistent with the fact that oxygen and uranium thermal motion are highly correlated [1].

Electronic properties

Uranium dioxide is an f-f Mott-Hubbard insulator, i.e. the origin of band gap is due to strong correlations between 5f electrons localised on uranium atoms. An O K-edge X-ray absorption near edge structure (XANES) spectrum of this material has recently been obtained [2]. This XANES study leads to the conclusion that the hybridisation between O 2p and U 5f electrons is not negligible even if uranium dioxide is predominantly ionic.

Moreover, first principles-based calculations using the Local Density Approximation or the LSDA + U approach are now able to reproduce cohesive properties such as the lattice parameter [3-5], the bulk modulus [3-4] or the cohesive energy [3-4], and even to predict the formation energy of point defects [6] in this nuclear fuel. Similar calculations would be very interesting for the interpretation of future experiments on actinide oxides.

(U,Pu)O₂ characterisation

Physical and structural properties

Plutonium recycling in French PWR began in the late 80s, but R&D support is still required to better characterise physical and structural properties of the (U,Pu)O₂ mixed oxide fuel (MOX). Moreover, better knowledge of MOX behaviour implies the determination of the local environment of fission products and doping species in the fluorite lattice.

Measurements of unit cell parameter [7], electrical conductivity [8-11], specific heat [12] and thermal conductivity [13-16] seem to exhibit discontinuities with plutonium content, in contradiction with a random distribution of the substitute plutonium cations in the uranium sites of the fluorite lattice. Such a non-monotonic variation of the physical properties would indicate that (U,Pu)O₂ is not an ideal solid solution.

M. Beauvy [12] notes that these anomalies occur when plutonium concentration is around 3.1 and 12.5 at%. They respectively correspond to one plutonium atom for eight unit cells and one plutonium atom for two unit cells. He postulated that these percolation thresholds could correspond to different plutonium local environments in UO₂ matrix.

Furthermore, some EXAFS results obtained on $(\text{U,Ce})\text{O}_2$, a non-active analogue of $(\text{U,Pu})\text{O}_2$, show the existence of different cerium arrangements as a function of cerium concentration [17]. Unfortunately, up to now, no new data were obtained on $(\text{U,Pu})\text{O}_2$.

The recent operation of the Rossendorf Beam Line (ROBL) appears to be a unique opportunity to progress in $(\text{U,Pu})\text{O}_2$ structural knowledge. EXAFS which can separate uranium and plutonium contribution could help to settle some basic questions concerning the existence of plutonium clusters, homogeneous defects, phase transition and the average valency of uranium and plutonium. This determination of the plutonium local environment with respect to plutonium concentration in $(\text{U,Pu})\text{O}_2$ is fundamental to determine whether the solid solution in $(\text{U,Pu})\text{O}_2$ nuclear fuels is ideal or not.

A study at the uranium absorption edge could also specify the existence of oxygen vacancies and interstitials and explain deviations of the physical properties of $(\text{U,Pu})\text{O}_2$ with stoichiometry. In particular variations of oxygen potential with oxygen partial pressure were widely studied [18], but the local order associated with variations of stoichiometry still needs some progress, especially on the association of plutonium ions with oxygen vacancies.

Densification

The dimensional stability of $(\text{U,Pu})\text{O}_2$ fuel pellets under irradiation is of crucial importance for power reactors. This stability is the consequence of a competition between fission gas induced fuel swelling and small porosity disappearance under irradiation [19]. The study of this phenomenon for uranium dioxide resulted in a modelling which brings in initial porosity profiles [20-23]. The experimental characterisation of this submicronic porosity, the first to disappear under irradiation, has to be determined in order to improve fuel modelling.

Small angle scattering of X-rays allows one to obtain structural information such as dimension, pressure and density in very small bubbles (lower than 0.2 microns) [24-25]. Such a technique, applied to $(\text{U,Pu})\text{O}_2$ fuel, could determine pore size distributions within the material.

Dimensional stability of industrial fuels is controlled by a resintering test of 24 hours at 1700°C under a controlled atmosphere. The result of this test, which is conducted to eliminate very unstable fuels, seems to be correlated to the behaviour observed under irradiation. The determination of the submicronic porosity time evolution during the resintering test could be done by anomalous small angle scattering of X-rays. This would be of great help for the explanation of mechanisms correlated with redensification during the resintering test and therefore in fuel behaviour modelling.

Characterisation of other actinide compounds

Investigations on actinide compounds and especially on neptunium compounds have been developed for more than 20 years to study the localisation of the 5f electrons. There is a transition between localisation and itineracy of the 5f electrons in the actinide series. This transition occurs at the U, Np, Pu level, and it is strongly dependant on the chemical environment of the actinide atom in the solid compound. Inversely, the knowledge of the electronic structure of actinides informs about the structure and chemical properties of compounds. During the 80s, after the discovery of heavy fermion behaviour for compounds like UPt_3 or NpSn_3 , a strong excitement was observed among

physicists [26-29]. The electronic structure of actinides has been determined by theoretical calculations correlated with measurements of physical properties, essentially on metals, intermetallic compounds, and more recently on some non-metallic compounds. However it remains difficult to predict the structure and chemical properties of other actinide compounds. The X-ray absorption fine structure spectroscopy is a particularly powerful tool to study the local environment (interatomic distances, neighbouring atoms co-ordination and disorder) of actinides in solid compounds. The chemical bonding and the oxidation state of uranium and neptunium in borosilicate glass have been analysed by EXAFS and optical spectroscopy [30,31]. Np^{3+} has been observed in this oxidised compound. The oxidation state of Pu in nuclear fuel and its variation during irradiation or during storage after irradiation is for instance an important parameter for the kinetics of the reprocessing with the PUREX process which could also be determined by EXAFS.

More generally, it is necessary to know the properties (chemical and physical) of the irradiated fuels to progress in nuclear technology, that is $(\text{U,Pu})\text{O}_{2+x}$ mixed with fission products as presented later in this paper. However the possibilities for the direct measurements of the properties of irradiated fuels are limited and simulation would be useful. EXAFS investigations on simulated fuels containing plutonium will strengthen the validation of our modelling by comparison with small samples of true irradiated fuel.

Several actinides (Am, Cm and Np) – inappropriately called “minor actinides” – in nuclear wastes must be managed with high accuracy for a long time. One of our proposals is to transmute actinides in nuclear reactors, using targets made of these actinides diluted in inert matrixes. The polyphase targets of actinide oxides dispersed in MgO or MgAl_2O_4 have been prepared and well characterised in our laboratory. Solid solutions of actinide oxide and for instance cerium oxide are also under investigation. Their behaviour under irradiation has shown a significant influence of the fabrication. The irradiation effects, especially ionisation and disorder due to the recoil of fission products, can be determined from XAS measurements on simulated samples irradiated with ions.

Irradiated fuel

Study of irradiated nuclear fuel is one of the most difficult and exciting challenges of modern solid state science. It is challenging because manufacture, operation and recycling of nuclear fuel is a key point for the reliability, profitability and safety of nuclear industry, i.e. its future. It is very difficult both on experimental and theoretical sides. Experimentally, samples can not be handled by hand because of the α , β and γ emitters they contain. For small samples, a minimum of ten centimetres of lead shielding is necessary to protect operators. Theoretically, fuel in operating conditions is a very complex system: it includes more than thirty different elements, either fission or activation products and it endures enormous thermal, mechanical and chemical gradients. It is difficult to have a complete understanding of such a material, which is why research on irradiated fuel is focused on its characterisation and specific experiments aimed at the test of specific models.

Synchrotron radiation facilities can provide a unique opportunity to get some new experimental results that can answer questions unresolved up to now.

X-ray fluorescence can provide a reliable quantification and localisation of fission products even at low concentration. This is of great importance because the concentration of some fission products which are relevant to safety, as iodine for instance, is too low to be detected by hot lab apparatus.

Anomalous small angle scattering can provide information on the formation of clusters of fission products. This will help to model fuel behaviour and especially its chemical evolution.

The chemical state of fission products could be determined by XAS in fluorescence mode, provided that the fluorescence line of one fission product can be isolated from the lines of the others.

High quality anomalous diffraction experiments could quantify the influence of some fission or activation products on the UO₂ structure.

Of course, all these experiments could also be performed with tuneable temperature (and maybe pressure) in order to study irradiated fuel evolution as a function of temperature.

Conclusion

A big challenge for the nuclear industry is to reduce its costs whilst increasing profitability and safety. Up to now this research has been conducted in high activity laboratories, however specific questions can not find any answer with the experiments available in these facilities. The use of synchrotron radiation can provide valuable information. That is why the CEA nuclear fuel department plans to realise experiments with nuclear fuel using synchrotron radiation in France at LURE and at the ESRF. The next step will consist of experiments realised in new facilities able to handle active samples. The Rossendorf beamline and the project of a “hot” line at SOLEIL are essential tools to carry out this research.

REFERENCES

- [1] N.T. Barrett, G.N. Greaves, B.T.M. Willis, G.M. Antonini, F.R. Thornley, *J. Phys. C: Solid State Phys.* 21, 1988, L791-L796.
- [2] F. Jollet, T. Petit, S. Gota, N. Thromat, M. Gautier-Soyer and A. Pasturel, *J. Phys.: Condens. Matter* 9, 1997, 9393.
- [3] P.J. Kelly and M.S.S. Brooks, *J. Chem. Soc. Faraday Trans. II*, 83, 1987, 1189.
- [4] T. Petit, B. Morel, C. Lemaignan, A. Pasturel and B. Bigot, *Phil. Mag. B*, 73, 1996, 893.
- [5] S.L. Dudarev, D. Nguyen Manh and A.P. Sutton, *Phil. Mag. B*, 75, 1997, 613.
- [6] T. Petit, C. Lemaignan, F. Jollet, B. Bigot and A. Pasturel, *Phil. Mag. B*, 77, 1998, 779.
- [7] F. Schmitz, G. Dean and M. Halachmy, *J. Am. Ceram. Soc.* 40, 1971, 325.
- [8] Progress Report NUMEC 2389-1 (1963).

- [9] H.E. Schmidt, Test Report 380, Euratom/CEA, Contract No. 037-60-12 RDF, Final Report (1964); Progress Report Nos. 4 and 6, EITE Karlsruhe (1967-1968).
- [10] W.E. Baily and W.L. Lyon, AEC Research and Development Report GEAP 4675 (1965).
- [11] E.A. Aitken, M.G. Adamson, D. Dutina, S.K. Evans and T.E. Ludlow, AEC Research and Development Report GEAP 12418 (1973).
- [12] M. Beauvy, *J. Nucl. Mater.* 188, 1992, 232-238.
- [13] J.M. Bonnerot, thèse CNAM Paris (1986).
- [14] M. Beauvy and J.M. Bonnerot, *High Temp.-High Press.* 19, 1987, 389.
- [15] M. Beauvy, *High Temp.-High Press.* 22, 1990, 631.
- [16] Y. Philipponneau, *J. Nucl. Mater.* 188, 1992, 194-197.
- [17] D.J. Jones, J. Roziere, G.C. Allen and P.A. Tempest, *J. Physique* (Paris), Colloque C8, 47, 1986, C8-745-C8-748.
- [18] Catalogue européen des propriétés de l'oxyde mixte (U, Pu)O₂, N. T. SPU/LPCA No.02 Nov. 1990.
- [19] S.R. Mac Ewen, I.J. Hastings, *Phil. Mag.* 31, 303, 1974.
- [20] M.D. Freshley, D.W. Brite, J.L. Daniel, P.E. Hart, *J. Nucl. Mater.* 62, 1976, pp 138-166.
- [21] M.D. Freshley, D.W. Brite, J.L. Daniel, P.E. Hart, *J. Nucl. Mater.* 81, 1979.
- [22] C. Struzik, M. Moyne, J.P. Piron, A.N.S. Portland, March 1997.
- [23] P. Garcia, C. Struzik, N. Veyrier, AIEA, Cadarache, March 1998.
- [24] H.G. Haubold, *Radiation Effects*, 78, 1983, 385-392.
- [25] J.P. Simon, S. Arnaud, F. Bley, J.F. Berar, B. Caillot, V. Comparat, E. Geissler, A. de Geyer, P. Jeantey, F. Livet and H. Okuda, *J. Appl. Cryst.*, 30, 1997, 900-904.
- [26] H. R4. Hott, Z. Fisk, Handbook on the Physics and Chemistry of Actinides, A.J. Freeman, G.H. Lander, eds., North Holland, 1987, 85.
- [27] J. Larroque, M. Beauvy, 17 *J. Actinides*, 1987, 99; M. Beauvy, J. Larroque, *J. Nucl. Mater.* 166, 1989, 83.
- [28] T. Charvolin, thèse, Université de Grenoble, 1993.
- [29] J. Larroque, Clefs CEA, 31, 25, 1995.

[30] I Poirot, thèse Paris VI, 1987; M. Beauvy, I. Poirot, J. Larroque, P. Giani, 18 *J. Actinides*, 1988, B-23.

[31] S. Pillon, thèse, Montpellier 1992; M. Beauvy, S. Pillon, 24 *J. Actinides*, 1995, 40.

Session III

USE OF RADIONUCLIDES AT SYNCHROTRON FACILITIES

Chair: G.H. Lander

**EXPERIMENTAL PROCEDURES AND SAFETY
CONSIDERATIONS FOR TRANSURANIC STUDIES AT THE
STANFORD SYNCHROTRON RADIATION LABORATORY**

Patrick G. Allen

Glenn T. Seaborg Institute for Transactinium Science
Lawrence Livermore National Laboratory
Livermore, CA 94551

David K. Shuh, Jerome J. Bucher and Norman M. Edelstein

Actinide Chemistry Group, Chemical Sciences Division
Lawrence Berkeley National Laboratory
Berkeley, CA 94720

Abstract

This paper describes the safety procedures and documentation used by the LBNL group at the Stanford Synchrotron Radiation Laboratory. A short introduction is given describing the background to the safety documentation and then the report Hazards Analysis Safety Document (LBNL-37452, UC-401) is given in the Appendix.

Introduction

The fundamental basis of the experimental and safety procedures for studying transuranics at the Stanford Synchrotron Radiation Laboratory (SSRL) was established in 1993 through a detailed and extensive Department of Energy (DOE) review of transuranic (TRU) experiments proposed by researchers from Los Alamos National Laboratory (S. Conradson, *et al.*) and was based on a safety analysis document prepared by this group. Since that time, numerous TRU experiments have been conducted safely at SSRL, each adhering to the safety considerations outlined in 1993.

When our group at LBNL initiated TRU experiments at SSRL, we prepared our own safety analysis document. This document is reproduced in the appendix (following this introduction.) Our initial experiments used only the isotope ^{237}Np . Subsequently, we have used other TRU isotopes up to curium. Although the use of other TRU isotopes is not mentioned in the appendix, all isotopes sent to SLAC/SSRL must be approved beforehand. In general, the amount of radioactive material should be kept to the minimum necessary to perform the experiment. The major guideline for these experiments is that the total amount of radioactive material at SSRL (beamlines and storage building together) must not exceed one-half of the US DOE limit for a Category 3 non-nuclear facility which is set by a standard in the US Code of Federal Regulations (CFR 1027-92). For each set of experiments, a sample list including the isotopes, their radioactivity (number of millicuries), and their chemical form must be approved before shipping. This is done at SSRL by approval of the SSRL Safety Officer. Other conditions which must be adhered to include: three levels of containment for all samples, continuous air monitoring for alpha-emitting isotopes inside the X-ray hutch and at the sample storage building on site, and the presence of one authorised experimenter (with radiological worker training) at the X-ray beamline at all times.

Furthermore, all samples are checked by SSRL/SLAC radiation control technicians upon arrival at the site. If any of the samples show any breach of any level of containment, they are repackaged and sent back to the sending institution. Handling or manipulating radioactive materials outside of the triple-level of containment is not allowed at SSRL. Experiments which are conducted at non-ambient temperature and/or pressure require additional safety approval.

The specific procedures pertaining to experiments conducted at SSRL by our groups from LBNL and LLNL are presented below in the Hazards Analysis Safety Document (LBNL-37452, UC-401) that was prepared and reviewed for these experiments.

Some acronyms used in the Appendix:

CAM	Continuous Air Monitor
CFR	Code of Federal Regulations
DOE	Department of Energy
DOT	Department of Transportation
HEPA	High Efficiency Particulate Arrestance
LBNL	Lawrence Berkeley National Laboratory
LLNL	Lawrence Livermore National Laboratory
OHP	Occupational Health Physics
SLAC	Stanford Linear Accelerator Center
SSRL	Stanford Synchrotron Radiation Laboratory (SSRL is a division of SLAC)
TRU	Transuranic
US	United States

Appendix

HAZARDS ANALYSIS SAFETY DOCUMENT – LBNL-37452

1.0 Overview of experiment

The objective of this experiment is to determine the oxidation state(s) and local structure of neptunium (Np) in representative environmental samples by X-ray absorption fine structure (XAFS). These data will be crucial in understanding the speciation of Np in the environment which will help in our understanding of migration and transport, etc. It is proposed to run these experiments at the Stanford Synchrotron Radiation Laboratory (SSRL). This laboratory is a DOE national user facility located at the Stanford Linear Acceleratory Center (SLAC).

Neptunium is a transuranium element with the following nuclear characteristics:

$$^{237}\text{Np} - t_{1/2} = 2.14 \times 10^6 \text{ years } 7.05 \times 10^{-4} \text{ Ci/gram}$$

The ^{237}Np nucleus decays by the emission of an alpha particle and this particle emission is the principal hazard in handling Np samples. This hazard is mitigated by physical containment of the sample which stops the alpha particles within the containment.

The total amount of Np material that will be shipped to and be at SSRL at any one time will be less than 500 mg. This limit on the amount of Np will ensure that SLAC remains a low hazard, non-nuclear facility.

The Np samples will be solids or Np ions in aqueous solution. The total volume of the solution samples will be less than 0.5 ml. The solid or aqueous solution neptunium samples will contain approximately 5 mg of Np per sample with an absolute maximum limit of 10 mg per sample. All sample preparation will be done at LBNL. The solution samples will be loaded in a cell containing a plastic spacer with a cut-out of dimensions $2 \times 20 \times 3$ mm. Two polyethylene windows will be sealed to the spacer to contain the solid or solution sample. This experimental arrangement has been used previously with solutions of uranium and no problems were found. For powdered, solid Np samples the Np solid will be diluted with an inert organic solid (e.g. polystyrene (bio-beads)) or an inert inorganic solid (e.g. boron nitride). The loaded sample cell described above will be placed in a polyethylene (PE) bag which will be heat sealed. A second PE bag will be placed around the sample cell and the primary PE bag and will be heat-sealed. Samples prepared this way will then be loaded into the sample containment cell for use on beamline 4-1 or 4-3.

The Np samples will be shipped to SSRL/SLAC OHP. SLAC OHP will inventory the samples and swipe the containers holding the triply contained samples, and then bring them to the SSRL actinide trailer located outside Building 131. The Np samples not in use at beamline will be stored in a 55 gallon drum in the locked trailer.

The following table gives the radioactivity for typical quantities of ^{237}Np :

Mass ^{237}Np (mg)	Radioactivity (μCi)
1	0.705
5	3.5
10	7.05
100	70.5
200	141.0
500	352.5

All samples will be prepared, sealed and inspected at LBNL and will be shipped to SLAC/SSRL in compliance with DOT regulations by LBNL EH&S shipping. All samples at SSRL will remain packaged as described above and will be handled and run under ambient conditions. After the runs are over they will be packaged and shipped back to LBNL by SLAC EH&S.

In addition, strict monitoring of the storage and experimental areas will be performed in accordance with SLAC/OHP radiation protection procedures to ensure against the release of contamination.

2.0 Non-nuclear, low hazard classification

2.1 Background

DOE Order 5481.1B, "Safety Analysis and Review System", states that hazards of a particular facility should be classified into one of the following three classes: low, moderate or high hazard. Hazard classification is a measure of the inherent potential for materials or energy sources to cause harm to the worker, the public or the environment.

DOE Order 5480.5, "Safety of Nuclear Facilities," defines a nuclear facility as "a facility whose operations involve radioactive materials in such a form and quantity that a significant hazard potentially exists to the employees or to the general public." Accelerators and their operations are not included as nuclear facilities. SLAC and SSRL are accelerator facilities and are not nuclear facilities.

2.2 Hazard classification of XAFS experiments (per standard 1027-92)

The DOE has issued DOE-Standard-1027-92, "Guidance on Preliminary Hazard Classification and Accident Analysis Techniques for Compliance with DOE Order 5480.23, Nuclear Safety Analysis Reports," dated October 1992. Hazard Category 3 under DOE Order 5480.23 is equivalent to a "low hazard" classification under DOE Order 5481.1B. Hazard Category 3 and "low hazard" are therefore synonymous, with the choice of terminology dictated by the DOE order to which they refer. The quantities presented in Section I for ^{237}Np are well below the threshold quantities for the Hazard Category 3. Operations or facilities with quantities below the threshold values may be categorised as "non-nuclear" and are potentially considered hazards generally accepted by the public (below a "low hazard" classification) because the potential impact on people not involved with the experiment is low, along with a negligible chance of actually receiving that impact. According to these standards, this is a "low hazard," "non-nuclear" experiment.

3.0 Details of neptunium speciation experiments

3.1 Samples, composition and characteristics

The samples will be prepared in the Actinide Chemistry Group laboratories at the Lawrence Berkeley Laboratory with the isotope ^{237}Np . The Np samples will be solids or Np ions in aqueous solution. The total volume of the solution samples will be less than 0.5 ml. The solid or aqueous solution neptunium samples will contain approximately 5 mg of Np per sample with an absolute maximum limit of 10 mg per sample. The solution samples will be loaded in a cell containing a plastic spacer with a cut-out of dimensions $2 \times 20 \times 3$ mm. Two polyethylene windows will be sealed to the spacer to contain the solid or solution sample. For powdered, solid Np samples the Np solid will be diluted with an inert organic solid such as polystyrene (bio-beads) or an inert inorganic solid such as boron nitride. The loaded sample cell described above will be placed in a polyethylene bag which will be heat sealed and acts as secondary containment. A second polyethylene bag will be placed around the sample cell and the first polyethylene bag and heat-sealed. This second polyethylene bag provides tertiary containment. Samples prepared this way will then be loaded into the sample containment cell (quaternary containment) for use on beamline 4-1 or 4-3.

3.2 Calculation of sample activity

The isotope ^{237}Np has a half-life of 2.14×10^6 years and a specific activity of 7.05×10^{-4} Ci/gram. A 10 mg ^{237}Np sample then has an activity of:

$$10 \times 10^{-3} \times 7.05 \times 10^{-4} \text{ Ci/gram} = 7.05 \times 10^{-6} \text{ Ci or } 7.05 \mu\text{Ci}$$

3.3 Description of sample cell

The samples will be loaded in a cell containing a polyethylene spacer with a cut-out of dimensions $2 \times 20 \times 3$ mm. Two polyethylene windows will be sealed to the spacer to contain the solid or solution sample. For powdered, solid Np samples the Np solid will be diluted with an inert organic solid such as polystyrene (bio-beads) or an inert inorganic solid such as boron nitride.

The loaded sample cell will be placed in a PE bag which will be heat-sealed (secondary containment). A second PE bag will be placed around the sample cell and the first PE bag and heat-sealed (tertiary containment). A schematic diagram of the sample cell and barriers is *not shown here*.

3.4 Description of the quaternary containment cell

The sample cells described above in Section 3.3 will be mounted on a slide mount which fits into fixed grooves in the quaternary sample containment cell. Up to 10 samples, each containing approximately 5-10 mg of ^{237}Np can be mounted with tape on this slide mount. The slide mount will be placed into the quaternary sample containment cell and this cell will be sealed with a gasket seal. This containment cell will be mounted on a support on the table in the hutch which contains vertical rails on which this cell will slide up and down. A linear Acme Screw actuator system will be used to lift the sample containment cell and to vertically align the samples contained inside with the X-ray beam. There are no horizontal degrees of freedom. A containment cell containing only one Np sample

and fixed in position will be prepared for the reference compartment. A schematic diagram of the quaternary sample containment cell is *not shown here*. These loading operations of the Np samples into the quaternary containment cell will be performed in the hood in the storage/loading area of the actinide trailer.

The total amount of ^{237}Np contained in 10 samples in the sample containment cell plus the one sample cell in the reference compartment will be less than 50 μCi . This amount will be the maximum in the experimental hutch at any one time.

3.5 *Operating conditions*

All of the experiments will be carried out under ambient temperature and pressure.

3.6 *Failure modes and effects*

The failure mode is the unlikely possibility that the secondary and tertiary PE bags will be breached. In that case the sealed polyethylene windows of the sample cell will contain the Np sample. If the polyethylene windows are also breached, the quaternary containment cell on the beamline will contain the Np sample. If the quaternary containment cell was also breached, the sample would fall on the table in the hutch where it could be wiped up from the plastic sheeting covering the table. In this case, the emergency operating procedures of Section 6.4 of this document would be activated.

4.0 Description of shipping procedures

The sample materials for the proposed XANES and XAFS experiments will be shipped in compliance with all requirements of Title 49 of the Code of Federal Regulations (49 CFR) which addresses the use of proper shipping containers, correctly preparing shipping papers, and the proper marking, labelling and transporting of radioactive material. In addition, all requirements of DOE Order 5480.3, "Safety Requirements for the Packaging and Transportation of Hazardous Materials, Hazardous Substances, and Hazardous Wastes", will be followed in shipping the sample materials. Each of the sample materials will be sealed within a sample cell (primary barrier), which, in turn, will be sealed within two additional PE bags which act as secondary and tertiary barriers. At LBNL, prior to placement into the shipping containers, these secondary and tertiary barriers will be loaded, sealed, checked, and surveyed for any surface contamination. The secured samples will be loaded into the DOT approved shipping containers. Thus, the sample materials will be contained within three barriers during shipment from LBNL to SSRL.

4.1 *Description of the shipping containers*

The shipping containers used will be those specified for shipping Type A samples. The Np samples will be placed in a metal can and the can will be sealed. This can will then be placed in a shipping carton which meets the specifications for a Type A container and will be labelled as required by Title 49 of the Code of Federal Regulations (49 CFR). For Np samples which have to be kept cold until used, the can containing the samples will be packed in dry ice, placed in a styrofoam container and then packaged in a Type A container.

4.2 Mode of shipment from LBNL to SLAC

The packaged Np samples will be shipped by Federal Express or by an alternate express delivery company to the SLAC/SSRL OHP receiving office.

4.3 Receiving, packing, and unpacking procedures

The Np samples will be received by SLAC/SSRL OHP where they will be checked for integrity and swiped. SLAC/SSRL OHP will deliver the samples to the designated storage/loading area. Further details of these procedures are described in Section 6.2.

4.4 Shipping documentation and accountability

All shipping papers will be completed in accordance with 49 CFR 172.202 and 172.203(d) which provide instructions on how to complete the documentation when shipping radioactive materials. All major common couriers (i.e. Roadway, Federal Express, etc.) are permitted to transport radioactive materials in the state of California. LBNL will use one of these common carriers to transport the samples to SSRL within DOT-approved shipping containers.

All accountability procedures will be followed in compliance with DOE Order 5633.3, "Controls and Accountability of Nuclear Materials", including the documentation of the transfer of material from LBNL to SSRL. This process will involve interactions between the LBNL Shipping/Receiving Section, the Accountability Section of the Material Control, and the SLAC/SSRL nuclear material representative, who is currently in the Health Physics group at SLAC. When appropriate, LBNL will notify the California State Highway Patrol under the MOU with DOE concerning shipments of transuranics in California.

5.0 Storage of samples

5.1 Description of storage

Samples will be stored in a 55 gallon drum except during the period when measurements are being performed on specific samples. These containers will be kept in the designated storage/loading area at SSRL. The current designated storage area is a modular building located immediately outside and between Buildings 120 and 131.

5.2 Security and documentation procedures

The storage/loading area will be kept locked, with a self-locking door, with the key controlled by designated SLAC/SSRL staff and the on-duty LBNL experimenter. Either designated SLAC/SSRL personnel or a LBNL experimenter must be present any time the storage area is not locked. These accesses and the status of the shipping containers (sealed/unsealed, samples within) will be recorded by either the LBNL experimenters or designated SLAC/SSRL personnel. One log book recording the location and disposition of each sample will be maintained. During the experiments, these log books will be kept by the LBNL group, and will be under the personal physical control of the LBNL experimenter on-duty.

5.3 *Physical security measures*

The self-locking ability of the door will be checked. The building containing the storage/loading area will be checked to ensure that unauthorised entry will be difficult and that it is in an area that is not too remote but routinely observed by site personnel. SLAC security will be notified of the presence of the materials.

6.0 Operations and procedures

6.1 *LBNL experimental team and SLAC RCT personnel*

The LBNL experimenters will be scientists or technicians whose principal responsibility will be sample handling and the performance of the XAFS measurements. At least one member of the team will have considerable synchrotron radiation experience and considerable experience with samples of the type being measured. These personnel need not be present at all times, but must be on call and available on short (ca. 1 hour) notice 24 hours a day. At least one member of the team with current (and documented) Radiological Worker I training will be present at all times when a sample is in the experimental area.

SLAC will provide Radiation Control Technician (RCT) support. The designated RCT will be on call via a pager/beeper/telephone and available on short (ca. 1 hour) notice 24 hours a day. The RCT will be present at all times when samples are being handled, including but not limited to, receipt and the initial surveys of the samples, transfer to and from the shipping/storage containers and transfer of the samples to and from the experimental area. The SLAC RCT will be present at those times regardless of whether they or a member of the experimental team is performing the sample handling.

The LBNL experimenter on-duty will be the senior member of the experimental team present at SSRL. The LBNL experimenter on-duty will be responsible for ensuring that all procedures are followed and will be in charge of all operations involved in preparing the areas at SLAC/SSRL and in handling the samples from the time they are delivered to the loading/storage area until they have left the loading/storage area for shipment back to LBNL. Should the need arise, he (she) will direct emergency personnel. For certain types of non-routine procedures where it would be advantageous, he (she) may, with their concurrence, delegate this authority to someone more capable in terms of training or experience, e.g. the SLAC Health Physics personnel.

6.2 *Site preparation at SLAC/SSRL*

Prior to the arrival of the samples at SLAC/SSRL and the initiation of the experiments, the affected areas, including the storage/loading area, experimental area, and personnel access control area, must be established and prepared by the LBNL and SLAC/SSRL personnel. In addition, all radiation protection equipment and instrumentation will be on site prior to the unloading of the samples. Security and fire personnel will be notified of the arrival of the materials so that they can initiate specific procedures.

6.2.1 *Monitoring*

The following is a general overview of the types of monitoring controls that will be present in the storage/loading area and in the hutch area for these experiments.

SLAC/OHP will be in charge of the continuous air monitor (CAM) monitoring.

There are two types of monitors that will be used to detect alpha particles which would be present in the event of a release:

- 1) CAMs which are electronically controlled. Air is continuously sampled and counted by the use of an *in situ* detector along with a multichannel analyser. One of the key parameters in using this type of monitor is determining the alarm set point (see below).
- 2) Swipe counters which rely on SLAC Health Physics personnel to accurately survey potential problem areas and insert the collected swipe into an alpha counter, record a reading and check against background.

Swipes of individual sample containers will be done as follows: a) before shipping from LBNL, b) during unpacking from shipping container and prior to locating at beamline, and c) on removal from the hutch and before repackaging into the shipping container.

General swipes are needed as follows: a) of the storage trailer to gather a baseline and confirm that the area is clean before any sample arrives, b) of the hutch to gather a baseline before the experiment goes on line, c) of the hutch and the storage trailer after the experiment is completed.

Active monitoring of the hutch and the trailer using the CAMs is required while samples are present inside the hutch and when they are being loaded/unloaded in the trailer.

6.2.2 CAM alarm set-point determination

Naturally occurring radon gas can result in a significant (relative to the desired minimum alarm level) background radiation level for the CAMs. The CAMs in use can discriminate radon from other alpha emitters on the basis of the different energies of their alpha emission. Prior to these experiments and the introduction to the site of any alpha emitter involved with these experiments, SLAC/OHP will determine the background levels at the experimental and other affected areas utilising this energy resolving capability. The CAM alarm set point will then be determined in consultation with SLAC/SSRL Health Physics to maintain an adequate sensitivity level while minimising the number of false alarms.

6.2.3 Storage area

Access to the storage area (actinide trailer) for the purpose of transferring samples will be co-ordinated in advance with SLAC/SSRL OHP.

The room will be doubly lined with plastic sheets. Work areas will be covered with additional plastic. This plastic will allow for containment and easy decontamination should a release occur and will, in conjunction with the filter system provide an additional barrier during sample transfer operations. A HEPA filtered blower (125 cfm) is attached so that the air flows into the room through the door at one end of the structure and out at the other end of the building. This will provide air flow from areas with the lowest potential for contamination to areas with a higher potential. The room air will be monitored using a Canberra Alpha Continuous Air Monitor (portable CAM) portable air sampler. The CAM will be operated during the times when a loading/unloading/transfer of TRU

samples occurs or on a continuous basis while samples are stored depending on SLAC OHP procedures. The portable trailer will be posted as a controlled area and access will be controlled. The radiation detectors used to survey and monitor the storage and sample containers will be installed and checked.

A hood or containment area exhausting through the existing ventilation duct and HEPA filter should be provided in the storage area for loading and unloading the Np samples from the shipping containers.

The Np samples will be loaded into the beamline sample containment cell in this hood or containment area. The beamline containment cell will be checked for activity after loading the samples in the hood or containment area.

6.2.4 Hutch area

The experimental area, consisting of the inside of the hutch, will be monitored for alpha contamination initially and then prior to running each separate experiment/changing samples, using a Ludlum Model 139 alpha instrument and an Eberline SAC-4 alpha instrument.

Air sampling using a Alpha Continuous Air Monitors (Portable CAM) will be set up to monitor for the presence of alpha particles in the hutch containing the sample container positioner. The hutch will exhaust into a HEPA filter installed at the opening to the hutch ventilation system, passing by inlets for an inline sampler and a CAM. The ventilation will be controlled by a variable inlet and checked to ensure that all air is exhausting past the CAM and through the HEPA filter.

The experimental area (the lift table and the area on the lift table under the sample) will be lined with plastic as a contamination barrier. The use of plastic as a protective liner in the experimental area will minimise the spread of contamination and facilitate clean-up efforts with damp cloths or tissues if any contamination is detected. The optical bench assembly used to support the experimental apparatus will be fixed to the top of the hutch lift table. Open penetrations in the hutch will be closed off.

6.2.5 Personnel access control area

A personnel access control area will be established by SLAC/SSRL in consultation with the LBNL staff as part of the scheduling process. It will include the experimental hutch, the loading/storage area, and any adjacent area where personnel not directly associated with the experiment should be excluded. This area will be posted with warning signs and temporary barriers where needed. Only authorised and trained personnel, those from LBNL involved with the experiment and those designated by SLAC/SSRL, will be permitted in this area. Samples will only be allowed into the personnel access control area when they are transferred from the storage area to the experimental area in a closed transfer container. Only one beamline sample container cell and one reference cell sample container (containing the Np samples) will be permitted in this area at any time.

6.3 Standard operating procedures at SLAC/SSRL

This section describes the step-by-step procedures at SLAC/SSRL involved in the actual handling of the samples, including receiving, performing the XANES and XAFS measurements, and

shipping. The samples and the areas will be frequently (or continuously) checked for contamination and the results noted on the radiation survey logsheets at the storage site and the beamline. In the unlikely event of the simultaneous failure of the primary (sample cell), secondary and tertiary PE bags, and the quaternary sample containment container due to simultaneous puncture or concurrent failure of the seals of all four barriers, release of contamination could occur. If contamination is found, the decontamination procedure described later will be followed. In the case of a CAM alarm or airborne contamination, the specific procedure described in Section 6.4 will be followed.

6.3.1 Receipt of samples at SLAC

The shipping containers will be delivered to SLAC Health Physics. Prior to unloading, the outsides of the containers will be swiped to show < 20 dpm/100 cm² removable contamination.

6.3.2 Transfer of samples to SSRL loading/storage area and verification

The samples inside the shipping containers will subsequently be transported to the loading/storage area at SSRL and remain there for the duration of the experiment. Security and documentation procedures will be implemented at this time. On receipt at the loading/storage area at SSRL, the SLAC/OHP RCT and other members of the experimental team will unpack the shipping container. LBNL personnel opening the shipping containers will wear gloves and lab coats. Surveys of the surfaces, e.g. walls, floors, tables, etc., will be obtained by wiping the surfaces with swipes which will subsequently be counted, and documented. This will be confirmed by checking each shipping container with a swipe which will be counted on the SAC-4 alpha instrument, verifying that they show < 20 cpm/100 cm² removable. For storage the samples will be placed in a resealable 55 gallon drum.

If alpha contamination is identified at any time during unpacking the process shall be stopped immediately. The secondary container will be decontaminated according to LBNL decontamination procedures; the area will be checked and, if necessary, decontaminated according to the LBNL procedures. The sample will be placed back in the shipping container and the container will be sealed for return shipment to LBNL.

If the CAM alarms at any time during unpacking, the process shall be stopped immediately. The storage/loading building will be evacuated and if the alarm is found to be valid by SLAC/OHP, the LBNL emergency response team will be called according to the procedures of Section 6.4. The LBNL emergency response team will be responsible for checking for contamination and surveying the area and containers for a possible release of contamination. The CAM will be operated during the times when a loading/unloading/transfer of TRU samples occurs or on a continuous basis while samples are stored depending on SLAC OHP procedures.

6.3.3 Placement of samples in the quaternary container

A separately ventilated hood area or containment area with a HEPA filter will be provided in the storage area for loading and unloading the Np samples from the shipping containers. The Np samples will be loaded into the beamline containment cell in this hood or containment area. The beamline containment cell is designed to hold up to 10 Np samples at one time. The beamline containment cell will be checked for activity after loading the samples in the hood or containment area. A separate

beamline containment cell will be used for the one sample (with surrounding primary, secondary and tertiary containment) which will be placed in the reference compartment at the beamline. The LBNL personnel performing these operations will wear lab coats and gloves and monitor the operations with a certified portable alpha counter.

The samples will be loaded into the quaternary sample container (the beamline containment cell). This quaternary sample container will be placed within a transfer container for protection during the transfer to the experimental area. Only one beamline containment cell plus the reference containment cell with the reference N_p sample may be outside of the storage area at any time. If the CAM alarms at any time during loading, the process shall be stopped immediately, and the storage/loading building will be evacuated. The building will be monitored by SLAC/OHP and re-entered when safe. If necessary the LBNL emergency response team will be called for decontamination. The CAM will be operated during the times when a loading/unloading/transfer of TRU samples occurs or on a continuous basis while samples are stored depending on SLAC OHP procedures.

If the sample containers are subjected to any treatment outside of the standard handling procedure (i.e. dropped), the containers will be surveyed for any release of the sample. If there is an indication that the containment system may have been damaged, the sample will be returned to the storage container and will not be used. The event will be logged and reported to the SLAC/SSRL Evaluation Team. The SLAC/SSRL Evaluation Team will review all incidents and decide whether and how to proceed with the remaining samples. If the event is sufficiently minor so that the LBNL experimental team believes that no damage has occurred and this supposition is supported by the absence of any signs of damage during the subsequent inspection or by appropriate tests, then they may proceed with the experiment.

6.3.4 Transport of quaternary container to experimental area

The quaternary sample container within the transfer container will be moved to the experimental area. A dolly or cart may be used to assist in transporting the transfer container. The transfer must follow the designated route. SLAC/OHP will escort the LBNL experimenter.

6.3.5 Mounting of quaternary container

The quaternary sample container will be removed from the transfer container and placed in the sample holding assembly in the beam line hutch. A CAM located within the hutch will be turned on.

6.3.6 XAFS measurements

XAFS measurements will be performed on the sample(s). At least one member of the LBNL experimental group must be in attendance at all times when a sample is present in the experimental area. In the case of a CAM alarm, the applicable procedures described in Section 6.4 will be implemented. Please refer to Section 6.4 for detailed information about emergency response to contamination and emergency response to CAM alarms.

If the sample containment cell or the samples within are dropped or any deviation from the standard procedure with regard to the containment vessel integrity occurs during this step, the procedure described in Section 6.3.3 will be followed. If the control and behaviour of the sample does

not follow the expected pattern for the specific experiment as described in Section 3, the experiment will be stopped until this event is reported to and evaluated by the SLAC/SSRL OHP, who will decide whether and how to proceed.

6.3.7 Completion of measurements, dismounting of quaternary container

Upon completion of the measurements for a sample or set of samples, and under the condition that the CAM monitoring the air around the beam line sample container shows no contamination, the quaternary sample container will be dismounted from inside the hutch and placed back in the transfer container.

6.3.8 Monitoring of experimental area

After the beamline containment cell is removed, the experimental apparatus and area will be monitored for alpha radiation and removable contamination. In the case of removable contamination, the area will be secured and the procedures of Section 6.4 will be followed. In the case of a confirmed CAM alarm (see Section 6.4), the building will be evacuated and the applicable procedures described in Section 6.4 will be implemented. In the case of a known or suspected release resulting from an accident or if contamination is detected during a survey, the procedures described in Section 6.4 will be implemented, as appropriate.

6.3.9 Return of samples to storage/loading area

The transfer container containing the quaternary sample container will be transferred back to the storage/loading area. It may not leave the designated path. The procedures outlined in Sections 6.3.3 and 6.3.4 will be followed.

6.3.10 Monitoring of samples

Once within the storage area, the quaternary sample container will be opened and the sample slide mount will be removed. The container will be inspected visually. If there are any indications that the sample containment may have been breached, then the whole apparatus will be placed in a plastic bag for containment purposes and returned to LBNL. The security of the seals will be confirmed by checking the inside of the beamline sample container with a swipe which will be counted on the SAC-4 alpha instrument, verifying that they show < 20 cpm/100 cm² removable alpha contamination. The packaged samples will be placed back into the 55 gallon drum, which will be resealed. If the CAM alarms at any time during this procedure, the process shall be stopped immediately, the storage/loading building will be evacuated, and the area and containers surveyed by qualified personnel for a possible release of contamination. The CAM will be operated during the times when a loading/unloading/transfer of TRU samples occurs or on a continuous basis while samples are stored depending on SLAC OHP procedures.

6.3.11 Completion of experiments

Samples will be repacked into appropriate DOT shipping containers following the same procedures used for the original packing. The outside of these containers will be nucon swiped and

the swipes counted on the SAC-4 alpha instrument to verify that they show < 20 dpm/100 cm² removable and no fixed alpha contamination. The health physics portion of the appropriate shipping documents will be completed. SLAC/SSRL will transport the sealed shipping containers from the storage/unpacking area to the SLAC OHP shipping area for shipment back to LBNL.

6.4 Emergency operating procedures

6.4.1 Response to an accidental release

Immediately following a release (or discovery of a release), the following list of procedures needs to be performed as appropriate to ensure the safety of those involved, to prevent spread of contamination, and finally clean up the contamination. The LBNL experimenter-on-duty will initially be the “person in charge” and have the responsibility for ensuring that these procedures are followed until such a time as he (she) may delegate this responsibility to someone more capable in terms of training and experience.

1. Provide for the safety of personnel involved:
 - First aid is given to serious injuries.
 - Contaminated personnel will be confined to the immediate area.
 - Help is summoned as needed.
2. Minimise the spread of contamination by maintaining or establishing controlled areas and post the areas as appropriate.
3. Call the LBNL emergency response team (see below).
4. Of less critical importance but also of immediate concern, the person in charge should:
 - Contact SLAC Fire Department by calling 9-911 and the SLAC Main Control Center by calling extension 2151 (926-2151 if off-site).
 - Assure necessary equipment and materials for clean-up are assembled.
 - Assign a “technical reporter” to accurately record the accident response activities.

Decontamination procedures

All decontamination procedures should be performed by qualified and certified personnel.

Personnel decontamination should be performed first followed by area decontamination. Waste generated during decontamination will be shipped back to LBNL in appropriate containers. Once the extent of the contamination is determined, a decontamination plan will be formulated using all available information. The decontamination procedures will be followed as appropriate.

Arrangements with LBNL

All waste (including liquid) generated during the accident response will be collected and sent back to LBNL for disposal. This will be performed by packing and shipping such waste as DOT type A, for which there is no restriction on the type of material. All samples are already type A, so that all waste generated during decontamination is also type A and would not require survey and division. Suitable shipping containers will be available at SLAC/SSRL during the experiments to be used in the event of a release. An LBNL Emergency Response Team will be on call in case of accidental release of radioactivity. Appendix 1 contains the names and telephone numbers of the LBNL Emergency Response Team.

6.4.2 Response to CAM alarms

Two types of CAM alarms may be distinguished: 1) CAM alarms from inside the hutch, and 2) CAM alarms within the loading/storage area. If the hutch CAM alarms, Ian Evans and SLAC/OHP will be called immediately (if not already present) and will decide how to proceed based on surveys of the area. If the loading/storage area CAM alarms or the hutch and plastic enclosure CAM alarm simultaneously, the following procedure will be followed:

1. The area will be evacuated immediately in response to a CAM alarm and personnel will assemble in a designated area. The SLAC Main Control Center (extension 2151, 926-2151 if calling off site), the Fire Department (9-911), and the SSRL Beamline Duty Operator will be notified of the alarm and the status of the neptunium.
2. SLAC/OHP will monitor all people who evacuated into designated areas after establishing controls to prevent inadvertent entry into the affected area. SLAC/OHP and the LBNL experimental team will determine if the LBNL emergency response team is to be called.
3. The LBNL emergency response team, if called, will evaluate the situation and perform appropriate decontamination procedures as needed.

6.4.3 Response to fire in the experimental area

Minor fire

Extinguish using available extinguishers. Close shutters, turn off high voltage power to ion chambers, fluorescence detector and DC power to optical bench and AC sample positioner stepping motors and Lytle detector. Leave all radiation monitoring equipment on. Contact the SLAC Main Control Center (extension 2151, 926-2151 if off site), the Fire Department (9-911), the SSRL Beamline Duty Operator and the Emergency Response Team and inform them of the fire and the status of the neptunium.

Major fire

Evacuate area immediately. Activate fire alarm. Report to the designated area. Contact the SLAC Main Control Center (extension 2151, 926-2151 if off site), the Fire Department (9-911), the SSRL Beamline Duty Operator and the Emergency Response Team and inform them of the fire and the status of the neptunium.

6.4.4 Response to fire alarm outside of the experimental area

Close shutters, turn off high voltage power to ion chambers, fluorescence detector and DC power to optical bench and AC sample positioner stepping motors and Lytle detector. Leave all radiation monitoring equipment on. Report at the designated area. Inform the SLAC Main Control Center (extension 2151, 926-2151 if off site), the Fire Department (9-911), the SSRL Beamline Duty Operator and the Emergency Response Team of the status of the neptunium.

6.4.5 Response to flooding or earthquake

Turn off high voltage power to ion chambers, fluorescence detector and DC power to optical bench and AC sample positioner stepping motors and Lytle detector. Leave all radiation monitoring equipment on. Inform the SLAC Main Control Center (extension 2151, 926-2151 if off site), the Fire Department (9-911), the SSRL Beamline Duty Operator and the Emergency Response Team of the status of the neptunium. If necessary, evacuate the building and follow standard SLAC/SSRL procedures.

6.4.6 Response to theft and vandalism

In the event that a sample is taken or is found to be missing, or if it appears that unauthorised entry into the loading/storage area or the sample storage containers has been performed or attempted, SLAC Security will be notified immediately by calling extension 2551 (926-2551 if off site).

7.0 Radiation protection and training

The proposed XAFS experiments to be performed at the Stanford Synchrotron Radiation Laboratory will be subject to the requirements and controls of the SLAC/SSRL radiation protection programme. The sample materials proposed for these experiments pose an additional set of radiological considerations. SLAC/SSRL and LBNL will provide programmatic, procedural, and personnel support to address any considerations unique to neptunium, plutonium, or actinides, as a class.

Certification of training

Training records of the LBNL Experimental Team certifying their expertise in handling radioactive materials will be provided to the health physics staff at SLAC prior to the arrival of the sample materials at SLAC/SSRL.

8.0 Restrictions and limitations

8.1 Material quantity limits

The quantities of material contained in any sample cell, as well as the total inventory of all sample materials for these experiments shall not exceed those quantities stated in Section 3, "Description of Experiments."

8.2 Storage restrictions

Samples will be sealed into the sample cell, and the secondary and tertiary sample containers at LBNL, and these seals will be left intact at all times until their return to LBNL. Any samples not in use will be stored in a sealed 55 gallon drum (solution and liquid samples must be transferred from their type A shipping container). The area, or room, containing the shipping containers will be kept locked at all times except when samples are being handled in that area. This area, or room, will be selected jointly with SLAC Health Physics and SSRL staff, and will be prepared to serve as another barrier during loading or unloading operations. The samples that have been used in the previous run will be removed and placed back into the storage container before the new samples are loaded. Only those samples that will be loaded into the beamline containment cell to be used in the next run or in the reference containment cell will be removed from the shipping container. *One of the experimenters with Radiation Worker I certification will be in attendance at the experimental area at all times when samples are in place.*

8.3 Limit on number of samples in use

Only one beamline sample containment cell (holding up to ten individual Np samples) and one beamline reference sample containment cell (containing one Np reference sample) will be outside the actinide storage area and in use at any time. The number of samples and the total quantity of transuranic elements in the quaternary sample containment vessel and in the reference sample container are listed in Section 3.

8.4 No detectable levels of contamination

The baseline for no detectable levels of contamination will be established by surveying the storage and experimental areas prior to the arrival of the samples. This survey will be performed with SLAC Health Physics to certify and verify any existing contamination prior to the experiment.

8.5 Accountability and ownership

Because the total amount of material is less than 50 g, the samples are Category 4 and will be classified as "LBNL Projects," so that LBNL will be accountable during the entire time they are off site. The materials will be logged in at SLAC and carried on SLAC's records indicating ownership as "LBNL Projects." SLAC will remove the materials from its inventory upon shipment back to LBNL. While at SLAC/SSRL, the materials will be owned by LBNL but SLAC/SSRL will be responsible for providing protection of the materials while they are on the SLAC/SSRL site. As part of the accountability procedures, the location and disposition of the samples while at SLAC/SSRL will be recorded in a log book.

9.0 Appendix

Memorandum listing appropriate emergency Response Team personnel.

**THE RADIOCHEMISTRY EXPERIMENTAL
STATION AT THE ROSSENDORF BEAMLIN**

**Harald Funke, Tobias Reich, Gert Bernhard, Vinzenz Brendler, Jürgen Claussner,
Gudrun Hüttig, Wolfgang Matz, Wolfgang Neumann, Winfried Oehme**
Forschungszentrum Rossendorf e.V., Dresden, Germany

Abstract

The radiochemistry experimental station at the Rossendorf beamline has been designed to perform a variety of X-ray absorption spectroscopy experiments on radionuclides. The safety system is a necessary and independent part of the radiochemistry station at the beamline. This paper describes the scientific possibilities provided by the beamline and the special features of the safety system.

Introduction

X-ray absorption spectroscopy (XAS) investigations on radionuclides are becoming increasingly important in many fields of radioecology. Environmental contaminations of radionuclides are manifold, and are mainly due to uranium mining and processing, nuclear weapons production and testing and nuclear reactor accidents. Further potential sources for radionuclide releases are proposed geologic high-level radioactive waste repositories as well as the storage and disposal of uranium and plutonium from weapons dismantlement. It is important to understand the chemical behaviour and forms of radionuclides under environmental conditions in order to design methods for the clean-up of contaminated sites, predict the transport behaviour in the environment and perform safety assessment studies for nuclear waste repositories.

A large part of the investigations performed on the Rossendorf Beamline (ROBL) will concentrate on the significant environmental contaminations of uranium which were caused by more than 40 years of uranium mining in Saxony in the eastern part of Germany. The contaminations are due to flooding of uranium mines, seepage waters from a large number of mine tailing piles and significant seepage from mill tailing ponds.

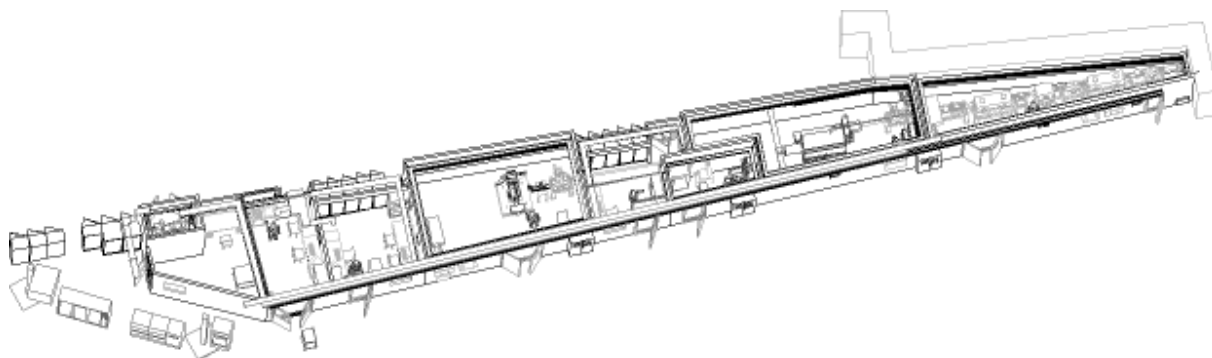
The Rossendorf Beamline

The Rossendorf Beamline is a collaborating research group (CRG) beamline at the European Synchrotron Radiation Facility (ESRF). ROBL has been designed for performing experiments on two different experimental stations located in lead shielded hutches: a radiochemistry hutch (RCH) and a materials research hutch (MRH). The main experimental technique in RCH is X-ray absorption spectroscopy, while in MRH it is X-ray diffraction and reflectometry. Both end stations operate alternatively (see Figure 1). The beamline was built and is operated by the Forschungszentrum Rossendorf (FZR) located near Dresden.

Most of the beamtime will be used for in-house research of the FZR. However, the beamline is also available for external groups to perform experiments either by collaborating with FZR or by submitting a proposal to the ESRF which receives 1/3 of the beamtime.

Figure 1. Layout of ROBL

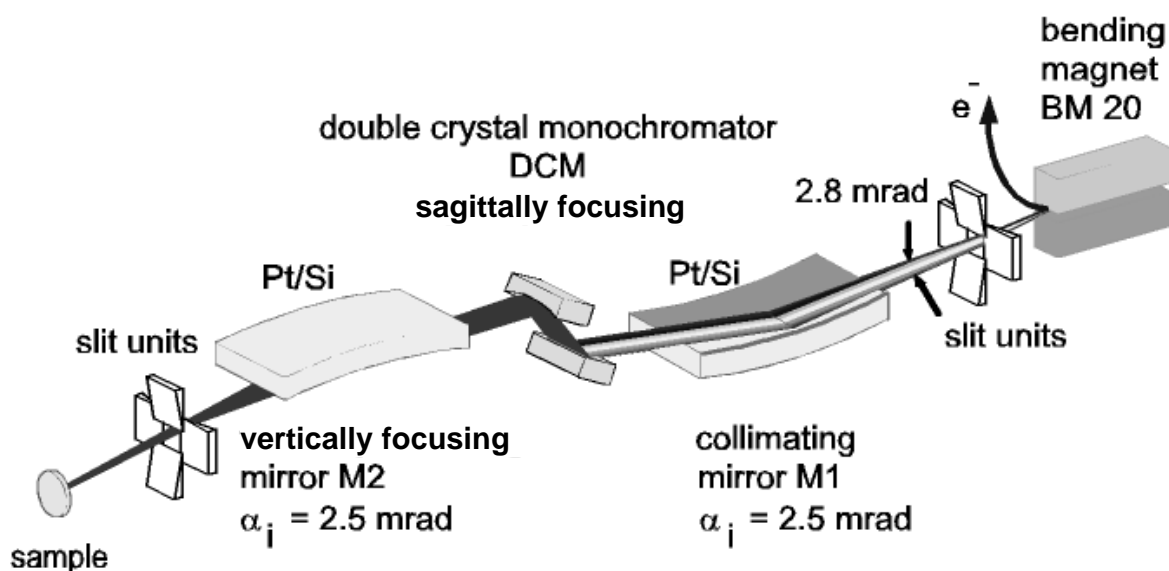
The optics in the first hutch deliver monochromatic radiation alternatively either to the radiochemistry or the materials research hutches. Three cabins are available for beamline and experiments control as well as for a workshop.



Beamline optics

ROBL is located at the bending magnet port BM 20 of the ESRF. The beamline optics allows investigations in the energy range of 5-35 keV. The general concept for the optics consists of a double crystal monochromator of fixed-exit type located between two mirrors (see Figure 2).

Figure 2. Scheme of the X-ray optics of ROBL



The two-mirror design with the same fixed incident angle for both mirrors was adopted in order to suppress the higher-order contamination in the monochromatic beam, to reduce monochromator heat load and to have a collimated beam at the first crystal and a vertically focused beam at the experimental stations.

The double crystal monochromator of fixed-exit type with a beam offset of 18 mm operates with either Si(311) or Si(111) crystals. The maximum photon energy transmitted by the Si(111) and Si(311) crystals is 25 and 35 keV, respectively. In the future the second (Si(311)) crystal will be equipped with a bender to permit sagittally focusing. For Quick-EXAFS, with a fixing of the second crystal a pseudo channel-cut mode of the monochromator can be realised. The beam height variation during a 500 eV scan in the pseudo channel-cut mode becomes less than 0.6 mm for energies above 14 keV.

The radiochemistry experimental station

The radiochemical end station has been designed for X-ray absorption spectroscopy of solid and liquid samples containing the most stable isotopes of the following radioactive elements: Tc, Po, Ra, Th, Pa, U, Np, Pu, and Am. Their absorption edges to perform EXAFS spectroscopy are in the energy range of 13.8-21 keV. Therefore, concentrated samples can be measured in transmission. Environmental samples often contain the radionuclide at low concentrations. The XAS spectra of these samples have to be recorded in fluorescence mode. The anticipated capabilities of the radiochemistry end station can be summarised as follows: XANES and EXAFS spectroscopy between 5-35 keV; spectrum measurement in transmission or fluorescence modes; sample temperature control between 15-295 K; remote control of sample positioning; time-resolved XAFS measurements (Quick-EXAFS); spatially resolved XAFS using a focused beam.

For the measurements the following equipment is available: gas ionisation chambers of various lengths (OHYOYO KOKEN KOGYO); four pixel Ge solid state fluorescence detectors (Lawrence Berkeley National Laboratory); fluorescence X-ray ion chamber detector (Lytle detector, EXAFS Company); closed-cycle He cryostat (Oxford Instruments); various remote controlled sample positioners (FZR).

Radionuclides

The scientific possibilities (and the safety regulations) in the RCH are determined and limited by the allowed radionuclides. These are the actinides ^{nat}Th , ^{231}Pa , ^{nat}U , ^{237}Np , ^{239}Pu , ^{242}Pu , ^{241}Am , ^{243}Am as well as ^{226}Ra , ^{208}Po , ^{209}Po and ^{99}Tc with a maximal equivalent activity of 185 MBq (5 mCi) for all samples at the same time (see Table 1).

Table 1. Table of the nuclides with the maximal allowed amounts of activity and the equivalent mass per sample [2]

Nuclide	Half time [year]	Activity (max.) [Bq]	Mass [g]
^{237}Np	2.10E+06	1.85E+08	6.97E+00
^{241}Am	433	1.85E+08	1.40E-03
^{243}Am	7 370	1.85E+08	2.50E-02
^{208}Po	2.9	1.85E+08	8.00E-06
^{209}Po	103	1.85E+08	3.01E-04
^{231}Pa	3.28E+04	1.85E+08	1.06E-01
^{239}Pu	2.40E+04	1.85E+08	8.00E-02
^{242}Pu	3.75E+05	1.85E+08	1.27E+00
^{99}Tc	2.10E+05	1.85E+10	2.91E+01
^{226}Ra	1 600	1.85E+08	5.00E-03
^{nat}U	4.47E+09	1.24E+07	1.00E+03
^{nat}Th	1.40E+10	4.06E+06	1.00E+03

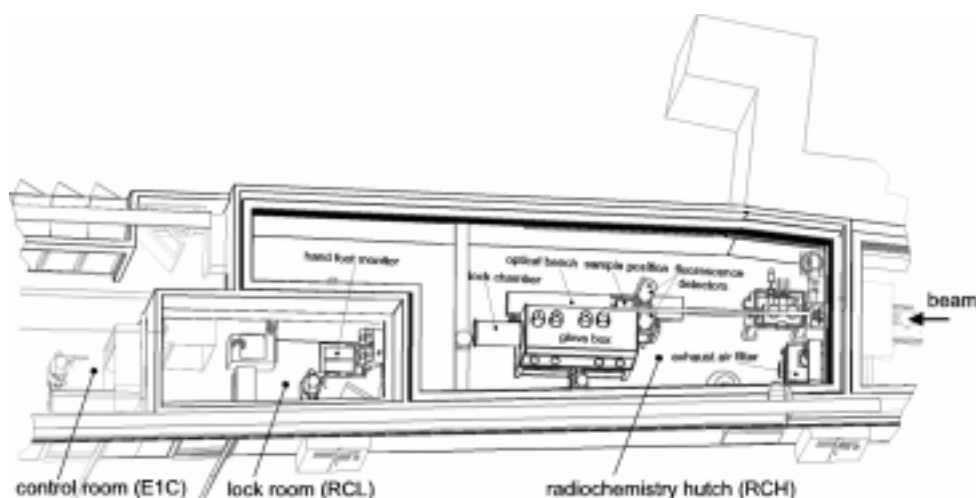
These elements do not have stable isotopes which could be used for equivalent chemical studies. As far as possible the isotopes with the largest lifetime – meaning with the lowest radioactivity – of these elements are chosen. While the knowledge of the chemical and structural state of the actinides, radium and polonium on molecular level is of environmental importance, the technetium-99m is the key nuclide for medical research.

Description of the construction

According to the safety requirements, the radioactive samples are positioned inside a glove box (Mbraun, FZR). The glove box is equipped with five 125 μm thick polyimide windows which are transparent to the incoming and transmitted X-ray beams and the fluorescence radiation. All detectors, e.g. gas ionisation chambers and fluorescence detectors, are mounted on an optical bench outside the glove box. This arrangement allows a direct and easy access to the detectors (see Figure 3).

Inside the glove box three different remote controlled sample positioners can be used depending on the sample geometry and type of experiment. The first sample positioner can hold up to eight solid and/or liquid samples for transmission and/or fluorescence measurements. With this sample holder it is

Figure 3. Survey of the radiochemistry experimental station



possible to switch automatically from one sample to another without need for the experimenter to enter the radiochemistry hutch. The second sample positioner holds the closed-cycle He cryostat. For measurements of very dilute samples, a third sample holder can incline the sample 45° with respect to the beam between two polyimide windows which are perpendicular to the beam. These windows allow the simultaneous recording of the fluorescence spectrum by two Ge solid state fluorescence detectors. Since the samples are safely contained in the glove box, it is possible to modify the chemical conditions of liquid samples just before or during the XAS measurement by adding non-radioactive substances like acid, base or complexing agents.

For energy calibration purpose, the XAS spectrum of a non-radioactive reference sample is recorded simultaneously with the sample using the gas ionisation chambers or the Lytle detector outside the glove box. The glove box is mounted on a support frame which allows it to be moved in a horizontal direction out of the beam, leaving the position of the optical bench and the detectors unchanged. This has the advantage that non-radioactive samples do not need to be brought into the glove box for XAS measurements since they can easily be mounted on the optical bench outside the glove box.

The radiochemistry safety system at ROBL

The radiochemistry hutch of ROBL is a unique experimental end station for X-ray spectroscopy with radioactive non-sealed samples, including liquids. In addition to the usual X-ray safety regulations for synchrotrons it was necessary to install a safety system, which is in accordance with all legal requirements for a radiochemical laboratory. The installation has to satisfy specific laws and regulations concerning environmental protection, personnel and nuclear safety. In addition, the transport of the samples and the disposal of radioactive waste has to satisfy the corresponding requirements.

The regulations agreed upon ESRF (see also [1]) are documented in the “Declaration of the ROBL Project” and must be confirmed and controlled by the French authority CIREA [2]. The legal basis for all procedures are the German and French laws on radionuclide laboratories as well as the EURATOM [3] transport and storage regulations. Only specially trained staff is allowed to operate this experimental station.

Principles

The construction of the Radiochemical Safety System (RCSS) is based on the principles of multi-layer containment of the samples and redundancy and automation of all safety components.

The radioactive samples are heat-sealed in X-ray transparent polyethylene foils serving as the first barrier. For the transport these samples are enclosed in a polyethylene “sample container”. Outside the glove box it must always be locked in a “working container” shielded with 1 cm lead walls to absorb all radioactive radiation up to 5 $\mu\text{Sv/h}$. Outside the hall the working container will be transported in certified “transport containers” made of steel. During experiments, the second and third barriers are the glove box and the RCH.

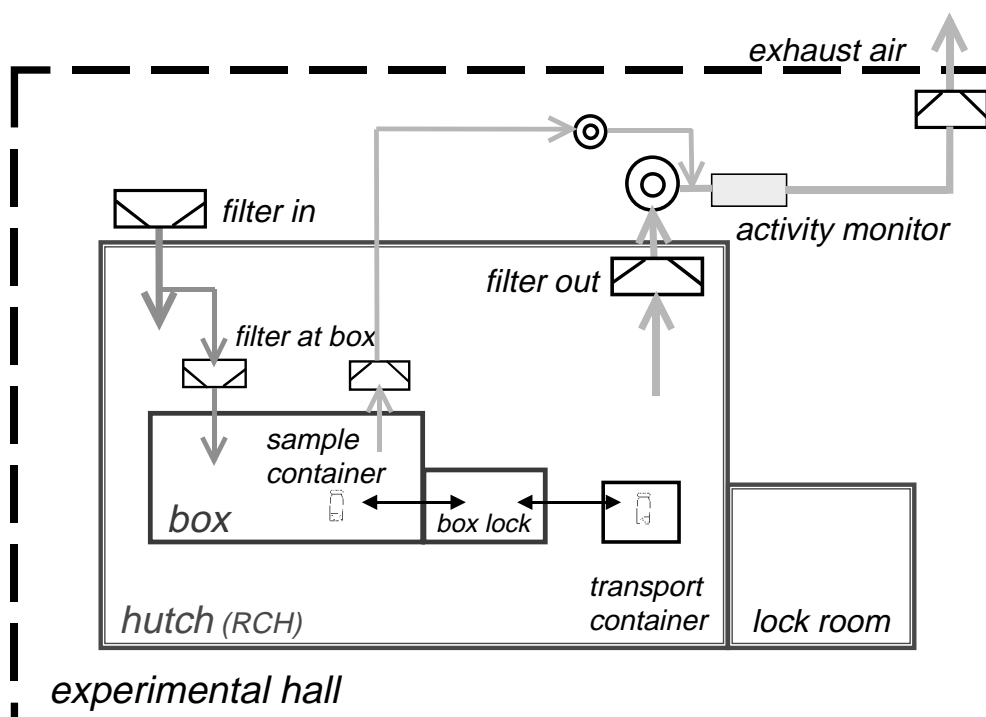
The air tightness of the RCH and the lock room is realised by an inner wall from steel panels, tightened by silicon. The floor is resistant compound filled by a tight epoxy resin layer.

An un-interruptable power supply (UPS) is installed for the ventilation system and the air exhaust monitoring to ensure the system operates well even during a electrical power cut of half an hour. During this time the experiment must be finished and the samples safely stored.

Ventilation

A separate ventilation system (Figure 4) guarantees graduated negative pressure differences between the hall and the RCH of about -10 Pa and between the RCH and the glove box. The negative pressure inside the glove box, where the samples are handled, is -200 Pa. The filtering system for ingoing and outgoing air is equipped with high absorption absolute filters.

Figure 4. Scheme of the safety system of the radiochemistry hutch



The filters and ventilators for RCH and glove box exist in duplicate and work in an automatically controlled redundant regime. In case of a failure of one component, its duplicate will automatically start to fulfil the function of the former one.

Before the air leaves the hall, a final filter is inserted serving as a last barrier to the environment.

Monitoring

The α - β activity and the dose rate in the outgoing air are continuously controlled by an automatic aerosol monitoring system outside the RCH. As a means of registering the radioactive background and all possible deviations from it, 10% of the outgoing air is separated in an isokinetic way. A similar aerosol monitoring device constantly controls the air inside the RCH.

A γ -spectrometer is incorporated in the glove box floor. A γ -spectrum of each sample must be measured to identify the radionuclide and to document its activity.

The radiation monitoring equipment is complemented by a hand-foot monitor in the lock room, movable α - β and dose rate monitors, and a α - β measuring station, e.g. for analysing wipe tests.

Signalisation

All safety-related data are collected in a signalisation system, which optically and acoustically indicates all changes, failures and deviations from standard values of the safety system. The worst case, emergency, means either the exceeding of the radiation limits, failure of the box ventilation or fire. In case of an emergency in the RCH, the signalisation system will cause the beam shutter and the vacuum valves to close via the interlock system of the ESRF.

The combined status signals emergency, failure, warning and maintenance are given for the main components of the RCSS: ventilation, monitoring, count-gas supply and UPS. Signalisation boxes are installed in the control cabin, the RCH and the lock room. They allow a quick overview of the RCSS status.

During the commissioning phase and the first EXAFS experiments with neptunium-237 and technetium-99 samples at the radiochemistry station of ROBL in December 1998, the experimental set-up and the safety system worked as anticipated in their design.

REFERENCES

- [1] P. Berkvens and P. Colomp, this volume.
- [2] ESRF Safety Group, La Ligne de Lumière Rossendorf BM20, Dossier CIREA, Grenoble 1998.
- [3] EURATOM Regulation No. 1493/93.

SAFETY CONSIDERATIONS FOR MEASUREMENTS OF RADIOACTIVE SAMPLES AT THE EUROPEAN SYNCHROTRON RADIATION FACILITY

Paul Berkvens, Patrick Colomp
European Synchrotron Radiation Facility
Grenoble, France

Abstract

The purpose of this paper is to explain to future ESRF users the different safety procedures involved in experiments using radioactive samples. In order to explain the origin of the different safety considerations, a review of the relevant French legal regulations is given, explaining, within this complex legal framework, the situation of the ESRF. Finally a number of practical considerations is given for users wishing to perform an experiment at the ESRF using radioactive samples.

Introduction

The number of users wishing to carry out experiments at the ESRF using radioactive samples is steadily increasing and will certainly continue to do so in the future, especially with the radiochemistry station at the ROBL beamline having been put into operation recently. It is therefore useful to give a review of the different safety procedures at the ESRF dealing with these experiments. A short review of the relevant French legal regulations is also given. Since, in principle, in these matters French law simply transcribes Euratom regulations, the same legal obligations should be found in other European member states.

French and European laws dealing with radioactive material

Introduction

The ESRF is a private company and is subject to French law. On matters dealing with radioactive material French law incorporates the different European regulations (Euratom), valid in all member states of the European Community. Different laws and regulations must be fulfilled, each of them dealing with a specific aspect: personnel safety, control of the movement and detention of radioactive material, environmental safety and nuclear safety. In the following paragraphs we treat each of these individual aspects.

Personnel safety

The general radiation protection rules applicable at the ESRF are defined in French law in the decree no. 86-1103 (02/10/86, modified by decree no. 88-662 and decree no. 91-963) [1].

This decree defines the classification of workers (exposed versus non-exposed workers), defines maximum annual exposure limits for the different categories, defines general operational rules, as well as administrative and medical rules. A special chapter deals with specific rules for the use of non-sealed sources (ex.: radioactive samples).

This decree will be modified at the latest in May 2000, as stipulated by the European Directive 96/29/EURATOM (13/05/96) [2]. In particular the annual dose limits for non-exposed workers will be reduced by a factor of 5 to give the following annual limits:

- Effective dose: 1 mSv/year.
- Equivalent dose to crystalline lens: 15 mSv/year.
- Equivalent dose to skin (any part of skin): 50 mSv/year.

Furthermore, the neutron quality factors must be multiplied by 2 with respect to the present values (from 10 to 20 for neutrons of unknown energy). Finally the ways to calculate exposure due to ingestion or inhalation are modified with respect to the present calculations based on annual limits on intake (ALI).

Control of movement and detention of radioactive material

As a general rule, the use of radioactive material (sources, samples,...) requires an explicit authorisation from the authorities if the following activities are exceeded:

- Radioisotopes of very high radiotoxicity (Group 1): 5 kBq.
- Radioisotopes of high radiotoxicity (Group 2): 50 kBq.
- Radioisotopes of moderate radiotoxicity (Group 3): 500 kBq.
- Radioisotopes of slight radiotoxicity (Group 4): 5 MBq.

In France the authority concerned is the Commission Interministérielle des Radioéléments Artificiels (CIREA).

Apart from the authorisation to use radioactive materials, the corresponding legal texts also define the French and European rules to be applied for the transfer of radioactive material between different sites. The following rules apply to bring radioactive samples (non-sealed sources) to or remove from an installation in France (e.g. the ESRF):

- 1) For samples arriving from another institute within France, the official CIREA document “Demande de fourniture en radioéléments artificiels en sources non-scellées” has to be filled out. Once an experiment has been accepted, the ESRF Radiation Protection Group sends this document to the institute who will bring the samples to the ESRF. The latter completes the form and returns it to the ESRF, who sends it to the CIREA. Only then can the radioactive samples be sent to the ESRF.
- 2) For samples arriving from an institute within a different country of the European Community, the rules to apply are defined in the Euratom Regulation no. 1493/93, which states that an institute that sends radioactive samples to an institute belonging to another member state must send to the authorities concerned of the destination country (CIREA for France), a three-monthly account, detailing all transfers to this country. In practice this means that European institutes outside France must communicate every three months to the CIREA the details of all transfers to the ESRF, and vice versa the ESRF must communicate to the authorities concerned of the home institute the details of all samples returned to the home institute. On top of this, the CIREA insists that the ESRF informs them beforehand of all radioactive samples arriving at the ESRF, in a similar way as described under 1) above.
- 3) For samples arriving from a country outside the European Community, a form dealing with the import and export of radioactive material has to be filled out. Before a sample can be shipped to the ESRF, the ESRF Safety Group fills out the form “Demande d’importation de radioéléments artificiels” and sends it to the CIREA for approval. Upon return from the CIREA, this document is sent to the institute who must attach the document with the samples. Without this document no clearance at the French customs will be obtained. A similar procedure is applied for the return of the samples. The document “Demande d’exportation de radioéléments artificiels” duly filled out by the ESRF Safety Group and signed by the CIREA is attached to samples to get the necessary clearance at the French customs. The home institute must provide the necessary documents to fulfil all legal obligations upon receipt in their home country. Note that there is no free limit in this case.

Environmental safety

Installations where radioactive material is used are subject to French environmental laws, as they are considered to be “Installation Classée pour la Protection de l’Environnement”(ICPE). The French authority concerned is the Direction Régionale de l’Industrie, de la Recherche et de l’Environnement (DRIRE). An ICPE can be subject to declaration or to authorisation, depending on the total equivalent activity present at a given time on site, as shown in the table below (for non-sealed sources).

Group of radiotoxicity	Declaration	Authorisation
Group 1	Between 3.7 MBq and 370 MBq	Between 370 MBq and 3.7 TBq
Group 2	Between 37 MBq and 3.7 GBq	Between 3.7 GBq and 37 TBq
Group 3	Between 37 MBq and 3.7 GBq	Between 3.7 GBq and 37 TBq
Group 4	Between 370 MBq and 37 GBq	Between 37 GBq and 370 TBq

Above the ICPE authorisation regime the site becomes a nuclear installation (INB, installation nucléaire de base).

If at a given installation, radioisotopes belonging to a different radiotoxicity group are used, one must calculate the equivalent activity A defined as:

$$A = a1 + \frac{a2 + a3}{10} + \frac{a4}{100}$$

with: a1: Total activity of radioisotopes belonging to Group 1.
a2: Total activity of radioisotopes belonging to Group 2.
a3: Total activity of radioisotopes belonging to Group 3.
a4: Total activity of radioisotopes belonging to Group 4.

The limits for Group 1 in the table above, applied to this equivalent activity A, determine the ICPE classification.

If on a given site, apart from non-sealed sources (e.g. radioactive samples), sealed sources (e.g. calibration sources) are also used or if a dedicated storage room for radioactive material is present, the limits for Group 1 in the above table must be applied to the total equivalent activity Q, defined as:

$$Q = A10 + \frac{A11}{10} + \frac{A20}{100}$$

with: A10: Total activity of radioactive material used, in the form of non-sealed sources.
A11: Total activity of radioactive material stored, in the form of non-sealed sources.
A20: Total activity of radioactive material used or stored, in the form of sealed sources.

Use of nuclear material

The following radioisotopes are classified as “nuclear material” because of their strategic importance: plutonium, uranium, thorium, deuterium and tritium.

The French authority concerned is the Institut de Protection et de Sûreté Nucléaire (IPSN). An installation can be subject to declaration or to authorisation, depending on the total activity imported or exported during 12 consecutive months. The corresponding limits are given in the table below.

Radioisotope	Declaration	Authorisation
Pu (all isotopes); ^{233}U	Between 1 g and 3 g	Above 3 g
U enriched = 20% ^{235}U	Between 1 g and 15 g ^{235}U	Above 15 g ^{235}U
U enriched < 20% ^{235}U	Between 1 g and 250 g ^{235}U	Above 250 g ^{235}U
U: natural or depleted in ^{235}U ; Th (all isotopes)	Between 1 kg and 500 kg	Above 500 kg
Deuterium	Between 1 kg and 200 kg	Above 200 kg
Tritium	Between 0.01 g and 2 g	Above 2 g
Lithium enriched in ^6Li	Between 1 g and 1 kg ^6Li	Above 1 kg ^6Li

Situation of the ESRF with respect to the different legal frameworks

The situation of the ESRF with respect to the different laws mentioned above is the following.

As regards personnel safety, nobody at the ESRF is considered to be a radiation worker. This concerns ESRF staff, external users and outside companies. This implies that the limits for the public must be respected at the ESRF. The ESRF is moving toward compliance with the new limits, which will become mandatory from the year 2000 onwards, and has fixed its own deadline of mid-1999.

The Experimental Hall at the ESRF is thus not a “supervised area” as defined by the law, but is a “limited access area”. Authorised people must have followed the necessary safety training. Beamlines where radioactive samples are used are also limited access areas. The access is limited to a small number of people. Apart from the general safety information, these people must be familiar with the specific safety rules and emergency procedures that have been defined and approved for the given experiment.

The respect of these limits, in case of experiments with radioactive samples is guaranteed by the double confinements and experimental protocols concerning exposure due to internal or external contamination, and by shielding of the sample if necessary concerning exposure due to external radiation.

Concerning CIREA-related matters, at present the following authorisations have been obtained at the ESRF:

- 1) General authorisation to use radioactive material in the form of sealed sources at the ESRF, for a total equivalent activity Q of 81.4 MBq.
- 2) Authorisation to use the following isotopes on the BM20 beamline (ROBL), limited to a total equivalent activity Q of 185 MBq:



The total equivalent activity of 185 MBq corresponds to the maximum activity present at the beamline at one time, the activity per individual sample being much smaller. The total equivalent activity for ROBL was set at 185 MBq to be sure not to exceed the 370 MBq equivalent activity limit for the entire ESRF (ICPE under declaration), thereby leaving a sufficient margin for future non-ROBL activities at the ESRF.

The use of both solid and liquid samples is allowed under well-defined experimental procedures, including a precise definition of sample holders. No sample preparation is allowed on the beamline, except dilution of liquid samples under a precisely defined protocol. Cooling to cryogenic temperatures is allowed for solid samples.

- 3) Authorisation to use ^{237}Np samples on ID20 beamline (magnetic scattering), under certain well-defined experimental conditions, including the use of a cryostat. The sample arrives at the ESRF pre-mounted in the cryostat. The total activity is limited to 200 kBq (approximately 30 kBq per sample).
- 4) Authorisation to carry out high-pressure experiments on the ID30 beamline (high pressure) for the following isotopes: ^{239}Pu (total activity: 250 kBq), ^{243}Am (total activity: 750 kBq), ^{248}Cm (total activity: 20 kBq), ^{237}Np (total activity: 5 kBq). The activity per sample is limited typically to a few kBq. The authorised experimental protocols include precise details on the high-pressure cells and the extra confinements provided around these cells.

Experiments on natural or depleted uranium samples can be authorised on all beamlines. On beamlines other than BM20, only solid samples are allowed. No sample preparation will be allowed at the ESRF, particularly for powder samples.

Concerning the ICPE legislation, the entire ESRF site is an ICPE under declaration as regards the use of sealed sources. This concerns the different calibration sources and the priming sources inside the different radiation monitors. The ROBL beamline is an ICPE under declaration for the use of non-sealed sources. In order to guarantee that the total equivalent activity Q for the entire ESRF site remains below 370 MBq, the total allowed activity on the ROBL beamline is limited to an equivalent activity Q of 185 MBq. The total activity of radioactive samples used on beamlines other than BM20 must be well below the ICPE limit. In the internal ESRF safety rules we have set the absolute maximum limit for the equivalent activity used on one beamline to one tenth of the ICPE lower limit, which is a value of 370 kBq (see also next paragraph). The correct scheduling of the different experiments must guarantee that at no time the 370 MBq limit for the entire ESRF site is exceeded.

Finally concerning the regulations dealing with nuclear material, at present the ESRF is registered under the regime of declaration for the following isotopes: plutonium, natural or depleted uranium, natural or depleted thorium. This means that the total amount of material imported to or exported from the ESRF site during twelve consecutive months must not exceed:

- Plutonium (sum of all isotopes): 3 g.
- Uranium (total weight): 500 kg.
- Thorium (total weight): 500 kg.

Whereas the limits for uranium and thorium do not present a practical limitation, the limit for plutonium may be tight. In this context, priority in the planning of experiments will be given to the ROBL beamline.

Practical rules at the ESRF concerning experiments with radioactive samples

General considerations

The transport of all radioactive samples to and from the ESRF must respect the international transport rules for dangerous goods, Class 7: radioactive material. The ESRF Safety Group can organise the return transport upon request of the user. The charges are for the user, and the choice of the transport company is made by the ESRF. All samples must be sent to the ESRF Safety Group. Together with the samples the following documents are required:

- Description of the samples (mass, activity, isotope composition).
- Certificate of non-contamination.
- Gamma spectroscopy of the samples (except for pure α or pure β emitters).

Failure to provide any of these documents may result in the refusal of the experiment.

All experiments using radioactive samples other than natural or depleted uranium will be “red” experiments, which implies that during the experiment at least one person must be present on the beamline 24h/24h. Access to the experimental hutch requires the presence of at least two people.

Experiments involving natural or depleted uranium or thorium

Experiments using natural or depleted uranium or thorium generally do not present particular radiation protection safety hazards. These experiments can in principle be carried out at any beamline. Only solid samples are allowed (except for beamline BM20). In the case of powder samples the sample conditioning must guarantee the absence of any risk of deterioration of the sample.

All samples must be reported to the ESRF Safety Group, respecting the general rules explained in the paragraph above.

Experiments with radioactive samples on BM20 (ROBL)

The authorisation from the CIREA (based on the declaration to the DRIRE) concerning experiments with radioactive samples on the ROBL beamline defines in great detail the experimental conditions to be used on this beamline. It is therefore advisable that users intending to carry out experiments at this beamline contact the ROBL team beforehand to make sure that the proposed experiment satisfies the accepted experimental protocols.

Any experiment not covered by the present authorisation has to be discussed between ROBL and the ESRF Safety Group, and the necessary steps towards the authorities concerned (DRIRE, CIREA) have to be undertaken. In this case a minimum delay of six months should be foreseen.

Experiments with radioactive samples other than U or Th on beamlines other than BM20

As mentioned above, only a limited number of experiments involving radioactive samples have been authorised at the ESRF on beamlines other than BM20. Experiments using the same radionuclides and using exactly the same experimental set-ups can be repeated in the future. The required authorisation from the authorities concerned will be obtained automatically upon simple request.

Any new experiment must be submitted to the ESRF Safety Group (using the standard “Request for beamtime at the ESRF” procedure). The proposal must give full details of the samples (mass and activity per sample, isotope composition of each sample, physico-chemical form, total number of samples). The conditioning of the samples must be given, explaining how a double confinement is obtained, the sample environment must be explained (cryostat, high-pressure,...).

The total allowed activity per sample will be defined by the ESRF Safety Group, depending on the above details. As a general indication the activity of a sample should not exceed the free handling activity $A_{volatile}$ as defined in [3]:

$$A_{volatile} = 10^{-2} ALI_{inhalation} / k$$

with $k = 1 \cdot 10^{-5}$ for solids [4].

As an example, the limit for a ^{239}Pu sample ($ALI_{inhalation, 1 \text{ mSv}} = 21.5 \text{ Bq}$ [3]) would thus be 21.5 kBq. This value can be increased by the ESRF Safety Group, to take into account the special confinement guarantees provided by the sample holder (e.g. high-pressure diamond cell). Under no conditions however can the activity per sample exceed one-tenth of the lower ICPE limit (= 3 700/10 = 370 kBq equivalent activity). The total activity of all the samples used during a given experiment (one sample at a time at the beamline) shall not exceed half of the lower ICPE limit, i.e. 1.85 MBq equivalent activity.

For some experiments the ESRF Safety Group may impose a hutch air extraction system equipped with absolute filters. For the time being, apart from BM20, only ID20 and BM28 are equipped with such a system.

Other restrictions on the total activity of a sample can be imposed due to the external radiation limits.

Once an agreement has been obtained between the proposer and the ESRF Safety Group, a safety assessment document has to be written (jointly by the proposer and the ESRF Safety Group) to submit to the CIREA. The contribution from the proposer must include the sections entitled “Justification” and “Experimental Procedure”. The justification aspect is of capital importance to the CIREA. This must incite users to correctly optimise sample size to limit the activity and to guarantee that no non-radioactive sample can replace the proposed active sample.

A minimum of three months must be foreseen between the submission of a new proposal and the authorisation to carry out the experiment.

REFERENCES

- [1] Journal Officiel de la République Française, “Protection contre les rayonnements ionisants”, textes législatifs et réglementaires, ISBN 2-11-073129-X – ISSN 0767-4538.
- [2] Journal Officiel des Communautés Européennes, L159, ISSN 0378-7060 (1996).
- [3] D. Delacroix, *et al.*, “Radionuclide and Radiation Protection Data Handbook 1998”, *Radiation Protection Dosimetry*, Vol. 76, Nos. 1-2, Nuclear Technology Publishing, 1998.
- [4] P. Bory, “La Radioprotection à l’intention des Personnes Compétentes”, partie “Sources non-scélées”, Internal CEA-INSTN-Grenoble publication, no date.

Web link

The web address of Regulation N° 1493/93, which has links to other Euratom web pages including related regulations and other languages, is: http://europa.eu.int/eur-lex/en/lif/dat/en_393R1493.html.

SYNCHROTRON RADIATION FACILITIES TO STUDY RADIOACTIVE MATERIALS AT THE PHOTON FACTORY AND SPRING-8

Shoichi Tachimori

Japan Atomic Energy Research Institute
Tokai-mura, Naka-gun, Ibaraki-ken 319-1195, Japan

Abstract

The two biggest synchrotron radiation (SR) facilities in Japan allow or will allow to treat radioactive materials for experiments. These are the Photon Factory (PF) of the High Energy Accelerator Research Organisation (KEK) in Tsukuba (electron energy ~ 2.5 GeV) and SPring-8 of the Japan Synchrotron Radiation Research Institute (JASRI) in Harima (electron energy ~ 8 GeV), which has just opened its beamlines to users. A brief description will be given about the design of the beamlines and how radioactive materials can be treated at the experimental stations of the Photon Factory and SPring-8.

Introduction

The Photon Factory of KEK started its operation in 1982, and was largely reconstructed in 1997 in order to obtain much lower beam emittance, which was reduced from 130 to 36 nm rad (the available minimum emittance is 27 nm rad). The new PF storage ring was commissioned in October 1997. At the same accelerator complex, a high energy ring – TRISTAN – had been constructed and its programme has been completed. The accumulation ring of TRISTAN has been used as a complementary synchrotron radiation source (~ 6.5 GeV) of PF.

The construction of SPring-8 (Super Photon ring – 8 GeV) of JASRI started in 1991 under the JAERI-RIKEN SPring-8 Project Team and the first synchrotron radiation from the storage ring was achieved in March of 1997. It is planned to install a total of 61 photon beamlines.

The main parameter values of the Photon Factory and SPring-8 are listed in Table 1.

Description

Photon factory [1]

At the Photon Factory, which opens 21 beamlines to world-wide scientists, the construction of a “Hot Sample Area (HSA)” and additional facilities such as a hot laboratory was planned by KEK-PF and JAERI in 1989 for studying actinide and other radioactive materials including uranium and thorium to accept the dipole radiation emitted from a bending magnet on BL-27. The plan view of the Photon Factory and the hot laboratory is shown in Figure 1. The BL-27 system consists of a front end and two branchlines. 27A is a soft X-ray beam line (the energy range of 1.8-6 keV) consisting of two experimental stations dedicated to X-ray photoelectron spectroscopy and radiation biology. 27B (the energy range of 5-24 keV) is equipped with an X-ray diffractometer in an X-ray shielded hutch and apparatus for XAFS studies as well as radiation biology located just upstream from the diffractometer in the same hutch. The experimental apparatuses at the HSA are listed in Table 2.

All the stations are located, along with sample preparation room and a sample stock room, in the HSA. In designing the system, the following conditions were considered:

- 1) Sufficient inspection and protection against an accidental scattering of radioisotopes (RI) both inside and outside of the evacuated beamlines.
- 2) Minimisation of the apparatus dimensions in the HSA which has strong limitations in space and working conditions.
- 3) Versatility of the instrumentation which is not easy to replace.
- 4) Full remote control of equipment for a data acquisition.

For RI inspection/protection, the soft X-ray beamline 27A was especially devised to protect the storage ring from the intrusion of RI, because the vacuum system connects the experimental chambers almost directly to the storage ring. The diffractometer, which was designed on the basis of the conventional six-circle one, is equipped for polarisation (or magnetic scattering) and anomalous scattering experiments (three additional new circles). This machine has thus satisfied the conditions 2), 3) and 4) mentioned above.

The radioactive materials allowed to be used and their maximum amounts licensed at the HSA of the Photon Factory are shown in Table 3.

SPring-8 [2]

At SPring-8, which will have 61 photon beamlines, a soft X-ray undulator beamline (BL23SU) for electron spectroscopy studies of actinide materials, as well as for other application of site-selective photochemical processes of surface molecules or in biological systems has been designed by JAERI. The beamline location was decided based on the following points:

- 1) The experimental station for actinide samples will be placed in a building that is separated from the common experimental hall and will be referred to as HSA.
- 2) The beamline will be equipped with special apparatus to protect the users, the experimental devices and the storage ring from intrusion of RI pollution.
- 3) Monitoring systems for radioactivity inside the evacuated devices will be placed at several points on the beamline.
- 4) To obtain a high resolving power of circularly and linearly polarised soft X-rays at the sample position, the combination of a grating monochrometer and a variably polarising undulator has been chosen.

Future plan

To successfully study the chemistry of actinides, the usage of not only uranium and thorium but also other actinides is a requisite. For this reason the idea of getting the license for the treatment of neptunium and americium at the HSA of the Photon Factory gains significance for the EXAFS study group at JAERI. After modification of EXAFS apparatus and connected instruments, the procedure will start. Based on the experiences at the Photon Factory, the licensing procedure at SPring-8 to have the permission of treatment of radioactive materials at the HSA almost similar amounts to the Photon Factory is supposed to commence in the near future. The experiments with non-radioactive samples at BL23SU will start this year.

REFERENCES

- [1] H. Konishi, *et al.*, *Nuclear Instruments and Methods in Physics Research A* 372, 322 (1996).
- [2] A. Yokoya, *et al.*, *J. of Synchrotron Radiation*, 5, 10 (1998).

Table 1. Main parameters of photon factory and SPring-8

	Photon factory		SPring-8
	PF Ring	TRISTAN A. Ring	
<i>Storage ring</i>			
Energy	2.5 GeV (~3.0)	6.5 GeV	8 GeV
Circumference	187 m	377 m	1 436 m
Critical photon energy	4 keV	26.1 keV	28.9 keV
Radio frequency	500 MHz	508.6 MHz	508.6 MHz
Maximum number of bunches	312	1	2 436
Beam current			
single bunch	65 mA	40 mA (200)	5 mA
multi-bunch	350 mA	20 mA	100 mA
Beam lifetime	60 h (300 mA)	4 h (10)	100 h
Horizontal emittance	27 nm.rad	290 nm.rad	5.66 nm.rad
<i>Injector linac</i>			
Energy	2.5 GeV		1 GeV
Repetition rate	25 Hz		60 Hz
Radio frequency	2 856 MHz		2 856 MHz
Total length	300 m		140 m

Table 2. Experimental apparatuses at hot sample area

Photon Factory

Soft X-Ray (BL-27A) 1.8~6 keV

1) XPS station: surface chemical state analyser

- i) A 50 mm hemispherical analyser for angle-resolved photoemission spectroscopy.
- ii) A double-focusing hemispherical analyser – analysing the X-ray induced desorbed ions.
- iii) Two kinds of sample manipulators.

2) Radiation biology station

Sample irradiation apparatus

In-vacuum type: 10⁻⁵ Pa, beam size: 20mm H × 4mm W

Atmospheric type: through two polyimide windows, beam size: 8mm H × 4mm W

Hard X-Ray (BL-27B) 5~24 keV

HX-Hutch (3.5m H × 3.4m × 2.5m W)

1) Versatile diffractometer

A nine-circle diffractometer for diffuse scattering measurement (single crystal, polycrystal, powdered crystal, amorphous material, liquid under various environments, such as high and low temperatures, high pressure, vacuum circumstances, magnetic field, etc.).

2) XAFS apparatus

(Ti-Rh K-edges and Cs-U L-edges), beam size: 1 mm (H) × 3 mm (W); a sample is sandwiched with two holding plates which have a 10 mm dia. window

3) HX radiation biology apparatus

SPring-8

Heavy Element Science Beamline (BL23SU) 1.8~6 keV

1) Photoelectron spectroscopy (PES)

To clarify the physical properties of actinide compounds (heavy fermion compounds)

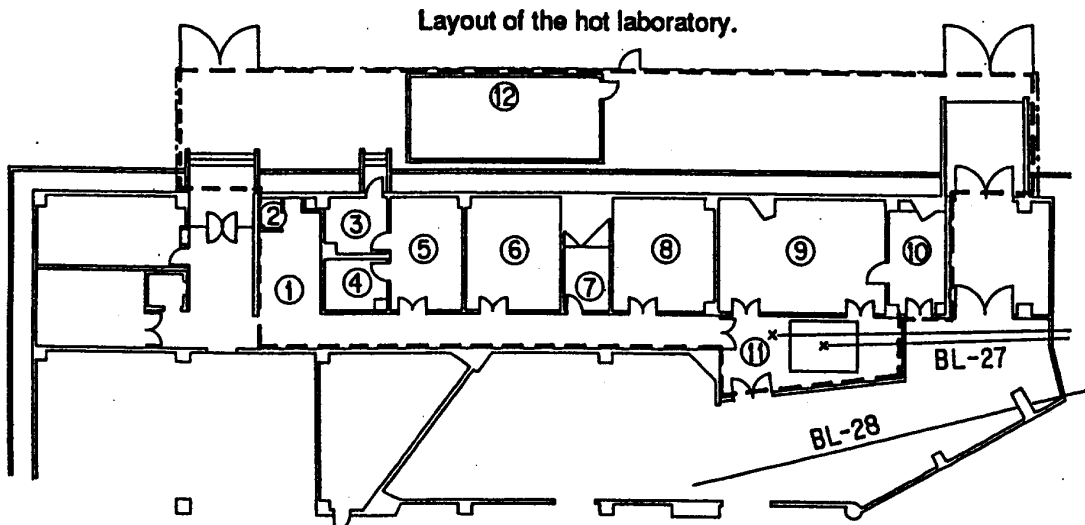
2) Magnetic circular dichroism (MCD)

To clarify magnetic state of ferromagnetic actinide compounds

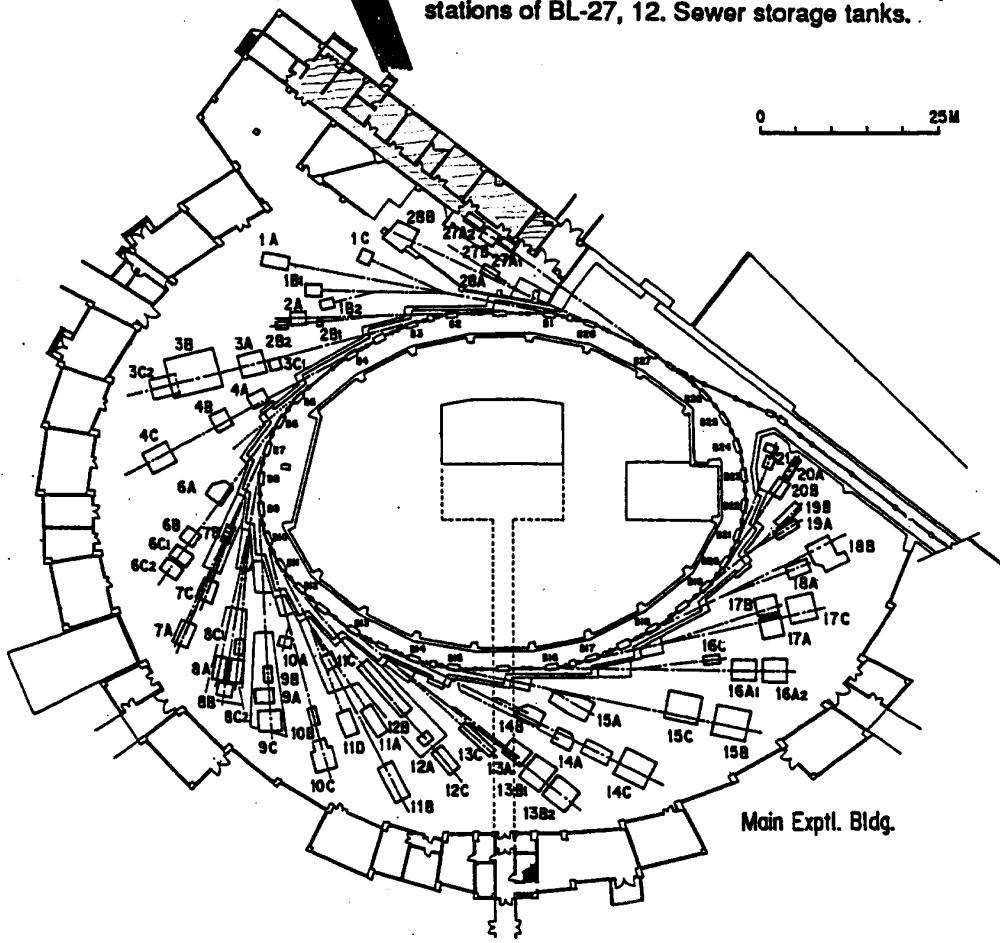
Table 3. Radioactive materials to be used for experiments in hot sample area at photon factory

	A-group materials	B-group materials	C-group materials
Purpose	Radiation biology experiments	Photoelectron spectroscopy, X-ray diffraction, EXAFS	X-ray diffraction, EXAFS, photoelectron spectroscopy
Form in use	Tracers in liquid	Hard solid plate (max. size: 20mm × 20mm × 2mm)	Solid, powder, liquid (completely sealed, leak-tested)
Nuclides	³ H, ¹⁴ C, ³² P, ³⁵ S as organic compounds or inorganic compounds	112 radioisotopes (except ³ H and ³² P) and U, Th, ²² Na, ³² Si, ⁴⁵ Ca, ⁴⁴ Ti, ⁴⁹ V, ⁵⁴ Mn, ⁶⁰ Co, ⁵⁹ Ni, ⁶⁴ Cu, ⁶⁵ Zn, ⁶⁸ Ge, ⁷³ As, ⁸⁵ Sr, ⁸⁸ Y, ⁹⁵ Zr, ⁹⁵ Nb, ⁹⁹ Mo, ⁹⁵ Tc, ¹⁰³ Pd, ¹¹¹ Ag, ¹²¹ Sn, ¹²⁶ Sb, ¹²⁹ Cs, ¹⁴⁷ Nd, ¹⁸⁷ W, ¹⁹¹ Pt, ¹⁹⁸ Au etc.	U, Th
Max. quantity	³² P: 3.7 MBq/day 185 MBq/3 mon. 370 MBq/year Others: 37 MBq/day 1.85 GBq/3 mon. 3.70 GBq/year	Total: 37 MBq/day 1.85 GBq/3 mon. 3.70 GBq/year	5 g/day 200 g/year

Figure 1. Plan view of the photon factory and layout of the hot laboratory with BL-27



1. Gate monitor, 2. Shower for de-contamination, 3, 4, 5. Radioisotope treatment rooms, 6. Culture room for mammalian cells, 7. Radioisotope storage room, 8. Culture room for microorganisms, 9. Analysis room, 10. Radioisotope measurement room, 11. Experimental stations of BL-27, 12. Sewer storage tanks.



ACTINIDE XAS ON D44 AT LURE

C. Den Auwer*, **R. Revel***

CEA Marcoule, DCC/DRRV/SEMP
Laboratoire de Chimie Théorique et Structurale
30207 Bagnols-sur-Cèze, Cedex, France
**LURE associate researcher*

Abstract

The use of synchrotron radiation to probe the structure of 4f-5f systems has been extensive lately. More precisely, XAS has become a major spectroscopic tool to investigate non-isotropic systems, going from solution studies to glass materials. Because of the radiological safety measures that are related to these systems, such experiments are not straightforward.

A set-up that has been developed on beamline D44 at LURE (Laboratoire d'utilisation du rayonnement électromagnétique) will be presented here. Various detection methods will be discussed as well as future cell developments on the beamline.

**RADIONUCLIDE FACILITIES AND EXAMPLES OF WORK
AT THE DARESBUY SYNCHROTRON RADIATION SOURCE**

A.J. Dent

C.L.R.C. Daresbury Laboratory
Daresbury, Warrington, Cheshire WA4 4AD, United Kingdom

Abstract

Station 9.2 and 9.3 are on the wiggler line and hence the L-edges of the actinides are accessible. Fluorescence measurements using a 13-element Ge solid state detector are often used so that the radioactive nuclides can be diluted. Recently commissioned Station 16.5 also offers the possibility of studying very diluted materials (sub-milligram quantities of material), as it offers a focused beam and high countrate 30-element detector. Examples of work studied include uranyl ion sorbed onto mineral surfaces, and investigations of organo-uranium chemistry on meso-porous silicas.

SAFETY CONSIDERATIONS FOR EXPERIMENTS WITH RADIOACTIVE MATERIALS AT THE ADVANCED LIGHT SOURCE

David K. Shuh and K.H. Heinzelman

MS 70A-1150/MS 80-100

Chemical Sciences Division/Environment, Health and Safety Division

Lawrence Berkeley National Laboratory

Berkeley, CA 94720M, USA

Abstract

The actinide surface science community has been unable to take advantage of synchrotron radiation methodologies in the vacuum ultraviolet (VUV) and soft X-ray regions, which revolutionised the approach to surface chemistry/physics over a decade ago, because of radiological safety concerns. These concerns arise from the difficulties of safely handling, preparing and performing measurements with actinide surfaces and materials at VUV/soft X-ray light source end stations that are largely under ultra-high vacuum and share vacuum with the storage ring. The scientific motivation for working in this energy region with actinide materials has been clearly identified by several workshops, some dating back nearly fifteen years. However, safety concerns, which were addressed in many of these same workshops, have severely limited the amount of actinide work done in the VUV/soft X-ray spectral region until now.

The advent of high-brightness, third-generation light sources operating in the VUV/soft X-ray and corresponding improvements in detectors and vacuum technology, have made it possible to perform experiments in this energy region with very small amounts of transuranic material at the advanced light source (ALS). Experimental safety considerations, based on a graded approach to hazard level and the use of actinide micro-samples, have allowed the performance of meaningful investigations. Safety considerations and the implementation of safety measures at the ALS, as well as the rationale behind their development, will be presented. Based on safety considerations and the scientific capabilities of the ALS, future approaches to actinide studies in the VUV/soft X-ray energy region will be discussed.

Acknowledgements

This work is supported by the Director of the US Department of Energy, Energy Research, Office of Basic Energy Sciences, Chemical and Materials Sciences Divisions under Contract No. DE-AC03-76SF00098.

Session IV

POSTER SESSION

X-RAY ABSORPTION SPECTRA IN URANIUM ALLOYS: URANIUM-MOLYBDENUM ALLOYS

Mitsuo Akabori, Akinori Itoh, Yoshihiro Okamoto, Haruhiko Motohashi*, Hideaki Shiwaku

Japan Atomic Energy Research Institute, Tokai-mura, Naka-gun, Ibaraki-ken 319-1195, Japan

*SPring-8 Service Co., Mihara, Mikazuki-cho, Sayo-gun, Hyogo-ken 679-5143, Japan

Abstract

Alloying behaviour among actinides, and between actinides and transition metals, is important to clarify the role of 5f electrons in the alloy systems. The 5f electron nature in actinide compounds is influenced by the ligand. In the Mo-U system, the phase diagram can be characterised by a significant asymmetry in the mutual solubility of these bcc metals: the solid solubility of U in Mo is only a few at%, while Mo is soluble up to ~40 at% in U. One explanation is that the low U solubility in Mo is due to the limited mixing of the U-f state with the Mo-d state. Our previous experimental results in the atomic volumes of U in Mo-U alloys, obtained from X-ray diffraction study, indicated that the valence of U in Mo-U alloys decreases from hexa- to pentavalent with increasing Mo content.

The L₃ edge X-ray absorption spectroscopy is a powerful technique to study the local and electronic structure of actinide compounds. The fluorescence EXAFS is more favourable for the dilute samples because of its large fluorescence yields (~0.5). A fluorescence system with semiconductor detector has been assembled on the BL-27B hard X-ray station of the Photon Factory in the Institute of Materials Structure Science of High Energy Accelerator Research Organisation, Tsukuba, Japan, operating at an energy of 2.5 GeV and an average current 300 mA. In the present study, the X-ray fluorescence excitation spectrum of Mo-diluted U alloy was measured to clarify the electronic structure of U.

The Mo-2w/oU, 83w/oU and 90w/oU alloys prepared by arc-melting and annealing at 1 273 K were measured in the fluorescence and transmission modes. In the fluorescence mode, a pure Ge SSD was placed at the side of a sample cell perpendicular to the beam. The alloy foils were positioned at 30~45° in relation to both the incident X-ray beam and the detector. An ion chamber was also used to measure the intensity of the incident beam.

The U-L₃ X-ray absorption near edge spectra (XANES) of Mo-U alloys were measured and compared with that of UO₂. The observed experimental results in the white-line energies, widths and intensities can be related to the states of 5f electrons. The white-lines for Mo-U alloys were shifted by 3-4 eV to higher energy relative to UO₂, suggesting that U atoms in Mo-U alloys possess higher valency than for UO₂. However, composition dependence of the energy shift was not very clear. Further work is in progress to better characterise the XANES spectra.

PuGa ALLOYS STRUCTURE STUDIED BY X-RAY ABSORPTION SPECTROSCOPY

N. Baclet, D. Bazin

Commissariat à l'Énergie Atomique – Centre de Valduc

21120 Is-sur-Tille, France

Tel: 03 80 23 51 54 • Fax: 03 80 23 52 17

Abstract

Plutonium metal can take six different phases between ambient temperature and its melting point (640°C). Among these, the δ -phase (fcc structure), stable from 320°C to 485°C, can be maintained at room temperature by alloying with a so-called “deltagen” elements such as Ga, Al, Ce, Am. The stabilising mechanisms induced by such additions are however still not well understood. X-ray absorption fine structure spectroscopy (EXAFS) was then investigated in order to study the local environment around Ga and Pu: interatomic distances, neighbouring atoms numbers and disorder. In a previous work [1], EXAFS and X-ray diffraction (XRD) measurements were performed at 300 K on different PuGa alloys stabilised in the δ -phase. Here, measurements were recorded at 80 K, in order to obtain information about the higher co-ordination shells.

Introduction

Plutonium metal can take six different phases between ambient temperature and its melting point (640°C). Among these, the δ -phase (fcc structure), stable from 320°C to 485°C, can be maintained at room temperature by alloying with a so-called “deltagen” elements such as Ga, Al, Ce, Am. The stabilising mechanisms induced by such additions are however still not well understood. X-ray absorption fine structure spectroscopy (EXAFS) was then investigated in order to study the local environment around Ga and Pu: interatomic distances, neighbouring atoms numbers and disorder. In a previous work [1], EXAFS and X-ray diffraction (XRD) measurements were performed at 300 K on different PuGa alloys stabilised in the δ -phase. Here, measurements were recorded at 80 K, in order to obtain information about the higher co-ordination shells.

Experimental details

Samples and confinement

PuGa alloys were elaborated with a Ga content ranging from 1.89 to 10.43 at.%. The PuGa alloys were cast into an arc furnace held at 550°C under argon. The massive samples were then laminated (thickness of about 10-100 μm), and the metallic structure of these strips was restored by a thermal treatment (1 h at 300°C); the oxides present at the surface were removed by electropolishing.

X-ray patterns were recorded in order to verify that the δ -phase existed as a single phase, and to determine the unit cell parameter. For all the alloys studied, it was checked that the martensitic transformation leading to the α' -phase did not occur at 80 K.

The laminated samples were then mounted in a special sample holder and placed in a liquid nitrogen cryostat, ensuring a triple confinement of the samples during X-ray measurements (Figure 1).

EXAFS measurements

EXAFS measurements were performed at the LURE (France) radiation synchrotron facility (DCI storage ring running at 1.85 GeV with a current of 300 mA). Spectra were recorded at the Pu L_{III} edge (18 057 eV) and at the Ga K edge (10 368 eV) in the transmission mode for most of the samples; the fluorescence mode was used to record the spectra at the Ga K edge for low Ga content alloys ([Ga] < 3 at.%).

The extraction of the EXAFS oscillations from the experimental absorption coefficient and the determination of the radial distribution function (i.e. Fourier transform of the EXAFS spectra) were performed according to a procedure detailed elsewhere [1]. The refinement was achieved using the FEFF6 code [2], which was previously validated on a reference sample with a known structure: the definite compound Pu₃Ga [3].

For the spectra recorded at 300 K, the information was limited to the first co-ordination shell around Ga and Pu [1]. Reducing the thermal damping by working at low temperature (80 K) allowed to obtain information about the higher co-ordination shells (second and third shells) at both the Ga and Pu edges (Figure 2).

Results

Multiple scattering

For high symmetrical structures, the possibility of multiple scattering becomes important; if not taken into account, this phenomenon can lead to erroneous interatomic distances R and neighbouring numbers N . The amplitude of the different multiple scattering paths was evaluated with the FEFF6 code (structure of Pu- δ for the Pu L_{III} edge, and a hypothetical cubic structure based on Ga exclusively surrounded by Pu atoms for Ga K edge); the main paths are illustrated in Figure 3. Results from the calculation are presented in Table 1, and show that the multiple scattering has to be taken into account to refine the third peak (R3) of the radial distribution function (distance R3*); this is confirmed by the comparison between the calculation with and without multiple scattering, and the experimental spectra at both the Ga and Pu edges (Figure 4).

Table 1. Relative contribution from the different paths in the PuGa alloys, as calculated with FEFF6 (the Debye-Waller temperature used in the calculation was set to 132 K)

	R (Å)	Path: number of legs	Amplitude
R1	3.27	2	100
R2	4.63	2	20
R2*	4.91	3	6
R3	5.66	2	42
R3*	6.10	3	21

In this paper, results from the refinements of the first (R1) and the second (R2) co-ordination shells are then presented, assuming single scattering.

Interatomic distances around Ga atoms

Whatever the Ga content, Ga-Pu distances are shorter than Pu-Pu distances, which reveals a contraction around Ga atoms. The interatomic distances in the fcc structure can be calculated from the cell parameter deduced with X-ray diffraction; these distances are noted $R_{j_{Ga}}(\text{XRD})$, ($j = 1,2$). Distances refined from EXAFS are noted $R_{j_{Ga}}(\text{EXAFS})$ ($j = 1,2$).

The relative contraction around Ga atoms can then be expressed as:

$$\frac{\Delta R_j}{R_j} = \frac{R_{j_{Ga}}(\text{EXAFS}) - R_j(\text{XRD})}{R_j(\text{XRD})}$$

$\frac{\Delta R_1}{R_1}$ was more representative than $R_{1_{Ga}}(\text{EXAFS})$ since the cell parameter a changed with Ga content. Figure 5 shows a decrease in the relative contraction around Ga atoms with Ga content, which can be explained by an increasing correlation between GaPu_{12} clusters as Ga content increases. Furthermore, the relative contraction for R1 and R2 are rather similar, which reveals that the short-range order around Ga atoms is close to an fcc structure whatever the Ga content studied here.

Interatomic distances around Pu atoms

Assuming that Ga atoms are randomly distributed in the Pu lattice, the number of Ga atoms in the co-ordination shell of Pu can be evaluated, and leads to 1 Ga atom and 1.4 Ga atom for PuGa 7.7 at.% and PuGa 10.43 at.%, respectively, which is in excellent agreement with the neighbouring numbers refined.

As previously discussed [1], the local lattice contraction around Ga atoms leads to bond length variations around Pu atoms, which depend on its proximity to the Ga atoms. The calculation of R1 and R2 was performed for PuGa 6.25 at.% Ga (Ga atoms accommodated in a bcc arrangement with a lattice constant twice that of the original fcc lattice, $R1(\text{XRD}) = 3.24 \text{ \AA}$); the crystallographic structure consisted of two non-equivalent Pu atoms, noted Pu(1) and Pu(2), that corresponded to 80% and 20% of the Pu atoms, respectively. The contraction around Ga atoms was estimated from EXAFS results on PuGa 7at.%; the calculation then gave the following distances around Pu atoms (all distance are expressed in \AA):

- First shell: 1 Ga + 2 Pu (3.18), 2 Pu (3.24) and 7 Pu (3.30) around Pu(1); 4 Pu (3.30) and 8 Pu (3.24) around Pu(2), leading to a mean distance $R1_{\text{mean}} = 3.26 \text{ \AA}$, and $\Delta R1/R1 = +0.6\%$.
- Second shell: 6 Pu (4.67) around Pu(1); 2 Ga + 4 Pu (4.58) around Pu(2), leading to a mean distance $R2_{\text{mean}} = 4.65 \text{ \AA}$, and $\Delta R2/R2 = +1.5\%$.

Ga substitution then appeared to be accompanied by a mean expansion in distances around Pu atoms; this was effectively observed for the different PuGa alloys, for which the higher the Ga content, the higher the expansion (Figure 6). Moreover, the relative expansion strongly increases from R1 to R2, revealing the strong disorder created by Ga substitution in PuGa alloys; this becomes obvious for the PuGa 10.43 at.% for which two distances had to be considered in order to achieve a satisfactory fit of the second co-ordination shell.

Cox, *et al.* studied the PuGa 3.3 at.% alloy [5]. The relative expansion around Pu atoms deduced from this work is in agreement with results from Cox, *et al.* ($\Delta R1/R1 = + 0.9\%$), whereas the contraction observed by these authors around Ga atoms decreased from R1 to R2 ($\Delta R1/R1 = -3.7\%$ and $\Delta R2/R2 = -0.9\%$).

Conclusion

EXAFS measurements recorded at 80 K on several PuGa alloys allowed to follow the changes in the first and second co-ordination shells versus Ga content. The collapse around Ga atoms was confirmed, revealing the hybridisation between Ga $4p^{3/2}$ and Pu $5f^{5/2}$ bands. Moreover, increasing correlations between GaPu_{12} clusters led to a decrease in the relative contraction around Ga atoms, as Ga content increased. For all the alloys studied, the environment around Ga atoms was close to an fcc arrangement, whereas the disorder around Pu atoms increased with Ga content.

The study of the evolution in the XANES spectra versus Ga content, at both Ga K edge and Pu (L,M) edges is planned to get more precious information concerning the changes in the electronic configurations of Pu and Ga atoms versus Ga content. Moreover, anomalous diffraction experiments will be performed in order to get information about higher co-ordination shells, without the problem of multiple scattering.

REFERENCES

- [1] Ph. Faure, B. Deslandes, D. Bazin, C. Tailland, R. Doukhan, J.M. Fournier and A. Falanga, *J. Alloys Comp.*, 244 (1996), p. 131.
- [2] J.J. Rehr and R.C. Albers, *Phys. Rev.*, B, 41 (1990), p. 8149.
- [3] F.H. Ellinger, C.C. Land and V.O. Struebing, *J. Nucl. Mater.*, 12 (2) (1964), p. 226.
- [4] A.C. Lawson, J.A. Goldstone, B. Cort, R.I. Sheldon and E.M. Foltyn, *J. Alloys Comp.*, 426 (1994), p. 213.
- [5] L.E. Cox, R. Martinez, S.D. Conradson and P.G. Allen, *Phys. Rev. B*, 51 (1995), p. 751.

Figure 1. Description of the sample triple confinement

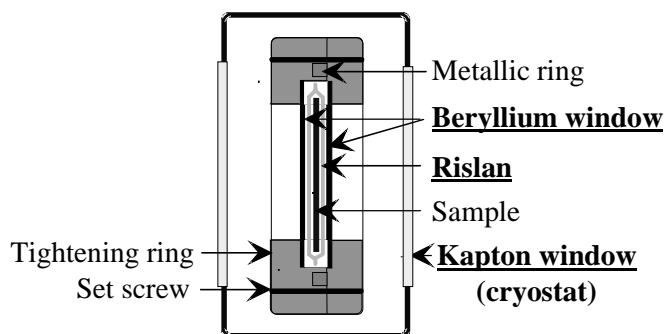


Figure 2. The effect of low temperature on the thermal damping (Pu L_{III} edge)

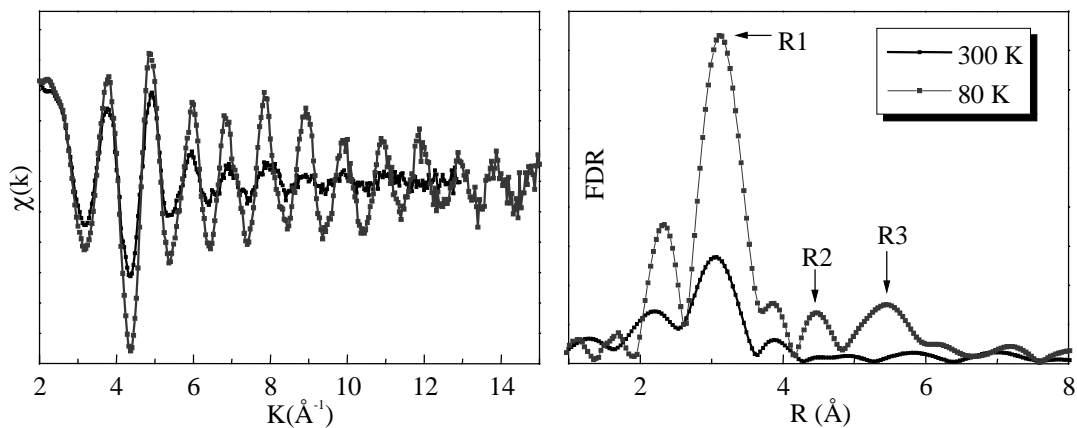


Figure 3. Single and multiple scattering paths in the cubic structure of PuGa alloys

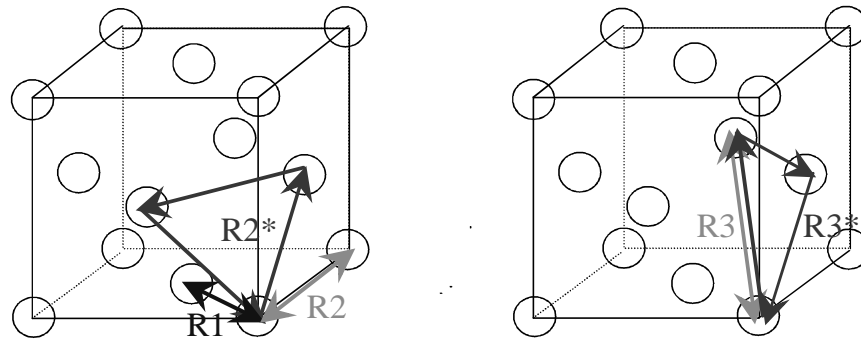


Figure 4. Influence of the multiple scattering at the Pu L_{III} edge (left) and the Ga K edge (right). The Debye-Waller temperature used in the calculation was set to 132 K according to Lawson, *et al.* [4].

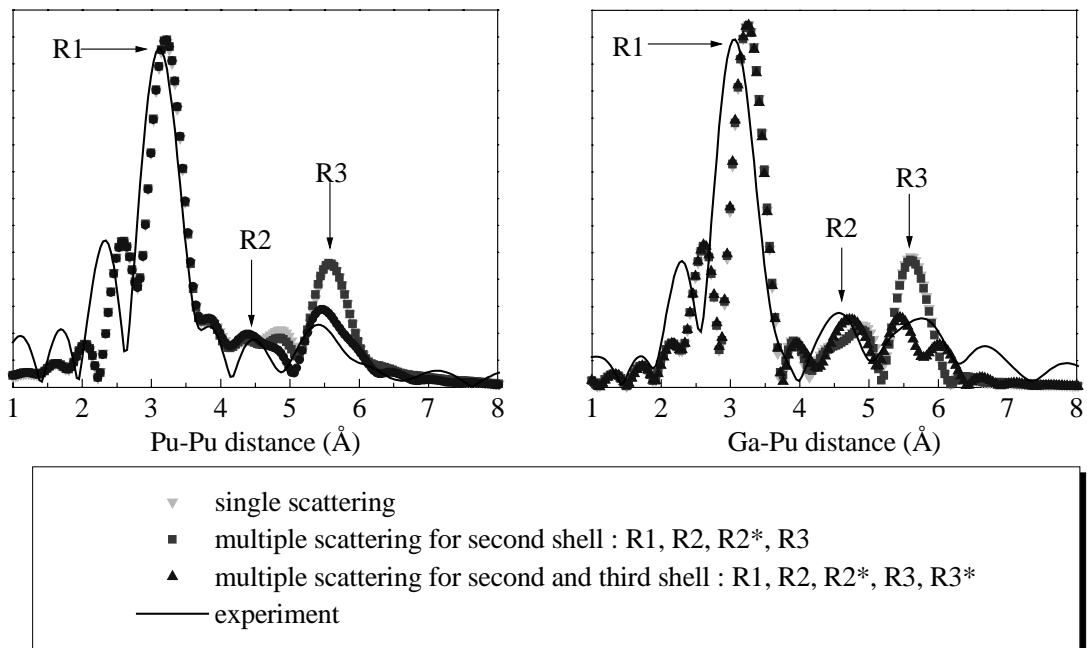


Figure 5. Interatomic distances refined at 300 K and 80 K at the Ga K edge (left) and relative contraction (right)

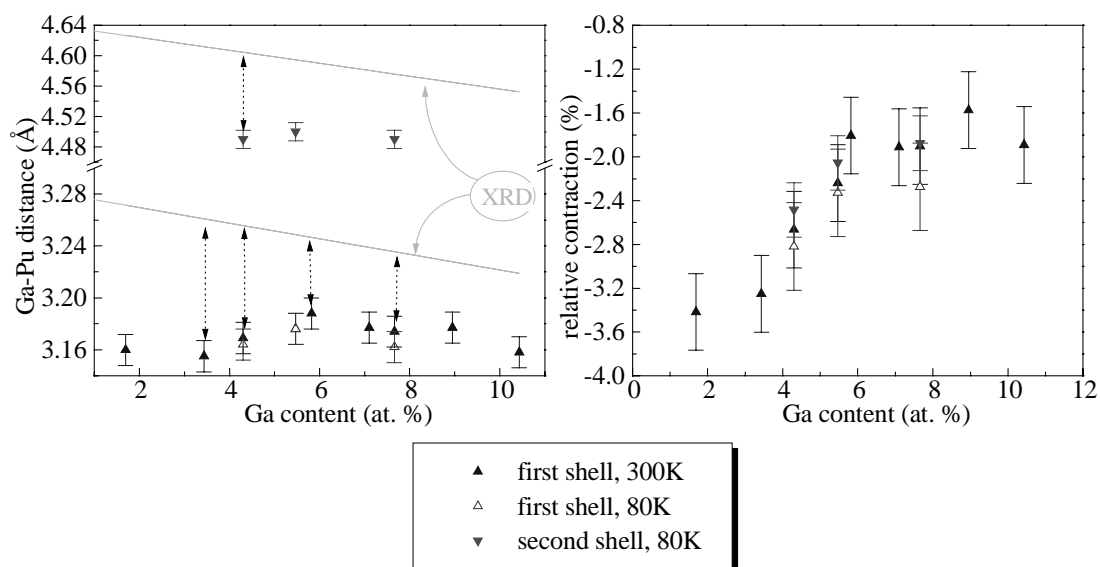
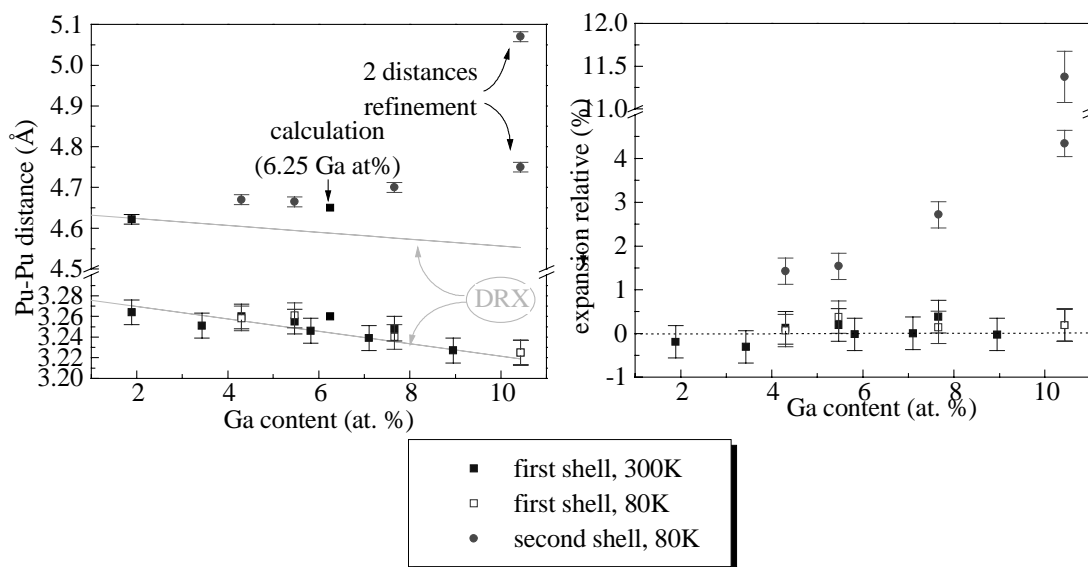


Figure 6. Interatomic distances refined at 300 K and 80 K at the Pu L_{III} edge (left) (the calculation for PuGa 6.25 at.% is also reported), and the relative expansion (right)



VALIDATION OF COMPLEX FORMATION OF Ca^{2+} , UO_2^{2+} AND CO_3^{2-}

G. Bernhard, G. Geipel, V. Brendler, T. Reich, H. Nitsche
Forschungszentrum Rossendorf, Institute of Radiochemistry, Germany

Abstract

A uranium species containing Ca^{2+} , UO_2^{2+} and CO_3^{2-} was found in natural mining-related waters [1]. To validate the stoichiometry and the formation constant, we measured different series of synthetic solutions containing Ca^{2+} , UO_2^{2+} and CO_3^{2-} by means of time-resolved laser-induced fluorescence spectroscopy (TRLFS).

All solutions were prepared so that more than 97% of uranium(VI) in the stock solution exist as tri-carbonato-complex. The TRLFS spectra of these solutions did not show any fluorescence. When increasing concentrations of Ca^{2+} were added, fluorescence spectra with increasing intensity were measured. The intensity increase depends directly on the concentration of the added Ca^{2+} ions. Slope analysis of the $\log(\text{fluorescence intensity})$ vs. $\log([\text{Ca}^{2+}])$ gave a value of two. This means that two calcium ions take part in the complex formation. By using the ratio $[\text{Ca}_2\text{UO}_2(\text{CO}_3)_3]/[\text{UO}_2(\text{CO}_3)_3^{4-}]$ instead, the fluorescence intensity slope becomes independent on the total uranium concentration and the complex formation constant can be determined. EXAFS measurements of the $[\text{Ca}_2\text{UO}_2(\text{CO}_3)_3]_{\text{aq}}$ complex showed, that its structure consists of the same $\text{UO}_2(\text{CO}_3)_3$ unit as in $\text{UO}_2(\text{CO}_3)_3^{4-}_{\text{aq}}$ and solid $\text{Ca}_2\text{UO}_2(\text{CO}_3)_3 \times 11 \text{H}_2\text{O}$. The EXAFS results do not contradict the possibility that two calcium atoms in $[\text{Ca}_2\text{UO}_2(\text{CO}_3)_3]_{\text{aq}}$ assume similar positions as in solid liebigite.

In summary our measurements indicate that this species $[\text{Ca}_2\text{UO}_2(\text{CO}_3)_3]_{\text{aq}}$ is an uncharged, soluble complex which can be seen as a first step forward the formation of the secondary mineral liebigite.

REFERENCES

- [1] G. Bernhard, G. Geipel, V. Brendler, H. Nitsche, Speciation of Uranium in Seepage Waters of a Mine Tailing Pile Studied by TRLFS, *Radiochim. Acta* 74, 87-91 (1996).

STRUCTURE AND ELECTRONIC STRUCTURE OF ACTINIDE $An/Fe(CN)_6$ COMPOUNDS

I. Bonhoure, C. Den Auwer

CEA, DCC/DRRV/SEMP Valrho, BP 171 30207 Bagnols sur Cèze, France

P. Moisy

CEA, DCC/DRRV/ Valrho, BP 171 30207 Bagnols sur Cèze, France

C. Madic

CEA, DCC Valrho, BP 171 30207 Bagnols sur Cèze, France

C. Cartier dit Moulin

LURE, Bâtiment 209D, Centre Universitaire Paris Sud, BP 34, 91898 Orsay Cédex, France

Abstract

In the frame of nuclear waste actinide/lanthanide separation, we propose here to study the selective precipitation of actinide versus lanthanide adducts with hexacyanoferrate. The focus was on both complexation driving forces and actinide-cyano bond formation. Thus, amorphous adducts of $An/Fe(CN)_6$ compounds ($An = U, Np, Pu$ and Am) have been prepared and characterised by classical spectroscopic techniques and XAS at both An and Fe edges. Influence of the initial An and Fe valence states on the final products was also explored and structurally characterised.

First data analysis suggests the hexacyanoferrate entity be not altered by the actinide ion participation. Indeed, the bridging role of the cyano ligand is assumed, with varying geometry as a function of the actinide atom. In addition, XANES and XPS data account for the valence modifications of both Fe and An atoms in the final products. Hints of complexation mechanisms are tentatively given.

CO-ORDINATION CHEMISTRY OF HEPTAVALENT NEPTUNIUM UNDER HIGHLY ALKALINE CONDITIONS

**D.L. Clark, S.D. Conradson, R.J. Donohoe, D.W. Keogh,
D.E. Morris, M.P. Neu, P.D. Palmer, W. Runde, B.L. Scott, C.D. Tait**

Los Alamos National Laboratory
Los Alamos, NM 87545 USA
Glenn T. Seaborg Institute for Transactinium Science
Los Alamos, NM

Abstract

The heptavalent state of actinide ions has been known for nearly three decades. The majority of heptavalent chemistry has been developed for neptunium, as it displays the greatest stability for the heptavalent state among actinide elements. In the solid state, three structural entities have been observed, the majority of which display an unusual tetra-oxo ion. Based on the molecular structure in the solid state, it has long been proposed that Np(VII) contained the unusual tetra-oxo $\text{NpO}_4(\text{OH})_2^{3-}$ ion in alkaline solution. To test this hypothesis, we employed a combination of cyclic voltammetry, extended X-ray absorption fine structure (EXAFS), ^{17}O NMR, and polarised red-Raman spectroscopy to examine the structural characteristics of Np(VII) in alkaline solution.

Concentrated solutions of Np(VII) were prepared in 2.5 M LiOH by bubbling with ozone overnight. The resulting solutions were analysed by EXAFS, NMR and Raman spectroscopies. ^{17}O -NMR spectroscopy on Np(VII) ions in 2.5-3.5 M OH^- revealed a water assisted chemical exchange between $\text{Np}=\text{O}$ and $\text{Np}-\text{OH}$ units, which was confirmed by Raman spectroscopy on ^{18}O -enriched samples. The NMR was also utilised to understand the co-ordination environment of Np(VII), i.e. tetraoxo vs. dioxo. Direct integration of the ^{17}O -NMR signal for the Np(VII) oxo ligands with a standard suggested a dioxo moiety in solution, contrary to the solid-state structural data. In order to probe this further, Raman spectroscopy was used along with group theoretical predictions for the number or Raman-active modes, one for the dioxo (A_{1g}) and two for the tetraoxo (A_{1g} and B_{1g}). The Raman spectra was recorded at varying hydroxide concentrations and showed a single invariant peak. Depolarisation ratio studies confirmed the presence of a single peak of A_{1g} symmetry, consistent with a trans-dioxo unit. EXAFS on Np(VII) solutions also suggested the presence of a trans-dioxo ion of the formula $\text{NpO}_2(\text{OH})_4^-$.

Single crystals of solid $[\text{Co}(\text{NH}_3)_6][\text{NpO}_4(\text{OH})_2] \cdot \text{H}_2\text{O}$ were prepared, and solid state crystal structure determination revealed a tetra-oxo ion as reported previously. Raman spectroscopy on the single crystal revealed only one vibrational mode (as compared to two modes predicted). Bulk precipitation of the Np(VII) with $[\text{Co}(\text{NH}_3)_6]\text{Cl}_3$ gave the same results as the single crystals. The question as to the absence of the B_{1g} mode is still under investigation. XAS data on the crystalline

[Co(NH₃)₆][NpO₄(OH)₂·H₂O solid revealed differences in both the XANES and EXAFS compared to the solution data. EXAFS data are consistent with the solid state structure and the presence of four oxo ligands in the solid state.

XAS INVESTIGATION OF THE MECHANISM BY WHICH LANTHANIDE(III) AND ACTINIDE(III) IONS ARE EXTRACTED FROM SOLUTION BY MALONAMIDE LIGANDS

Christophe Den Auwer

CEA Marcoule, DCC/DRRV/SEMP
Laboratoire de Chimie Théorique et Structurale
30207 Bagnols sur Cèze, Cedex, France

Michael G.B. Drew, Michael J. Hudson, Peter B. Iveson, Mark L. Russell

Department of Chemistry, University of Reading
Whiteknights, Reading, RG6 6AD, Berkshire, UK

Charles Madic

CEA Marcoule, Direction du Cycle du Combustible
B.P. 171, 30207 Bagnols sur Cèze, Cedex, France

Abstract

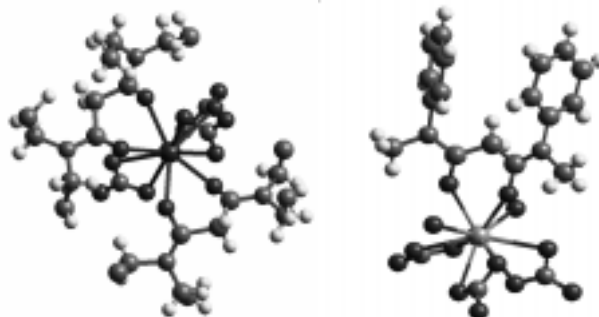
In order to understand the mechanisms involved in the extraction of lanthanide(III) and actinide(III) ions by malonamide ligands, the co-ordination environment around the metal ion in solution has been probed by XAS. Bromo-substituted malonamide ligands and their metal complexes have been prepared to facilitate the structural elucidation.

One of the aims in future nuclear reprocessing is to consider the transmutation of the long-lived actinides to short-lived isotopes by irradiation with neutrons [1]. In order to achieve this, it is necessary to separate the trivalent actinides from the trivalent lanthanide fission products by solvent extraction because lanthanides absorb neutrons too efficiently. Separation of the chemically similar actinide(III) and lanthanide(III) ions has been found difficult to achieve in practise. One option is to co-extract the actinides and lanthanides prior to their separation from each other [2]. Malonamides of type $(R^1R^2NCO)_2CHR^3$ ($R^1, R^3 =$ alkyl groups, $R^2 =$ alkyl or phenyl group) have the potential to be excellent extraction agents [3]. To fine-tune their design we need to understand the extraction mechanisms and the structures of the complexes in solution, for which XAS spectroscopy is the major investigation tool.

As a preliminary to the XAS investigation the crystal structures of a range of malonamides and their metal complexes were determined [4,5]. The metal complexes fell into two groups with one or two malonamides per metal e.g. $La(NO_3)_3(TEMA)_2$ and $Nd(NO_3)_3(DMDPMA)(H_2O)_2$ (Figure 1) where $TEMA = N,N'$ tetraethyl malonamide and $DMDPMA = N,N'$ -dimethyl- N,N' -diphenyl malonamide.

Initial experiments were carried out at the Ln L_{III} edge on both the above mentioned La complex and on $Nd(NO_3)_3(TEMA)_2$. Comparison of the Fourier transform of the EXAFS spectra in the solid state show very little structural differences between these two complexes. The average Ln-O bond lengths

Figure 1



increase in agreement with the corresponding increase in ionic radii between Nd(III) and La(III). A further comparison between the solid state and Nd(NO₃)₃(TEMA)₂ complexes in solution show no significant structural changes. EXAFS studies in solution have also recently been carried out on the complex(es) formed between Am(III) and TEMA. Preliminary results indicate that there are few structural differences between the complexes formed by either Am(III), La(III) and Nd(III) in solution.

In order to enhance some of the MS contributions, one of the two hydrogens on the central carbon atom of the above ligands was replaced by a bromine atom. This had the effect of increasing the backscattering amplitude function from this part of the ligand. The structures of both ligands (BRTEMA and BRDMDPMA) and a corresponding Yb(III) complex have been determined by X-ray crystallography. Preliminary EXAFS studies at the Ln L_{III} and Br K absorption edges show solution structures consistent with the solid state arrangements.

EXAFS measurements were carried out at LURE at the DCI high energy ring on the EXAFS IV experimental hutch and at the CLRC Daresbury laboratories on Stations 7.1 and 9.2. X-ray crystallographic studies were carried out using the MARresearch image-plate system at the University of Reading for which the EPSRC and the university are thanked for funding. We are grateful for financial support under the Partitioning Experiment and Waste Minimisation E.C. Research Programme Contract NEWPART (F141-CT-96-0010).

REFERENCES

- [1] J. Tommasi, M. Delpech, J.P. Grouiller, A. Zaetta, *Nuclear Technology*, 1995, 111, 133.
- [2] C. Musikas, *Inorg. Chim. Acta*, 1987, 140, 197.
- [3] C. Musikas, H. Hubert, *Ion Exch. Solvent Extr.*, 1987, 5, 877.
- [4] P. Byers, M.G.B. Drew, M.J. Hudson and N.S. Isaacs, *Polyhedron*, 1994, 13, 349.
- [5] G.Y.S. Chan, M.G.B. Drew, M.J. Hudson, P.B. Iveson, J-O. Liljenzin, M. Skålberg, L. Spjuth and C. Madic, *J. Chem. Soc. Dalton Trans.*, 1997, 649.

U L_{III} POLARISED XAFS STUDIES ON Ba[UO₂PO₄]₂ · 8H₂O

C. Hennig, A. Roßberg, T. Reich, H. Nitsche

Forschungszentrum Rossendorf e.V., Institut für Radiochemie
PF 510119, D-01314 Dresden

M.A. Denecke

Forschungszentrum Karlsruhe, Institut für Nukleare Entsorgungstechnik
PF 3640, D-76021 Karlsruhe

G. Zahn

TU Dresden, Institut für Kristallographie und Festkörperphysik
Zellescher Weg 16, D-01062 Dresden

Abstract

A characteristic feature of XAFS measured by synchrotron radiation is the spectral dependence on the polarisation vector $\vec{\epsilon}$ for oriented samples such as single crystals. We investigated the U L_{III} edge XANES and EXAFS of a single-crystal barium uranyl phosphate hydrate (Ba[UO₂PO₄]₂ · 8H₂O) which is built up by layers of [UO₂]²⁻ co-ordinated by [PO₄]³⁻ tetrahedra. These layers are bridged by Ba²⁺, H⁺ and H₃O⁺ cations, giving a near tetragonal molecule and crystal symmetry. The crystal orientation was determined by X-ray diffraction. XANES and EXAFS measurements were performed with the polarisation vector aligned in the equatorial U-O plane parallel to [100] and [110], as well as the polarisation vector oriented with 90°, 45° and 30° angles to axial U-O binding which is nearly parallel to [001].

The polarisation dependent uranium L_{III} edge XANES spectra were characterised by significant variations of the spectral features arising primarily from uranyl species and contributions from the surrounding equatorial oxygen atoms. Two different explanations for the second absorption maximum, the resonance 15 eV above the L_{III} edge white-line maximum, have been discussed. One explanation, based on pressure dependent measurements of UO₃, attributed this feature to shake-up processes [1]. Another interpretation identified this feature as a multiple-scattering resonance associated with the axial U-O bonds in various uranyl compounds [2,3]. This interpretation stemmed from polarisation dependent measurements and *ab initio* multiple-scattering calculations using the FEFF code [4]. Our experimental investigations show that the relative intensity of this resonance increases if the polarisation vector is aligned nearly along the axial U-O bonds. This observation confirms the multiple-scattering assignment of this feature and is supported by our own theoretical FEFF calculations.

The U L_{III} edge EXAFS shows a strong polarisation dependence which is evident in the Fourier transforms at distances corresponding to the axial and equatorial oxygen of the uranyl group. From fits to the spectrum recorded when the polarisation vector is oriented 90° to [001] in the direction [100],

the effective bond distance for the axial U-O calculated using scattering parameters from the FEFF code is $1.76(\pm 0.01)$ Å. In the polarisation vector oriented with a 30° angle to [001], the effective distance slightly increases to $1.83(\pm 0.01)$ Å. These atomic distance differences originate from the polarisation dependence of the phase function [5]. The polarisation also strongly influence the effective co-ordination numbers.

REFERENCES

- [1] S. Bertram, G. Kaindl, J. Jové, M. Pagès, J. Gal, *Phys. Rev. Lett.* 63 (1989) 2680.
- [2] E.A. Hudson, P.G. Allen, L.J. Terminello, M.A. Denecke, T. Reich, *Phys. Rev. B* 54 (1996) 156.
- [3] E.A. Hudson, J.J. Rehr, J.J. Buchner, *Phys. Rev. B* 52 (1995) 13815.
- [4] S.I. Zabinsky, J.J. Rehr, A. Ankudinov, R.C. Albers, M.J. Eller, *Phys. Rev. B* 52 (1995) 2995.
- [5] J. Stöhr, R. Jaeger, *Phys. Rev. B* 27 (1983) 5146.

**CHARACTERISATION OF THE PREFERRED ORIENTATION
IN EXAFS SAMPLES USING BRAGG-BRENTANO X-RAY DIFFRACTION**

C. Hennig¹, G. Nolze²

¹Forschungszentrum Rossendorf e.V., Institut für Radiochemie, PF 510119
D-01314 Dresden, Germany

Rossendorf Beamline (ROBL) at ESRF, B.P. 220, F-38043 Grenoble

²Bundesanstalt für Materialforschung und -prüfung, Unter den Eichen 87, D-12205 Berlin

Abstract

Preferred orientation in powder samples influences extended X-ray absorption fine structure (EXAFS) measurements due to the polarisation of synchrotron radiation. The polarisation effect at the uranium L_{III} edge EXAFS and the analysis of preferred orientation is demonstrated using the natural mineral metatorbernite. For simple textures an X-ray diffraction measurement in Bragg-Brentano geometry allows to determine the crystallite orientation basing on a full pattern refinement including a preferred orientation model according to March-Dollase.

Introduction

EXAFS spectroscopy has been applied successfully to analyse materials like amorphous solids as well as polymers, solutions and gases because of its short-range order sensitivity and the independence of the states of matter. Until now, a lot of EXAFS measurements have also been carried out on polycrystalline materials. It is well known, however, that the majority of polycrystalline materials are characterised by a more or less strong texture, e.g. caused by a uniaxial pressure during sample preparation, layering by rubbing on foils or sedimentation processes. Owing to the polarised synchrotron radiation, under certain circumstances a preferred orientation can lead to an incorrect determination of the co-ordination number N_i , especially for compounds with an anisotropic co-ordination centre. Therefore, an analysis of the preferred orientation at EXAFS samples is desirable to verify the sample anisotropy. Exemplary, this will be shown here for polycrystalline metatorbernite, $\text{Cu}[\text{UO}_2\text{PO}_4]_2 \cdot 8\text{H}_2\text{O}$, a mineral with a pronounced layer structure.

EXAFS

The EXAFS measurements were carried out at the U L_{III} edge. L_{II} and L_{III} edge EXAFS involve transitions from initial p states to dipole-allowed s ($l = 0$) and d ($l = 2$) final states. The s states have no orientation dependence, but the d states cause a polarisation dependence. These final states generate different phase and amplitude functions, complicating the general EXAFS expression [1]. Quantitatively, at the U L_{III} edge the d final state partial wave contribution dominates [2]. Additionally, a term must be considered arising from the interference between s and d final states [3]. Since the absorption coefficient μ is a tensor of second-rank order, the EXAFS for cubic or higher symmetry is independent on the sample orientation. However, for lower crystal symmetry the EXAFS may be affected by the crystallite orientation. The EXAFS amplitude term as a function of the wave vector k is given by the summation over all j atoms in the neighbour co-ordination shells i :

$$A_i(k) = S_0^2 \sum_i \frac{N_i F_i(k, R_i)}{kR^2} \exp(-2R_i/\lambda(k)) \exp(-2\sigma_i^2 k^2) \quad (1)$$

with N_i backscatter atoms at distances R_i from the absorbing atom. This function includes factors for intrinsic core-hole relaxation losses S_0^2 , the backscattering amplitude $F_i(k, R_i)$ from each of the neighbouring atoms, the photoelectron mean free path λ connected with inelastic losses in the scattering process, and the Debye-Waller factor σ_i^2 including statistical disorder and thermal vibrations. Polarisation effects at the L_{III} edge may introduced into Eq. (1) using effective co-ordination numbers N_i^{eff} :

$$N_i^{\text{eff}} = 1/2 N_i (1 + 3\cos^2 \alpha_{ij}) \quad (2)$$

where α_{ij} represents the angle between the X-ray electric field vector E of the synchrotron radiation and the interatomic vector R_i from the absorbing atom to the backscatterer. For the L_{III} edge this first order approximation only assumes d final states and neglects any angular dependence of the sd interference terms. Neighbouring atoms aligned parallel to the X-ray polarisation vector ϵ scatter preferentially, whereas atoms located perpendicular to polarisation vector give small scattering contributions as has been demonstrated for single crystals with uranyl ions [4,5]. Polycrystalline samples, which are characterised by a pronounced preferred orientation, should influence the EXAFS

amplitude similarly. One way to examine such an effect is the comparison of two EXAFS spectra measured by varying the sample surface normal orientation n with respect to the polarisation vector ϵ in the plane with the electric field vector E [4,6].

Preferred orientation analysis by X-ray diffraction

For the characterisation of a texture in terms of a qualitative and/or quantitative crystallographic description, commonly X-ray, neutron or electron diffraction experiments will be used. Especially for an application of X-rays and neutrons without any special detector, a complete texture analysis is very time-consuming, because the orientation distribution of several lattice planes must be measured to get a reliable texture description, e.g. in the form of spherical harmonics. Additionally one must consider that for such measurements special equipment is necessary. But under certain circumstances (crystals with needle or plate habit and mostly higher symmetry) the measurements may be shortened if the sample is prepared, e.g. by an axial pressure, whereby a rotation-symmetrical orientation distribution can be assumed, e.g. the so-called fibre texture. In those cases a measurement in Bragg-Brentano geometry, which only detects interferences of lattice planes parallel to the surface, allows to estimate a one-component texture, but not a complex orientation distribution because each intensity information results from different crystallites in dependence of the current diffraction angle (except reflections of higher order). Combining this comparatively fast technique with one of the existing refinement programs, an effective multiplicity for each Bragg reflection can be determined using suitable models. A very user-friendly – because simple – expression for a description of a preferred orientation is given by March and Dollase [7]. There, the preferred orientation is characterised by a well-defined lattice vector and the strength of preferred orientation:

$$I_{corr} = I_{str} (G^2 \cos^2 \alpha_k + G^1 \sin^2 \alpha_k)^{-3/2} \quad (3)$$

For a given reflection hkl , this formula describes the relation between the corrected intensity I_{corr} and the integral intensity I_{str} resulting from known crystal structure data. I_{str} will be corrected by the preferred orientation in dependence on the orientation parameter G and the angles α_k between the reciprocal lattice vectors H_k of all symmetry-equivalent lattice planes and the preferred orientation vector H_p . The orientation parameter G must be fitted in a special refinement procedure. The advantage of the March-Dollase function in contrast to other expressions like Rietveld-Toraya is that its integral is always identically, independent from the used parameter size [8]. This is of course only important for the quantitative analysis of phase mixtures where it is generally in use. The parameter G varies from $G = 0$ (complete orientation) to $G = 1$ (random orientation). Thus the size of G represents a quantitative expression of the existing preferred orientation, whereas H_p reflects qualitatively the character of the assumed preferred orientation.

Material characterisation and sample preparation

The observed natural mineral metatorbernite, $\text{Cu}[\text{UO}_2\text{PO}_4]_2 \cdot 8\text{H}_2\text{O}$, comes from Kolwezi, Prov. Shaba, Republic Kongo. The chemical analysis was performed by X-ray spectrometry. As remarked above, uranyl phosphates are built up as stable layer structures. Uranium is six-fold co-ordinated by oxygen. An axial uranyl ion $[\text{UO}_2]^{2+}$ is equatorially surrounded by four oxygen atoms, each of them belonging to tetrahedrally co-ordinated phosphate units. The connection between the square plane centred by uranium and the $[\text{PO}_4]^{3-}$ tetrahedron involves alternating uranyl positions within the $[\text{UO}_2\text{PO}_4]^{-1}$ sheets. Therefore, the two non-equivalent axial oxygen atoms give different bond

distances. The charge neutrality of the $[\text{UO}_2\text{PO}_4]^{-1}$ sheets is realised by hydrated Cu^{2+} interlayer cations. Along [001] the uranyl phosphate sheets alternate with water and hydrated Cu^{2+} , following by a tetragonal crystal symmetry. This crystal structure causes a major cleavability after {001} according to the uranyl phosphate layers.

For metatorbernite α - and β -modifications are known [9]. Ross, *et al.* [10] determined the α -form with the space group P 4/n, $a = 6.969 \text{ \AA}$, $c = 17.306 \text{ \AA}$. There the P atoms are located at the position with site symmetry $\bar{4}$. This structure was later confirmed by Stergiou, *et al.* [11]. The β -form proposed by Calos, *et al.* [9] in the space group P 4/nmm, $a = 6.950 \text{ \AA}$, $c = 8.639 \text{ \AA}$, is indicated by a higher site symmetry for the P positions ($\bar{4}2m$). X-ray powder diffraction measurements identified the investigated material as α -form.

Two samples with different strength of preferred orientation were prepared. At first the mineral was manually grounded in an agate mortar. Commonly, this procedure gives a coarse-grained powder (Sample 1). The second sample has been crushed in a conventional vibrating mill producing a fine-grained powder (Sample 2). Both powders have been mixed with boron nitride as buffer material and pressed in a hydraulic press with an uniaxial pressure at 10^5 N , parallel to the normal sample.

Experimental

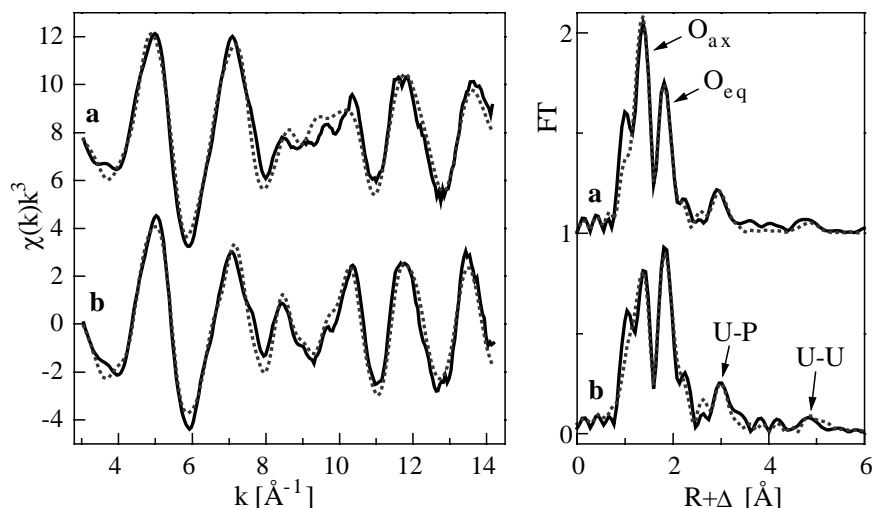
Uranium L_{III} edge EXAFS spectra were collected in transmission mode at room temperature. Sample 1 was measured at the Stanford Synchrotron Radiation Laboratory (SSRL) on beamline 4-1 using a Si(220) double-crystal monochromator and Sample 2 was investigated at the Hamburger Synchrotronstrahlungslabor (HASYLAB) on beamline X1.1 using a Si(311) double crystal monochromator. A simultaneously measured U(VI) solution was used for energy calibration. The threshold energy E_0 was defined 20 eV above the first inflection point of the corresponding absorption edge of 17.166 keV [12]. To avoid sample thickness effects [13] the sample mass was optimised to give a difference in the absorption coefficient of $\Delta\mu x = 1$ across the U L_{III} absorption edge, where $\Delta\mu$ is the absorption coefficient and x is the sample thickness, with regard to a sample normal parallel to the beam direction. The X-ray diffraction measurements were carried out on a conventional Bragg-Brentano diffractometer using $\text{CuK}\alpha$ radiation (step width: 0.05° , counting time: 10 s).

Results and discussion

For analysing the interaction between polarisation of synchrotron radiation and the crystallite orientation, the EXAFS measurements were carried out for two different geometrical arrangements, defined by β , the angle between the sample surface normal orientation n and the X-ray electric field vector E or alternatively the polarisation vector ε and the sample surface direction lying in the same plane. The U L_{III} edge EXAFS spectra for the coarse grounded Sample 1 are shown in Figure 1. spectrum (a) was measured with $\beta = 45^\circ$, and spectrum (b) with $\beta = 0^\circ$.

At Figure 1 the k^3 -weighted k -space EXAFS data are compared to the R -space plots of the Fourier transformed spectra. The Fourier transformed EXAFS spectrum represents a radial distribution function of the neighbouring backscatterers. Owing to the electron scattering phase shift a peak maximum at lower R value relative to the true bond distance appears. This phase shifts, the theoretical scattering amplitudes for each pair of atoms and the inelastic scattering corrections based

Figure 1. U L_{III} edge k^3 -weighted EXAFS (left) and corresponding Fourier transforms (right) for Sample 1 with $\beta = 45^\circ$ (a) and $\beta = 0^\circ$ (b). The solid line is the experimental data, and the dashed line represents the theoretical fit.



on the photoelectron mean free path were calculated using the XAS code FEFF 7.02 [14]. EXAFS data analysis was carried out using the EXAFSPAK software, developed by G. George and I. Pickering at SSRL. The quantitative data analysis was performed as least-square fittings of the k^3 -weighted EXAFS. An amplitude reduction factor S_0^2 of 0.9 was used. During these calculations the shift in threshold energy ΔE_0 for all co-ordination shells was hold constant at -14.2eV. In comparison between each other, the EXAFS Debye-Waller factor σ_i^2 was fixed for the axial and the equatorial oxygen to 0.003 and 0.004, respectively. These values are in agreement with other EXAFS investigations on uranyl compounds. Further, the U-P and U-U intersection gives low intense peaks at 3.6 Å and 5.2 Å, respectively. These contributions were included using a fixed σ_i^2 of 0.015. The structural parameter results for the first and second co-ordination shell are summarised in Table 1.

Table 1. Structural parameter results of fits to U L_{III} edge EXAFS for Samples 1 and 2, only for the first and second co-ordination shell with fixed Debye-Waller factors

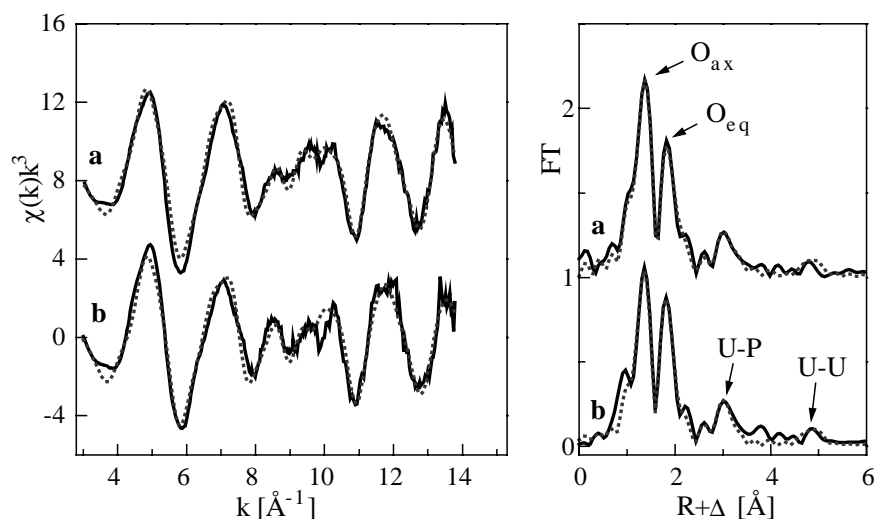
Sample	β [°]	Shell	R [Å]	N_i^{eff}	σ_i^2 [Å ²]
1	45	U-O _{ax}	1.79	2.2	0.003
		U-O _{eq}	2.29	3.5	0.004
	0	U-O _{ax}	1.78	1.6	0.003
		U-O _{eq}	2.30	4.6	0.004
2	45	U-O _{ax}	1.80	2.3	0.003
		U-O _{eq}	2.30	3.6	0.004
	0	U-O _{ax}	1.79	1.9	0.003
		U-O _{eq}	2.30	4.2	0.004

However, the different oxygen axial bond distances, determined by X-ray diffraction, were treated as one shell to simplify the EXAFS data analysis. The corresponding radial distribution function at the Fourier transformed EXAFS is centred around 1.79(±0.02) Å. The difference between

the two bond lengths resulting from the crystal structure data for metatorbernite (α -form: 1.798 Å and 1.940 Å [10]) is not discriminated by the Fourier transformed EXAFS because of the limited k range, but it may influence the Fourier transform side lobes. Axial multiple scattering effects, which are often observed in centrosymmetric uranyl compounds [4], were not considered here because of the axial bond length differences. The second Fourier transform peak arising from the equatorial oxygen co-ordination shell gives a bonding length of 2.30(\pm 0.02) Å. According to the angle β , the intensity ratio of the Fourier transform peaks significantly changes with respect to the first and second co-ordination shells. As can be seen in Table 1, the co-ordination number N_i for the axial oxygen atoms O_{ax} is calculated too large at $\beta = 45^\circ$ and too small at $\beta = 0^\circ$, whereas the co-ordination number of the equatorial oxygen atom O_{eq} is too small at $\beta = 45^\circ$ and too large at $\beta = 0^\circ$. It is known that because of different experimental effects the absolute precision of N_i^{eff} can be low [13]. But for the used experimental arrangement using one and the same sample for measurements at different angles β , the relative precision in N_i^{eff} is ± 0.1 within one data set.

This measurement demonstrates the strangeness of the effect in the case of a high strength of preferred orientation, but it should not be regarded by the preferred orientation analysis, because it is not a typical effect, obtained in well-prepared samples, usually. Such a preparation was performed to receive a fine-grained powder: Sample 2. Figure 2 shows the U L_{III} edge EXAFS spectra for Sample 2, likewise spectrum (a) is measured for $\beta = 45^\circ$, whereas spectrum (b) is measured for $\beta = 0^\circ$. The results for the first and second co-ordination shell are summarised in Table 1.

Figure 2. U L_{III} edge k^3 -weighted EXAFS (left) and corresponding Fourier transforms (right) for Sample 2 with $\beta = 45^\circ$ (a) and $\beta = 0^\circ$ (b). The solid line is the experimental data, and the dashed line represents the theoretical fit.



As can be seen, the angle dependent peak intensity differences between the first and second co-ordination shells is decreased as compared to Sample 1, but it remains obtainable. This behaviour suggests a common preferred orientation, but with different strength.

Additionally, the influence of the preparation on the orientation distribution has been checked using a common texture goniometer. Thus, the assumed C_∞ symmetry has been confirmed. In such cases an X-ray diffraction measurement in Bragg-Brentano geometry should be applicable for an analysis of preferred orientation.

The resulting powder diffraction pattern has been fitted by the program PowderCell [15] using a least-square algorithm. To this purpose the atomic co-ordinates of α -metatorbernite [10] have been fixed and the preferred orientation parameter (March-Dollase function, see Eq. (3)) beside the general parameters have been optimised. The experimental data as well as the refined curve are shown in Figure 3, and the refined parameters are given in Table 2.

Figure 3. Experimental and calculated X-ray diffraction pattern for Sample 2 with essential indices

MT = metatorbernite, BN = boron nitride

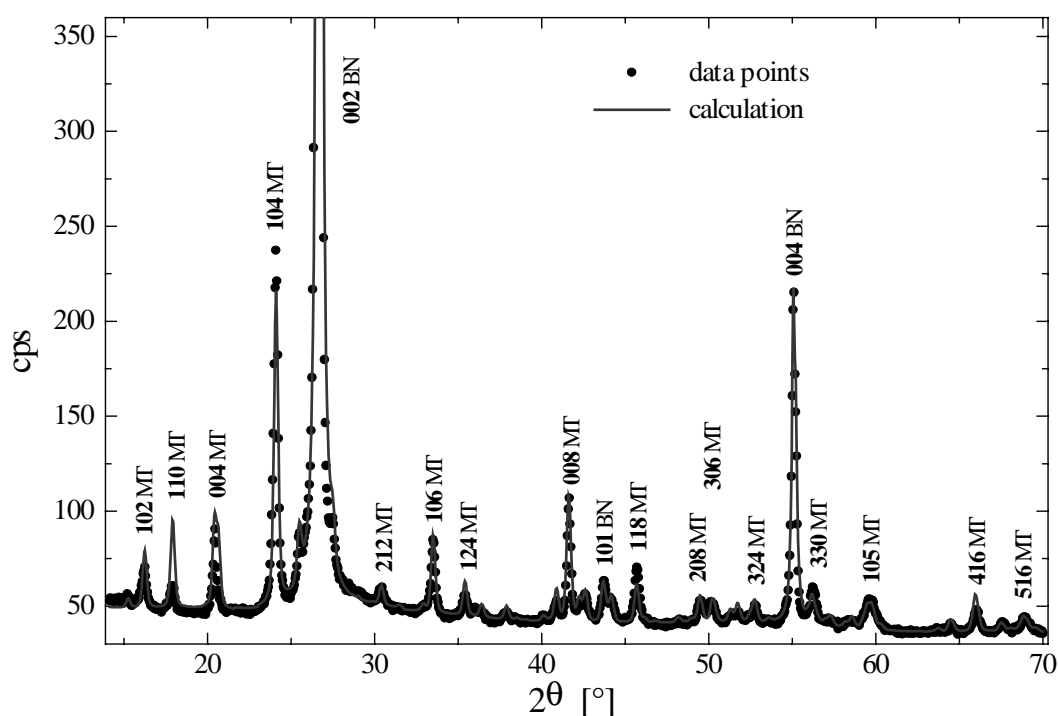


Table 2. Parameters from full pattern refinement for the sample $\text{Cu}[\text{UO}_2\text{PO}_4]_2 \cdot 8\text{H}_2\text{O}$ including the buffer material h-BN at Sample 2

Parameters		h-BN	$\text{Cu}[\text{UO}_2\text{PO}_4]_2 \cdot 8\text{H}_2\text{O}$
Lattice constants	a, b	2.4977 Å	6.9634 Å
	c	6.6561 Å	17.3214 Å
Profile function		Pseudovoigt 1	Pseudovoigt 1
	n_a/n_b	0.32/0	0.54/0
Scaling factor		0.2663	0.0850
Mass fraction		75.8	24.2
Preferred orientation vector H_p		[001]	[001]
Orientation parameter G		0.34	0.53

A complete analysis requires a simultaneous calculation for metatorbernite and boron nitride buffer material. The final fit gives reliability values of $R_p = 8.5$ and $R_{wp} = 14.0$. However, the refinement yields a preferred orientation of $\text{Cu}[\text{UO}_2\text{PO}_4]_2 \cdot 8\text{H}_2\text{O}$ described by $H_p = [001]$ and $G = 0.53$.

Because of the acceptable agreement between simulation and experiment one can assume that the given texture can be described quite well by a single preferred orientation (one-component texture). This is possible because only in such an exclusive case is it acceptable to use a powder pattern obtained by X-ray diffraction in Bragg-Brentano geometry for the characterisation of preferred orientation effects.

In consequence, the uranyl ion axes are preferentially oriented parallel to the sample normal direction, while the equatorially co-ordinated oxygen atoms are parallel to the sample surface plane. A preferred scattering process for equatorial oxygen atoms arises if they are parallel to the polarisation vector ϵ at $\beta = 0^\circ$ and decreases with increasing β . The co-ordination number of axial co-ordinated oxygen increases with increasing β .

The X-ray powder diffraction may offer a possibility for fast and simple testing of the deviation in co-ordination numbers. Especially the comparable regarding the existence of a preferred orientation in powder samples has advantages in the interpretation of EXAFS measurements. However, the used method is applicable only for very simple textures. For materials or sample geometries with lower symmetry only a complete texture description using X-rays or electron backscattered diffraction (EBSD) can be used to implement preferred orientation effects into the complex interpretation of EXAFS data. However, for the given example it was possible to show that a preferred orientation influence must be considered during the evaluation of EXAFS data.

Acknowledgements

This work was supported by NATO Collaborative Research Grant No. SA.5-2-05(CRG.971641) 218/97/AHJ-501.

REFERENCES

- [1] S.M. Heald, E.A. Stern, *Phys. Rev. B* 16 (1977), 5549.
- [2] C. Brouder, *J. Phys.: Condens. Matter* 2 (1990), 701.
- [3] J. Stöhr, R. Jaeger, *Phys. Rev. B* 27 (1983), 5146.
- [4] E.A. Hudson, P.G. Allen, L.J. Terminello, M.A. Denecke, T. Reich, *Phys. Rev. B* 54 (1996), 156.
- [5] C. Hennig, M.A. Denecke, A. Roßberg, G. Zahn, T. Reich, H. Nitsche, *Z. Krist. Suppl.* 15 (1998), 156.
- [6] A. Manceau, D. Chateigner, W.P. Gates, *Phys. Chem. Minerals* 25 (1998), 347.

- [7] W.A. Dollase, *J. Appl. Cryst.* 19 (1986), 267.
- [8] H.B. O'Connor, D.Y. Li, H. Sitepu, *Adv. in X-Ray Analysis*, 34 (1991), 409.
- [9] N.J. Calos, C.H.L. Kennard, *Z. Krist.* 211 (1996), 701.
- [10] M. Ross, H.T. Evans Jr., D.E. Appleman, *Am. Miner.* 49 (1964), 1603.
- [11] A.C. Stergiou, P.J. Rentzeperis, P.J. Sklavounos, *Z. Krist.* 205 (1993), 1.
- [12] J.A. Bearden, A.F. Burr, *Rev. Mod. Phys.* 39 (1967), 125.
- [13] E.A. Stern, K. Kim, *Phys. Rev.* B23 (1981), 3781.
- [14] S.I. Zabinsky, J.J. Rehr, A. Ankudinov, R.C. Albers, M.J. Eller, *Phys. Rev. B* 52 (1995), 2995.
- [15] W. Kraus, G. Nolze, *CPD Newsletter* 20 (1998), 27.

EXAFS INVESTIGATIONS OF URANYL SORPTION ON FERRIHYDRITE

C. Hennig, T. Reich, T. Arnold, A. Roßberg, H. Nitsche
Forschungszentrum Rossendorf e.V., Institut für Radiochemie
PF 510119, D-01314 Dresden

Abstract

Structural parameters of the near-neighbour surrounding of uranium(VI) sorbed onto ferrihydrite surfaces have been determined by U L_{III} edge EXAFS investigations. Ferrihydrite was precipitated from 1×10^{-3} Mol/L iron(III) nitrate solution by slowly raising the pH to 7. This suspension was aged for 60 minutes before the pH was lowered to 5 and the ionic strength adjusted to 0.1 M NaNO₃. The sorption samples were prepared in air at room temperature by continuously stirring suspensions of ferrihydrite with uranyl nitrate for 65 hours. The uranium concentrations for two samples at pH 5.8 were 10^{-4} and 10^{-5} Mol/L, the uranium concentration for one sample at pH 7.8 was 10^{-5} Mol/L. Equilibrium with atmospheric CO₂ was achieved by adding an appropriate amount of NaHCO₃ to the samples. For EXAFS measurements, the samples were separated by centrifugation, transferred as a wet paste into polyethylene cuvettes and sealed air-tight.

Uranium L_{III} edge EXAFS spectra were collected simultaneously in transmission and fluorescence mode at SSRL/Stanford using the Si(220) double-crystal monochromator on beamline 2-3. At DESY/Hamburg, the measurements were repeated for comparison using the Si(311) double-crystal monochromator on beamline X1.1. Theoretical scattering amplitudes and phases were calculated with FEFF7 [1]. Data analysis was performed using the EXAFSPACK software from G. George and I. Pickering.

Four-shell fits to the experimental EXAFS data show in common that the uranium is surrounded by two O_{ax} atoms at 1.80 ± 0.02 Å. Approximately five O_{eq} atoms are co-ordinated to the uranyl group at 2.35-2.39 Å in the equatorial plane. A large Debye-Waller factor obtained for this shell indicates a rather broad distribution of U-O_{eq} distances. The observation of a single, although broad, O_{eq} shell contradicts the detection of O_{eq1} and O_{sorp} shells at 2.35 and 2.52 Å, respectively, for a sample which was prepared under similar conditions by Waite, *et al.* [2]. These differences may be partly explained by significant structural differences of ferrihydrite related to minor variation of the preparation conditions [3]. One iron atom is detected at a U-Fe distance of 3.42 Å. The Debye-Waller factor for this shell is enlarged for the samples obtained at pH 5.8 which can be explained by a presence of more than one surface species. This U-Fe interaction indicates the formation of an inner-sphere surface complex [4]. Since the attempt to fit this shell as U-U interaction instead of U-Fe was unsuccessful, we conclude that no multinuclear uranyl species are sorbed at the surface.

REFERENCES

- [1] S.I. Zabinsky, J.J. Rehr, A. Ankudinov, R.C. Albers, M.J. Eller, *Phys. Rev. B* 52 (1995) 156.
- [2] T.D. Waite, J.A. Davis, T.E. Payne, G.A. Waychunas, N. Xu, *Geochim. Cosmochim. Acta* 58 (1994) 5465.
- [3] U. Schwertmann, J. Friedel, H. Stanjek, *unpublished*.
- [4] T. Reich, H. Moll, T. Arnold, M.A. Denecke, C. Hennig, G. Geipel, G. Bernhard, H. Nitsche, P.G. Allen, J.J. Buchner, N.M. Edelstein, D.K. Shuh, *J. Electron Spectroscopy*, *in press*.

EXAFS SPECTROSCOPY OF TECHNETIUM AND RHENIUM COMPLEXES RELEVANT TO NUCLEAR MEDICINE

R. Jankowsky, S. Kirsch, M. Friebe, H. Spies and B. Johannsen

Forschungszentrum Rossendorf

Institut für Bioanorganische und Radiopharmazeutische Chemie

Postfach 510119, D-01314 Dresden, Germany

Abstract

Technetium and rhenium in the form of special complexes are important metals for the use in nuclear medicine. In order to design such complexes, detailed knowledge about the complexation behaviour of ligands and complex structures is required. EXAFS spectroscopy using synchrotron radiation provides the possibility to investigate complex structures in solid and soluted state. In the present study, EXAFS spectroscopy was applied to study the co-ordination spheres of technetium-99 and rhenium-187 complexes of different kinds of complexes. Rhenium complexes of model peptides were investigated and the extent to which the co-ordination mode depends on the peptide sequences was shown. EXAFS measurements at different pH values revealed changes in the metal co-ordination spheres. In case of the dipeptide Cys-Gly, a 1:2 complex with a Re(V) oxo core and a formal S₂N₂ co-ordination sphere is formed. By increasing the pH, a Re(V) dioxo core is generated. The tripeptide Gly-Gly-Cys was shown to exhibit a formal S_N3 co-ordination with the Re(V) oxo metal centre. Using multiple scattering analysis, the involvement of the peptide backbone in the metal co-ordination was found. Under alkaline conditions, the co-ordination of a hydroxyl group at the metal core takes place. EXAFS spectroscopy was further applied to study the technetium binding sites in large, biologically relevant peptides. The technetium complex of an endothelin derivative was shown to be a 1:2 Tc(V) oxo complex with a formal S₄ co-ordination as realised by the peptide cysteine residues. A LHRH derivative bearing a cysteine residue at the side chain of a lysine residue was analysed to represent a 1:2 Tc(V) oxo complex with a formal S₂N₂ co-ordination sphere. Thereby, the metal co-ordination is ensured by the free cysteine residues of the peptides. The investigation of mixed ligand complexes of technetium and rhenium using the „3+1”-concept showed characteristic EXAFS features of this class of complexes. The co-ordination spheres as known from XRD analyses could be confirmed for solution. Reaction pathways leading to different products during the formation of „3+1” complexes were monitored and helped to understand reaction mechanisms. Furthermore, stability studies of the mixed-ligands complexes under biological conditions were performed and showed the possibility to record EXAFS data *in situ*. As a further complex category, mixed ligand Tc and Re carbonyl compounds were studied. The metal co-ordination spheres gave typical EXAFS patterns with the carbonyl co-ordination detectable by single and multiple scattering effects, with excellent correlation between EXAFS and known XRD data found. By measurements in solution, significant changes in the metal environment of the metal carbonyl precursor molecules were observed. In conclusion, EXAFS spectroscopy is an excellent tool for structural analysis of technetium and rhenium complexes relevant to nuclear medicine.

**HEAVY ELEMENT SENSITIVE TOMOGRAPHY
USING SYNCHROTRON RADIATION ABOVE 100 KEV**

J. Jolie, Th. Materna

Institute of Physics, University of Fribourg
CH-1700 Fribourg, Switzerland

B. Masschaele, W. Mondelaers

Vakgroep subatomaire en stralingsfysika
University of Ghent
B-900 Ghent, Belgium

V. Honkimaki, A. Koch, Th. Tschentscher

European Synchrotron Radiation Facility
PB 220, F-38043 Grenoble Cedex, France

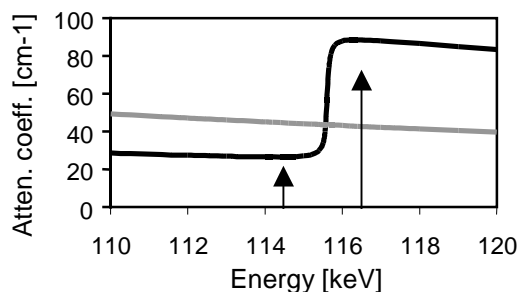
Abstract

X-ray tomography is one of the most used non-destructive methods of sample analysis. In this category, dual-energy tomography is the only process that makes this technique really sensitive to elements. With the advent of synchrotron radiation sources producing photons with energies above 100 keV, element sensitive scanning becomes possible for actinides. Here we report on a first experiment at the European Synchrotron Radiation Facility. Several samples containing uranium in various concentrations have been scanned using an especially designed detector – a phosphor screen observed by a CCD camera. Excellent results for artificial samples and also for natural specimens were obtained. The spatial resolution of the three-dimensional reconstruction is estimated to be about 50 μm .

Introduction and concept

The concept of element sensitive tomography is so attractive because of its simplicity from the analytical point of view [1]. By scanning a sample using photons having two different energies, one just below and one just above the energy of the K edge of the element of interest, the different images become sensitive to this element only [2,3]. Across the K edge, the attenuation coefficient in uranium differs by a factor of 3, whereas in lead and other elements, the difference is negligible [4]. Figure 1 shows, in the region of the uranium K edge, the variation with energy of the X-ray absorption in uranium and lead. If two images are recorded, one with energy just below the edge, one just above, the image created by the subtraction will thus show only uranium [5,6].

Figure 1. The X-ray attenuation coefficient of uranium and lead plotted against the energy of the photons, in the region of the uranium K edge. The arrows indicate the energies we use in our experiment to visualise uranium: 114.6 and 116.6 keV.



A standard procedure for a scan is to measure the attenuation at several orientations of the sample. The recorded patterns are then used to reconstruct the three-dimensional attenuation distribution for the whole sample. Finally, the difference between the three-dimensional reconstruction for photon energies above and below the K edge yields the spatial distribution of the corresponding element under study. Because the K edge energies are characteristic, the method can be applied specifically to each element. It is therefore possible to visualise independently the distribution of different elements, inside the same sample. This property can be of great interest in geology and nuclear waste storage, by selectively studying the spatial distribution of radioactive elements and their daughters produced by disintegration.

For heavy elements, like actinides, the photon energies required are above 100 keV. The high energy of these photons, leading to a large penetration depth, permits the use of thick and dense samples. On the other hand, there are two disadvantages: it is difficult to produce tuneable photons above 100 keV and, because of their strong penetration, they are also difficult to record. Here we show how these problems associated with heavy element tomography can be overcome. Our approach relies on synchrotron radiation above 100 keV and a position-sensitive detector capable of working at these energies.

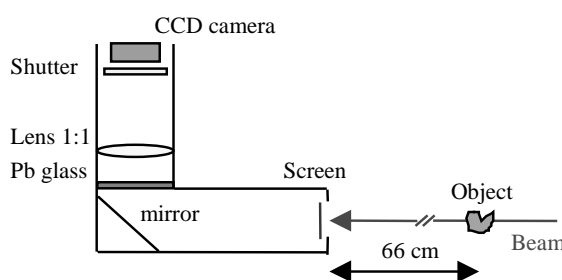
Set-up and experiment

Our earlier work on heavy element detection relied on crystal diffraction of bremsstrahlung to provide the incident beam and semiconductor detectors for the detection [5]. Because of limited source intensity and detector sensitivity, these studies yielded only integrated two-dimensional distribution maps [6,7]. The tremendous improvements in synchrotron radiation as provided at the European Synchrotron Radiation Facility (ESRF, France) [8] allowed the transfer of the technique to photon

beams with intensities that are several orders of magnitudes higher. At the high-energy beamline ID15a of the ESRF, two 5 mm thick asymmetric-cut Si crystals working in fixed exit Laue – Laue mode provided the monochromatic beam. The crystals were bent such that a reasonable homogeneity of the beam was obtained over a 5 mm high and 20 mm wide surface at the sample position. To reduce background scattering by air, a vacuum tube was placed between the crystal and the sample. Two energies close to the K edge of uranium were then chosen to perform the tomographies: 114.6 keV and 116.6 keV with an energy resolution of about 0.25 keV. The intensity of the beam at the sample was of the order of 10^8 photons/s/mm².

A new detection system had to be developed, because under such high intensities traditional gamma ray detectors cannot operate. Since the detector, preferentially, should be able to handle high counting rates combined with a low granularity for the position sensitivity, we opted for a powder phosphor screen consisting of an 80 microns thick Gd₂O₂S:Tb layer. Using a 1:1 lens-optic, the screen is observed via a mirror by a CCD camera. The mirror keeps the camera out of the direct beam. The CCD has a sensitive area of 24.6×24.6 mm² for 1024×1024 pixels, a 14-bits dynamical range and is cooled to reduce electronic background. The resolution of the detection system is limited at high energies due to the light scattering in the phosphor screen [9]. We measured it to be approximately 50 μ m. This detector is illustrated in Figure 2.

Figure 2. Position-sensitive detector developed at ESRF to record high-energy photons



Various samples were scanned, including artificial objects. All were chosen such that the uranium concentration, distribution and granularity were very different, allowing the assessment of the possibilities of the method. Due to this wide variety of samples, the CCD camera had to measure with exposure times ranging from 0.025 to 2 seconds. The quantity of data was also adapted to the structure of the sample, by binning (or gathering) the pixels of the CCD to record photons using 100×100 μ m² or 50×50 μ m² macro-pixels.

The procedure used during the experiments was to position the sample, select the first photon energy and measure the attenuation for 200 different rotations of the sample. The samples being generally higher than the beam, the same procedure was repeated for different heights. After the whole sample was scanned, the beam energy was changed and the whole process repeated at the second energy. Moreover, after each energy change, the beam intensity and homogeneity were measured with the sample removed in order to normalise the data. Including the time to change energy, to rotate or move up the sample and the readout time of the CCD (2-3 seconds), a typical double scan of a $2 \times 2 \times 2$ cm³ sample took about two hours.

Results

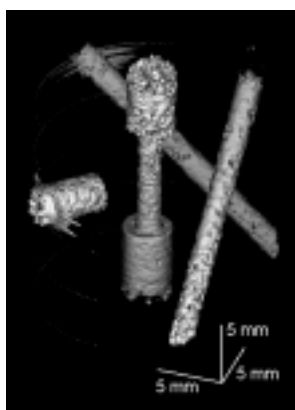
The quality of our data allowed us to analyse them using the filtered back-projection reconstruction technique. This is a well-known method, used in different kinds of medical

tomographies such as the classic computer tomography (CT), micro CT, positron emission tomography, etc. [10,11,12]. Because it is a direct method in contrast with iterative algorithms, it is also rather fast. On a PII-266 MHz PC, the reconstruction of a $2 \times 2 \times 2 \text{ cm}^3$ sample takes about one and a half hours. The software was developed on Labview and Visual C++. Only small modifications have been necessary to adapt this experiment to the algorithm, which is detailed in a previous paper [7].

A first example of the possibility of visualising uranium with the dual energy tomography is illustrated Figure 3a. The scan was done for an artificial sample consisting of an aluminium cylinder with holes drilled at different positions and filled with uranyl nitrate, a chemical compound ($\text{UO}_2(\text{NO}_3)_2 \cdot 6\text{H}_2\text{O}$) containing uranium.

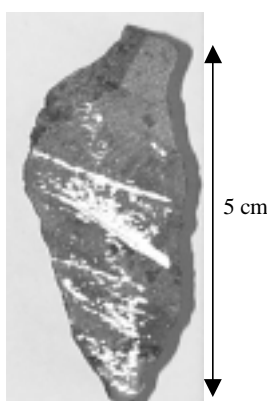
Figure 3a. Three-dimensional reconstruction of the uranium content of an artificial sample

Several holes were drilled at different positions and with different angles in an aluminium cylinder. The holes were then filled with uranyl nitrate (the mean density of uranium in this powder equals 1 g/cm^3). Granules can be clearly observed in the upper, less compressed part.



In the reconstruction, the aluminium container is not perceptible; moreover, the uranium distribution even shows inhomogeneities produced during the filling of the holes. Figure 3b shows a first application of this tomographic method to detect uranium in a volcanic rock from Newfoundland (Canada). The layered deposit of uranium can be precisely located and observed inside the stone.

Figure 3b. Three-dimensional reconstruction (in white) superposed on a picture of a 5 cm high volcanic stone containing uranium. It is seen that the uranium settled preferentially in layers.



The same method was then used to study five small crystallites of auternite found in Tessin (Switzerland) containing uranium. All were placed together in an aluminium container to be scanned

at the same time. Figure 4 shows the quality of the raw data for one out of the 200 projections. The figure illustrates how after subtraction of the two radiographs only the uranium distribution in the sample remains. Figure 5 displays the distribution in a slice of the sample, revealing the inner uranium repartition in the crystallites.

Figure 4. Image of the sample taken below (top) and above (middle) the K edge of uranium. The lower part shows the corresponding difference image yielding the uranium distribution.

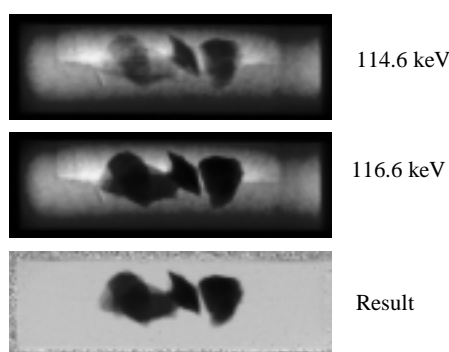
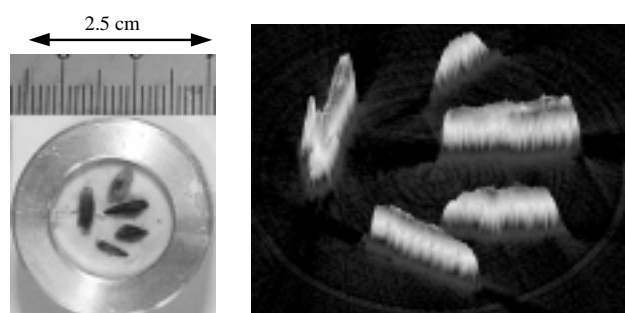


Figure 5. Left: Picture of the sample containing five crystallites found in Tessin (Switzerland). Right: Resulting 50 μm slice of the same sample; height is proportional to the uranium density



Another example of the possibilities of the method is the study of a stone containing pitchblende. This ore contains a large quantity of uranium oxide (U_3O_8) but the tomography shows that the compound neglects entire zones in the centre of the piece. This is shown on Figure 6.

Conclusion

It was shown that the heaviest natural element could be visualised by element sensitive tomography using synchrotron radiation above 100 keV. Important applications could lie in the study of diffusion processes of actinides, which is important for geology (Pb, Bi, Th, U), health physics (Rn) and nuclear waste storage (U, Ac, Pu).

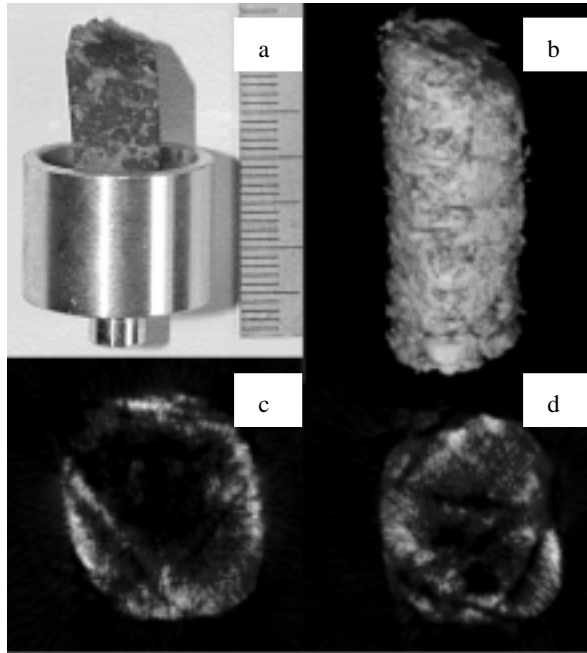
With this experiment, it was proved that the dual-energy tomography could be an impressive tool in the field of actinide research. First, the high energies used permit to scan quite thick and dense samples with a good spatial resolution. Then, the choice of a CCD-camera as detection system allows fast scans: the scanning time was only limited by the readout time of the CCD. It would also be of several magnitudes shorter than the time required to scan a sample using our earlier set-up at the linear accelerator in Ghent. Finally, the data analysis is fast enough to be performed during the experiment.

Figure 6. Here it is shown that uranium is not uniformly spread and neglects entire zones inside a stone with pitchblende (an ore containing essentially U_3O_8)

a. Picture of the stone in its aluminium support as it was scanned at the ESRF beamline.

b. Three-dimensional reconstruction of the uranium content.

c, d. Two slices taken at different heights. The thickness of the slices is 100 μm . Uranium is represented by white.



Acknowledgements

J.J. and Th.M. acknowledge financial support by the Swiss National Science Foundation, B.M. and W.M. from the Flemish Fund for Scientific Research – Flanders (Belgium) (FWO) and from the Research Board of the Gent University. We would like to thank Prof. M. Magetti and Dr. H. Zurbeck for lending us some of the samples.

REFERENCES

- [1] R. Lewis, *Phys. Med. Biol.* 42, 1213-1243 (1997).
- [2] L. Grodzins, *Nucl. Instr. and Meth.* 206, 547-552 (1983).
- [3] J. Fryar, K.J. McCarthy and A. Fenelon, *Nucl. Instr. and Meth.* A259, 557-565 (1987).

- [4] E. Storm and H.I. Israel, *Nucl. Data Tables* A7 (6) (1970).
- [5] M. Bertschy, M. Crittin, J. Jolie, W. Mondelaers and N. Warr, *Nucl. Instr. and Meth.* B103, 330-338 (1995).
- [6] M. Bertschy, J. Jolie and W. Mondelaers, *Applied Physics* A62, 437-443 (1996).
- [7] Th. Materna, J. Jolie, and W. Mondelaers, *Nucl. Instr. and Meth.* B149, 141-146 (1999).
- [8] Th. Tschentscher and P. Suortti, *J. Synchrotron Rad.* 5, 286-292 (1998).
- [9] A. Koch, *Nucl. Instr. and Meth.* A348, 654-658 (1994).
- [10] G.T. Herman, *Image Reconstruction from Projections*, New York: Academic Press, 1980.
- [11] A.C. Kak and M. Slaney, *Principles of Computerized Tomographic Imaging*, IEEE Press, 1988.
- [12] J.A. Parker, *Image Reconstruction in Radiology*, Boston: CRC Press, 1990.

CO-ORDINATION CHEMISTRY OF PENTA- AND HEXAVALENT ACTINIDE IONS (U, Np, Pu) UNDER HIGHLY ALKALINE CONDITIONS

**D.W. Keogh, D.L. Clark, S.D. Conradson, R.J. Donohoe, David E. Morris,
M.P. Neu, P.D. Palmer, R.D. Rogers, W. Runde, B.L. Scott, C.D. Tait**

Los Alamos National Laboratory
Los Alamos, NM 87545 USA
Glenn T. Seaborg Institute for Transactinium Science
Los Alamos, NM, USA

Abstract

From a historical perspective, the chemistry of actinide ions under strongly acidic conditions is relatively well known, while actinide chemistry under strongly alkaline conditions, such as those found in ageing waste tanks within the DOE complex, is less well understood. Highly alkaline conditions can favour actinide ions in high oxidation states such as V, VI and even VII. We have used EXAFS, single crystal X-ray diffraction (XRD), Raman and multinuclear NMR spectroscopy to determine the molecular structures of a variety of limiting penta- and hexavalent actinide complexes under highly alkaline solution conditions. The co-ordination chemistry, molecular and electronic structures, and ligand exchange dynamics will be discussed.

The hexavalent neptunyl and plutonyl ions (AnO_2^{2+}) are extremely soluble in 2-3.5 M NaOH and LiOH solution due to formation of anionic species, $\text{AnO}_2(\text{OH})_n^{2-n}$ ($\text{An} = \text{Np}, \text{Pu}; n = 4, 5$). The uranyl ion forms similar species in tetramethylammonium hydroxide (TMAOH) solution. Single crystal X-ray diffraction of An(VI) ions crystallised under alkaline conditions (tetramethylammonium hydroxide) revealed discrete molecular $\text{AnO}_2(\text{OH})_4^{2-}$ ($\text{An} = \text{U}, \text{Np}$) complexes in the solid state. Strong bonding of equatorial OH^- ligands result in a lengthening of the $\text{An} = \text{O}$ bond and large shifts (100 cm^{-1}) to lower energy in the Raman-active ν_1 stretch of these species. EXAFS spectroscopy indicates the presence of $\text{AnO}_2(\text{OH})_5^{3-}$ ($\text{An} = \text{U}, \text{Np}$) in solution. ^{17}O -NMR spectroscopy on UO_2^{2+} ions in 2.5-3.5 M OH^- reveals a water assisted chemical exchange between $\text{An} = \text{O}$ and An-OH units, and is confirmed by Raman spectroscopy on ^{18}O -enriched samples.

Luminescence spectroscopy of the U(VI) system showed that luminescence was almost entirely quenched at room temperature. However at liquid nitrogen temperature, the emission was greater than the U(VI) hydrolysis polymers. The emission spectroscopy also indicated the presence of two species in solution. A study was performed varying the hydroxide ion concentration, and showed the concentration of one of the species decreasing while the other increased. This data was coupled with the solution EXAFS data, which indicated a larger number of equatorial hydroxide ligands present in the solution ($n = 5$) compared to the solid ($n = 4$).

The pentavalent state can also be stabilised under these highly alkaline conditions. Cyclic voltammetry of the U(VI) species in 2.5 M TMAOH showed a reversible reduction, indicating a stabilisation of the U(V) state. Np(V) has also been prepared and studied using Raman spectroscopy and EXAFS. Both of these techniques show lengthened and weakened Np = O bonds with presumably shorter and stronger Np-OH bonds. The identical oxo-hydroxo exchange observed for the hexavalent system is also observed in the pentavalent case. The pentavalent systems are still under investigation and the most recent results will also be discussed.

EXAFS CHARACTERISATION OF EUROPIUM DIFFUSION IN HYDROXYAPATITE

Ph. Martin, A. Chevarier, N. Chevarier

Institut de Physique Nucléaire de Lyon

G. Panczer

Laboratoire de Physico-Chimie des Matériaux Luminescents
Université Claude Bernard – Lyon 1, 69622 Villeurbanne Cedex

C. Den Auwer

Commissariat à l'Énergie Atomique – DCC/DRRV/SEMP/LCTS
Marcoule, Bagnols sur Cèze 30207 Cedex

Abstract

In the context of radioactive waste disposal related to the back end of the nuclear fuel cycle, we studied the diffusion of europium in hydroxyapatite ($\text{Ca}_{10}(\text{PO}_4)_6(\text{OH})_2$), a material considered to be possible migration barrier in the nuclear waste storage process. Europium has been chosen here as a representative element of the group of fission products and of actinides elements.

Europium was implanted in the apatite targets using ion implantation with a nominal dose of $5 \cdot 10^{16}$ at.cm⁻² at an energy of 200 keV which places the europium in the subsurface of the samples (300 → 600 Å). Each target was annealed in air for different times within the temperature range of 400-600°C. Thermal diffusion was investigated using Rutherford Backscattering Spectroscopy. Results were analysed according to the Fick's second law, which provides the expression of the diffusion coefficient D. The diffusion coefficients obtained are low ($D = 1.5 \cdot 10^{-16}$ cm².s⁻¹ at 500°C) and a possible explanation is that europium ions substitute the calcium ions in the apatite structure and diffuse through these positions.

This assumption was backed by Time Resolved Laser Induced Fluorescence measurements showing that the europium ions substitute the calcium ions in both hydroxyapatite sites: i) the Ca^I site that is surrounded by nine oxygen atoms, and ii) the Ca^{II} site that is surrounded by six oxygen atoms and one hydroxyl group. However this technique is only sensitive to the europium ions which are in a crystallographic site (i.e. Ca positions).

In order to follow the europium environment after implantation and for different annealing conditions we performed Extended X-ray absorption fine structure (EXAFS) measurements using total yield detection. At constant temperature (500°C) an evolution of the EXAFS spectra is observed as a function of the annealing time. In the early stage of the diffusion process the europium ions are randomly distributed in the structure. But after twenty minutes of treatment the europium environment is stabilised, clearly showing the signature of the europium ions in the Ca^{II} sites. For lower

temperature (400°C), the same evolution is observed but for longer annealing time. This study shows that under thermal treatment the europium ions quickly moves to the Ca^{II} site and diffuse into the hydroxyapatite to the Ca sites.

**STRUCTURE OF URANIUM(VI), URANIUM(IV)
AND THORIUM(IV) SPECIES IN SOLUTION**

H. Moll, I. Farkas, F. Jalilehvand, M. Sandström, Z. Szabó, I. Grenthe

Department of Chemistry, Inorganic Chemistry
The Royal Institute of Technology
Teknikringen 30, 10044 Stockholm, Sweden

M.A. Denecke

Forschungszentrum Karlsruhe, INE
P.O. Box 3640, 76021 Karlsruhe, Germany

U. Wahlgren

Department of Physics, University of Stockholm
Box 6730, 11385 Stockholm, Sweden

Abstract

EXAFS investigations of aqueous U(IV) and Th(IV) solutions as well as of U(VI) in acidic and in highly alkaline systems are presented. Little structural information is available regarding the U(VI) hydroxide species formed in strong alkaline solutions. Therefore, we performed U L_{III} edge EXAFS measurements of a 0.05 M UO₂²⁺ solution in 0.1 M HClO₄ and of 0.055 M UO₂²⁺ solutions in tetramethylammonium hydroxide (TMA-OH), in order to determine uranium-oxygen bond distances and to verify the number of co-ordinated water molecules. Results are compared to geometry optimised data obtained from *ab initio* quantum chemical calculations. The number of co-ordinated water molecules in acidic solutions of approximately 0.05 M U(IV) and Th(IV) obtained from L_{III} edge EXAFS data are compared to that observed in large angle X-ray scattering experiments.

Introduction

Extended X-ray absorption fine structure (EXAFS) spectroscopy is a standard technique, providing information on co-ordination numbers and distances of a chosen atom to its nearest neighbours [1]. With this method information can be obtained on the speciation and structure of actinide complexes in aqueous and non-aqueous solutions as well as in solids. The application of synchrotron-based XAS in actinide research is becoming more and more important.

Little structural information is available on the uranium(VI) species in the high, $\text{pH} > 11$, region. The goal of the experiments presented here is to obtain more detailed information about the species formed, like $\text{UO}_2(\text{OH})_3^-$, $\text{UO}_2(\text{OH})_4^{2-}$ or $\text{UO}_2(\text{O})(\text{OH})_2^{2-}$. The EXAFS measurements should also clarify if trinuclear U(VI) hydroxide species are formed, as indicated by a solution chemical study by Palmer, *et al.* [2]. We have previously made theoretical quantum chemical calculations on the relative energy of $\text{UO}_2(\text{OH})_4^{2-} \cdot \text{H}_2\text{O}$ and $\text{UO}_2(\text{O})(\text{OH})_2^{2-} \cdot \text{H}_2\text{O}$, including geometry optimisation, which we want to validate with experimental observations. The structural parameters for U(VI) in highly alkaline systems are compared to those of the U(VI) aqua ion in acidic solutions.

As part of our study on the water exchange on actinide ions [3] we investigated the first hydration sphere of Th(IV) and U(IV) in acidic solutions in order to determine the bond distance and the co-ordination number of the co-ordinated water molecules. The structure of crystalline $\text{UO}_2(\text{s})$, and $\text{ThO}_2(\text{s})$ were investigated mainly for calibration purposes. EXAFS studies on the U^{4+} and Th^{4+} aqua ion are scarce. The co-ordination of Th(IV) and U(IV) in aqueous solutions containing perchlorate, chloride and nitrate was measured previously by large angle X-ray scattering [4,5]. This technique however, requires relatively high M^{4+} concentrations, 2 M or higher.

A comparison of the co-ordination number and bond distance of water in the M^{4+} aqua ions measured at lower metal concentrations (0.05 M) will be given.

Experimental

Sample preparation

The U(VI) and Th(IV) perchlorate stock solutions were prepared as described earlier [6,7]. The U(IV) stock solution was prepared from acidified $\text{UO}_2(\text{ClO}_4)_2$ solution by electrolysis using separated mercury cathode and platinum anode at a potential of 4 V. The stock solution was stored under argon. Appropriate aliquots of the stock solutions were taken to get a final concentration of approximately 0.05 M. The atomic surrounding of UO_2^{2+} was determined at two different tetramethylammonium hydroxide (TMA-OH) concentrations, 1 M and 3 M, respectively. TMA-OH was used to avoid the precipitation of insoluble alkali metal uranates in the high pH region. The structural parameters of the UO_2^{2+} , U^{4+} and Th^{4+} aqua ions were investigated in aqueous solutions of HClO_4 . The path length of the solutions containing uranium and thorium of approximately 0.05 M was 13 mm. The crystalline $\text{UO}_2(\text{s})$ used was supplied by ASEA ATOM. ThO_2 was prepared as described elsewhere [7]. Approximately 25 mg of MO_2 were mixed with polyethylene and pressed as 13 mm diameter pellets. This amount was calculated to give an edge jump of ~ 1.0 across the Th and U L_{III} absorption edges.

EXAFS measurements

The EXAFS investigations were performed at room temperature at SSRL in Stanford and HASYLAB in Hamburg. The EXAFS spectra were collected in transmission mode. The measurements at SSRL were performed on wiggler beamline 4-1 using a Si(220) double-crystal monochromator. The EXAFS transmission spectra measured at HASYLAB were recorded at the beamline A1 using a Si(311) double-crystal monochromator. The incident beam flux was reduced to ~50% of its maximum. Three EXAFS scans were collected from each sample and then averaged. For energy calibration of the sample spectra, the spectrum from a foil of yttrium was recorded simultaneously. The ionisation energies of the U L_{III} and the Th L_{III} electrons, E_0 , was arbitrarily defined as 17 166 eV and 16 300 eV, respectively. The data were treated using the WinXAS software [8]. Theoretical backscattering phase and amplitude functions used in data analysis were calculated for the model compounds, ThO_2 [9], UO_2 [10], and $\alpha-UO_2(OH)_2$ [11] using the FEFF7 [12] program. The theoretical U-O and Th-O phase and amplitude functions were tested by fitting Fourier-filtered first shell EXAFS of UO_2 and ThO_2 . The obtained results agreed within 1.5% for the M-O distance and within 12.5% for the co-ordination number. The MS path O-U-O (four-legged path) of the linear UO_2^{2+} unit was included in the model fitting of the U(VI) samples. The amplitude reduction factor, S_0^2 , was held constant at 1.0 for all the fits. The EXAFS oscillations were isolated using standard procedures for pre-edge subtraction, data normalisation and spline removal [1].

Results and discussion

The non-linear least squares curve fits were done over the range 3-13.5 \AA^{-1} for UO_2^{2+} in 0.1 M $HClO_4$ and 3.8-15.1 \AA^{-1} for UO_2^{2+} in TMA-OH on the raw EXAFS data. The bond length and co-ordination numbers obtained are summarised in Table 1.

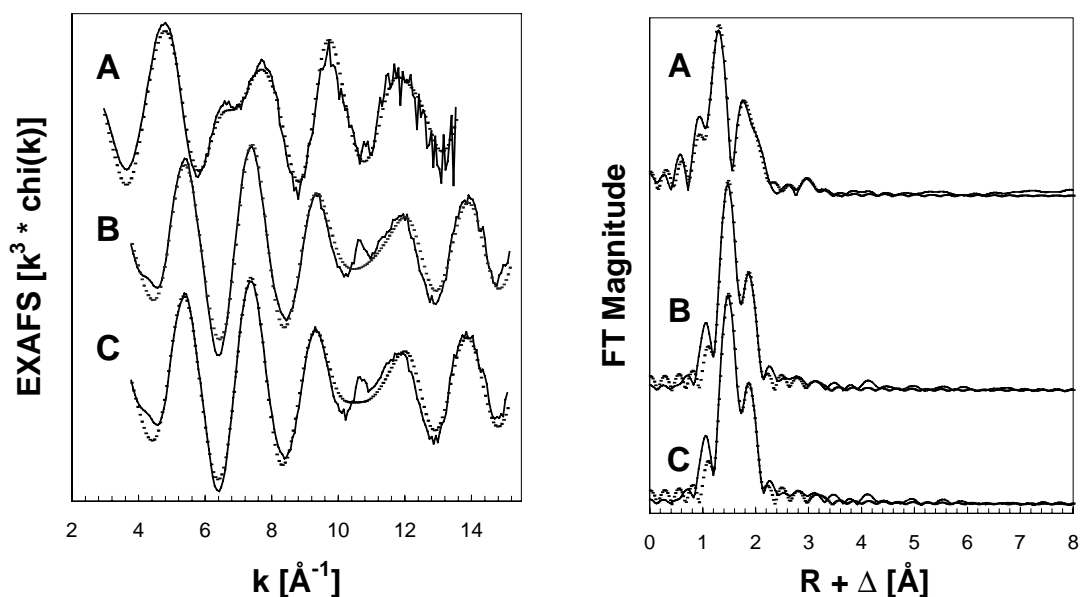
The EXAFS spectra measured and the corresponding FTs are shown in Figure 1. The EXAFS oscillations of U(VI) in 1 M TMA-OH and 3 M TMA-OH are very similar. The uranyl sample in the acidic pH region shows a different pattern of the EXAFS oscillation. The differences are more transparent in the FTs. The FTs are not corrected for the EXAFS phase-shift so that peaks appear at shorter distances ($R + \Delta$), relative to the true near-neighbour distances (R). The most intensive first peak in Figure 1 corresponds to the two axial oxygen atoms, O_{ax} , of the linear uranyl unit. The following peak represents the equatorial oxygen atoms, O_{eq} , co-ordinated around uranium in the equatorial plane. No significant intensity from U-U interactions at higher R-values could be observed in any of the spectra. The results show clearly that only mononuclear species are formed under high alkaline conditions in TMA-OH. The observation of mononuclear species contrasts reports of the formation of trinuclear U(VI) hydroxide species based on interpretation of solution chemical studies in Ref. [2]. The main difference between samples shown is a lengthening of the uranium-“yl” oxygen distance and a shortening of the U- O_{eq} distance, compared to the U(VI) aqua cation. This lengthening of the uranium-“yl” oxygen distance was also observed in U(VI) oxide precipitates prepared at pH values above 7 [13]. The co-ordination numbers and bond distances for the U(VI) aqua ion determined by EXAFS are consistent with results obtained by X-ray diffraction experiments published in Ref. [14]. The EXAFS analysis yielded 5 ± 0.5 oxygen atoms at 2.24 \AA for the UO_2^{2+} in TMA-OH samples, which is consistent with the formation of anionic hydroxyl complexes of the type $UO_2(OH)_n^{2-n}$. In order to draw more definite conclusions on the co-ordination number we have used the following additional information.

Table 1. EXAFS structural results measured for U^{4+} , Th^{4+} and UO_2^{2+} in acidic solution and UO_2^{2+} in highly alkaline solutions compared with structural parameters determined by quantum chemical calculations and large angle X-ray scattering experiments

Sample	Scattering path	N	R (\AA) ^a	σ^2 (\AA^2)	ΔE_0 (eV)	Reference
0.05 M U^{4+} in 1.5 M $HClO_4$	U-O	11.0 \pm 0.8	2.39 ₅	0.0095	1.1	This work
2 M U^{4+} in $HClO_4$	U-O	7-10.5	2.43			[5]
0.055 M Th^{4+} in 1 M $HClO_4$	Th-O	11.0 \pm 0.7	2.43 ₀	0.0069	1.3	This work
1-2.52 M Th^{4+} in 4.42-11.0 M $HClO_4$	Th-O	8	2.48 ₅			[4]
0.05 M UO_2^{2+} in 0.1 M $HClO_4$	U-O _{ax} U-O _{eq}	2.0 f 4.5 \pm 0.4	1.78 ₃ 2.41 ₄	0.0015 0.0062	-6.7 ^b	This work
1 M UO_2^{2+} in 1 M $HClO_4$	U-O _{ax} U-O _{eq}	2.0 5.0	1.702 2.421			[14]
$[UO_2(H_2O)_5]^{2+}$ <i>ab initio</i> quantum chemical calc.	U-O _{ax} U-O _{eq}	2.0 5.0	1.675 2.530			This work
0.055 M UO_2^{2+} in 1 M TMA-OH	U-O _{ax} U-O _{eq}	2.0 f 5.0 \pm 0.5	1.82 ₂ 2.24 ₇	0.0015 0.0056	3.7	This work
0.055 M UO_2^{2+} in 3 M TMA-OH	U-O _{ax} U-O _{eq}	2.0 f 5.2 \pm 0.5	1.82 ₂ 2.24 ₁	0.0014 0.0055	3.5	This work
$[UO_2(OH)_4]^{2-} \cdot H_2O$ <i>ab initio</i> quantum chemical calc., co-ordinated water	U-O _{ax} U-O _{eq1} U-O _{eq2}	2.0 2.0 2.0	1.720 2.410 2.485			This work
$[UO_2(OH)_4]^{2-} \cdot H_2O$ <i>ab initio</i> quantum chemical calc., non co-ordinated water	U-O _{ax} U-O _{eq1} U-O _{eq2}	2.0 2.0 2.0	1.719 2.327 2.360			This work

f: Parameter fixed during the fit, ^a: uncertainty of ± 0.005 to ± 0.01 \AA , ^b: E_0 defined as 17 185 eV.

Figure 1. Raw L_{III} edge k^3 -weighted EXAFS data and corresponding FTs measured for (A) 0.05 M UO_2^{2+} in 0.1 M $HClO_4$, (B) 0.055 M UO_2^{2+} in 1 M TMA-OH, and (C) 0.055 M UO_2^{2+} in 3 M TMA-OH. The solid line is the experimental data, and the dashed line represents the best theoretical fit of the data.

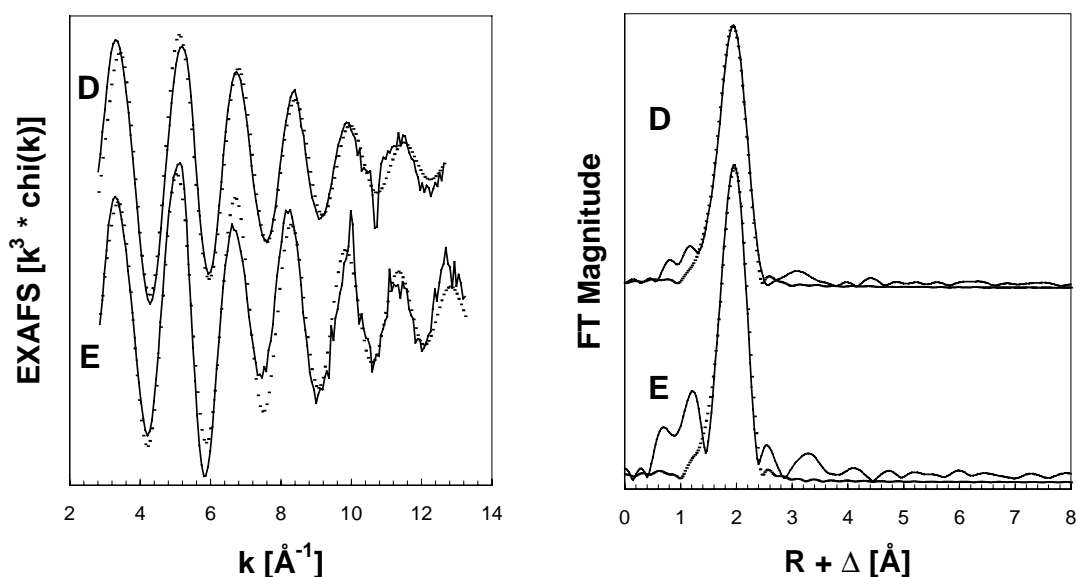


The structural parameters determined in this study, which was started two years ago, agree with results presented at the Actinides'97 conference by Clark, *et al.* [15]. Clark, *et al.* [15] reported an U-OH distance of 2.258 Å in the crystal $[Co(NH_3)_6]_2[UO_2(OH)_4]_3 \cdot 2H_2O$. In this solid structure U(VI) is surrounded by 4 OH⁻ ligands with a distance similar to the value determined in highly alkaline solutions. This suggests that also in the solutions tested the dominant co-ordination number should be 4. The formation of $UO_2(OH)_4^{2-}$ species results in lengthening of the U-O_{ax} bond distance of about 0.04 Å, compared to the U(VI) aqua ion. The OH⁻ ligands are strongly bonded to U(VI), indicated by the short bond distance of 2.24 Å of the O_{eq} atoms. This short distance is a strong indication of a decreased co-ordination number in the species present at high alkaline conditions compared to the U(VI) aqua species. *Ab initio* quantum chemical calculations including geometry optimisation were performed on $UO_2(OH)_4^{2-} \cdot H_2O$ containing either a co-ordinated or a non-co-ordinated water, c.f. Table 1. The calculations showed that only the average bond distance for the model with the non-co-ordinated water is compatible with the experimental observations. Hence, there are only four co-ordinated OH⁻ ions in the complex. Theoretical calculations were also made on $UO_2(H_2O)_5^{2+}$. A comparison of the uranium "yl"-oxygen distances shows that the bond distance is 0.044 Å longer in $UO_2(OH)_4^{2-}$ than in $UO_2(H_2O)_5^{2+}$. This agrees very well with the EXAFS data. The absolute distance values show differences, whereas the relative values agree quite well. This problem will be discussed in a lecture of U. Wahlgren during the Actinide-XAS'98 conference. The calculations also showed a shortening of the average U-O_{eq} bond distance of about 0.19 Å in $UO_2(OH)_4^{2-}$, compared to the U(VI) aqua ion. The experimental value of 0.17 Å is again in very good agreement. Both EXAFS measurements and *ab initio* quantum chemical calculations support that the mononuclear species, $UO_2(OH)_4^{2-}$, is dominant in high alkaline solutions. No further evidence for the appearance of the equivalent species $UO_2O(OH)_2^{2-}$ was observed. The calculations also indicated that the preferred

geometry is four co-ordinated. The co-ordination of an additional water molecule results in a lengthening of the U-O_{eq} distance (see Table 1) which was not observed. IR and Raman measurements are in progress to obtain more detailed experimental information about the geometry of the mononuclear anionic hydroxide complexes of U(VI) formed in the high alkaline region.

The isolated EXAFS oscillations from U⁴⁺ and Th⁴⁺ in acidic solution are shown in Figure 2.

Figure 2. Raw L_{III} edge k³-weighted EXAFS data and corresponding FTs for (D) U⁴⁺ and (E) Th⁴⁺ samples in perchloric acid. The solid line is the experimental data, and the dashed line represents the best theoretical fit of the data.



The EXAFS oscillations of both samples is dominated by the M-O interaction of the first hydration sphere. The oscillation of Th(IV) has a slightly longer period length which results from a longer M-O bond distance. The difference between the U-O (N: 10-12, R: 2.39 Å) and Th-O (N: 10-12, R: 2.43 Å) in the aqua ion is around 0.04 Å. This reflects the difference of the ionic radii of U(IV) and Th(IV) of 0.05 Å [16], indicating that the co-ordination number is the same (see Table 1). The reported hydration numbers of tetravalent actinides cover a range of values [4,5,17]. The structural parameters of the co-ordination around U⁴⁺ in aqueous ClO₄⁻ solutions determined by EXAFS and large angle X-ray scattering experiments (N: 7-10.5, R: 2.43 Å) are in agreement [5]. The EXAFS M-O bond distances are slightly shorter. An EXAFS amplitude comparison of U⁴⁺ in perchloric acid (Figure 2), UO₂ where U(IV) is 8-coordinated, and Ba₂U(C₂O₄)₄·8H₂O where U(IV) is 9-coordinated indicated a co-ordination number of H₂O higher than 9 for the U(IV) aqua ion. The Th⁴⁺ results showed an oxygen co-ordination number of around 11. Johansson, *et al.* determined eight water molecules with a distance of 2.48 Å. In [4], higher co-ordination numbers than eight of the first co-ordination sphere of Th(IV) in aqueous Cl⁻ and NO₃⁻ solutions are reported. This increased co-ordination numbers result from inner-sphere complex formation of Th⁴⁺ with Cl⁻ and NO₃⁻. A weak inner-sphere complex formation of Th⁴⁺ with ClO₄⁻ in dilute solutions described in [4] may also explain the co-ordination number measured. However, the results presented in this paper suggest that the number of bonded water molecules in the first hydration sphere of Th⁴⁺ and U⁴⁺ is higher (N: 10-12) than 8 as reported in previous published papers [4,5]. Furthermore, the uncertainties in the

co-ordination number determination by EXAFS is $\pm 25\%$, making it impossible to distinguish between hydration numbers of 10 and 12 at the 95% confidence level. The results are also consistent with structural parameters for the tetravalent actinide element neptunium, Np^{4+} : $N = 11.2$, $R = 2.40 \text{ \AA}$, published in [17]. Further measurements and quantum chemical calculations will be carried out to validate the number of co-ordinated water molecules.

Acknowledgements

This work was supported by the European Commission within the Training and Mobility of Researcher (TMR) Programme under contract no. ERBFMBICT972296. A part of the measurements were done at SSRL which is operated by the US Department of Energy. The other experiments were performed at HASYLAB.

REFERENCES

- [1] X-ray Absorption: Principles, Applications, Techniques for EXAFS, SEXAFS and XANES, D.E. Koningsberger, R. Prins, eds., Wiley-Interscience: New York (1988).
- [2] D.A. Palmer, C. Nguyen-Trung, *J. Sol. Chem.* 24 (12), 1281-1291 (1995).
- [3] I. Bányai, I. Farkas, I. Grenthe, Water Exchange on Actinide Ions: A Variable Temperature ^{17}O NMR Study of U^{4+} , Th^{4+} and UO_2^{2+} , in preparation (1998).
- [4] G. Johansson, M. Magini, H. Ohtaki, *J. Sol. Chem.* 20 (8), 775-792 (1991).
- [5] S. Pocev, G. Johansson, *Acta Chem. Scand.* 27 (6), 2146-2160 (1973).
- [6] L. Ciavatta, D. Ferri, I. Grenthe, F. Salvatore, *Inorg. Chem.* 20, 463 (1981).
- [7] I. Grenthe, B. Lagerman, *Acta Chem. Scand.* 45, 231-238 (1991).
- [8] T. Ressler, *J. Synchrotron Rad.* 5, 118-122 (1998).
- [9] F. Hund, W. Duerrwächter, *Z. anorg. Allg. Chem.* 265, 67-72 (1951).
- [10] S.A. Barrett, A.J. Jacobson, B.C. Tofield, B.E.F. Fender, *Acta Cryst.* B38, 775-2781 (1982).
- [11] J.C. Taylor, *Acta Cryst.* B27, 1088-2022 (1971).
- [12] S.I. Zabinsky, J.J. Rehr, A. Ankoudinov, R.C. Albers, M.J. Eller, *J. Phys. Rev.* B52 (4), 2995-3008 (1995).

- [13] P.G. Allen, D.K. Shuh, J.J. Bucher, N.M. Edelstein, C.E.A. Palmer, R.J. Silva, S.N. Nguyen, L.N. Marquez, E.A. Hudson, *Radiochim. Acta* 75, 47-53 (1996).
- [14] M. Åberg, D. Ferri, J. Glaser and I. Grenthe, *Inorg. Chem.* 22, 3986-3989 (1983).
- [15] D.L. Clark, S.D. Conradson, D.W. Keogh, M.P. Neu, P.D. Palmer, R.D. Rogers, W. Runde, B.L. Scott, C.D. Tait, Co-ordination Chemistry of Actinide Ions under Highly Alkaline Conditions, lecture presented at the Actinides'97 International Conference, Baden-Baden, Germany, 21-26 September 1997.
- [16] Chemistry of the Elements, N.N. Greenwood, A. Earnshaw, Pergamon Press: Oxford, (1984).
- [17] P.G. Allen, J.J. Bucher, D.K. Shuh, N.M. Edelstein, T. Reich, *Inorg. Chem.* 36, 4676-4683 (1997).

**STUDY OF CHEMICAL STATE OF TOXIC METALS DURING THE LIFE CYCLE
OF FLY ASH USING X-RAY ABSORPTION NEAR-EDGE STRUCTURE**

János Osán, Balázs Török, Szabina Török

KFKI Atomic Energy Research Institute
P.O. Box 49, H-1525 Budapest, Hungary

Keith W. Jones

Brookhaven National Laboratory
Upton, NY 11973, USA

Abstract

The X-ray absorption near edge structure (XANES) method was applied for the quantitative determination of chromium and arsenic species in coal fly ash. In order to study the chemical state changes caused by deposition and sedimentation of the particles, land fill and river sediment samples obtained in the neighbourhood of power plants were also investigated. For achieving quantitative results on the ratio of close lying oxidation state forms, a non-linear fitting model was developed to process the obtained XANES spectra. The features of the spectra such as the white line, the multiple scattering resonance peak and the absorption edge are modelled with analytical functions. The results obtained show that chromium is present mostly (> 95%) as Cr(III) in fly ash and the chemical state remains the same after deposition and sedimentation. Arsenic is present in pentavalent form in fly ash and land fill samples, while the possible As(III) content of sediment samples is around 40%.

Introduction

The toxicity of metals depends strongly on their oxidation state, therefore studying exclusively the chemical composition of environmental samples is not sufficient. Fly ash related environmental samples are often heterogeneous; they include metals in a mixture of different chemical state forms. Therefore the aim of our present research was twofold: (i) to obtain quantitative analytical results for the ratios of the different oxidation states of trace elements by fitting the major features of the XANES spectra by analytical functions, and (ii) to study the chemical state of chromium and arsenic during the deposition and weathering of fly ash using the XANES method.

The XANES method uses high intensity monochromatic X-ray beams originating either from laboratory sources or synchrotron radiation. From the near edge part of the absorption spectrum one can deduce information on the chemical state of the element of interest. Changes in the charge distribution around a given atom in different chemical environments can alter the binding energies of core electron orbits, so that the XANES spectrum shows a shift in the absorption edge. A more oxidative chemical environment results in deeper core state binding energies, which in turn cause an absorption edge shift towards higher energies in the XANES spectrum. The order of magnitude of the shift is around 1-3 eV per valence change. The presence or absence of the possible pre-edge structure and the energies of the near-edge structures (white line and multiple scattering resonance peak) are also dependent on the oxidation state of the absorbing atom.

XANES spectroscopy has a wide range of environmental applications. Kawai *et al.* [1] studied the depth profile of the oxidation state of sulphur on coal fly ash samples using simultaneous detection of the fluorescent X-ray photons and the sample current. The disadvantage of the method is that the surface sensitive total electron yield method can only be applied in the low energy range. Huffman, *et al.* applied the XANES method for sulphur speciation in coal [2]. Changes of the sulphur oxidation state were observed during high temperature oxidation and pyrolysis of coal [3]. Waldo, *et al.* [4,5] studied the chemical environment of sulphur in petroleum and in heavy oil. The sulphur analyses were characterised by low X-ray energy, wide oxidation state range and concentrations in the percentage range. Bajt, *et al.* [6] studied the oxidation state of chromium in cemented wastes, which is of high importance because the toxic chromate ion is much more mobile, so that it can leach easier into the soil above the waste.

Interest in the fly ash emitted by coal-fired power stations has risen in recent years because of the diminishing public acceptance of nuclear power and the realisation that reliance on coal-fired plants may be necessary. The yearly production of ash in Hungary amounts to two million tonnes [7]. Coal fly ash has relatively elevated concentrations of toxic metals such as chromium, arsenic and lead. In the lignite fired power plants in Hungary, where the fuel is obtained from open pit mines in the neighbourhood of the power plants, the obtained ash is returned to the mine pit in a slurry form for disposal. During deposition and due to weathering processes the toxic metals in the fly ash can be transported to soil, rivers and vegetation.

Materials and methods

Samples

The fly ash samples were obtained from the electrostatic filters of three Hungarian coal fired power plants. In the Ajka power plant located in the western part of Hungary brown coal is burnt.

The Borsod and Visonta power plants are located in the north-eastern region of Hungary and use young lignite as fuel. The land fill sample from about 30 cm beneath the surface was taken near the village of Markaz (1 km away from the Visonta power plant) using a soil borer. River sediment for sampling was obtained by means of an Ekman–Birger sediment grab sampler at a distance of 1 m from the bank of the river Sajó, which is near the Borsod power plant. The samples were stored in a refrigerator prior to analysis. For the XANES measurements bulk samples containing 0.5-1 g of fly ash, soil or sediment material were pelletised. The thickness of the bulk samples was 1-2 mm. Single fly ash particles of a diameter of 50-100 μm obtained from the Borsod power plant were mounted onto Formvar film.

XANES measurements

The measurements were carried out at the X26 beam line of the Brookhaven National Synchrotron Light Source (NSLS, Upton, NY, USA). The NSLS source is characterised by the following parameters: electron energy 2.53 GeV, critical energy 5.0 keV, maximum ring current about 250 mA. The X-ray microscope (XRM) installed at this beam line utilises the continuous X-ray spectrum produced by the bending magnet. The flux for photon energies above 4 keV is about 2×10^7 photons $\mu\text{m}^{-2} \text{s}^{-1} \text{mA}^{-1}$ at 9 m from the X-ray ring. In our experiments a Si(Li) detector with an area of 30 mm^2 and an energy resolution of 160 eV placed at 90° to the incident beam was used to detect the fluorescent X-rays. Samples were mounted on an x-y sample stage and visualised by an optical microscope.

The absorption spectra were recorded in the fluorescent mode, tuning the excitation energy near the absorption edge of the element of interest by stepping a channel cut Si(111) monochromator. The corresponding fluorescent X-rays were detected by the Si(Li) detector. The beam size was defined by a $100 \times 100 \mu\text{m}$ slit just upstream from the sample. The beam size was optimised in order to obtain sufficient beam intensity for measurements on samples with concentrations of the element of interest less than 100 $\mu\text{g/g}$. The minimum detection limit of this technique for the elements of interest (Cr, As) was in the range of 10 $\mu\text{g/g}$ for bulk samples. The energy resolution of the monochromator at 6 keV was 1 eV and the beam intensity at this energy was about 4×10^{10} photons s^{-1} at 200 mA ring current [8].

Fitting model for XANES spectra

The aim of the analysis is the quantitative determination of the ratio of different chemical state forms that can be achieved by different approaches. Studying exclusively the absorption edge shift is not sufficient, since the white line ($1s \rightarrow np$ transition) can overlap with the true absorption edge. In such elements, where a pre-edge peak shows up in the XANES spectrum ($1s \rightarrow nd$ transition is allowed, e.g. CrO_4^{2-} , Ti^{4+} , V^{5+} , Mn^{7+}) [9], which is specific for a given oxidation state, the ratio is proportional to the normalised intensity of the pre-edge peak. The peak area is normalised to the absorption in the infinity. This method is applicable for chromium where the pre-edge peak is characteristic for Cr(VI) [6]. In the present study this method was applied for chromium spectra.

If standards are measured for all the forms of the element of interest possibly present in the sample, the spectrum of the unknown can be approximated as the linear combination of the standard spectra. Waldo, *et al.* applied this method for the XANES spectra of sulphur [4]. Gorbaty, *et al.* developed a differential method for modelling the sulphur XANES spectra and showed that the peak

amplitudes in the third derivative spectrum are proportional to the relative amounts of sulphidic and thiophenic sulphur [10]. For separation of close lying oxidation states the least squares fitting of XANES spectra provides better results than the methods mentioned above. This method was first applied to the spectra obtained at the sulphur K absorption edge by Huffman, *et al.* [2]. This model fits a series of s → p transition peaks, resonance scattering peaks and an arctangent function representing the transition from the core state to the continuum.

The model developed by our group is also based on least squares fitting of analytical functions to the XANES spectra. For each oxidation state the spectrum can be approximated by the linear combination of three analytical functions: one for the white line, one for the multiple scattering peak and one for the absorption edge. For each oxidation state form the white line should be approximated by Lorentzian curves, however, for thick or concentrated samples the curves broaden to almost pure Gaussian curves because of scattering effects. For the spectra of bulk samples we used only Gaussian curves for the fitting of both the white line and the multiple scattering resonance peak. For the description of the absorption edges we used arctangent functions. The approximating function was the following:

$$\tau(E) = \sum_{i=1}^n \left[I_{wi} \exp\left(-\frac{(E - E_{wi})^2}{2\sigma_{wi}^2}\right) + I_{si} \exp\left(-\frac{(E - E_{si})^2}{2\sigma_{si}^2}\right) + C_i \left(\frac{1}{\pi} \arctan \frac{E - E_{ei}}{\Gamma_i / 2} + \frac{1}{2}\right) \right] \quad (1)$$

where n is the number of the oxidation state forms, I_{wi} and I_{si} are the heights of the white line and the resonance scattering peaks for the i^{th} oxidation state, σ_{wi} and σ_{si} are the corresponding widths, E_{wi} and E_{si} are their maximum energy, C_i is the height of the absorption edge, E_{ei} is the energy of the inflexion point and Γ_i is the parameter of the arctangent step. For the single particle spectra where the self-absorption was negligible, the best fitting results were obtained when the shape of the white line was approximated as a mixture of Lorentzian and Gaussian contribution [11].

Results and discussion

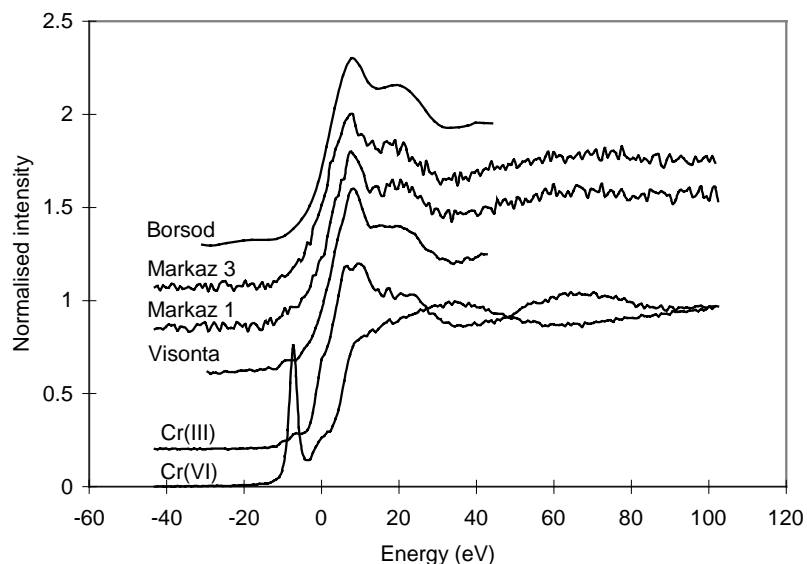
Chromium K edge

XANES spectra for the chromium K edge were collected on bulk fly ash (Visonta, Borsod) and soil (Markaz) samples. Due to the low chromium concentration (<50 µg/g) measurement of single fly ash particles was not possible. Figure 1 shows XANES spectra of the Cr(III), Cr(VI) standards (Cr₂O₃ and K₂CrO₄) and of the environmental samples studied. The zero of the energy scale was set to the inflexion point of the Cr(III) standard. Spectra of each sample show the two broad peaks corresponding to Cr(III). The normalised intensity of the pre-edge peak characteristic for the more toxic Cr(VI) form was calculated according to Bajt *et al.* [6]. Since the normalised pre-edge peak intensity is below 5% for all the samples investigated, the chromium is present in fly ash and land fill mostly (> 95%) in the less toxic +3 oxidation state form. The oxidation state of chromium did not change significantly during the weathering process of fly ash.

Arsenic K edge

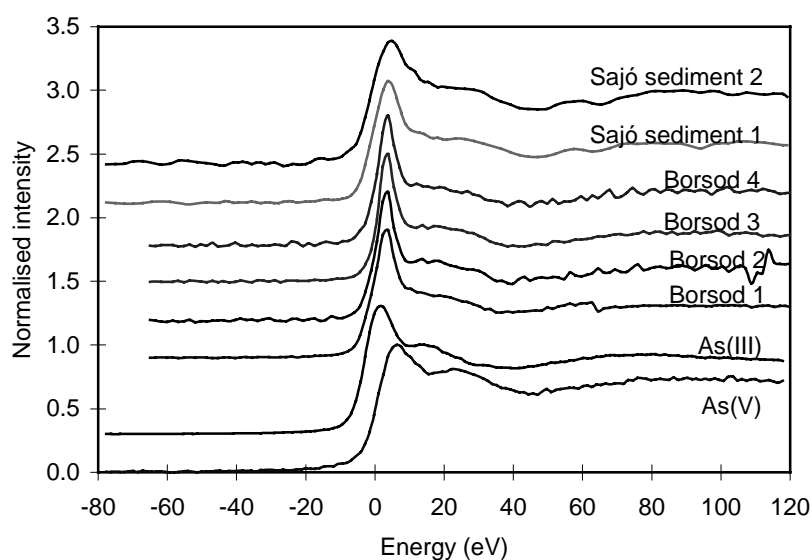
XANES measurements were also carried out near the K absorption edge of arsenic. Fly ash particles obtained from the electrostatic filters of Hungarian coal fired power plants (Ajka, Borsod),

Figure 1. XANES spectra obtained at the chromium K edge for fly ash (Visonta, Borsod) and land fill (Markaz) samples and two standards for Cr(III) and Cr(VI). The zero of the energy scale is set to the absorption edge of Cr₂O₃



land fill (Markaz), river sediment (Sajó) and dried plant leaf materials were investigated. The arsenic concentration of the Borsod fly ash sample was sufficiently large (around 600 $\mu\text{g/g}$) for single particle XANES measurements. XANES spectra around the As K edge were measured on bulk samples. As₂O₃ and Na₂HAsO₄ were used as standards for As(III) and As(V). The X-ray absorption spectra obtained are shown in Figure 2. The zero of the energy scale is set to the 1s \rightarrow 4p transition energy of As₂O₃.

Figure 2. XANES spectra around the arsenic K edge for four single fly ash particles (Borsod), two sediment samples from river Sajó and standards for As(III) and As(V). The zero of the energy scale is set to the 1s \rightarrow 4p transition energy of the As₂O₃ standard.



The spectra of single fly ash particles were not significantly different. Spectra of all other environmental samples show similar shape to those of the single fly ash particles, but the broadening of the white line is higher due to the larger sample thickness. The spectra of the two standards differ significantly in the absorption edge position, the difference of the edges is 4 eV. All arsenic XANES spectra contain a strong white line and scattering resonance peaks, which mask the true position of the absorption edge. For samples having higher arsenic concentration or higher thickness the self-absorption can become important resulting in broadening of the lines. Therefore the processing of the arsenic XANES spectra was carried out using the least squares fitting model.

Peak areas obtained by the least squares fitting method are tabulated in Table 1. The quality of the fit is described by the root mean square of deviations. Results of all samples show that arsenic in fly ash and in the land fill material is mostly (> 90%) in As(V) form. The As(III) content of the sediment sample is significantly different from all of the others, the possible As(III)/total As ratio is around 40%. Obviously the sediment might contain particles of various origin, not exclusively fly ash.

Table 1. Peak area percentages and fitting parameters of the white lines of the two oxidation states according to Eq. (1)

	As(III) (%)	As(V) (%)	I_{w1}	I_{w2}	σ_w (eV)	Root mean square
Ajka	9	91	0.24	2.30	3.59	0.032
Borsod 1	1	99	0.03	2.80	3.59	0.047
Borsod 2	2	98	0.08	4.27	3.01	0.046
Borsod 3	0	100	0.00	3.58	2.82	0.038
Borsod 4	0	100	0.00	3.31	3.08	0.079
Markaz	4	96	0.10	2.29	3.64	0.016
Sajó 1	40	60	1.03	1.53	3.41	0.028
Sajó 2	14	86	0.39	2.35	3.31	0.048

Conclusions

XANES is useful for non-destructive chemical speciation of toxic metals and using the new spectrum processing method it can provide quantitative results as well. For concentrations above 100 µg/g even single particles of a diameter of 50-100 µm can be analysed non-destructively. Thus, the use of synchrotron XRM can be extended to refine the detailed characterisation of fly ash particles or other industrial dust. Information on the toxicity change of chromium and arsenic during the life cycle of fly ash can be obtained by XANES study of the oxidation state.

Several new synchrotron facilities (ESRF, APS, SPring-8) in operation now will offer X-ray beams which are three to four orders of magnitude brighter than those produced by the NSLS. The use of these sources and the possibility of demagnifying the SR beam by advanced focusing techniques such as Bragg-Fresnel lenses or capillary optics will decrease the incoming beam size, enabling small area trace element speciation.

Acknowledgements

This work was supported by the Hungarian Science Foundation (OTKA 2894), the US-Hungarian Joint Board on Scientific and Technological Co-operation (Grant No. 111/91) and the Division of Chemical Sciences, Office of Basic Energy Sciences, US Department of Energy (Contract No. DE-AC02-76CH00016).

REFERENCES

- [1] J. Kawai, S. Hayakawa, F. Esaka, S. Zheng, Y. Kitajima, K. Maeda, H. Adachi, Y. Gohshi and K. Furuya, *Anal. Chem.* 34, 1526 (1995).
- [2] G.P. Huffman, S. Mitra, F.E. Huggins, N. Shah, S. Vayida and F. Lu, *Energy Fuels* 5, 574 (1991).
- [3] M.M. Taghiei, F.E. Huggins, N. Shah and G.P. Huffman, *Energy Fuels* 6, 293 (1992).
- [4] G.S. Waldo, R.M.K. Carlson, J.M. Moldowan, K.E. Peters and J.E. Penner-Hahn, *Geochim. Cosmochim. Acta* 55, 801 (1991).
- [5] G.S. Waldo, O.C. Mullins, J.E. Penner-Hahn and S.P. Cramer, *Fuel* 71, 53 (1992).
- [6] S. Bajt, S.B. Clark, S.R. Sutton, M.L. Rivers and J.V. Smith, *Anal. Chem.* 65, 1800 (1993).
- [7] Statistical Data, *Hungarian Electricity Board*, Budapest, 1 (1992).
- [8] W.M. Kwiatek, A.L. Hanson and K.W. Jones *Nucl. Instrum. Methods Phys. Res.* B50, 347 (1990).
- [9] A. Bianconi, E. Fritsch, G. Calas and J. Petiau, *Phys. Rev.* B32, 4292 (1985).
- [10] M.L. Gorbaty, G.N. George and S.R. Kelemen, *Fuel* 69, 939 (1990).
- [11] J. Osán, B. Török, Sz. Török and K.W. Jones, *X-Ray Spectrom.* 26, 37 (1997).

**STRUCTURAL ANALYSIS OF THE INTERACTION OF URANIUM(VI)
WITH HUMIC ACID AND SIMPLE CARBOXYLIC ACIDS USING EXAFS**

T. Reich, V. Brendler, M.A. Denecke, M. Bubner, S. Pompe, H. Nitsche

Forschungszentrum Rossendorf e. V.
Institute of Radiochemistry
P.O. Box 510119, D-01314 Dresden, Germany

P.G. Allen

Lawrence Berkeley National Laboratory
Chemical Sciences Division
Berkeley, California 94720, USA

Abstract

Structural analysis of eight aqueous uranyl carboxylates by EXAFS reveals three basic types of near-neighbour environments: bidentate ligation of the COO^- group, monodentate ligation of the COO^- group with and without oxo-bridge between the uranyl units. In uranyl humates, the COO^- group acts predominantly as monodentate ligands.

Introduction

In the vicinity of former uranium mining and processing sites in Erzgebirge, Germany, uranium(VI) can be present in the environment in the form of aqueous uranyl complexes or surface complexes sorbed onto soil, rocks or minerals. In aqueous solution, the interaction of uranyl ions, UO_2^{2+} , with humic substances can play an important role in determining the migration behaviour of uranium in the environment. Humic acids (HAs) as part of humic substances are polyelectrolytic organic macromolecules which possess a variety of functional groups [1]. Among them, COO^- and phenolic OH groups are the most important. To understand the complexation and transport behaviour of HAs, it is necessary to examine the co-ordination chemistry of uranyl ions with simple carboxylic acids which have the same functional groups as in HA. X-ray absorption spectroscopy (XAS) can provide structural information like bond distances and co-ordination numbers for the interaction of uranyl ions with COO^- and OH groups of carboxylic acids in solid and aqueous systems [2].

We determined extended X-ray absorption fine structure (EXAFS) structural parameters of eight different uranyl complexes with simple aliphatic and aromatic carboxylic acids in aqueous solution. Depending on the co-ordination geometry adopted by the ligands, characteristic bond distances were observed between uranium and its neighbouring oxygen and carbon atoms. This can guide the interpretation of EXAFS structural parameters of uranyl humate.

Experimental

Aqueous solutions of uranyl complexes with acetic, phthalic, maleic, malonic, succinic, malic, citric and tartaric acids were prepared by dissolving uranyl nitrate hexahydrate and the corresponding acid in double-distilled water. Prior to sample preparation, the desired uranium to ligand ratio (U:L) and pH value were calculated so that only one uranyl species would be present in the solution. For the speciation calculation we used the software package RAMESSES [3] and published complexation and dissociation constants of the carboxylic acids [4-8]. The speciation calculations also included the hydrolysis equilibrium of the uranyl ion [9]. According to the speciation calculations, more than 95% of the uranium in solution is present in the form of the desired uranyl complex with a specific U:L ratio (see Table 1). The final pH readings and uranium and ligand concentrations of the prepared solutions are given Table 1.

Uranyl humate was prepared by dissolving 70g HA/L synthetic HA [1] and adding a uranyl perchlorate solution. The pH of the solution was adjusted to 3.9 and the ionic strength to 1 mol/L. The uranium concentration of the solution was 10^{-3} mol/L. This amount of uranium equals 7.5% of the proton exchange capacity of the HA which is measured as the number of COO^- groups.

XAS measurements were performed at room temperature using Si(220) double-crystal monochromators on wiggler beamlines 4-1 and 4-3 and on the bending magnet beamline 2-3 at the Stanford Synchrotron Radiation Laboratory (SSRL). Most spectra were measured in transmission mode, where the incident and transmitted X-ray flux were monitored by Argon-filled ionisation chambers. Due to a lower uranium concentration in solutions with maleic acid and HA, the XAS spectra were measured in fluorescence mode using a four-pixel Ge solid state detector. For energy calibration purposes, a uranyl reference was placed downstream from the sample and measured simultaneously. EXAFS data reduction followed standard procedures, using the EXAFSPAK software package [10].

Results and discussion

Figure 1 shows the raw k^3 -weighted EXAFS data for the uranyl acetate (1), phthalate (2), maleate (3), malonate (4), succinate (5), malate (6), citrate (7) and tartrate (8) solutions. Solely on the basis of similarities and differences in the raw data, the EXAFS spectra of the uranyl carboxylates can be placed into Classes A, B, and C. Class (A) consist of Samples 1 and 5. Their EXAFS spectra show a pronounced shoulder at 6.2 \AA^{-1} which is absent in all other spectra (see Figure 1). A weak increase in EXAFS amplitude of Samples 2 and 3 in the range of $6.2\text{-}7.6 \text{ \AA}^{-1}$ is characteristic for Class (B). Finally, Samples 4 and 6-8 form Class (C). Its characteristic feature is a reproducible fine structure on top of a decreasing EXAFS amplitude over the $6.6\text{-}8.0 \text{ \AA}^{-1}$ range. Spectra belonging to the same class show a close agreement in the phase as well in the amplitude of all features in k space.

Figure 2 shows FTs for one representative of each Class (A)-(C), e.g. uranyl acetate (1), maleate (3), and malonate (4). The first peak in the FT at 1.3 \AA (uncorrected for scattering phase shift), which is due to oxygen atoms, O_{ax} , of the linear UO_2^{2+} group, is similar for all classes. The second uranium co-ordination shell consists of oxygen atoms, O_{eq} , lying in the equatorial plane of the UO_2^{2+} group. For Samples 3 and 4, this O_{eq} co-ordination shell gives rise to a peak at 1.8 \AA . As can be seen in Figure 2, for Sample 1 this peak is broadened and shifted toward a larger distance to the uranium. Another noticeable difference between Classes (A)-(C) is the appearance of a peak at 3.8 \AA in the FTs of Samples 1 and 4. In contrast, the FT of Sample 3 does not show any intensity in that region. Based on the inspection of the EXAFS data and the FTs, one can conclude that uranyl complexes belonging to Class (B) (Sample 2 and 3) show evidence of only two oxygen co-ordination shells. In Class (C), which includes Samples 4 and 6-8, the uranium has a similar near-neighbour environment for the first two oxygen co-ordination shells as Class (B). But an additional third co-ordination shell is observed at a larger distance. Three co-ordination shells are also observed for complexes in Class (A) (Samples 1 and 5) but with a somewhat larger U- O_{eq} bond distance than for Classes (B) and (C).

The raw k^3 -weighted EXAFS spectrum of uranyl humate (9) solution exhibits similar spectral features (not shown here) as solutions belonging to Class (B). As in the case of uranyl phthalate (2) and maleate (3) solutions (see Figure 2), the FT of uranyl humate (9) shows evidence of two U-O co-ordination shells.

Structural parameters of the first two to three co-ordination shells were obtained by modelling and curve-fitting on the raw EXAFS data. The results are summarised in Table 2. The bond distance between the uranium and the two axial oxygen atoms, O_{ax} , of the uranyl group, UO_2^{2+} , is $1.78 \pm 0.02 \text{ \AA}$ for Samples 1-9. The MS path MS1 originating from the four-legged path within the uranyl unit [11] was also included in the fit. The MS1 path gives rise to a relatively weak peak in the FTs centred at 2.8 \AA (uncorrected for scattering phase shift) (see Figure 2). The equatorial plane around the uranyl group, UO_2^{2+} , consists of about five O_{ax} atoms. The error in determining the co-ordination number is $\pm 20\%$. The interatomic U- O_{ax} distance is 2.44 and 2.48 \AA for uranyl acetate (1) and succinate (5), respectively. In crystalline UO_2Ac_2 the U- O_{eq} bond length for the COO^- group with symmetric bidentate geometry is 2.45 \AA [12]. For the monodentate co-ordinated COO^- groups, the U- O_{eq} bond length is much shorter, e.g. 2.37 \AA . Therefore, the COO^- groups of acetic and succinic acids in Samples 1 and 5 (Class A) appear to act as bidentate ligands to the uranyl ion. In agreement with the qualitative discussion of the FTs shown in Figure 2, all other samples (Classes B and C) exhibit a significantly shorter U- O_{ax} distance of about $2.37 \pm 0.02 \text{ \AA}$ which is typical for a monodentate co-ordination of the COO^- groups via one of its oxygen atoms. The possibility to differentiate

between monodentate and bidentate co-ordination of the COO^- groups on the basis of the U-O_{eq} bond lengths measured by EXAFS has also been demonstrated for solid uranyl carboxylates of known crystal structure [13].

To investigate the nature of the peak centred at 3.8 Å in the FTs of Classes (A) and (C), a Fourier-filtering technique was applied. Two possible origins of the 3.8 Å peak were considered. i) SS interaction between two neighbouring uranium atoms, or ii) scattering along paths involving carbon atoms of the ligands. Light elements like carbon and oxygen are not normally detected in room-temperature solutions at a distance greater than 3 Å, unless a MS enhancement of the EXAFS amplitude is operative. When the carboxylate group adopts a symmetric bidentate co-ordination where the distal carbon atom, C_2 , is collinear with the uranium atom and the carboxylic carbon atom, C_1 , three-legged ($\text{U} \rightarrow \text{C}_1 \rightarrow \text{C}_2 \rightarrow \text{U}$) and four-legged ($\text{U} \rightarrow \text{C}_1 \rightarrow \text{C}_2 \rightarrow \text{C}_1 \rightarrow \text{U}$) MS paths can occur. For samples in Class (C), phase and amplitude calculated from a SS U-U path were in good agreement with the extracted EXAFS data. A poor match to the data was obtained when parameters of the MS U-C-C paths were used. Therefore, we interpret the 3.8 Å peak in the spectra of Samples 4 and 7-8 as a U-U interaction with an interatomic distance of 3.94-3.97 Å (Table 2). A detailed analysis of the extracted EXAFS data of Samples 7-8 with the U-U SS path and the sum of three-legged and four-legged MS U-C-C paths has been published in [14]. Based on the detection of U-U interaction in uranyl malate, citrate and tartrate solutions it was possible to assign a structure to the 2:2 dimer present in these solutions. Each uranyl group is linked with two acid molecules by one oxygen atom of the COO^- group and bridged with a second uranyl group by a-hydroxyl groups of the acids (see [14] for a structural model).

The reversed situation was observed in the analysis of the extracted EXAFS of Class (A) samples. The SS U-U path offered a poor match to the data (not shown here), whereas the MS U-C-C paths were in good agreement with the data. The detection of distant C atoms at 4.34 and 4.37 Å due to MS enhancement points to a bidentate co-ordination of the COO^- group of the carboxylic acids in solutions 1 and 5, respectively. This is consistent with the observation of long U-O bonds in the equatorial plane of the uranyl ion in these solutions. A structural model for the uranyl acetate solution (1), where three acetate ions adopt a bidentate geometry with the uranyl group, is shown in Figure 3.

For the uranyl humate solution (9) similar structural parameters were measured as for uranyl phthalate (2) and maleate (3) solutions. In the equatorial plane, the uranyl ions are surrounded by approximately 4-5 oxygen atoms at a distance of 2.38 ± 0.02 Å (Table 2). Due to the possibility for the uranyl ion to interact with one or two of the numerous COO^- and/or OH groups of a HA molecule, the obtained structural parameters have to be considered as an average value. Although, under the chosen conditions most of uranyl ions are expected to be bound to HA molecules, a small amount of other uranyl species may be present in the solution. Based on the comparison with the structural parameters of the equatorial oxygen shell in model solutions 1-8, we conclude that the majority of the HAs COO^- groups act as monodentate and not as a bidentate ligand to the uranyl ion.

Conclusions

Structural parameters for aqueous uranyl complexes with simple carboxylic acids and synthetic HA have been determined by uranium L_3 EXAFS analysis. Although a variety of aliphatic and aromatic uranyl carboxylates have been studied, the near-neighbour environment of uranium in these aqueous complexes can be reduced to three basic types. One type of co-ordination is characterised by

a predominantly bidentate ligation of the COO⁻ group with a U-O_{eq} bond distance larger than 2.42 Å. The assignment of bidentate co-ordination is supported by the detection of an additional carbon co-ordination shell at 4.3 Å due to MS enhancement along a linear U-C₁-C₂ arrangement. The other two types are characterised by predominantly monodentate ligation of the COO⁻ group with a typical U-O_{eq} distance of 2.37 Å. In addition to monodentate ligation, it was possible to detect the formation of U-U dimers in several aqueous complexes by the appearance of SS U-U interaction at 4.3 Å. EXAFS measurements of different model solutions allowed to interpret EXAFS structural parameters for the interaction of uranyl ions with HAs. A similar approach can be applied to the structural analysis of uranyl interaction with other complex polyfunctional organic macromolecules like fulvic acids and lignins.

In summary, XAS fine structure spectroscopy is one of the few techniques which can provide valuable structural information on the speciation of uranium in aqueous solutions. In addition, due to the energy of the incident X-rays needed for uranium L₃ edge XAS measurements, the structural analysis can be performed *in situ*.

Acknowledgements

We thank V. Brendler for calculation of uranyl speciations, G. Grambole, A. Otto, and S. Pompe for assistance in the sample preparation, and J. Bucher, N. Edelstein, and D. Shuh for assistance in the XAS measurements. Experimental measurements were made at SSRL, which is operated by the US Department of Energy, Office of Basic Energy Sciences, Divisions of Chemical Sciences and Materials Science.

REFERENCES

- [1] S. Pompe, M. Bubner, M.A. Denecke, T. Reich, A. Brachmann, G. Geipel, K.H. Heise, H. Nitsche, *Radiochim. Acta* 74 (1996), 135.
- [2] D.C. Koningsberger, R. Prins, X-Ray Absorption: Principles, Applications, Techniques of EXAFS, SEXAFS and XANES, John Wiley & Sons: New York (1988).
- [3] V.W.H. Leung, B.W. Darvell, P.C. Chan, *Talanta* 35 (1988), 713.
- [4] S. Ahrland, *Acta Chem. Scand.* 5 (1951), 199.
- [5] K.S. Rajan, A.E. Martell, *J. Inorg. Nucl. Chem.* 29 (1967), 523.
- [6] K.S. Rajan, A.E. Martell, *J. Inorg. Nucl. Chem.* 26 (1964), 1927.
- [7] G. Markovits, P. Klotz, L. Newman, *Inorg. Chem.* 11 (1972), 2405.

- [8] K.S. Rajan, A.E. Martell, *Inorg. Chem.* 4 (1965), 462.
- [9] I. Grenthe, J. Fuger, R.J. Lemire, A.B. Muller, C. Nguyen-Trung, H. Wanner, *Chemical Thermodynamics of Uranium*, 1st ed., Elsevier Science: Amsterdam (1991).
- [10] G. George, I. Pickering, EXAFSPAK: A Suit of Computer Programs for Analysis of X-Ray Absorption Spectra, Stanford Synchrotron Radiation Laboratory, Stanford, CA, USA (1995).
- [11] E.A. Hudson, P.G. Allen, L.J. Terminello, M.A. Denecke, T. Reich, *Phys. Rev. B* 54 (1996), 156.
- [12] J. Howatson, D.M. Grev, B. Morosin, *J. Inorg. Nucl. Chem.* 37 (1975), 1933.
- [13] M.A. Denecke, T. Reich, M. Bubner, S. Pompe, K.H. Heise, H. Nitsche, P.G. Allen, J.J. Bucher, N.M. Edelstein, D.K. Shuh, *J. Alloys Compounds* 271-273 (1998), 123.
- [14] P.G. Allen, D.K. Shuh, J.J. Bucher, N.M. Edelstein, T. Reich, M.A. Denecke, H. Nitsche, *Inorg. Chem.* 35 (1996), 784.

Table 1. Sample composition and calculated U(VI) speciation using published complex formation constants

No.	Ligand (L) Acid	mol/L	U(VI) mol/L	pH	U(VI):L ratio (of the complex)	Ref.
<u>1</u>	acetic	1.10	0.05	3.7	1:3	[4]
<u>2</u>	phthalic	0.06	0.02	4.6	1:1	[5]
<u>3</u>	maleic	0.01	0.001	4.2	1:1	[5]
<u>4</u>	malonic	0.20	0.05	3.9	1:2	[5]
<u>5</u>	succinic	0.50	0.05	4.0	1:1	[5]
<u>6</u>	malic	0.10	0.05	3.2	2:2	[6,7]
<u>7</u>	citric	0.10	0.05	3.9	2:2	[7,8]
<u>8</u>	tartaric	0.10	0.05	3.4	2:2	[6,7]

Table 2. EXAFS structural parameters of aqueous uranyl complexes and uranyl humate

No.	Uranyl complex	U-O _{eq}			U-X	
		R(Å)	N	$\sigma^2(\text{Å}^2)$	X	R(Å)
<u>1</u>	acetate	2.44	6	0.008	C	4.34
<u>2</u>	phthalate	2.37	6	0.010		
<u>3</u>	maleate	2.37	6	0.010		
<u>4</u>	malonate	2.36	5	0.007	U	3.96
<u>5</u>	succinate	2.48	5	0.008	C	4.37
<u>6</u>	malate	2.37	5	0.005	U	3.97
<u>7</u>	citrate	2.38	5	0.007	U	3.94
<u>8</u>	tartrate	2.36	4	0.006	U	3.95
<u>9</u>	humate	2.38	4	0.008		

U-O_{ax} (Samples 1-9): N = 2, R = 1.78±0.02 Å, $\sigma^2 = 0.002 \text{ Å}^2$

Figure 1. U L_3 edge k^3 -weighted EXAFS data for aqueous uranyl acetate (1), phthalate (2), maleate (3), malonate (4), succinate (5), malate (6), citrate (7), and tartrate (8)

The solid lines are the experimental data. The dashed lines are the best theoretical fit of the data.

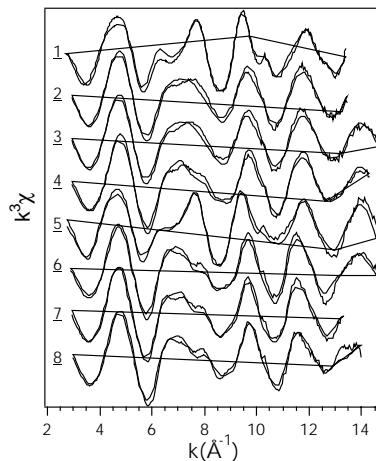


Figure 2. Fourier transforms of U L_3 edge EXAFS data for aqueous uranyl acetate (1), maleate (3), malonate (4)

The solid lines are the experimental data. The dashed lines are the best theoretical fit of the data.

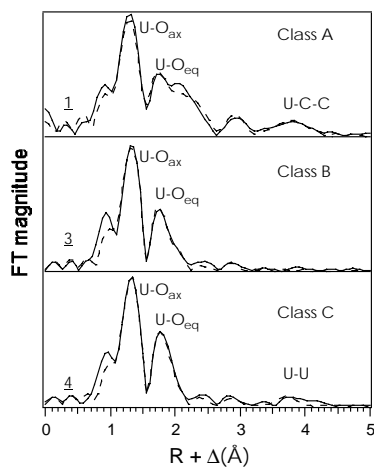
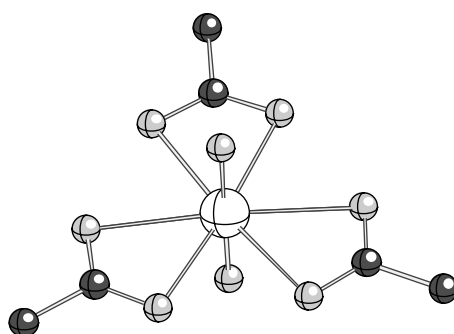


Figure 3. Structural model for the uranyl tri-acetate having the empirical formula $\text{UO}_2(\text{Ac})_3$



**DETERMINATION OF MOLECULAR-LEVEL STRUCTURAL INFORMATION
OF URANIUM IN ENVIRONMENTALLY RELEVANT SAMPLES BY EXAFS**

A. Roßberg, T. Reich, C. Hennig, L. Baraniak, K.H. Heise, A. Günther, H. Nitsche
Forschungszentrum Rossendorf e.V., Institut für Radiochemie
P.O. Box 510119, D-01314 Dresden, Germany

M.A. Denecke
Forschungszentrum Karlsruhe, Institut für Nukleare Entsorgungstechnik
P.O. Box 3640, D-76021 Karlsruhe

Abstract

Synchrotron-based extended X-ray absorption fine structure (EXAFS) spectroscopy is a powerful technique to study many chemical elements in different states of aggregation. Information can be obtained on the speciation and the complexation behaviour of radionuclides in solutions. The obtained structural parameters give molecular-level structural information from ligands surrounding a central radionuclide ion.

Investigations for mining related topics

It is important to search for species which determine the fate of radionuclides in mining waters.

A widely available organic substance is wood (i.e. lignin) degradation products, in particular in the flooded closure pits. To explain the complexation behaviour of uranium(VI) with regard to phenolic wood degradation products, the uranium(VI) complexes with model compounds were investigated. The structural parameter obtained by EXAFS spectroscopy can explain the complexation behaviour of the carboxylic and phenolic groups in these products. Humic acids are always present in natural systems. Humic acids have different functional groups and a great affinity to interact with radionuclides. Investigations of these interactions of the humic acids and model compounds with uranium(VI) were carried out. The results indicate that humic acid carboxylate groups are bound in a monodentate fashion with the uranyl cations.

A new topic for our research is the study of the interactions of uranium(VI) with plant metabolism compounds. Plants are potential accumulators for radionuclides. To limit the sum of relevant uranium complexing compounds the plants grow under well defined conditions. EXAFS investigations with selected pieces of the plants, e.g. roots, stems, are carried out. The structural parameters obtained by EXAFS show that the uranyl cation is involved in the metabolism of the plant.

REFERENCES

- [1] M.A. Denecke, T. Reich, S. Pompe, M. Bubner, K.H. Heise, H. Nitsche, P.G. Allen, J.J. Bucher, N.M. Edelstein, D.K. Shuh, Differentiating Between Monodentate and Bidentate Carboxylate Ligands Co-ordinated to Uranyl Ions Using EXAFS, *J. Phys. IV France* 7, C2-637 (1997).

X-RAY PHOTOELECTRON STUDY OF SYNTHETIC AND NATURAL THORIUM COMPOUNDS

**Yu.A. Teterin, I.O. Utkin, I.V. Melnikov, A.Yu. Teterin,
A.M. Lebedev, K.E. Ivanov, A.S. Nikitin**
RRC "Kurchatov Institute", Kurchatov sq., 1, 123182 Moscow, Russia

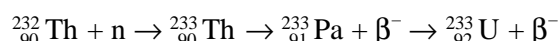
L. Vuckchevich
Natural-Mathematical Department, Podgorica, Yugoslavia

Abstract

X-ray photoelectron spectra of synthetic ThO_2 , ThF_4 , $\text{Th}(\text{OH})_4$ and of natural ThSiO_4 , $\text{ThSiO}_4 \cdot n\text{H}_2\text{O}$, $(\text{Th},\text{Fe})\text{SiO}_4$ thorium compounds were obtained and analysed in the range of electron binding energies from 0 to 1 000 eV. Based on the spectra structure, it was supposed that electrons of filled $\text{Th}6p$ and $\text{O}(\text{F})2s$ atomic orbitals take active part in the chemical bond. The largest oxidation degree of Th was found for ThF_4 . Fine structure was observed in the spectra of $\text{Th}6s$, $5d$, $5p$, $4f$, $4d$ and $4p_{3/2}$ electrons. The mechanisms of its appearance and correlation of such structures with physical and chemical properties of the studied compounds are also discussed. In particular, it is assumed that the spectra structure in the range of $\text{Th}4p$ and $\text{Th}4d$ electron binding energies is generally caused by dynamic effect. It should be noted that the considered structure depends on the thorium environment in the studied compounds.

Introduction

Thorium compounds are very important in science and technology. This is due to a possible usage of such compounds in atomic energetics. The determination of physical and chemical properties of compounds of heavy elements is necessary for the development of industrial nuclear-chemical technologies applying to all stages of the production of nuclear power from searching and working mines up to utilisation of products of spent nuclear fuel [1,2]. Natural thorium contains practically one isotope ^{232}Th with the decay half time $T_{1/2} = 1.39 \cdot 10^{10}$ years and the cross-section of capture of thermal neutrons 7.31 barn. The valence electronic configuration of thorium atom is $\{6s^2 6p^6 6d^2 7s^2\}$. Ionisation energy ($\text{Th}^0 \rightarrow \text{Th}^+$) is equal to 6.95 eV [2]. Thorium isotope ^{232}Th is an important source for obtaining of secondary nuclear fuel ^{233}U appearing as a result of reaction:



The advantages of thorium over uranium include its higher melting temperature and the absence of phase transitions during heating up to 1 400°C. The isotope ^{233}U has a high value of reproducing of thermal neutrons, providing its high usage in nuclear reactors [2]. The disadvantage of thorium is the necessity of adding decaying substances for realisation of nuclear reactions. At present the USA, Great Britain, Germany and other countries apply reactors, in which as an active zone metallic thorium, its carbide, Th_5Bi_5 and its other compounds are used in the mixture with uranium and its compounds. The usage of certain actinide compounds in nuclear energetics mainly depends on their price. Thorium compounds are widely used in the industry, for example, for production of constructional heat stable materials, catalysts and other [3].

Thorium content in the earth's crust is $8 \cdot 10^{-4}$ wt.% [2]. Basic industrial thorium minerals are monazite, thorite and thorianite. Monazite $(\text{Ce,La,Th})\text{PO}_4$, which may have yellow, red, black and brown colour, contains 2.5-12% ThO_2 , 0.1-0.4% UO_2 and others. Thorite $(\text{Th,Fe})\text{SiO}_4$ contains up to 77% of ThO_2 and 8% of Fe_2O_3 , as well as uranium and rare earth elements. Hydrated thorite $(\text{Th,Fe})\text{SiO}_4 \cdot n\text{H}_2\text{O}$ is named orangite. Thorite may be orange, black and brown. Thorianite $(\text{Th,U})\text{O}_2$ contains 45-93% of ThO_2 , 4.7-39.2% of UO_2 and up to 8% of various lanthanide oxides. It may be brown, black and grey. Main thorium sources are coastal friable layers of monazite (Brazil, USA, India), lode monazite layer (Stinkampskraal of RSA), endogenous layer of thorianite (Madagascar) and others [2]. It should be noted that the most available layer for Russia is situated in Kirghizia, but it is practically preserved now.

Despite comprehensive investigations of thorium compounds, many problems persist with regard to electronic structure and the nature of chemical bonds in its substances. Establishing correlations between characteristics of electronic structure and physical-chemical properties of synthetic and natural thorium compounds allows to understand the dependencies of their formation, to create materials on their basis with previously set properties and to use spectral methods for control intermediate products on the various stages of production of such substances. In this connection studying of electronic structure of heavy element compounds, in particular of thorium, is an important and actual scientific problem nowadays. The development of precise X-ray photoelectron spectrometers [4] and X_{α} - methods for electronic structure calculation [5] stimulated intensive studies of the electronic structure of actinide compounds [5,6]. In XPS spectra of all electrons of actinide compounds fine structure is observed. So far as this structure reflects oxidation degree of actinide compounds, their magnetic properties and their structure, and also allows to determine the nature of chemical bond in them, the XPS method becomes more widespread during studying new synthetic actinide compounds and ores containing them [7,8].

Experimental

X-ray photoelectron spectra of synthetic ThO_2 , ThF_4 , $\text{Th}(\text{OH})_4$ and natural ThSiO_4 , $\text{ThSiO}_4 \cdot n\text{H}_2\text{O}$ and $(\text{Th,Fe})\text{SiO}_4$ thorium compounds were obtained under vacuum $1.3 \cdot 10^{-7}$ Pa at room temperature with the electrostatic spectrometer HP5950A developed by Hewlett-Packard, using monochromatized $\text{AlK}_{\alpha 1,2}$ ($h\nu = 1486.6$ eV) X-ray excitation and the gun of low-energy electrons for compensation of electrostatic samples charging. The spectrometer resolution measured as full width on the half-maximum of $\text{Au}4f_{7/2}$ electron line was 0.8 eV. The values of binding energies E_b (eV) were taken relatively to the binding energy of C1s electrons of hydrocarbons on the sample surface, which is accepted to be equal to 285.0 eV. On the gold substrate $E_b(\text{C1s}) = 284.7$ eV and $E_b(\text{Au}4f_{7/2}) = 83.8$ eV. The widths of lines Γ (eV), measured at their half maximum are brought relatively to the width of C1s electron line of hydrocarbonates, which is accepted to be equal to 1.3 eV. The error of electron binding energy values and line widths did not exceed 0.1 eV and of relative intensities of lines was 10%. The samples of studied thorium compounds were prepared from finely dispersed powders ground in agate mortar and then pressed in indium on a titanium substrate as dense thick layers with mirror surface. The surface of such samples can be mechanically cleaned by a scraper under vacuum 10^{-5} Pa in the preparation chamber of the spectrometer (in situ), if necessary. For all samples the quantitative element analysis was carried out with the use of the following ratio: $n/n_j = S_j/S_j k_{ij}$, where n/n_j is the relative concentration of considered atoms, S_j/S_j is the relative intensity of the inner electron lines of these atoms, k_{ij} is an empirical factor. For such an analysis the most intensive electron lines of the elements in the compounds were used: $\text{Th}4f_{7/2}$, $\text{Si}2p$, $\text{Fe}2p_{3/2}$, $\text{Al}2p$, $\text{O}1s$, $\text{F}1s$ and $\text{O}1s$. The samples of thorium ore were taken from the ore deposit in Kirghizia.

Results and discussion

Element content of the compounds

X-ray photoelectron spectra and electron binding energies of studied fractions of thorium ores and other studied compounds are shown in Tables 1-2 and Figures 1-4. In transition from metallic thorium to its compounds an increase of binding energies of inner electrons is observed (Table 1). In spite of the fact that in all considered compounds thorium has formal valence four, its oxidation degree in fluoride ThF_4 is essentially higher than in oxide ThO_2 . This agrees with the fact that in thorium fluoride the chemical bond has more ionic character than in the oxide ThO_2 . The values of thorium electron binding energies in the studied natural thorium compounds are close to those of $\text{Th}(\text{OH})_4$. It indicates the bond of thorium with hydroxyl groups in such compounds. The oxidation degree of iron is close to Fe(IV), of silicon is slightly smaller than in aluminium silicate and quartz SiO_2 , and of aluminium is the same as in aluminium silicate and Al_2O_3 . Based on the values of intensities of inner electron lines the quantitative element analysis was carried out (Table 2). From the obtained results it follows that the samples of considered ore deposit practically do not contain lanthanides and uranium and are highly enriched by thorium. They basically represent varieties of thorite: ferrothorite $(\text{Th,Fe})\text{SiO}_4$ and orangite $\text{ThSiO}_4 \cdot n\text{H}_2\text{O}$, and the thorium content in them is higher than in the ores of many world known thorium deposits. For example, Samples (1), (2) and (3) contain 70.6%, 84.0% and 75.7% of thorite, respectively (Table 2). This is a very important result.

The area of spectra of weakly bound electrons

In X-ray photoelectron spectra of studied thorium ores (Figure 1) the band, connected with the electrons of outer valence molecular orbitals (OVMO), is observed in the range 0 - 15 eV of electron

Table 1. Electron binding energies E_b (eV) in the thorium compounds

MO		(Th,Fe)SiO ₄	ThSiO ₄	ThSiO ₄ nH ₂ O	ThO ₂	Th(OH) ₄	ThF ₄	Th [9]
OVMO		5.7 9.6	6.4 9.5	6.7 9.5	5.8	5.6	8.3	
IVMO	Th6p _{3/2}	17.5	16.9	17.4	16.5	17.5	18.4	16.6
	Th6p _{1/2}				25.5		25.6	24.5
	O2s	24.3	24.1	24.4	22.0	22.5		
	F2s						29.8	
	Th6s	43.7			41.9	42.6	44.5	41.4
CMO	Th5d _{5/2}	86.9	86.8	86.9	86.3	86.8	88.5	85.4
	Th5d _{3/2}	93.9	93.5	93.7	93.3	93.8	95.5	92.5
	Th5p _{3/2}	178.1	178.1	175.8 179.3	175.1 178.6	179.2	177.8 181.0	177.2
	Th4f _{7/2}	335.0	334.8	335.3	334.3	335.0	336.6	333.1
	Th4f _{5/2}	344.3	344.1	344.5	343.6	344.2	345.9	342.4
	Th4d _{5/2}	676.3	676.1	676.3	675.6	676.4	678.4	675.2
	Sat	685.1	684.6	685.2				
	Th4d _{3/2}	713.2	713.5	713.5	712.7	713.9	715.5	712.4
	Si2p _{3/2}	102.5	101.9	102.3				
	Si2s	153.5	153.0	153.1				
	Al2s	119.3	119.3	119.3				
	Fe3p _{3/2}	57.4						
	Fe2p _{1/2}	725.7						
	O1s	531.7	531.3	531.7	530.2	532.0	685.5 (F1s)	

Table 2. The content (%) of thorium ore samples*

	(Th,Fe)SiO ₄ Sample (1)	ThSiO ₄ Sample (2)	ThSiO ₄ nH ₂ O Sample (3)
ThO ₂	39.3	56.0	51.2
SiO ₂	31.3	28.0	24.5
(ThSiO ₄)	(70.6)	(84.0)	(75.7)
Al ₂ O ₃	12.9	9.7	11.9
FeO ₂	7.9		
H ₂ O	8.6	6.3	12.4

* Analysis was carried out under assumption that thorite consists of simple

oxides: (1) ThSi_{3.5}Al_{1.7}Fe_{0.6}O_{16.1}

(2) ThSi_{2.2}Al_{0.9}O_{9.6}

(3) ThSi_{2.1}Al_{1.2}O₁₂

Figure 1. XPS of weakly bound electrons of natural thorium compounds

For comparison, XPS of SiO₂ is given where vertical lines reflect theoretical results of electronic structure calculation of Si₂O₇⁶⁻ cluster [6]

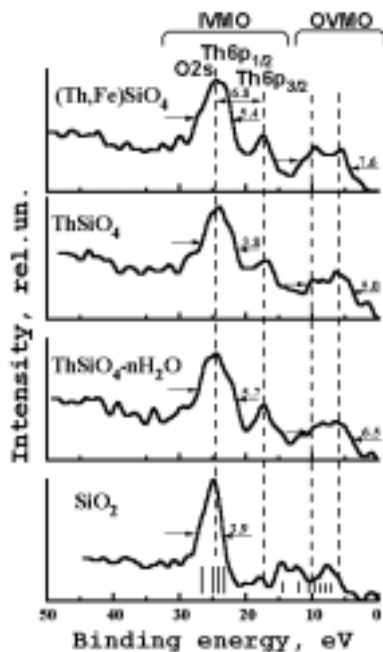


Figure 2. The scheme of MO formation in the ThO₈¹²⁻ cluster of O_h symmetry group and XPS of weakly bound electrons of thorium oxide ThO₂

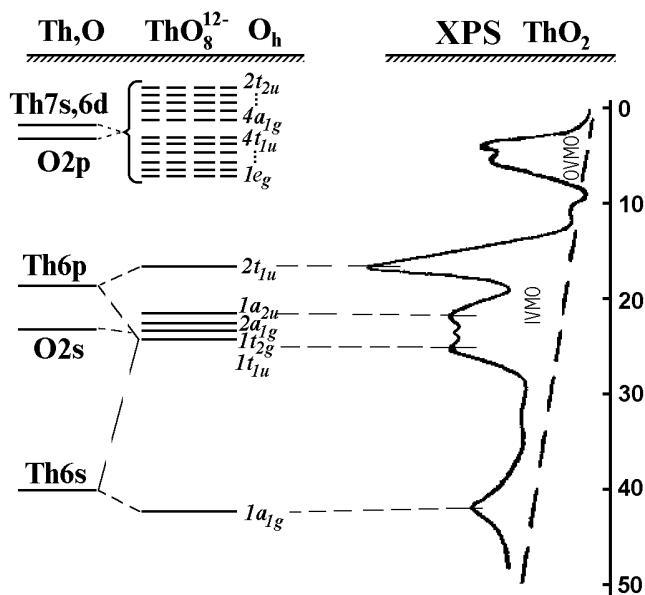


Figure 3. XPS of Th4f electrons of natural thorium compounds in comparison with the XPS of synthetic Th(OH)₄

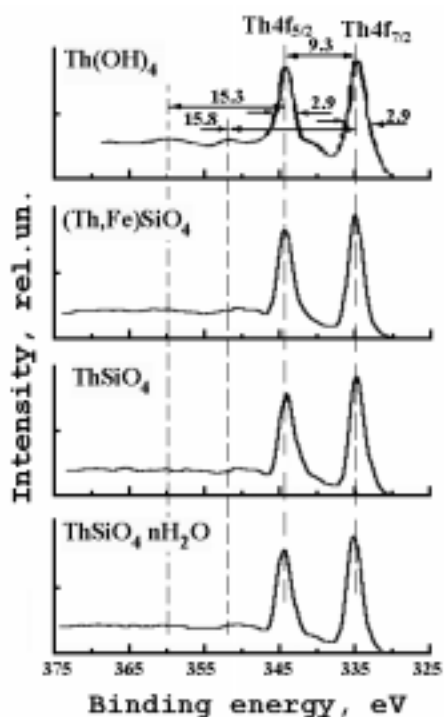
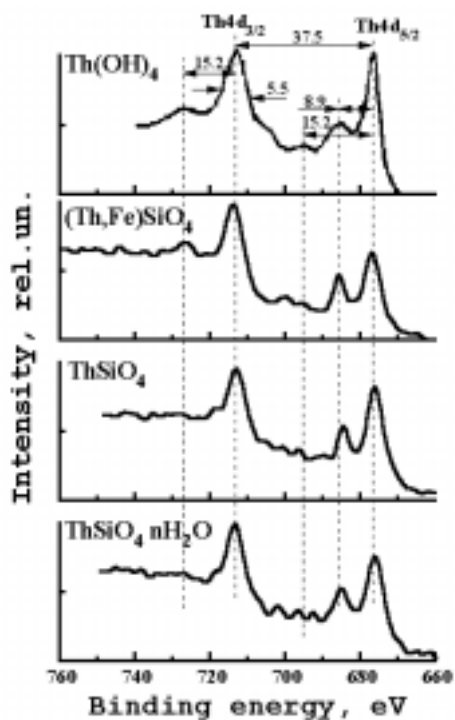


Figure 4. XPS of Th4d electrons of natural thorium compounds in comparison with the XPS of synthetic Th(OH)₄



binding energies. In particular, it reflects the participation in the chemical bond of $\text{Th}6d^{27}s^2$ and $\text{Ln}p$ electrons of thorium and ligands (L) surrounding it, and also of the other elements in the ores. The values of the widths of these bands for the Samples (1-3) are equal to 7.6, 5.0 and 6.5 eV, respectively. In the range 15-50 eV of electron binding energies the structure, in particular connected with $\text{Th}6p$, $6s$ and $\text{Ln}s$ electrons of thorium and ligands, is observed. This structure is more complex than that expected for the sum of atomic spectra of separate non-interacting elements, being in the content of considered substances (Figure 1). Such fine structure is mainly caused by the electrons of inner valence molecular orbitals (IVMO) [6]. The scheme of MO formation in ThO_2 , based on calculation of electronic structure of the ground state of ThO_8^{12-} cluster of O_h symmetry group in the approximation of non-relativistic spin-restricted SCF X_α -SW method [10], is shown in Figure 2. From the results it follows that the system of molecular orbitals (MO) may be divided into two groups. The group of OVMO consists of $1\bullet_g$, $1t_{2u}$, $2t_{2g}$, $3t_{1u}$, $2a_{2u}$, $3t_{2g}$, $3a_{1g}$, $1t_{1g}$, $1e_u$ and $4t_{1u}$ occupied MO and of $4\bullet_{1g}$, $5t_{1u}$, $2t_{2u}$ unoccupied MO. Another group consists of $1a_{1g}$, $1t_{1u}$, $1t_{2g}$, $2a_{1g}$, $1a_{2u}$ and $2t_{1u}$ IVMO. The content analysis of these MO shows that OVMO basically consist of unfilled valence $\text{Th}5f$, $7s$, $6d$, $7p$ and $\text{O}2p$ atomic orbitals (AO) of the neighbouring thorium and oxygen atoms, while on the contrary IVMO mainly consist of fully occupied $\text{Th}6s$, $6p$ and $\text{O}2s$ AO of these atoms. So, for example, IVMO $1t_{1u}$ and $2t_{1u}$, the first of which may be considered as bonding and the second as anti-bonding orbital, consist of 13% $\text{Th}6p$ + 87% $\text{O}2s$ and 82% $\text{Th}6p$ + 13% $\text{O}2s$ + 5% $\text{O}2p$, respectively. Lesser mixing of $\text{Th}6s$ and $\text{O}2s$ AO occurs in the formation of bonding $1a_{1g}$ and anti-bonding $2a_{1g}$ IVMO, consisting of 97% $\text{Th}6s$ + 3% $\text{O}2s$ and 5% $\text{Th}6s$ + 95% $\text{O}2s$ AO, respectively. The values of energies of the neighbouring occupied OVMO slightly differ and are in the range 2-5 eV. IVMO are observed in the wider interval and have characteristic energy for the given cluster. These results agree well with the data obtained for the cluster ThO_8^{12-} of O_h symmetry group, calculated in SCF X_α -SW approximation [11]. The results of calculation of electronic structure of $[\text{Si}_2\text{O}_7]^{6-}$ cluster by SCF X_α -DV method [6] predict the observable interaction between electrons of $\text{Si}3s$ and $\text{O}2s$ AO of the neighbouring silicon and oxygen atoms leading to IVMO formation. This even more complicates the fine structure of spectra of low energy electrons of thorite.

X-ray photoelectron spectra of inner level electrons

The fine structure of spectra of inner electrons of various thorium compounds is characteristic for the particular compound and may be used for its identification [8]. Many electron excitation leads to the appearance of shake-up satellites in the spectra of $\text{Th}4f$ - electrons of the studied compounds. The structure of such satellites has complex character and for the studied samples is close to the structure of thorium hydroxyl $\text{Th}(\text{OH})_4$ (Figure 3). In the spectra of $\text{Th}4d$ electrons in thorium compounds fine structure, which intensity is the characteristic for various compounds, is observed (Figure 4). This structure, as it was noted in the work [8], is caused by dynamic effect (Giant Coster-Cronig transitions) leading to the appearance of interacting final state configurations after photoemission of $\text{Th}4d$ electron as: $4d^9 4p^6 5f^n \leftrightarrow 4d^{10} 4p^4 5f^{n+1}$. The most intensive structure near $\text{Th}4d_{5/2}$ electron line is observed in the spectra of $\text{Th}(\text{OH})_4$ and orangite $\text{ThSiO}_4 \cdot n\text{H}_2\text{O}$. This confirms an assumption about hydrating of thorium ions in the studied substances.

Conclusion

Based on the obtained results we may conclude that XPS may be effectively used for carrying out express non-destructible qualitative and quantitative analysis of chemical state of ions, being in the content of geological thorium ores. The obtained results also show that the samples from the

considered ore deposit practically do not contain lanthanides and uranium and are highly enriched by thorium (ThSiO_4 84 wt.%). They mainly represent varieties of thorite: ferrothorite $(\text{Th,Fe})\text{SiO}_4$ and orangite $\text{ThSiO}_4 \cdot n\text{H}_2\text{O}$. Their thorium content is essentially larger than in the ores of many world known thorium layers. Oxidation degree of thorium in the studied substances is between that of in ThO_2 and ThF_4 . The oxidation degree of iron in ferrothorite is close to Fe(IV) , of silicon is slightly smaller than in aluminium silicate and quartz SiO_2 , of aluminium is the same as in aluminium silicate and Al_2O_3 . From the data obtained it follows that the studied compounds are in the hydrated form of $\text{ThSiO}_4 \cdot n\text{H}_2\text{O}$, which radically differ from the mixture of ThO_2 and SiO_2 , and iron atoms partly substitute thorium ones in thorite. The characteristics of the fine structure of $\text{Th}4f$ electrons, caused by many electron excitation, and of $\text{Th}4d$ electrons, connected with dynamic effect, show that thorite is in the hydrated state. Based on the parameters of the fine structure of weakly bound electrons (15-50 eV) it was shown that in thorite $\text{ThSiO}_4 \cdot n\text{H}_2\text{O}$ strong interaction between $\text{Th}6p$, $\text{Si}3s$ and $\text{O}2s$ electrons of the shells of the neighbouring atoms occurs resulting in the formation of the inner valence molecular orbitals. This agrees with the calculation results of electronic structure of ThO_8^{12-} (O_h) and $\text{Si}_2\text{O}_7^{6-}$ (D_{3h}) clusters, reflecting surroundings of thorium and silicon in thorite and made in the approximation of SCF X_α -SW and X_α -DV methods. The results of the present work are necessary for creating of the scientific fundamentals of searching and evaluation of thorium layers, and also for the enriching of ores in order to use in industry.

Acknowledgements

The authors are grateful for INTAS-96-1927 and to the Russian Fund for Fundamental Researches for their support of this work.

REFERENCES

- [1] J.J. Katz, E. Rabinovich, Uranium Chemistry, *Izdat. Inostr. Literat.* (1954) 491.
- [2] The Actinide Elements, G.T. Seaborg and J.J. Katz, eds., New York (1954) 701.
- [3] The Metal Thorium, Proceedings of the Conference on Thorium, 11 October 1956, Cleveland, Ohio, Harley A. Wilhelm, ed., 1958, 303.
- [4] Practical Surface Analysis by Auger and X-Ray Photoelectron Spectroscopy, D. Briggs and M.P. Seach, eds., John Wiley & Sons Ltd. (1983) 600.
- [5] V.A. Gubanov, E.Z. Kurmaev, A.L. Ivanovskii, Quantum Chemistry of Solids, *Nauka* (1984) 304.
- [6] Yu.A. Teterin, S.G. Gagarin, Inner Valence Molecular Orbitals and the Structure of X-Ray Photoelectron Spectra, *Russian Chemical Reviews*, 65 (10), 825 (1996).

- [7] Yu.A. Teterin, V.M. Kulakov, A.S. Baev, *et al.*, *Phys. Chem. Minerals* 7, 151 (1981).
- [8] Yu.A. Teterin, A.S. Baev, S.G. Gagarin, V.D. Klimov, *Radiochemistry* 27 (1), 3 (1985).
- [9] J.C. Fuggle, A.F. Burr, L.M. Watson, D.J. Fabian, *J. Phys. F: Metal Phys.* 4 (2), 335 (1974).
- [10] Yu.A. Teterin, A.S. Baev, R.V. Vedrinsky, A.L. Gubskiy, A.G. Zelenkhov, A.P. Kovtun, V.M. Kulakov, V.P. Sachenko, *Docl. Acad. Nauk SSSR* 256(2), 381 (1981).
- [11] V.A. Gubanov, A. Rosen, D.E. Ellis, *J. Inorg. Nucl. Chem.* 41, 975 (1979).

**THE INFLUENCE OF DYNAMIC EFFECT ON THE STRUCTURE
OF X-RAY PHOTOELECTRON SPECTRA OF ACTINIDE COMPOUNDS**

**Yu.A. Teterin, I.O. Utkin, A.M. Lebedev,
A.Yu. Teterin, K.E. Ivanov, A.S. Nikitin**
RRC "Kurchatov Institute"
Kurchatov sq., 1, 123182 Moscow, Russia

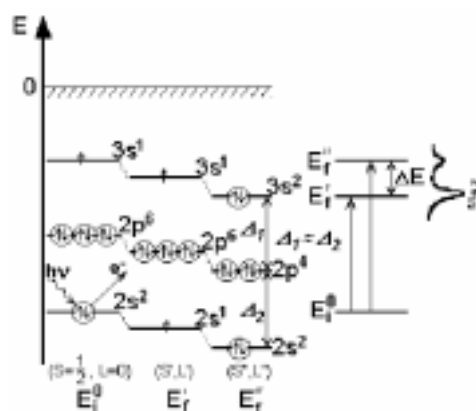
Abstract

In the present work the fine structure of An 6s, 5p, 5s, 4d, 4p electron spectra, caused by dynamic effect, was studied in thorium compounds $\text{Th}(\text{NO}_3)_4 \cdot 4\text{H}_2\text{O}$, $\text{Th}(\text{OH})_4$, $\text{Th}(\text{CO}_3)_2 \cdot n\text{H}_2\text{O}$, ThF_4 and ThO_2 , uranium compounds UO_2 , U_2O_5 , U_3O_8 and $\gamma\text{-UO}_3$ and finally in neptunium compounds $\text{RbNpO}_2(\text{NO}_3)_2 \cdot 2\text{H}_2\text{O}$, $\text{Cs}_2\text{NpO}_2(\text{CH}_3\text{COO})_3$, $\text{Cs}_3\text{NpO}_2\text{Cl}_4$, $\text{Cs}_2\text{NpO}_2\text{Cl}_4$ and $\text{NaNpO}_2(\text{CH}_3\text{COO})_3$. It is noted that this structure is characteristic for these compounds. It is supposed that the dynamic effect has resonance character.

Introduction

In the study of actinide compounds by X-ray photoelectron spectroscopy, along with a traditional information (the values of electron binding energies, line intensities of electrons of inner levels) the characteristics of fine structure are widely used. This is because, in practically the entire range of binding energies available for measurements (0-1 250 eV), fine structure is observed in the spectra of actinide substances. On the one hand, this structure complicates the determination of traditional information from a spectra. On the other hand, the characteristics of fine structure give important information about physical and chemical properties of actinide compounds and about the secondary electron processes taking place during photoionisation. One of the reasons for the fine structure in XPS may be the dynamic effect. The dynamic effect is characterised by simultaneous appearance of several final states of an ion or atom during photoemission of an electron [1-6]. In this case these additional final states are caused by giant Coster-Cronig electronic transitions between inner and outer levels during photoemission of an electron from the deepest of them. It should be noted that dynamic effect leads to configuration interaction in a final state. This phenomenon may be illustrated by the example of a hypothetical atom A of sodium type having configuration $A1s^22s^22p^63s^1$ (Figure 1). During photoemission of A2s electron besides the basic final state $E_f'(1s^22s^12p^63s^1)$ of atom A the additional two-hole final state $E_f''(1s^22s^22p^43s^2)$ may take place due to dynamic effect. One of the conditions of appearing of such a state is the multiplicity of energies of the levels $E_b(A2s) \cong 2E_b(A2p)$, i.e. $\Delta_1 \approx \Delta_2$ (Figure 1). It should be noted, however, that such an additional final state arises with the largest probability when giant Coster-Cronig electronic transitions happen between the levels with the same main quantum number. In particular, the probability of appearance of the additional final state $1s^22s^22p^43s^2$ with two holes in Na is essentially small [5]. The spectrum structure of actinide compounds, caused by the dynamic effect, is very complex [7-11]. In some cases this phenomenon leads to such a strong dispersion of a structure of an electron spectra that it can not be observed. In the present paper fine structure of X-ray photoelectron spectra of An 6s, 5p, 5s, 4d, 4p electrons of thorium compounds $Th(NO_3)_4 \cdot 4H_2O$, $Th(OH)_4$, $Th(CO_3)_2 \cdot nH_2O$, ThF_4 and ThO_2 , of uranium substances UO_2 , U_2O_5 , U_3O_8 and $\gamma-UO_3$ and of neptunium ones $RbNpO_2(NO_3)_2 \cdot 2H_2O$, $Cs_2NpO_2(CH_3COO)_3$, $Cs_3NpO_2Cl_4$, $Cs_2NpO_2Cl_4$ and $NaNpO_2(CH_3COO)_3$ was studied in order to determine the mechanisms of its appearance. Great attention is paid to the influence of the dynamic effect.

Figure 1. The illustration of the dynamic effect in the sodium type atom A leading to complicating of XPS of A2s electrons



Experimental

X-ray photoelectron spectra of the studied actinide compounds were obtained under vacuum $1.3 \cdot 10^{-7}$ Pa at room temperature with the electrostatic spectrometer HP 5950A by Hewlett-Packard using monochromatized $AlK_{\alpha_{1,2}}$ ($h\nu = 1486.6$ eV) X-ray excitation and the gun of low-energy electrons for compensation of electrostatic samples charging. The spectrometer resolution measured as full width on the half-maximum of $Au4f_{7/2}$ electron line was 0.8 eV. The values of binding energies E_b (eV) were taken relatively to the binding energy of C1s electrons of hydrocarbons on the sample surface, which is accepted to be equal to 285.0 eV. On the gold substrate $E_b(C1s) = 284.7$ eV and $E_b(Au4f_{7/2}) = 83.8$ eV. The error of electron binding energy values and line widths did not exceed 0.1 eV and of relative intensities of lines was 10%. The samples of studied actinide compounds were prepared from finely dispersed powders ground in agate mortar and then pressed in indium on a titanium substrate as dense thick layers with mirror surface. The surface of such samples can be mechanically cleaned by a scraper under vacuum 10^{-5} Pa in the preparation chamber of the spectrometer (in situ), if necessary.

Results and discussion

Thorium compounds

The dynamic effect may strongly influence the XPS of thorium compounds [6,7,9-11]. This is linked to the fact that the ratios between values of electron binding energies of various thorium electronic levels are as follows: $E_b(6s) \cong 2E_b(6p)$; $E_b(5d) \cong 2E_b(6s)$; $E_b(5p) \cong 2E_b(5d)$; $E_b(4f) \cong 2E_b(5p)$; $E_b(4d) \cong 2E_b(4f)$; $E_b(4p) \cong E_b(4d) + E_b(5s)$. It leads with the largest probability to the appearance of the following final states: $6s^1 6p^6 6d^m(5f^0) \leftrightarrow 6s^2 6p^4 6d^{m+1}(5f^1)$, $5p^5 5d^{10} 5f^0(6d^m) \leftrightarrow 5p^6 5d^8 5f^1(6d^{m+1})$ (Figure 2);

Figure 2. XPS of Th5p and Th4d electrons in thorium compounds

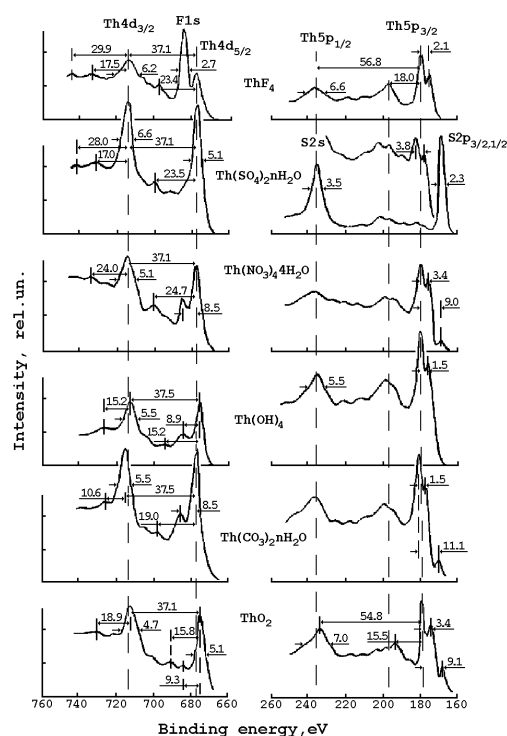
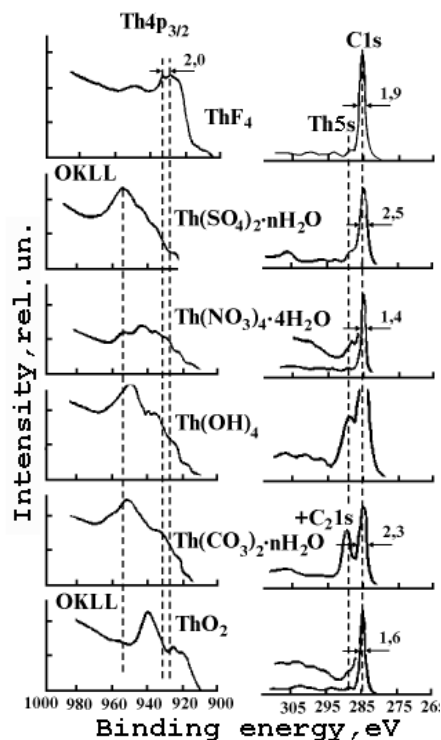


Figure 3. XPS of Th4p and Th5s electrons in thorium compounds

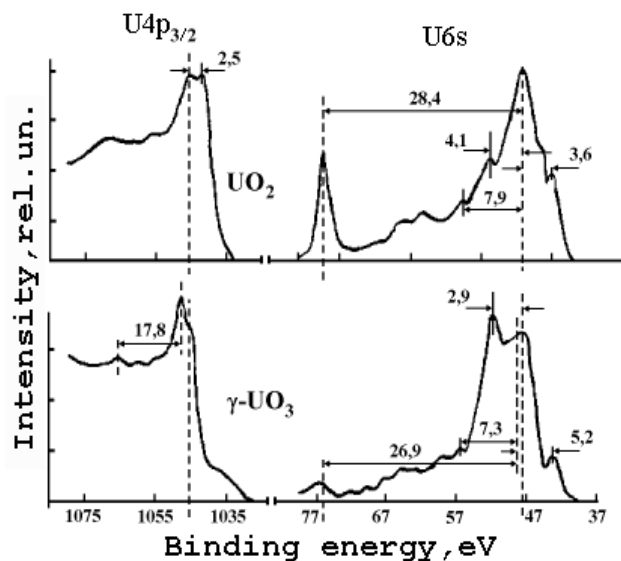


$5s^1 5p^6 5d^{10} 5f^0(6d^m) \leftrightarrow 5s^2 5p^5 5d^9 6d^1 5f^1(6d^{m+1})$ (Figure 3). This means, for example, that for Th6s electrons, the dynamic effect leads to the configuration interaction of $Th6s^1 6p^6 6d^m$ and $Th6s^2 6p^4 6d^{m+1}$ final states or of $Th6s^1 6p^5 f^0$ and $Th6s^2 6p^4 5f^1$, where superscripts are equal to the number of electrons on the appropriate electronic levels. An assumption may also be made that the dynamic effect arises in the spectra of Th4p_{3/2} electrons (Figure 3). It may lead to the appearance of the following final states: $4p^5 4d^{10} 5s^2 5f^0(6d^m) \leftrightarrow 4p^6 4d^9 5s^1 5f^1(6d^{m+1})$ (Figure 3). It is hard to observe the structure of Th5s electron spectra, caused by the dynamic effect, because of its overlap with the structure of C1s electron spectra (Figure 3). It is easy to select two relatively wide doublet components of Th4d_{5/2} and Th4d_{3/2} electrons from the structure of the spectra of Th4d electrons with average splitting $\Delta \bar{E}_{so}(Th4d) = 37.2$ eV (Figure 2). In the region of larger binding energies from main line of Th4d_{5/2} electrons an additional line is observed in the spectra of Th4d electrons of $Th(NO_3)_4 \cdot 4H_2O$, $Th(OH)_4$ and $Th(CO_3)_2 \cdot nH_2O$. Also in this region F1s electron line arises in ThF_4 . The question of why the analogous structure is not observed in the spectra of Th4d electrons in ThO_2 and $Th(SO_4)_2 \cdot nH_2O$ may be explained that the dynamic effect may have resonance character, i.e. due to chemical bonding the conditions $E_b(4d) \cong 2E_b(4f)$ and $\Delta_1 \approx \Delta_2$ may be changed that in turn results to impossibility of the dynamic effect for Th4d electrons.

Uranium compounds

The values of obtained binding energies of U6s electrons differs by dozens eV [12-14]. In the present work it was found that the spectra of these electrons have complex structure in the range ~40 eV of electron binding energies (Figure 4) instead of an expected single, relatively narrow line. This structure basically is not connected with multiplet splitting, because there are no U5f electrons in

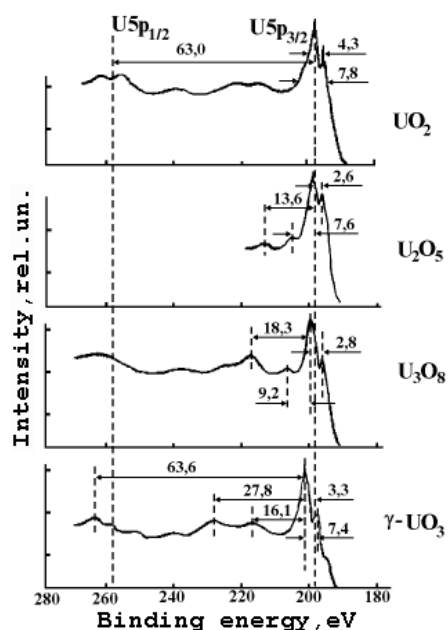
Figure 4. XPS of U4p and U6s electrons of uranium oxides



γ - UO_3 . The lines, caused by multi-electron excitation, may arise in these spectra, but their relative intensity should not exceed $\sim 20\%$ [15,16]. The observed splitting effects are too large to be associated with the participation of U6s atomic subshell in MO formation in the compounds. They are also not connected with the splitting in the crystal field, because U6s level is non-degenerative. The observed structure in U6s electron spectra has a lot of similarities with that of Th6s electrons. Therefore it was supposed that this structure is caused by the dynamic effect leading to the appearance of the following final states: $6s^1 6p^6 6d^m(5f^m) \leftrightarrow 6s^2 6p^4 6d^{m+1}(5f^{m+1})$, because $E_b(\text{U6s}) \cong 2E_b(\text{U6p})$. This assumption agrees qualitatively with the results of calculation of U6s electron spectra in ionic approximation of U(VI) [17].

The analogous considerations may be carried out in order to explain the appearance of a complex structure in the spectra of U4p_{3/2} (Figure 4) and U5p (Figure 5) electrons. It is represented in the splitting of U5p_{3/2} electron line and in the strong dispersion of U5p_{1/2} doublet component. Earlier (see Refs. [13,18]), it was supposed that the reason for the doublet splitting of the U5p_{3/2} electron line is crystal field. However, in the spectra of U5p_{3/2} electrons of UO₂ and γ -UO₃ oxides, no doublet is observed but rather a complex structure. In transition from UO₂ to γ -UO₃ oxide the value of splitting of the most intensive components of U5p_{3/2} electron line decreases from 4.3 eV to 3.3 eV, which is contrary to [18]. This fact agrees with the results of other investigation [19]. The similar structure is observed in the spectra of U4p_{3/2} electrons (Figure 4). In this case the splitting, the value of which decreases in transition from UO₂ to γ -UO₃, is also observed. From the comparison of the splitting values of the main components of U6s, U5p and U4p_{3/2} electron spectra it follows that they are weakly changed with the increase of electron binding energy from ~ 50 eV to ~ 1000 eV; this is not connected with the influence of the crystal field. It should be noted that such a structure is characteristic for the various oxidation degrees of uranium. We may suppose that the structure in the spectra of U5p, 4p electrons is mainly caused by the dynamic effect and as its result by the appearance of the final states $5p^5 5d^{10} 5f^m(6d^m) \leftrightarrow 5p^6 5d^8 5f^{m+1}(6d^{m+1})$ and $4p^5 4d^{10} 5s^2 5f^m(6d^m) \leftrightarrow 4p^6 4d^9 5s^1 5f^{m+1}(6d^{m+1})$, respectively. This structure is complicated by the mixing with the satellites connected with multi-electron excitation. The obtained results for U5p electrons agree with the results of theoretical work [11].

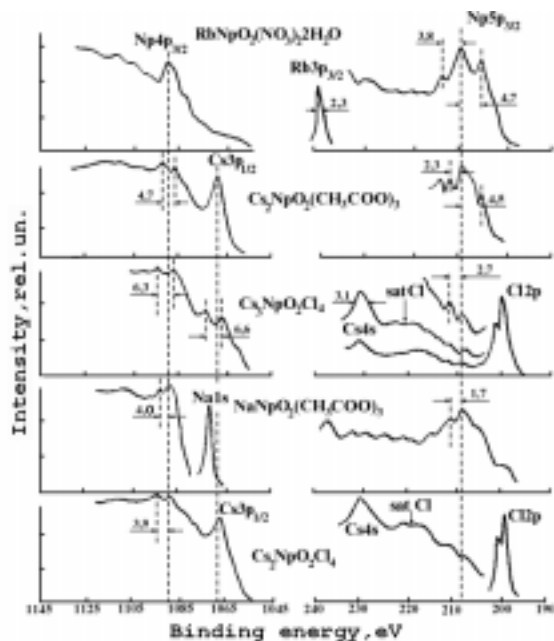
Figure 5. XPS of U5p electrons of uranium oxides



Neptunium compounds

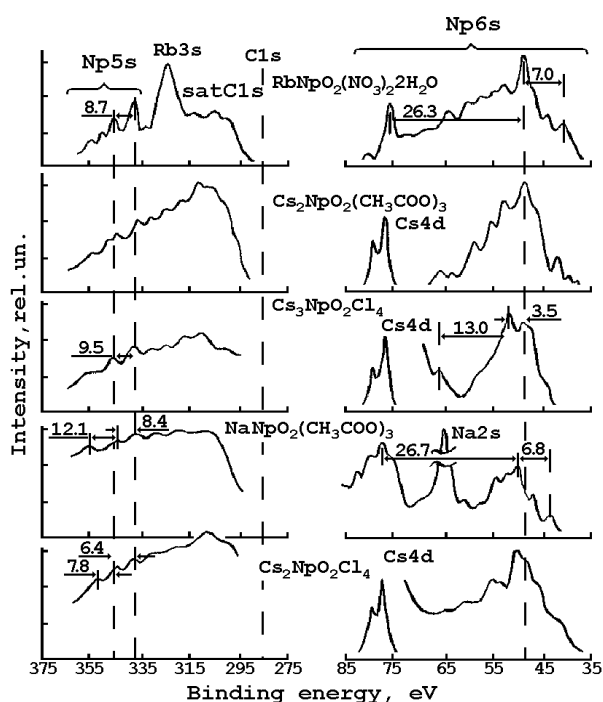
In the area of Np5p electron spectra of the studied neptunium compounds the lines of electrons of inner levels of ligand atoms are observed (Figure 6). The structure of Np5p_{1/2} electron spectra can not be clearly observed, because its binding energy is approximately equal to $E_b(\text{Np}5p_{1/2}) = 283.0$ eV (see Ref. [12]). This leads to the overlap of their lines with the intensive lines of C1s electrons of CH₃COO groups and of molecules of the residual hydrocarbons of vacuum oil on the sample surface. However, it is possible to observe the individual spectrum of the region of Np5p_{3/2} electron binding energy for several compounds (Figure 6). The neptunium binding energies $E_b(\text{Np}5p_{3/2}) = 206$ eV and $E_b(\text{Np}5d_{5/2}) = 101$ eV [12]. The values of these binding energies approximately satisfy to the condition $E_b(\text{Np}5p_{3/2}) \approx 2E_b(\text{Np}5d_{5/2})$. It allows to suppose that the structure of Np5p_{3/2} electron spectra may be caused by the dynamic effect with several final states: $5p^5 5d^{10} 5f^n (6d^m) \leftrightarrow 5p^6 5d^9 5f^{n+1} (6d^{m+1})$. The additional widening of this band may occur due to multiplet splitting, because all studied neptunium compounds contain uncoupled Np5fⁿ electrons. Some of the maximums may be shake-up satellites. The lines of the spectra of Np4p_{3/2} electrons of neptunium compounds, containing caesium, are mixed with the satellites of the lines of Cs3p_{1/2} electrons (Figure 6). There are no lines of ligand electrons in the spectra of Np4p electrons of RbNpO₂(NO₃)₂ · 2H₂O in the wide energy interval. In spite of this fact, a fine structure is observed in this area. The binding energies of neptunium electrons, according to Ref. [12], are equal: $E_b(\text{Np}4p_{3/2}) = 1087$ eV, $E_b(\text{Np}4d_{5/2}) = 773$ eV and $E_b(\text{Np}5s) = 338$ eV. These values approximately satisfy the ratio: $E_b(\text{Np}4p_{3/2}) \approx E_b(\text{Np}4d_{5/2}) + E_b(\text{Np}5s)$. Based on this fact we may suppose that the structure of Np4p_{3/2} electron spectra is connected with the dynamic effect and the appearance of the final state: $4p^5 4d^{10} 5s^2 5f^n (6d^m) \leftrightarrow 4p^6 4d^9 5s^1 5f^{n+1} (6d^{m+1})$. As far as the magnitude of experimental value of the binding energy of Np6s electrons is not presented in literature, we chose the energy interval according to the theoretical value $E_b(\text{Np}6s) = 57.2$ eV [20]. The experimental difficulty is that Np6s electron spectra have a very complex structure [21]. In spite of this fact methods of sample preparing and of conduction of the experiment, used in the present

Figure 6. XPS of Np4p and Np5p electrons of neptunium compounds



work, allow us to obtain the spectra of the energy range of Np6s electrons (Figure 7). The structure of Np6s electron spectra is spread in the range ~40 eV. Besides relatively wide bands at ~50 eV and ~75 eV in the spectra of $\text{RbNpO}_2(\text{NO}_3)_2 \cdot 2\text{H}_2\text{O}$ and $\text{NaNpO}_2(\text{CH}_3\text{COO})_3$, the structure with relatively high intensity is observed. The spectra of these compounds most fully reflect the structure of Np6s electron spectra in the considered energy interval.

Figure 7. XPS of Np5s and Np6s electrons of neptunium compounds



The theoretical values $E_b(\text{Np}6p_{3/2}) = 24.6$ eV, $E_b(\text{Np}6p_{1/2}) = 36.2$ eV and $E_b(\text{Np}6s) = 57.2$ eV [20] satisfy the condition $E_b(\text{Np}6s) \approx 2E_b(\text{Np}6p)$. Based on this fact, it was supposed that one of the possible mechanisms of appearance of the fine structure in such a wide energy range in the spectra of Np6s electrons is the dynamic effect, leading to the final states of the following type: $6s^1 6p^6 6d^m (5f^n) \leftrightarrow 6s^2 6p^4 6d^{m+1} (5f^{n+1})$. The presence of uncoupled Np5fⁿ electrons in the studied compounds may lead to an additional structure, connected with multiplet splitting. Also shake up satellites must be observed in these spectra. In the present work Np5s electron spectra were also observed (Figure 7). In the area of the binding energies of these electrons the structure, which is not presented in the spectra of C1s electrons, is observed on relatively intensive background of satellite wide band from C1s electrons of CH₃COO groups and residual hydrocarbons on the sample surfaces. In all cases it is possible to select two lines in the structure of these spectra. These lines are not a result of multiplet splitting, because the difference in the values of binding energies can not exceed $2 \div 3$ eV. The following ratio occurs: $E_b(\text{Np}5s) \approx E_b(\text{Np}5p) + E_b(\text{Np}6s)$. According to this fact it was supposed that the fine structure of Np5s electron spectra may appear as a result of the dynamic effect: $5s^1 5p^6 6s^2 5f^n (6d^m) \leftrightarrow 5s^2 5p^5 6s^1 5f^{n+1} (6d^{m+1})$.

Conclusions

The dynamic effect leads to the strong dispersion of the structure of An5s, 6s electrons in the studied compounds. As a result the fine structure of An6s electron spectra is observed in a wide energy interval ~40 eV. The intensity of the high energy component of An5p_{1/2} is strongly suppressed and in the area of spectra of An5p_{3/2} electrons complex structure is observed. In all cases a complex structure is observed in the spectra of An4p_{3/2} electrons. Based on the ratio of the values of electron binding energies of the various levels it was supposed that the complex structure of An 6s, 5p, 5s, 4d, 4p electron spectra is caused by the dynamic effect leading to the appearance of the following final states: $6s^1 6p^6 6d^m (5f^n) \leftrightarrow 6s^2 6p^4 6d^{m+1} (5f^{n+1})$; $5p^5 5d^{10} 5f^n (6d^m) \leftrightarrow 5p^6 5d^8 5f^{n+1} (6d^{m+1})$; $5s^1 5p^6 6s^2 5f^n (6d^m) \leftrightarrow 5s^2 5p^5 6s^1 5f^{n+1} (6d^{m+1})$; $4p^5 4d^{10} 5s^2 5f^n (6d^m) \leftrightarrow 4p^6 4d^9 5s^1 5f^{n+1} (6d^{m+1})$, respectively.

Acknowledgements

The authors are grateful for INTAS-96-1927 and to the Russian Fund for Fundamental Researches for the support of their work.

REFERENCES

- [1] P.S. Bagus, A.J. Freeman, F. Sasaki, *Phys. Rev. Lett.*, Vol. 30 (18), 850 (1973).
- [2] P.S. Bagus, A.J. Freeman, P. Sasaki, *Int. J. Quant. Chem. Symp.*, Vol. 7, 83 (1973).
- [3] E.-K. Viinikka, Y. Öhrn, *Phys. Rev. B*, Vol. 11 (11), 4168 (1975).

- [4] V.F. Demekhin, V.L. Sukhorukov, T.V. Shelkovich, S.A. Yavna, V.A. Yavna, Yu.I. Bairachnii, *Z. Struct. Chimii.*, Vol. 20 (1), 38 (1979) (in Russian).
- [5] U.C. Sing, D.D. Sarma, C.N.R. Rao, *Chem. Phys. Lett.*, Vol. 85, 278 (1982).
- [6] G. Wendin, *Structure and Bonding*, Vol. 45, 1 (1981).
- [7] Yu.A. Teterin, A.S. Baev, S.G. Gagarin, V.D. Klimov, *Radiochimiya*, Vol. 27 (1), 3 (1985) (in Russian).
- [8] Yu.A. Teterin, V.M. Kulakov, A.S. Baev, N.B. Nevzorov, I.V. Melnikov, V.A. Streltsov, L.G. Mashirov, D.N. Suglobov, A.G. Zelenkov, *Phys. Chem. Minerals*, Vol. 7, 151 (1981).
- [9] G.T. Bancroft, T.K. Sham, S. Larsson, *Chem. Phys. Lett.*, Vol. 46 (3), 551 (1977).
- [10] T.K. Sham, G. Wendin, *Phys. Rev. Lett.*, Vol. 44 (12), 817 (1980).
- [11] M. Boring, R.D. Cowan, R.L. Martin, *Phys. Rev. B*, Vol. 23 (2), 445 (1981).
- [12] K. Siegbahn, *et.al.*, ESCA – Atomic, Molecular and Solid State Structure Studies by Means of Electron Spectroscopy (Almquist and Wiksells, Boktryckeri AB, Stockholm, Sweden, 1967); Nova Acta Regiae Soc. Sci. Upsaliensis, Ser. IV (20), 1967.
- [13] J. Verbist, J. Riga, J.J. Pireaux, R.J. Caudano, *Electron Spectr. Related Phenom.*, Vol. 5, 193 (1974).
- [14] A.S. Baev, Yu.A. Teterin, L.G. Mashirov, D.N. Suglobov, *Radiochimiya*, Vol. 28 (4), 460 (1986) (in Russian).
- [15] Yu.A. Teterin, A.S. Baev, S.G. Gagarin, The Structure of XPS of Oxides of 3-D Transitional Metals, Tez. dokl, XIV Vsesoyusnogo soveshaniya po rentgenovskoi i electronnoi spectroscopii, Irkutsk, 1984, 76 (in Russian).
- [16] Yu.A. Teterin, T.N. Bondarenko, A.Yu. Teterin, A.M. Lebedev, I.O. Utkin, XPS of Lanthanoide Orthoniobates, *J. Electron Spectrosc. Relat. Phenom.*, 1998 (in press).
- [17] V.L. Sukhorukov, S.A. Yavna, V.F. Demekhin, *Fizika Tverdogo Tela.*, Vol. 24 (6), 1856 (1982) (in Russian).
- [18] T. Novakov, J.M. Hollander, *Phys. Rev. Lett.*, Vol. 21 (16), 1133 (1968).
- [19] B.W. Veal, D.J. Lam, W.T. Carnall, H.R. Hoekatra, *Phys. Rev. B*, Vol. 12 (12), 5651 (1975).
- [20] K.N. Huang, M. Aojogi, M.H. Chen, B. Graseman, H. Mark, Neutral Atom Electron Binding Energies from Relaxed-Orbital Relativistic Hartree-Fock-Slater Calculations, *Atom Data and Nucl. Data Tables*, Vol. 18, 243 (1976).
- [21] Yu.A. Teterin, A.S. Baev, L.G. Mashirov, D.N. Suglobov, *Dokl AN SSSR*, Vol. 278 (1), 154 (1984) (in Russian).

**XPS STUDY OF INTERACTIONS OF URANYL GROUP UO_2^{2+}
WITH HYDROXYL- AND FLUORAPATITE IN WATER SOLUTIONS**

Yu.A. Teterin, A.Yu. Teterin, A.M. Lebedev, A.P. Dementjev, I.O. Utkin
RRC "Kurchatov Institute", Kurchatov sq., 1, 123182 Moscow, Russia

I.V. Melihov
Chemical Department, Moscow State University

V.I. Nefedov, D.G. Berdonosova
N.S. Kurnakov Institute of General and Inorganic Chemistry of RAS, Moscow, Russia

G.N. Bek-Uzarov
Institute of Nuclear Sciences, Belgrade, Yugoslavia

L. Vukchevich
University of Podgorica, Podgorica, Yugoslavia

Abstract

The interaction of the uranyl group UO_2^{2+} with hydroxylapatite and fluorapatite in water solutions was studied using X-ray photoelectron spectroscopy (XPS). The presence of CO_3^{2-} was found in all examined apatite samples. It was revealed that in the reaction of uranyl nitrate $\text{UO}_2(\text{NO}_3)_2 \cdot 2\text{H}_2\text{O}$ with hydroxylapatite in water solutions there are no U(IV) compounds, but rather uranyl compounds are created with U(VI). These compounds may have hydroxyl and carboxyl groups in the equatorial plane of the uranyl group, which are partially substituted by fluorine in uranyl compounds in the reaction with fluorapatite. It was found that the interaction of the uranyl group UO_2^{2+} with fluorapatite in water solution is much stronger than with hydroxylapatite.

Introduction

The application of nuclear power leads to the appearance of ecological problems on preservation of unprofitable sources of uranium, utilisation of radionuclides and restoration/remediation of the environment. One of the prior arising questions when attempts to solve these problems are being made is the determination of the chemical state of radionuclides in the environment [1,2]. The XPS method allows to determine the relative content of a radionuclide in a sample, its oxidation degree, the relative ion composition and the structure of actinide ion neighbouring in a compound [3,4]. Before this work appeared, we had already studied chemical states of uranium ions in samples from block IV of the Chernobyl Nuclear Power Plant, masses containing uranium fuel [5] and in “new products” of them [6], interaction of uranyl group with calcite [7], diabase [7,8] and humic acids [9,10] in water solutions. In this work we applied XPS to study the interaction of uranyl group UO_2^{2+} with hydroxylapatite and fluorapatite with the aim to clarify the conditions of the formation of stable uranyl compounds on the surface of these apatites.

Experimental

In this work samples based on the hydroxylapatite (I-IV) and fluorapatite (V-VIII) were studied. The chemical formula of calcium apatite is $[\text{Ca}_3(\text{PO}_4)_2]_3\text{CaR}_2$, where $\text{R} = \text{OH}^-$ in hydroxylapatite (HA) and $\text{R} = \text{F}^-$ in fluorapatite (FA). The samples were prepared as follows:

- *Sample I.* HA with chemical composition of $\text{Ca}_{10}(\text{PO}_4)_6(\text{OH})_2$. Free specific surface is about $200 \text{ m}^2/\text{g}$. Photo-images of nano-particle by electron microscope show threadlike crystals of 80 nm length; the diameter of the crystals is 5 nm. The sample was prepared with the following stages: a) drying of sediment at 180°C until the mass was constant; b) grinding in a mortar; c) sieving (the diameter of the sieve is $d = 200$ microns).
- *Sample II.* High-temperature HA. The sample was prepared with the following stages: a), b) and c), as in the case of Sample I, and d) roasting at 950°C during three hours; e) grinding in a mortar; f) sieving ($d = 200$ microns). RFA (X-ray diffraction phase analysis) data: hexagonal singony, the cell parameters: $a = 9.394 \text{ \AA}$; $c = 6.881 \text{ \AA}$; $V_{\text{cell}} = 525.95 \text{ \AA}^3$.
- *Sample III.* Uranyl-HA with uranyl ion content (UO_2^{2+}) $2.4 \cdot 10^{-6} \text{ mol}/(\text{g HA})$. The uranium content was determined spectrophotometrically at 650 nm using ARSENAZA-3 as reagent. The sample was prepared by: a) sorption of uranyl nitrate from neutral water solutions onto threadlike crystals of HA suspension (the solid phase of 6.6% weight) with free specific surface of $200 \text{ m}^2/\text{g}$; b) deriving of sediment; c) drying till constant mass.
- *Sample IV.* Uranyl-HA with uranyl ion content (UO_2^{2+}) $1.19 \cdot 10^{-4} \text{ mol}/(\text{g HA})$. The sample was prepared as Sample III.
- *Sample V.* Crystal of natural fluorapatite.
- *Sample VI.* Natural crystalline FA with UO_2^{2+} sorbed (the overall area of the sample is about 2 cm^2 , the amount of uranium sorbed is about $4 \cdot 10^{-7} \text{ mol}/(\text{g FA})$).

- *Sample VII.* FA powder (fraction of 60-165 microns), obtained by grinding the crystal of Sample V.
- *Sample VIII.* FA powder analogous to sample VII with UO_2^{2+} sorbed. The amount of uranium sorbed is about $(8 \pm 1) 10^{-6}$ mol/(g FA). The specific surface of the samples is about 20 m²/g.

XPS spectra of these samples were taken using the electrostatic spectrometer MK II VG Scientific with the AlK_{α} line as exciting X-ray radiation under a vacuum of 10^{-7} Pa at room temperature. The spectrometer resolution measured as width of the $\text{Au}4f_{7/2}$ line at its half height was 1.2 eV. The samples were also measured with the electrostatic spectrometer HP 5950A using monochromatised $\text{AlK}_{\alpha,2}$ radiation (1 486.6 eV) under a vacuum of $1.3 10^{-7}$ Pa at room temperature. The spectrometer resolution was about 0.8 eV. The values of binding energies were measured relative to the C1s level of hydrocarbons on the surface of the samples which is accepted as 285.0 eV. The accuracy of binding energy determination is 0.2 eV and that of relative line intensities is about 10%. Samples V and VI were studied as crystals. Powders were also prepared before and after milling in an agate mortar as dense thick layers pressed into indium on a titanium substrate. Quantitative analysis was carried out for all samples based on the assumption that spectral line intensities are proportional to the concentration of the atoms. The following relationship was used: $n_i/n_j = (S_i/S_j)k_{ij}$, where n_i/n_j is the relative concentration of studied atoms, S_i/S_j is the relative intensity (area) of the lines of inner shells of those atoms, k_{ij} is the experimental relative sensitivity coefficient: 1.0 (C1s); 2.8 (O1s); 6.1 (Ca2p); 1.4 (P2p); 4.2 (F1s) and 18.4 ($\text{U}4f_{7/2}$). The results obtained by the two spectrometers were identical in the accuracy range.

Results and discussion

The valence zone of hydroxylapatite $[\text{Ca}_3(\text{PO}_4)_2]_3\text{Ca}(\text{OH})_2$ stretches from 0 to 30 eV. This is caused by the formation of outer valence molecular orbitals (OVMO) and inner valence molecular orbitals (IVMO) originating mostly from an interaction of $\text{Ca}3p^64s^2$, $\text{P}3s^23p^3$ and $\text{O}2s^22p^4$ shells of neighbouring atoms. Unfortunately, on account of weak intensities of the spectrum of low energy electrons of the uranyl compounds formed on the surface of Samples III, IV, VI and VIII it is very difficult to reliably interpret its structure which overlaps with the intense spectra of the considered apatites. We were thus unable to determine the bond lengths between uranium and its nearest neighbours in these uranyl compounds as was performed earlier in the case of calcite [7], diabase [7,8] and humic acids [9,10]. Moreover, the intensities of lines of U4f electrons are so weak in the uranium spectrum of Sample III that they cannot be reliably identified.

On the basis of the structure of the spectra of C1s electrons of the apatite samples, one may deduce the presence of carboxyl groups CO_3^{2-} (Figure 1). At the higher energy part of the C1s line at 285 eV, which is caused by hydrocarbonates of the vacuum pump oil on the sample surface, an additional line at 289 eV is observed and its intensity is proportional to the quantity of CO_3^{2-} groups (Table 2). Due to the increase of the relative line intensity and approaching of a constant value for the milled samples, one may conclude that these groups are present in the samples and were not formed at their surface during the sample preparation as a result of interaction of its surface with carbon oxides from the air (Table 2). The appearance of the structure of the line of C1s electrons of CO_3^{2-} group is observed in the spectra of the samples of apatites in which there is a content of uranyl group. In other words, if the apatite as a uranyl impurity, then in the spectrum of C1s electrons the CO_3^{2-}

Table 1. The binding energies E_b (eV)^{a)} of elements of studied apatite Samples I-VIII

No.		C1s(CO ₃ ²⁻)	O1s ^{b)}	Ca2p _{3/2}	P2p _{3/2}	U4f _{7/2}	F1s
I	Unmilled	288.7	531.4	347.6	133.5	–	–
	Milled	287.9	531.3	347.5	133.3	–	–
II	Unmilled	288.4	531.0	347.1	133.1	–	–
	Milled	288.1	531.2	347.3	133.3	–	–
III	Unmilled	288.5	531.4	347.4	133.4	–	–
	Milled	287.9	531.4	347.8	133.5	–	–
IV	Unmilled	289.5	531.5	347.6	133.5	381.4	–
	Milled	287.9	531.4	347.5	133.6	381.5	–
V	Crystal	288.4	531.7	347.7	133.7	–	684.6
	Milled	288.6	531.5	347.5	133.6	–	684.7
VI	Crystal	288.5	531.7	347.7	133.7	381.8	684.8
VII	Unmilled	288.5	531.2	347.3	133.3	–	684.8
	Milled	289.4	531.2	347.5	133.5	–	684.8
VIII	Unmilled	289.2	531.3	347.4	133.5	381.8	684.7
	Milled	288.9	531.6	347.5	133.6	381.7	684.8

a) The values of electron binding energies were determined from the maximum of lines relatively to E_b (C1s) = 285.0 eV.

b) All samples showed a single O1s line with an average line width of 2.5 eV.

Figure 1. XPS spectrum of C1s electrons of milled apatite samples: a) Sample II, b) Sample VIII

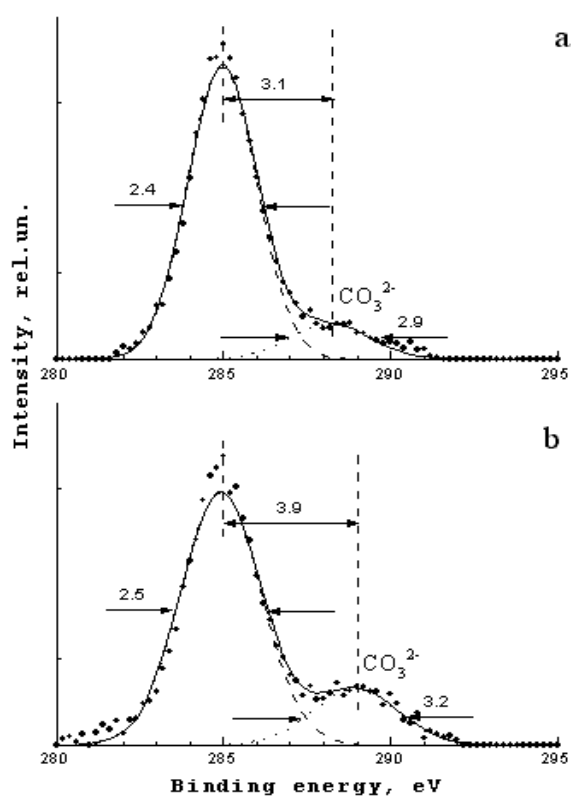


Table 2. Relative content^{a)} of the elements in apatite Samples I-VIII, determined using XPS data

No.		C1s ^{b)}	C1s(CO ₃ ²⁻)	P2p	U4f _{7/2}	F1s
I	Unmilled	1.24	0.12	0.70	–	–
	Milled	0.95	0.18	0.70	–	–
II	Unmilled	1.53	0.12	0.71	–	–
	Milled	1.53	0.31	0.70	–	–
III	Unmilled	0.64	0.12	0.73	–	–
	Milled	0.62	0.31	0.75	–	–
IV	Unmilled	1.32	0.18	0.75	0.035	–
	Milled	1.71	0.24	0.74	0.035	–
V	Crystal	10.83	1.11	0.71	–	0.14
	Milled	2.03	0.31	0.70	–	0.07
VI	Crystal	14.76	-0.80	0.61	0.42	0.10
VII	Unmilled	1.31	0.26	0.67	–	0.07
	Milled	0.79	0.31	0.61	–	0.06
VIII	Unmilled	2.81	0.18	0.52	0.70	0.12
	Milled	1.67	0.31	0.58	0.105	0.07

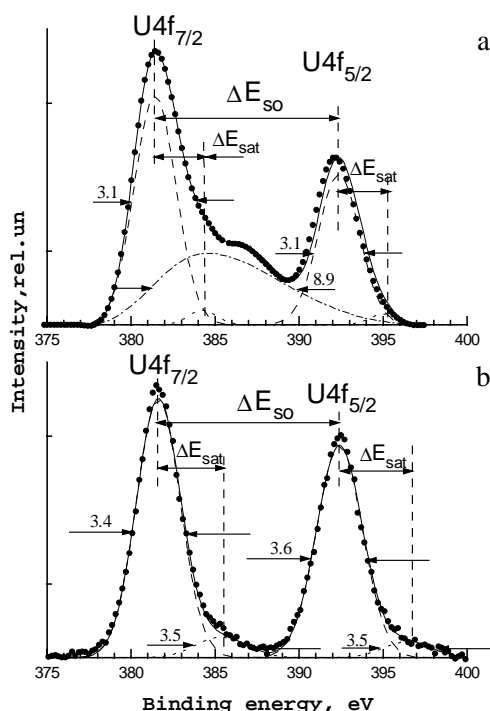
a) The values are given relatively to the content of calcium atoms.

b) The C1s intensity is due to hydrocarbons only.

group is observed (padding fine structure). The mechanic-chemical reaction of hydroxylapatite with CO₂ corroborates by the results of other independent researches [11,12]. As one may expect, in the process of the milling of the samples the line intensity of the oil hydrocarbons decreases while the relative intensity of the line of P2p electrons of phosphor remains constant (Table 2). However, at the same time the decrease of F1s fluorine line is revealed in the spectra of the fluorapatite samples. The diffusion of the fluorine to the sample surface and also its extraction from the sample during the process of milling may be the reason for this phenomenon. These results agree well with those of thermodynamical analysis: CO₃²⁻ groups diminish bonds of F in compounds [11,12]. It is should be noted that such a mechanic-chemical reaction is very intense: milling in the agate mortar immediately leads to the appearance of HF smell. The sample milling does not change the uranium content because the milling does not decrease the size of apatite micro-crystals in the suspension. However, the milling of Sample VIII causes a dramatic decrease of the uranium amount (Table 2).

The absence of the line of N1s electrons at E₀ = 407.8 eV in the spectra of the apatite samples (III, IV, VI, VIII) with a uranyl group content allows to conclude that uranyl group surfaces the apatite not in the form of uranyl nitrate as a result of physical adsorption but reacts chemically with the surface to produce there uranyl compounds. In the equatorial plane of these products are oxygen ions of phosphate, hydroxyl and carboxyl groups in the case of hydroxylapatite. On the surface of fluorapatite these groups may be substituted by ionic fluorine to form more stable compounds. The latter presumption follows from the fact that the interaction of the uranyl group UO₂²⁺ with fluorapatite in water solutions is approximately by one order of magnitude stronger than with hydroxylapatite. Actually, the uranium content on the surface of Samples IV, VI and VIII before milling differs by dozens accordingly (Table 2), although the overall amount of uranium in Sample IV is greater than in Samples VI and VIII. The XPS spectrum of U4f electrons at the surface of the apatite samples consists of two main lines due to spin-orbital splitting with ΔE_{so} = 10.8 eV and of shake-up satellites observed at the higher energy part of the lines at 3.7 eV with a relative intensity 12% (Figure 2).

Figure 2. XPS spectrum of U4f electrons of milled apatite samples: a) Sample IV, b) Sample VIII



It is known [3,6] that such satellite structure is the case for uranium in uranyl compounds with U(VI). The binding energy of $U4f_{7/2}$ electrons in the uranyl compounds at the hydroxylapatite surface is equal to 381.5 eV. This is in good agreement with the respective value of 381.6 eV for $CaUO_4$, and different from the values of $E_b = 381.1$ eV for $UO_2(NO_3)_2 \cdot 2H_2O$, $E_b = 382.7$ eV for $UO_2HPO_4 \cdot 2H_2O$ and $E_b = 382.8$ eV for $(UO_2)_3(PO_4)_2 \cdot 4H_2O$. For uranyl compounds at the fluorapatite surface, the binding energy of such electrons is to some extent greater what may be due to the fluorine influence in the equatorial plane of the uranyl group.

Conclusions

Along with the presence of PO_4^{3-} , OH^- and F^- groups in the studied samples, the presence of CO_3^{2-} groups was detected. This is probably caused by the presence of CO_3^{2-} in the samples and not by absorption of carbon from the air during sample preparation. It was determined that in a reaction of uranyl nitrate with apatite in water solutions the formation of uranyl compounds with U(VI) and not with U(IV) takes place. In the case of fluorapatite, the hydroxyl and carboxyl groups in the equatorial plane of the uranyl compounds may partially substituted by fluorine. It was found that the interaction of the uranyl group UO_2^{2+} with the surface of fluorapatite in water solution is approximately one order of magnitude stronger than in the case of hydroxyl apatite.

Acknowledgements

The authors are grateful to the Russian Fund for Fundamental Researches (grant no. 96-03-32058a) and INTAS-96-1927 for their support of this work.

REFERENCES

- [1] S. Pompe, M. Bubner, M.A. Denecke, T. Reich, A. Brachmann, G. Geipel, R. Nicolai, K.H. Heise, H. Nitsche, *Radiochim. Acta*, Vol. 74, 135 (1996).
- [2] K.R. Czerwinski, G. Buckau, F. Scherbaum, J.I. Kim, *Radiochim. Acta*, Vol. 65, 111 (1994).
- [3] Yu.A. Teterin, A.S. Baev, K.E. Ivanov, L.G. Mashirov, D.N. Suglobov, *Radiochimia*, Vol. 38 (5), 395 (1996).
- [4] V.I. Nefedov, Yu.A. Teterin, T. Reich, H. Nitsche, *Dokl. Akad. Nauk.*, Vol. 348 (5), 634 (1996) (in Russian).
- [5] A.S. Baev, Yu.A. Teterin, K.E. Ivanov, A.Yu. Teterin, S.A. Bogatov, *Radiochimia*, Vol. 39 (2), 171 (1997) (in Russian).
- [6] Yu.A. Teterin, A.S. Baev, A.Yu. Teterin, K.E. Ivanov, L.G. Mashirov, D.N. Suglobov, *Radiochimia*, Vol. 39 (2), 177 (1997) (in Russian).
- [7] Yu.A. Teterin, V.I. Nefedov, K.E. Ivanov, A.S. Baev, G. Geipel, T. Reich, H. Nitsche, *Dokl. Akad. Nauk.*, Vol. 344 (2), 206 (1995) (in Russian).
- [8] Yu.A. Teterin, V.I. Nefedov, K.E. Ivanov, A.S. Baev, G. Geipel, T. Reich, H. Nitsche, *Z. Neorg. Chimii.*, Vol. 41 (11), 1884 (1996) (in Russian).
- [9] V.I. Nefedov, Yu.A. Teterin, A.M. Lebedev, A.Yu. Teterin, A.P. Dementjev, M. Bubner, T. Reich, S. Pompe, K.H. Heise, H. Nitsche, *Inorganica Chimica Acta*, Vol. 273 (1-2), 234 (1998).
- [10] Yu.A. Teterin, V.I. Nefedov, A.Yu. Teterin, A.M. Lebedev, K.E. Ivanov, A.P. Dementjev, G. Geipel, M. Bubner, T. Reich, S. Pompe, K.H. Heise, H. Nitsche, *Poverhnost'*, No. 2, 79 (1999).
- [11] V.P. Orlovskii, S.P. Ionov, *Z. Neorg. Chimii.*, Vol. 40 (12), 1961 (1995) (in Russian).
- [12] G.V. Rodicheva, V.P. Orlovskii, I.M. Romanova, *Z. Neorg. Chimii.*, Vol. 41 (11), 754 (1996) (in Russian).

HEAVY METAL SPECIATION ANALYSIS IN SOILS USING SYNCHROTRON RADIATION

Edmund Welter, Stefan Mangold
Technical University of Hamburg-Harburg, Germany

Abstract

The chemical binding form of lead in highly contaminated soils was determined using PbL₃-XAFS spectra of the soil samples. The investigation was done by a fingerprint method in which linear combinations of reference compound spectra were used to approximate the measured soil sample spectra and to calculate the relative amounts of the respective Pb-compounds in the soil samples. The chosen method was tested on synthetic mixtures of up to four reference compounds.

Introduction

The fine structure of X-ray absorbance edges offers a unique opportunity to determine the chemical binding form of a wide range of heavy metals in solid environmental samples like soil samples or sediments [e.g. 1,2]. Knowledge about the speciation of a metal in environmental compartments can play an important role in risk assessment and in decisions about appropriate decontamination procedures [3]. The methods most often used in environmental sciences are different sequential extraction procedures [e.g. 4,5]. However useful these procedures might be to characterise heavy metal contaminations to a certain degree, they offer no information about the chemical binding form in an analytical sense.

The ideal analytical procedure for the determination of chemical binding forms should:

- Be easy to perform.
- Be widely available.
- Yield information about the actual chemical compounds.
- Not require a complex sample preparation which might lead to alterations of the speciation.

Obviously XAFS spectroscopy does not fulfil the first two objectives, but it does offer one of the few available opportunities to fulfil the third and fourth objectives. The demand for easy feasibility can be fulfilled by use of a fingerprint method as it is established in many other analytical methods (e.g. mass spectroscopy or IR spectroscopy). A possible strategy to evaluate XAFS spectra by use of a fingerprint method will be discussed on the basis of results from Pb-contaminated soils and from synthetic mixtures of up to four Pb compounds.

Experimental

Sample preparation

Sample preparation consisted of grinding the samples and pressing them in a KBr press using PE-powder as binding agent. The soil samples originated from the vicinity of a battery factory in Hanover, Germany. The total Pb concentrations were between 40 and 140 g/kg. The samples were air-dried and sieved. The fraction smaller than 2 mm was used for the measurements.

Insoluble inorganic Pb compounds and Pb adsorbed to montmorillonite and complex bound to humic acids were used as reference compounds. The inorganic compounds (PbCO₃, basic PbCO₃, PbO, PbO₂, Pb₃O₄, PbSO₄ and PbS) were of p.a. grade and were used as delivered. PbCl₂ was obtained by precipitation of a PbNO₃ solution with an excess of NaCl. The humic acid complexes and the adsorbed species were obtained by shaking the respective substances with PbNO₃ solutions (c_(Pb) 10-100 g/L) for 24 h. After washing with deionised water the solid residues were air-dried and pressed to pellets as described before.

XAFS measurements

XAFS spectra were measured at the HASYLAB at DESY (Hamburg, Germany) at experimental station RÖMO 2. All spectra were measured in the transmission mode, using an elemental metal foil as standard for energy calibration. Spectra of the PbL₃ edge were recorded between 12 800 eV and

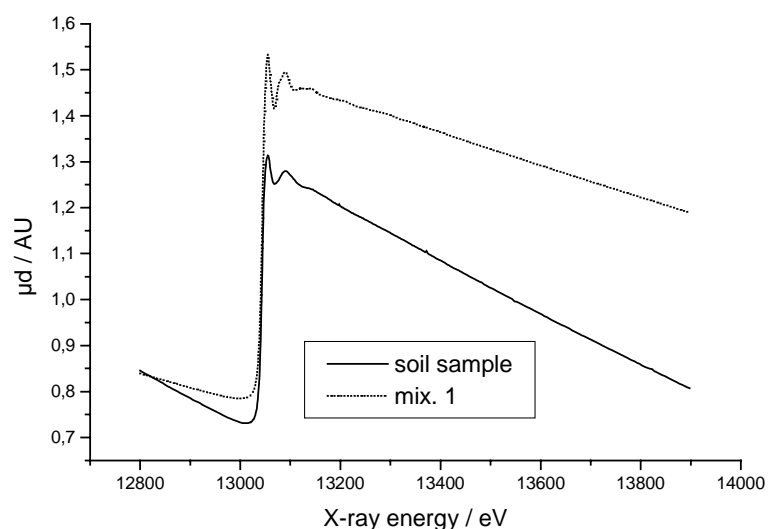
13 900 eV, covering the pre-edge, edge and post-edge region of the PbL_3 absorbance edge. The overall energy range was divided into five sub-regions in which the spectra were recorded with different energy resolutions; the highest energy resolution of 1 eV/channel was used in the edge region.

Spectrum evaluation procedure

Near edge region

As usual in XANES evaluation procedures the first steps of the evaluation procedure were subtraction of the background and normalisation of the spectra to an edge jump of 100. The high background in soil sample spectra, produced by the matrix which in soil samples mainly consists of Si, Al and Fe, made the background correction difficult. In most cases two polynomial functions of higher order had to be used to subtract the pre- and post-edge background properly (Figure 1). The high background is also the reason why spectra from soil samples containing less than 20 g/kg lead could not be evaluated. The noise level in this spectra is higher than the fine structure oscillations.

Figure 1. PbL_3 XAS raw spectra of a soil sample containing 50 g/kg Pb and of a synthetic mixture of two Pb compounds (27.1% PbO and 72.9% $PbCO_3$ w/w)



The next step has to be a very careful recalibration of the energy scale. As a result of inevitable shifts in the monochromator the first maximum of the first derivative spectrum of the lead-foil reference showed small shifts of the order of ± 1 eV. After correction of the energy shifts the absorbance values at the original energy values were recalculated by interpolation between neighbouring data points, so that all spectra owned the same energy values, a necessary precondition for the calculation of linear combinations and the comparison of spectra (Figure 2).

The best linear combination of reference spectra was calculated by a self written computer program [6] which tested the linear combinations of up to four reference compounds of all available reference spectra by means of the least square radix method (Figures 3 and 4). It was tried to minimise the range of potential reference compound spectra by preliminary investigations of the soil samples, especially SEM/EDX-investigations (Figures 5 and 6), and by taking into account their origin and history. Otherwise the amount of time needed for the calculations would increase to unacceptable high values even with fast CPUs.

Figure 2. Near edge region of the spectra in Figure 1 after background correction, normalisation and energy recalibration

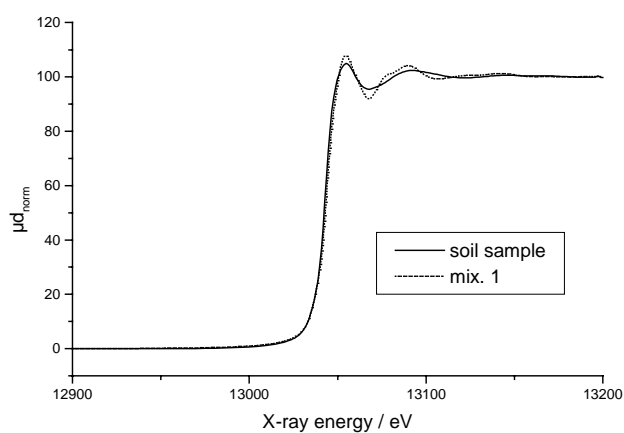


Figure 3. First derivative spectra of a soil sample and a synthetic mixture of Pb compounds with their respective linear combinations (cal. spectrum) of single reference spectra (see Table 1)

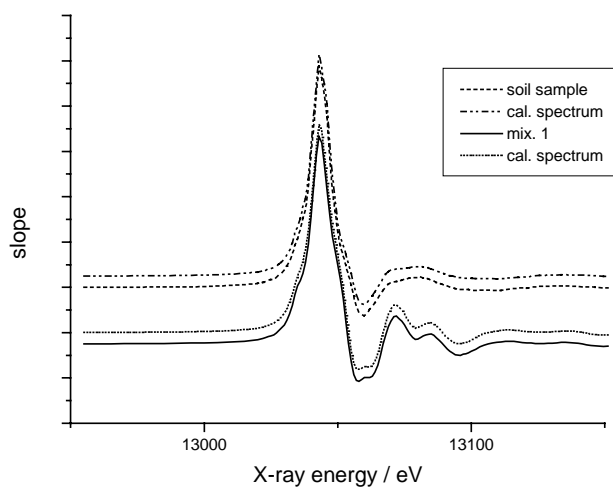


Figure 4. EXAFS spectrum of Mixture 1 and linear combination of three reference spectra (75% PbCO₃, 21% PbO and 4% (Pb(OH)₂ 2PbCO₃)

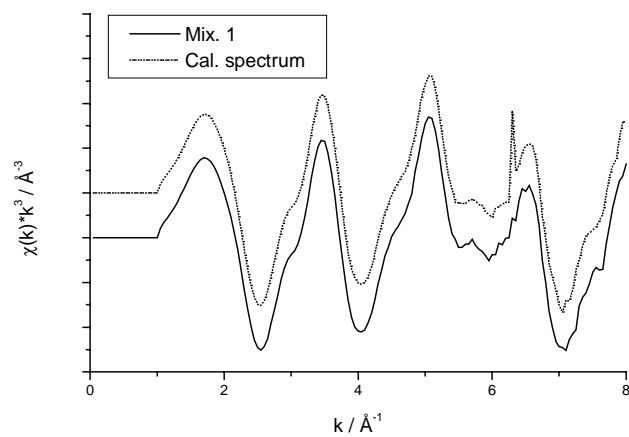


Figure 5 shows one of the typical lead-containing particles in the soil sample. These particles, which seem to contain the major part of the total lead content, only show X-ray fluorescence peaks of Pb, C and O in their EDX spectra. There is some evidence for the presence of sulphur, but the S *K* peak is unfortunately overlaid by the Pb *M* peaks.

Figure 5. Pb-containing particle in the soil sample

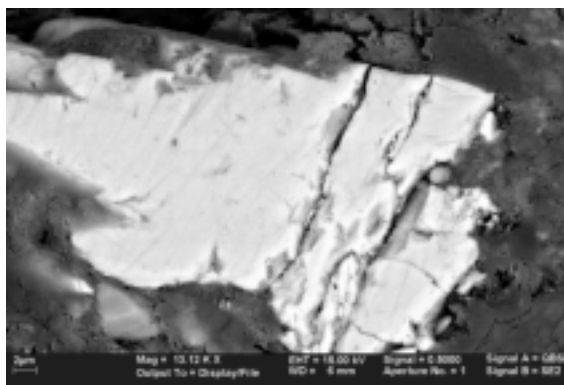
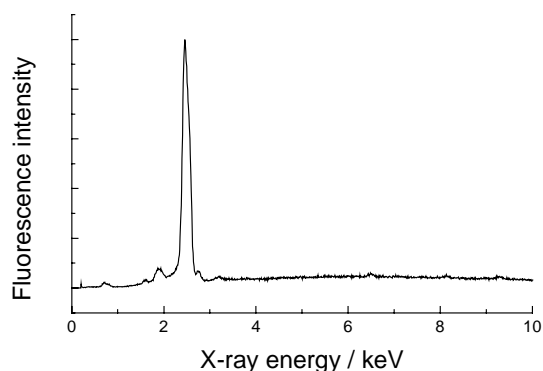


Figure 6. EDX spectrum from the bright particle in Figure 5 (detector with normal Be-window)



EXAFS region

The EXAFS region was evaluated using the program Autobk and from the University of Washington package [7] to create the $\chi(k)*k^3$ functions. Linear combinations of these functions were calculated with the same program used for the linear combinations of XANES region spectra. In the case of the lead spectra the linear combinations were fitted between 1 and 6.5 \AA^{-1} . Above 6.5 \AA^{-1} the results of linear combinations are heavily affected by the increasing noise in the spectra (Figure 4).

Results and discussion

Table 1 summarises the results for some two and four compound mixtures and for the soil sample whose spectrum is shown in Figures 1-3. A comparison of the real, weighed amounts of the different compounds in the mixtures with the calculated compounds shows that the maximum error is about 5%. Part of this error can be assigned to weighing errors.

Table 1. Relative amounts (in % w/w) of reference compounds (Pb-Mont = Pb²⁺ sorbed on montmorillonite, Pb-H. Acid = Pb²⁺ complexed by humic acid) in a soil sample (Soil s.) as calculated by linear combinations of XANES reference compound spectra and of synthetic mixtures (Mix. 1-Mix. 3) of Pb compounds (calculated by weight and by linear combinations of XANES or EXAFS reference spectra)

Mix. 1	<i>PbCO₃</i> / %	<i>b-PbCO₃</i> / %	<i>PbO</i> / %	
weight	72.9	0	27.1	
XANES	79	0	22	
EXAFS	75	4	21	
Mix. 2	<i>PbCO₃</i> / %	<i>b-PbCO₃</i> / %	<i>PbO</i> / %	
weight	52.1	0	47.9	
XANES	54	0	48	
EXAFS	55	1	45	
Mix. 3	<i>PbCO₃</i> / %	<i>b-PbCO₃</i> / %	<i>PbSO₄</i> / %	<i>PbS</i> / %
weight	32.1	30	20.9	17.1
XANES	36	28	19	17
Soil s.	<i>PbCO₃</i> / %	<i>Pb-H.Acid</i> / %	<i>PbSO₄</i> / %	<i>Pb-Mont.</i> / %
XANES	6	43	13	38

Compounds which were not constituents of the mixtures were in no case found by the described evaluation method. However, in most cases the spectra from soil samples show greater differences to the calculated linear combinations than the spectra of mixtures. This fact is probably a result of small amounts of compounds which are not included in the set of reference spectra, of more than four Pb compounds in the soil and of differences in the degree of crystallinity between the reference compounds and the respective compounds in the soil samples.

Perspectives

Due to the limited availability of synchrotron radiation facilities XAFS spectroscopy will never be a method routinely used for the determination of heavy metal binding forms. It is nevertheless one of the few methods available which enable speciation analysis in environmental samples at all. After the first results indicate that it is possible to identify a broad range of different heavy metals in soils by use of a fingerprint method it is necessary to investigate how the major drawbacks by now, the high detection limit and the limitation to four reference compounds, might be overcome.

One major aspect of our current research is how more than four compounds can be identified in a sample within reasonable time on a PC. Another question is whether the spectra contain enough information to identify more than four compounds with reasonable certainty.

The high detection limit is mainly caused by the high background absorption of soil samples. For this reason it is even more difficult to identify compounds containing metals with lower energy absorbance edges like Cu or Cr. The use of the fluorescence mode to overcome this problem is one promising possibility to overcome this problem. [e.g. 1,2]

Acknowledgement

The authors wish to thank the HASYLAB at DESY (Hamburg, Germany) for the beamtime to perform the XAFS measurements and especially Dr. L. Tröger (HASYLAB at DESY) for his support during our first steps into the world of X-ray absorption spectroscopy.

REFERENCES

- [1] A. Manceau, M.C. Boisset, G. Sarret, J.L. Hazemann, M. Mench, P. Cambier, R. Prost, *Environ. Sci. Technol.* 30, 1540 (1996).
- [2] G.V. Korshin, A.I. Frenkel, E.A. Stern, *Environ. Sci. Technol.* 32, 2699 (1998).
- [3] W. Calmano “Schwermetalle in kontaminierten Feststoffen.” Verlag TÜV Rheinland, Köln (1989).
- [4] M. Kersten, U. Förstner, Chemical Speciation in the Environment, A.M. Ure, C.M. Davidson, eds., Chapman & Hall, London (1995), pp. 234-275.
- [5] A. Tessier, P.G.C. Campbell, *Anal. Chem.* 51, 844 (1979).
- [6] S. Mangold, “Entwicklung von Auswerteverfahren zur Schwermetall – Speziesanalytik an Böden unter Anwendung von XAFS”, Diploma thesis Phillips University Marburg, Germany (1998).
- [7] E.A. Stern, M. Newville, B. Ravel, Y. Yacoby, D. Haskel, *Physica B* 208, 154 (1995).

AN X-RAY ABSORPTION STUDY OF THE REACTIONS OF Tc WITH MACKINAWITE (FeS)

M.J. Wharton¹, B. Atkins¹, J.M. Charnock^{1,2,3}, F.R. Livens¹, R.A.D. Patrick², D. Collison¹

¹Department of Chemistry, The University of Manchester, Manchester M13 9PL

²Department of Earth Sciences, The University of Manchester, Manchester M13 9PL

³CLRC Daresbury Laboratory, Warrington WA4 4AD

Abstract

The interaction of Tc species with microcrystalline iron minerals is important with respect to the environment. In reducing conditions, mackinawite (tetragonal FeS) is the first-formed sulphide and in this study we report the characterisation, by EXAFS spectroscopy, of the products of reactions of Tc(IV) and TcO_4^- with mackinawite.

Three Tc compounds (PPh_4TcO_4 , Tc_2S_7 and TcS_2) were synthesised and diluted with BN for use as models. Technetium coprecipitates with mackinawite were prepared from aqueous Fe(II) solution, containing Tc^{4+} or TcO_4^- as required, at controlled pH by the addition of Na_2S solution. Since the Tc speciation changes accompanying oxidation of the host FeS are also of interest, an oxidised sample was prepared by standing in air. The following three samples were prepared: a) FeS/ TcO_4^- coprecipitate; b) FeS/Tc(IV) coprecipitate; c) FeS/ TcO_4^- coprecipitate, oxidised.

All Tc samples were mounted in N_2 -filled, gas-tight, triple-contained cells. Technetium K edge X-ray absorption spectra were collected on Station 16.5 at the CLRC Daresbury Synchrotron Radiation Source. Data for all Tc samples were recorded in fluorescence mode, using a 30-element Ge detector. The spectra were calibrated and background subtracted using the Daresbury Laboratory programs EXCALIB and EXBACK, then analysed using the EXCURV97 program.

Table 1 shows the edge positions. For Tc(VII) and Tc(IV) compounds, the edges are at 21 027.9 eV and 21 035.0 eV respectively. The edge positions for the FeS samples show that Tc, initially present as TcO_4^- , is reduced to Tc(IV) on coprecipitation whereas Tc(IV) remains unchanged. When the host precipitate is oxidised, Tc remains in oxidation state IV.

The results of data fitting are summarised in Table 2. In the Tc-loaded samples, the co-ordination number of Tc in the FeS/ TcO_4^- sample is 6, as is found for TcS_2 , suggesting that Tc has been reduced to Tc(IV) and a TcS_2 -like phase has formed. The fit for the FeS/ TcO_4^- sample is not, however, improved significantly by using the three different S shells identified for TcS_2 and the distance (2.416 Å) is longer than the mean Tc-S distance in TcS_2 (2.279 Å), perhaps because the TcS_2 coprecipitate is poorly ordered. The FeS/Tc(IV) sample again shows Tc in 6 co-ordination, although here the best fit is given by two shells of S atoms. This suggests that a mixture of phases may have been formed and is

consistent with the rather high Debye-Waller factors for both shells. On oxidation of the host FeS lattice, the co-ordination environment of Tc changes, with complete replacement of the S first shell by six O atoms. The co-ordination number and Tc-O distances suggest formation of a TcO₂-like phase [1].

Table 1. X-ray absorption edge positions for Tc samples

Oxidation states for FeS samples are unknown and are denoted not applicable (n.a.)

Sample	Formal oxidation state	Edge position (eV)
PPh ₄ TcO ₄	+7	21027.9
Tc ₂ S ₇	+4	21027.9
TcS ₂	+4	21035.0
FeS/Tc(IV)	n.a.	21035.6
FeS/TcO ₄ ⁻	n.a.	21036.3
FeS/TcO ₄ ⁻ (oxidised)	n.a.	21035.8

Table 2. Results of EXAFS data fitting

Interatomic distances in Å, Debye-Waller factors ($2\sigma^2$) in Å². R-values are a measure of overall goodness of fit. Uncertainties in co-ordination numbers are ± 1 and in distances are ± 0.020 .

Sample	Shell	C.N., type	Distance	$2\sigma^2$	R
PPh ₄ TcO ₄	1	4 O	1.704	0.009	36.2
Tc ₂ S ₇	1	4 S	2.396	0.012	31.5
	2	2 Tc	2.769	0.014	
TcS ₂	1	2 S	2.080	0.019	33.4
	2	2 S	2.225	0.018	
	3	2 S	2.531	0.011	
TcO ₄ ⁻ /FeS	1	6 S	2.416	0.018	27.3
Tc(IV)/FeS	1	1 S	1.977	0.022	39.0
	2	5 S	2.491	0.023	
TcO ₄ ⁻ /FeS reoxidised	1	6 O	2.022	0.021	44.2

REFERENCES

- [1] Almahamid, *et al.*, *Inorg. Chem.*, 34 (1995) 193-198.

**XAFS STUDIES OF URANIUM(VI)-AMIDE
ORGANOPHOSPHOROUS COMPOUND COMPLEXES IN ETHANOL**

T. Yaita, S. Suzuki, H. Narita, S. Tachimori, K. Takai
Japan Atomic Energy Research Institute
Naka-gun, Ibaraki 319-1195, Japan

H. Motohashi
Spring-8 Service
Akoh-gun, Hyogo 678-12, Japan

K. Kobayashi
High Energy Accelerator Research Organisation
Oho, Tsukuba-shi, Ibaraki 305-0801, Japan

Abstract

The local structure of uranium(VI)-amide and TBP complexes in ethanol solution were determined by extended X-ray absorption fine structure spectrometry. The ligands used in this study were TBP, and the following amides: N,N-dihexyl-2-ethylhexanamide (DH2EHA), N,N-dihexyl-3-ethylhexanamide (DH3EHA), N,N-dihexyloctanamide (DHOA). Sample solutions were prepared by dissolution of uranyl nitrate into ethanol including these ligands. The bond distance between uranium and oxygen of DH2EHA is 2.31 Å, while, oxygen of DH3EHA and DHOA are 2.39 Å. Accordingly, DH2EHA, whose substituent branches out at closest position to carbonyl carbon of all the amides, interacts with uranyl ions more strongly than the others. The radial structural function of the TBP complex indicated that the structure above 3.0 Å region is flexible compared to amide complexes.

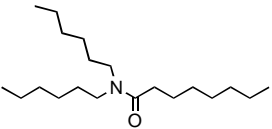
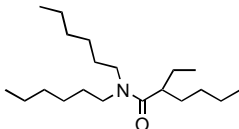
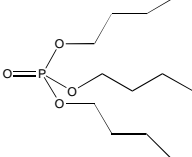
Introduction

Amide compounds have been regarded as a hopeful extractant for actinide and lanthanide ions and as a possible alternative to TBP by many researchers. Until now, many studies regarding extraction were reported [1-5]. Their extraction mechanisms, however, are not completely clarified by extraction studies alone. Structural studies often supplement an elucidation for the detailed extraction mechanism of ion, because structural parameters give us the noble information regarding the co-ordination properties and the steric effects. Especially, a complex structure in solution is important for the safety of the present reprocessing processes and the development of feature processes. In these purposes, the EXAFS method is very powerful for the determination of the local structure around metal in solution. Furthermore, recently synchrotron radiation as X-ray source has made it possible to measure a local structure of a trace amount of sample like radioactive materials, and contributed to nuclear science and industry [6-8]. In this study, we focus on the substituent effect of amide for uranium extraction. Especially, so as to clarify the difference in distribution behaviour of uranium extraction with several amides differing in their substituent, we measured the EXAFS spectra of uranium(VI)-amide complexes in ethanol solution, and also TBP complexes for comparison with those for the amides.

Ligand and experimental

The ligands used in this study were TBP, and the amides: N,N-dihexyl-2-ethylhexanamide (DH2EHA), N,N-dihexyl-3-ethylhexanamide (DH3EHA) and N,N-dihexyloctanamide (DHOA). These amides represented by the same compositional formula as $C_{20}H_{41}NO$ are shown Table 1. Their physical and chemical properties are very similar.

Table 1. Ligand formula in this study and comparison of distribution ratio ($*D_U$) of U(VI) from nitric acid solution

 <p>N,N-dihexyloctanamide (DHOA) $D_U = 10$</p>	 <p>N,N-dihexyl-2-ethylhexanamide (DH2EHA), $D_U = 1$</p>
 <p>N,N-dihexyl-3-ethylhexanamide (DH3EHA), $D_U = 11$</p>	 <p>Tributylphosphate (TBP) $D_U = 30$</p>

* These values were determined by the extraction with about 1 M ligand in dodecane from 6 M HNO_3 .

Sample solutions were prepared by dissolution of uranyl nitrate in ethanol including the ligands. We confirmed that the local structure for DH3EHA complex in this study agreed with that for the extraction complex of DH3EHA [6]. These samples were sealed in a polyethylene bag including a

1 mm Teflon spacer. The X-ray absorption spectra around the L_{III} edge (17.16 keV) of uranium were measured in transmission mode at the BL-27B station of KEK, Japan. Beam currents ranged from 270 to 370 mA. The obtained absorption spectra were analysed by the usual method [6]. In the fit to the EXAFS oscillations, we used the WinXAS97 program, and the phase shifts and backscattering factors calculated by the FEFF7 code [9].

Results and discussion

Figure 1 shows the radial structural function (RSF; the phase shift were not corrected.) of uranium-amide complexes calculated by the FEFF7 code. The adopted crystal data was Bis (N,N diethylformamide) dinitrato-dioxouranium(VI) [10]. In this RSF, the peaks were mainly attributed to A: axial uranyl oxygen (single scattering: SS), B: oxygen of phosphoryl group for TBP and carbonyl group (SS), C, D: oxygen and nitrogen of nitrate ion (SS), E: axial uranyl oxygen (multiple scattering: MS), F: U \rightarrow C (carbonyl) \rightarrow O (carbonyl) \rightarrow U (MS), and G: oxygen of nitrate ion (MS). Figure 2 shows the RSF of uranyl nitrate-amides and TBP complexes in ethanol, and uranyl nitrate salt in ethanol and uranyl nitrate in 6 M HNO_3 . The RSF's phase shifts associated with absorber-scatterer interactions were also not corrected (0.2~0.5 Å). These functions mainly consist of three big peaks at about 1.3~2.2 Å in all the samples, and furthermore three broad peaks above 2.6 Å region for amide complexes. In the comparison between TBP and amide complexes, we found significant differences in the structure above 2.6 Å. The amide complexes have three distinct peaks, but the TBP complex does not. Auwer, *et al.* [7] also reported the radial structural function and other XAS results of U-TBP complexes. It could be possible that increased Debye-Waller factors weakened their structures in the EXAFS signals. The TBP complex, therefore, seems to be flexible in the structure above 2.6 Å, compared to the amide complexes.

Figure 1. Theoretical radial structural function of $UO_2(NO_3)_2$ formamide complex calculated by FEFF7

The phase shifts were not corrected

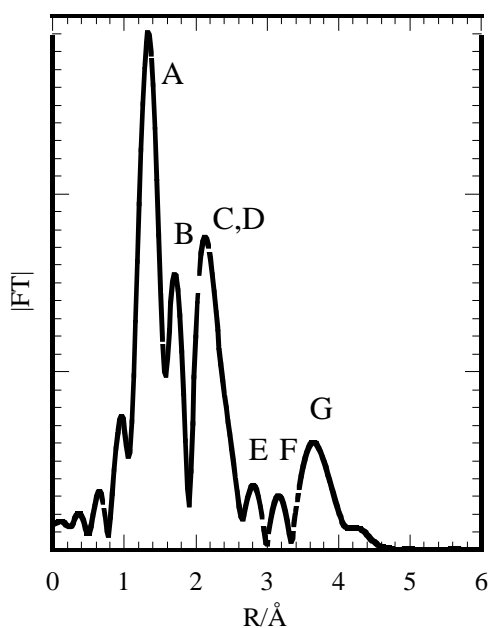


Figure 2. Radial structural functions of uranium complexes in EtOH and 6 M HNO₃ solutions.
1: TBP-U, 2: DH3EHA-U, 3: DH2EHA-U, 4: DHOA-U, 5: U in EtOH, 6: U in 6 M HNO₃

Samples 1~5 were dissolved into EtOH.

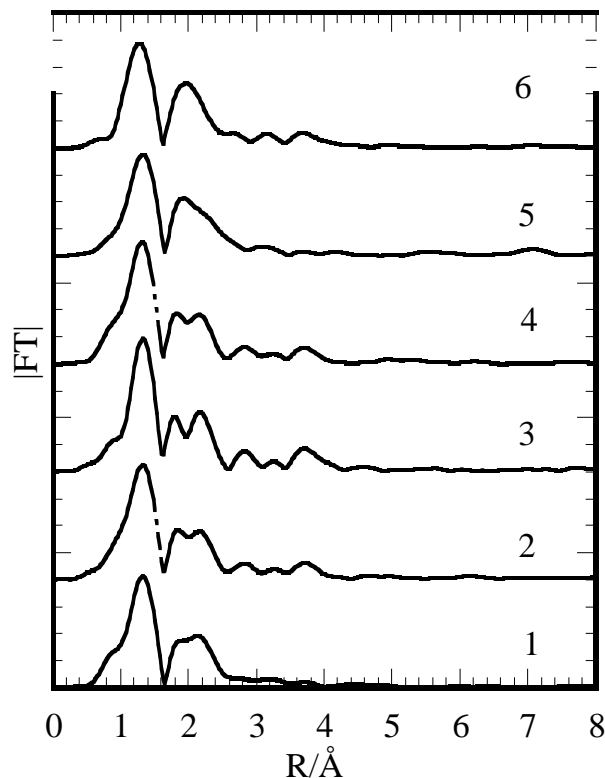


Figure 3 shows the raw k^3 -weighted EXAFS oscillations and the fitting results of single scattering contributions in the samples, demonstrating the fitting quality over k range. We confirmed the fitting qualities for each shell by fitting to the partial Fourier transform. The fitting results in the quantitative determination are listed in Table 2. The bond distance between uranium and axial oxygen are all 1.76 Å. The second peak positions of DH2EHA are 2.31 Å, and relatively short when compared to the other amides (2.39 Å). Unexpectedly, we observed that DH2EHA interacts with uranium more strongly than the other amides. In the solvent extraction of uranium(VI) [5] in Table 1, the distribution ratio of uranium for DH2EHA are one-tenth of those for DH3EHA and DHOA, and one-thirtieth of that for TBP. As mentioned previously, the DH2EHA has the substituent that branches out at the closest position to carbonyl carbon of the other amides, and therefore the substituent seems to cause steric hindrance. In this study, however, the branching for DH2EHA makes the donor ability of oxygen increase, rather than steric hindrance. The distance for TBP is approximately equal to that for DH3EHA, and DHOA (2.39 Å). The TBP complex has no significant structure beyond 2.6 Å, while amide complexes clearly show three peaks. These results suggested that the TBP complex has a high flexibility in the solvation region. Extractability of uranium should be discussed not only by co-ordination properties but also by solvation of the co-ordination complex. The U-O distance of the nitrate ion is 2.51~2.52 Å, and the nitrate ion locates at about 0.1 Å longer position than the ligands. This position agreed with lanthanide nitrate results [11]. Although there were no differences in U-O (nitrate ion) and U-N distances between the TBP and the amide complexes, oxygen of the nitrate ion for the TBP structure above 2.6 Å was also not observed.

Figure 3. EXAFS oscillations of uranium complexes in EtOH and 6 M HNO₃ solutions. 1: TBP-U, 2: DH3EHA-U, 3: DH2EHA-U, 4: DHOA-U, 5: U in EtOH, 6: U in 6 M HNO₃.

Samples 1-5 were dissolved into EtOH.

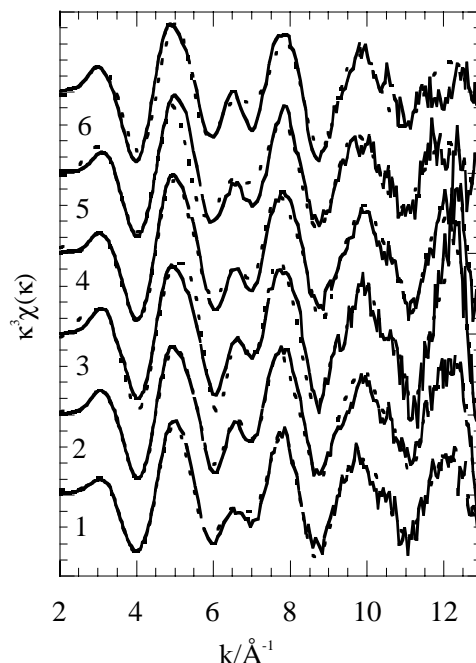


Table 2. EXFAS fitting results

	U-O _{AXIAL}	U-O _{LIGAND OR WATER}	U-O _{O₂NO}	U-N _{O₂NO}
DH2EHA**	R = 1.75 Å N = 2* $\sigma^2 = 0.0015$	R = 2.31 Å N = 2* $\sigma^2 = 0.003$	R = 2.51 Å N = 4* $\sigma^2 = 0.007$	R = 2.90 Å N = 2* $\sigma^2 = 0.009$
DH3EHA**	1.76 Å N = 2* $\sigma^2 = 0.0015$	R = 2.39 Å N = 2* $\sigma^2 = 0.003$	R = 2.51 Å N = 4* $\sigma^2 = 0.008$	R = 2.91 Å N = 2* $\sigma^2 = 0.009$
DHOA**	1.76 Å N = 2* $\sigma^2 = 0.0015$	R = 2.39 Å N = 2* $\sigma^2 = 0.003$	R = 2.52 Å N = 4* $\sigma^2 = 0.007$	R = 2.92 Å N = 2* $\sigma^2 = 0.01$
TBP**	1.77 Å N = 2* $\sigma^2 = 0.0015$	R = 2.39 Å N = 2* $\sigma^2 = 0.003$	R = 2.52 Å N = 4* $\sigma^2 = 0.008$	R = 2.91 Å N = 2* $\sigma^2 = 0.009$
EtOH***	1.76 Å N = 2* $\sigma^2 = 0.0015$	R = 2.40 Å N = 2* $\sigma^2 = 0.003$	R = 2.51 Å N = 4* $\sigma^2 = 0.009$	R = 2.91 Å N = 2* $\sigma^2 = 0.009$
6 M HNO ₃ ***	1.76 Å N = 2* $\sigma^2 = 0.0015$	R = 2.41 Å N = 2* $\sigma^2 = 0.003$	R = 2.52 Å N = 4* $\sigma^2 = 0.008$	R = 2.90 Å N = 2* $\sigma^2 = 0.009$

* Co-ordination number (N) held constant during the fit

** Ligand: uranyl nitrate-ligand-EtOH systems

*** EtOH: uranyl nitrate-ethanol; 6 M HNO₃: uranyl nitrate-6 M HNO₃ systems

Conclusion

The local structures of uranium-DH2EHA, DH3EHA, DHOA and TBP complexes in ethanol were determined by EXAFS. The bond distance of U-O (ligand) for DH2EHA is about 0.1 Å shorter than that for DH3EHA, DHOA and TBP, indicating that DH2EHA interacts with uranium more strongly than the others. This result does not correlate with the extractability of the uranium. The TBP complex would be flexible in the solvation region, and shows advantages for the solvation of the complex.

REFERENCES

- [1] T.H. Siddal III, *J. Phys. Chem.* 64,1863 (1960).
- [2] G.M. Gasparini and G. Grossi, *Sep. Sci. Technol.* 15 (4), 825 (1980).
- [3] C. Musikas, *CEA-CONF*, 10771 (1991).
- [4] N. Condamines and C. Musikas, *Sol. Extr. Ion Exch.*, 10 (1), 69 (1992).
- [5] S. Suzuki, K. Tamura, S. Tachimori, and Y. Usui, proceedings of the fall meeting of the AESJ, K24, pp. 606 (1996).
- [6] T. Yaita, H. Narita, S. Suzuki, S. Tachimori, H. Shiwaku, H. Motohashi, *J. Alloys. Compds.* 271-273, 184 (1998).
- [7] C.D. Auwer, C. Lexouteux, M.C. Charbonnel, C. Madic and R. Guillaumont, *Polyhedron* 16 (13), 2233 (1997).
- [8] P.G. Allen, J.J. Bucher, D.L. Clark, N.M. Edelstein, S.A. Ekberg, J.W. Gohdes, E.A. Hudson, N. Kaltsoyannis, W.W. Lukens, M.P. Neu, P.D. Palmer, T. Reich, D.K. Shuh, C.D. Tait and B.D. Zwick, *Inorg. Chem.* 34, 4797 (1995).
- [9] S.I. Zabinsky, J.J. Rehr, A. Ankudinov, R.C. Albers and M.J. Eller, *Phys. Rev. B.* 52, 2995 (1995).
- [10] J. Martin-Gil, F.J. Martin-Gil, A. Perales, J. Fayos and M. Martinez-Ripoll, *Acta C*39, 44 (1983).
- [11] T. Yaita, H. Narita, S. Suzuki, S. Tachimori, H. Shiwaku, H. Motohashi, *J. Radioanal. Nucl. Chem. Articles*, in press.

Annex 1
LIST OF PARTICIPANTS

FINLAND

KEKKI, Tommi
VTT Chemical Technology
P.O. Box 1404
02044 VTT, Espoo
Tel: +358 (0)9 456 6375
Fax: +358 (0)9 456 6390
Eml: tommi.kekki@vtt.fi

VUORINEN, Ulla S.
VTT Chemical Technology
P.O. Box 1404
02044 VTT, Espoo
Tel: +358 (0)9 456 6389
Fax: +358 (0)9 456 6390
Eml: ulla.vuorinen@vtt.fi

FRANCE

BACLET, Nathalie
CEA
Centre de Valduc
F-21120 Is Sur Tille
Tel: +33 (0)3 80 23 51 54
Fax:
Eml:

BEAUVY, Michel
CEA
CE Cadarache DRN/DEC
F-13108 St Paul-lez-Durance
Tel: +33 (0)4 42 25 72 72
Fax: +33 (0)4 42 25 76 76
Eml: beauvy@decade.cea.fr

BERKVENS, Paul
ESRF
Avenue des Martyrs
B.P. 220
F-38043 Grenoble Cedex
Tel: +33 (0)4 76 88 20 71
Fax: +33 (0)4 76 88 20 20
Eml: berkvens@esrf.fr

BILLARD, Isabelle
Institut de Recherches Subatomiques (IReS)
CHNU, Batiment 35
B.P. 28
F-67037 Strasbourg Cedex 2
Tel: +33 (0)3 88 10 10 64 01
Fax: +33 (0)3 88 10 10 64 31
Eml: isabell.billard@ires.in2p3.fr

BONHOURE, Isabelle
LURE Bâtiment 209D
Centre Universitaire Paris Sud
F-91405 Orsay Cedex
Tel: +33 (0)1 64 46 80 99
Fax: +33 (0)1 64 46 41 48
Eml: bonhoure@lure.u-psud.fr

BOULORE, Antoine
CEA Cadarache
SDC/LMC, Bât. 315
F-13108 St Paul-lez-Durance
Tel: +33 (0)4 42 25 44 15
Fax: +33 (0)4 42 25 29 49
Eml: boulore@come.cad.cea.fr

BOURDELOIE, Remi ESRF Avenue des Martyrs B.P. 220 F-38043 Grenoble Cedex	Tel: +33 (0)4 76 88 23 63 Fax: +33 (0)4 76 88 20 20 Eml: bourdeloie@esrf.fr
COLOMP, Patrick ESRF Avenue des Martyrs B.P. 220 F-38043 Grenoble Cedex	Tel: +33 (0)4 76 88 22 54 Fax: +33 (0)4 76 88 20 20 Eml:
DAVID, Francois H. Institut de Physique Nucléaire Université Paris XI F-91406 Orsay Cedex	Tel: +33 (0)1 69 15 73 48 Fax: +33 (0)1 69 15 64 70 Eml: david@ipno.in2p3.fr
DEN AUWER, Christophe CEA Marcoule DCC/DRRV/SEMP F-30207 Bagnols-sur-Cèze Cedex	Tel: +33 (0)4 66 79 65 89 Fax: +33 (0)4 66 79 65 31 Eml: denauwer@amandine.cea.fr
DESGRANGES, Lionel CEA CE Cadarache SDC/LEC Bat 316 F-13108 St. Paul-lez-Durance	Tel: +33 (0)4 42 25 31 59 Eml: desgrang@come.cad.cea.fr Fax: +33 (0)4 42 25 48 78
DURAUD, Jean-Paul Laboratoire Pierre Sue CEA-CNRS CE Saclay F-91191 Gif-sur-Yvette Cedex	Tel: +33 (0)1 69 08 48 65 Fax: +33 (0)1 69 08 69 23 Eml: + jpdurand@drecam.cea.fr
FABRE, Françoise LURE Bâtiment 209D Centre Universitaire Paris Sud F-91405 Orsay Cedex	Tel: +33 (0)16446 8225 Fax: +33 (0)16446 4102 Eml: fabre@lure.u-psud.fr
FAURE, Philippe CEA Centre de Valduc F-21120 Is sur Tille	Tel: +33 (0)3 80 23 44 73 Fax: +33 (0)3 80 23 52 82
FUNKE, Harald ROBL – CRG ESRF B.P. 220 F-38043 Grenoble Cedex	Tel: +33 (0)47688 2005 Fax: +33 (0)47688 2372 Eml: funke@esrf.fr
GOULON, Jose ESRF B.P. 220 Avenue des Martyrs F-38043 Grenoble Cedex	Tel: +33(0)4 76 88 20 21 Fax: +33(0)4 76 88 21 60 Eml: goulon@esrf.fr

HENNIG, Christoph ROBL – CRG ESRF B.P. 220 F-38043 Grenoble Cedex	Tel: +33 (0)4 76 88 23 39 Fax: +33 (0)4 76 88 25 05 Eml: hennig@esrf.fr
HUBERT, Solange Institut de Physique Nucleaire Université Paris XI F-91406 Orsay CEDEX	Tel: +33 (0)1 69 15 73 44 Fax: +33 (0)1 69 15 71 50 Eml: shubert@ipno.in2p3.fr
JACQUAMET, Lilian CEA – DRFMC/SP2M/NM 17 rue des Martyrs F-38054 Grenoble Cedex 9	Tel: +33 (0)4 76 88 95 09 Fax: +33 (0)4 76 88 50 90 Eml: jacquame@drfmc.ceng.cea.fr
KILVINGTON, Anthony Ian ESRF Avenue des Martyrs B.P. 220 F-38043 Grenoble Cedex	Tel: +33 (0)4 7688 2435 Fax: +33 (0)4 7688 2020 Eml: kilvington@esrf.fr
KUNZ, Christof ESRF Avenue des Martyrs B.P. 220 F-38043 Grenoble Cedex	Tel: +33 (0)4 76 88 25 08 Fax: +33 (0)4 76 88 21 60 Eml: ckunz@esrf.fr
LEQUIEN, Stephane ESRF Avenue des Martyrs B.P. 220 F-38043 Grenoble Cedex	Tel: +33(0)4 76 88 24 51 Fax: +33 (0)4 76 88 25 42 Eml: lequien@esrf.fr
LIDSTROM, Erik ESRF Avenue des Martyrs B.P. 220 F-38043 Grenoble Cedex	Tel: +33 (0)4 76 88 26 39 Fax: +33 (0)4 76 88 20 20 Eml: eli@esrf.fr
LUETZENKIRCHEN, Klaus IRES Chimie Nucléaires B.P. 28 F-67037 Strasbourg Cedex 2	Tel: +33 (0)3 88 10 64 04 Fax: +33 (0)3 88 10 64 31 Eml: klutz@in2p3.fr
MADIC, Charles CEA/VALRHO Direction du Cycle du Combustible DRDD/SEMP, B.P.171 F-30207 Bagnols-sur-Cèze Cedex	Tel: +33 (0)4 66 79 69 85 Fax: +33 (0)4 66 79 60 63 Eml: madic@amandin.cea.fr

MANCEAU, Alain Groupe de Géochimie de l'Environnement LGIT/IRIGM Université Josph Fourier BP 53 F-38041 Grenoble	Tel: +33 (0)4 76 82 80 15 Fax: +33 (0)4 76 82 81 01 Eml: manceau@ujf.grenoble.fr
MARTIN, Phillippe IPNL Universite Claude Bernard-Lyon 1 (UMR 5620 CNRS) F-69622 Villeurbanne Cedex	Tel: +33 (0)4 72 71 81 60 Fax: +33 (0)4 72 44 80 04 Eml: martinph@ipnl.in2p3.fr
MAZZANTI, Marinella CEA – DRFMC/SP2M/NM 17 rue des Martyrs F-38054 Grenoble Cedex 9	Tel: +33 (0)476 88 39 55 Fax: +33 (0)476 88 50 90 Eml: mazzanti@drfmc.ceng.cea.fr
PETIT, Thierry DEC/SECC, CEA/Grenoble 17 rue des Martyrs F-38054 Grenoble Cedex 9	Tel: +33 (0)4 76 88 32 43 Fax: +33 (0)4 76 88 51 51 Eml: petit@ntp.cea.fr
RAMBERT, Nicolas CEA Centre de Valduc F-21120 Is Sur Tille	Tel: +33 (0)3 80 23 45 80 Fax: +33 (0)3 80 23 52 82 Eml:
REICH, Tobias ROBL – CRG ESRF B.P. 220 F-38043 Grenoble Cedex	Tel: +33 (0)4 76 88 23 39 Fax: +33 (0)4 76 88 25 05 Eml: reich@esrf.fr
REVEL, Renaud LURE, Bâtiment 209D Centre Universitaire Paris Sud F-91405 Orsay Cedex	Tel: +33 (0)1 64 46 82 79 Fax: +33 (0)1 64 46 41 48 Eml: revel@lure.u-psud.fr
RIPERT, Michel CEA CE Cadarache SDC/LMC, Bât. 315 F-13108 St Paul-lez-Durance	Tel: +33 (0)4 42 25 28 08 Fax: +33 (0)4 42 25 29 49 Eml: ripert@come.cad.cea.fr
ROGALEV, Andrei ESRF B.P. 220 Avenue des Martyrs F-38043 Grenoble Cedex	Tel: +33(0)4 76 88 21 32 Fax: +33 (0)47688 2160 Eml: rogalev@esrf.fr
RUELLO, Pascal CEA CE Cadarache SDC/LMC Bat 315 F-13108 St. Paul-lez-Durance	Tel: +33 (0)4 42 25 31 59 Fax: +33 (0)4 42 25 48 78 Eml:

SEMON, Laurent
IRES Chimie Nucleaires
B.P. 28
F-67037 Strasbourg Cedex 2

Tel: +33 (0)3 88 10 64 00
Fax: +33 (0)3 88 10 64 31
Eml:

SIMONI, Eric
Institut de Physique Nucléaire
Université Paris XI
F-91406 Orsay Cedex

Tel: +33 (0)1 69 41 65 04
Fax: +33 (0)1 69 41 72 50
Eml: simoni@ipno.in2p3.fr

SITAUD, Bruno
CEA
Centre de Valduc
F-21120 Is Sur Tille

Tel: +33 (0)3 80 23 45 88
Fax: +33 (0)3 80 23 52 82
Eml:

GERMANY

BERNHARD, Gert
Forschungszentrum Rossendorf e. V.
Institute of Radiochemistry
P.O. Box 510 119
D-01314 Dresden

Tel: +49 (0)351 260 32 80
Fax: +49 (0)351 260 35 53
Eml: bernhard@fz-rossendorf.de

DENECKE, Melissa A.
Forschungszentrum Karlsruhe – INFP
Postfach 3640
D-76021 Karlsruhe

Tel: +49 (0)7247 82 5536
Fax: +49 (0)7247 82 3927
Eml: denecke@ine.fzk.de

FANGHAENEL, Thomas
Forschungszentrum Karlsruhe
Institut fuer Nukleare Entsorgungstechnik
Postfach 3640
D-76021 Karlsruhe

Tel: +49 (0)7247 825 485
Fax: +49 (0)7247 825 994
Eml: thomas@ine.fzk.de

JANKOWSKY, Ruediger
Forschungszentrum Rossendorf e. V.
Institut. of Bioinorganic & Radiopharma. Chem.
P.O. Box 510 119
D-01314 Dresden

Tel: +49 (0) 351 260 2439
Fax: +49 (0) 351 260 3232
Eml: jankow@fz-rossendorf.de

LANDER, Gerard H.
EITU
Postfach 2340
D-76125 Karlsruhe

Tel: +49 (0)724 9951 382
Fax: +49 (0)724 7951 599
Eml: lander@ill.fr

MANGOLD, Stefan
Department of Environmental Science & Tech.
Technical University Hamburg-Harburg
Eissendorfer Strasse 40
D-21073 Hamburg

Tel: +49 (0)40 7718 2864
Fax: +49 (0)40 7718 2315
Eml: mangold@tu-harburg.de

MATZ, Wolfgang
Forschungszentrum Rossendorf e. V.
Institute of Materials Research
P.O. Box 510 119
D-01314 Dresden

Tel: +49 (0)351 2603122
Fax: +49 (0)351 2603438
Eml: matz@fz-rossendorf.de

NITSCHKE, Heino
Forschungszentrum Rossendorf e. V.
Institute of Radiochemistry
P.O. Box 510 119
D-01314 Dresden
Tel: +49 (0)351 260 32 10
Fax: +49 (0)351 260 35 53
Eml: H.Nitsche@fz-rossendorf.de

PANAK, Petra
Forschungszentrum Rossendorf e. V.
Institute of Radiochemistry
P.O. Box 510 119
D-01314 Dresden
Tel: +49 (0)351 2602951
Fax: +49 (0)351 2603553
Eml: panak@fz-rossendorf.de

PELLEGRIN, Eric J.
Forschungszentrum Karlsruhe GmbH
ANKA Projekt Group (PEA)
Postfach 3640
D-76021 Karlsruhe
Tel: +49 (0)7247 82 6189
Fax: +49 (0)7247 82 6172
Eml: pellegrin@anka.fzk.de

POMPE, Susanne
Forschungszentrum Rossendorf e. V.
Institute of Radiochemistry
P.O. Box 510 119
D-01314 Dresden
Tel: +49 (0)351 260 2436
Fax: +49 (0)351 260 3553
Eml: s.pompe@fz-rossendorf.de

ROSSBERG, Andre
Forschungszentrum Rossendorf e. V.
Institute of Radiochemistry
P.O. Box 510 119
D-01314 Dresden
Tel:
Fax:
Eml:

SCHMEIDE, Katja
Forschungszentrum Rossendorf e. V.
Institute of Radiochemistry
P.O. Box 510 119
D-01314 Dresden
Tel: +49 (0)351 260 2436
Fax: +49 (0)351 260 3553
Eml: schmeide@@fz-rossendorf.de

TAUT, Steffen
Forschungszentrum Rossendorf e. V.
Institute of Radiochemistry
P.O. Box 510 119
D-01314 Dresden
Tel: +49 (0)351 260 2895
Fax: +49 (0)351 260 3553
Eml: s.taut@fz-rossendorf.de

WELTER, Edmund
Department of Environmental Science & Tech.
Technical University Hamburg-Harburg
Eissendorfer Strasse 40
D-21073 Hamburg
Tel: +49 (0)40 7718 2864
Fax: +49 (0)40 7718 2315
Eml: welter@tu-harburg.de

GREECE

MISAEALIDES, Panagiotis
Radiochemical Laboratory
Aristotle University
P.O. Box 1547
GR-54006 Thessaloniki
Tel: +30 31 99 77 89
Fax: +30 31 99 77 53
Eml: misailid@chem.auth.gr

HUNGARY

OSAN, Janos
KFKI Atomic Energy Research Institute
P.O. Box 49
H-1525 Budapest

Tel: +36 1 395 9164
Fax: +36 1 395 9042
Eml: osan@sunserv.kfki.hu

ITALY

FILIPPONI, Adriano
Dipartimento di Fisica
Universita dell' Aquila
Via Vetoio
I-67010 Coppito L' Aquila

Tel: +39 862433034
Fax: +39 862433033
Eml: adriano.filipponi@aquila.infn.it

JAPAN

AKABORI, Mitsuo
JAERI
Tokai-mura, Naka-gun
Ibaraki-ken 319-1195

Tel: +81 29282 5431
Fax: +81 29292 6097
Eml: akabori@popsvr.tokai.jaeri.go.jp

TACHIMORI, Shoichi
JAERI
Tokai-mura, Naka-gun
Ibaraki-ken 319-1195

Tel: +81 29282 5198
Fax: +81 29292 6723
Eml: tachi@mummy.tokai.jaeri.go.jp

YAITA, Tsuyoshi
JAERI
Tokai-mura, Naka-gun
Ibaraki 319-1195

Tel: +81 (0)29 282 6162
Fax: +81 (0)29 282 6723
Eml: yaita@mummy.tokai.jaeri.go.jp

THE NETHERLANDS

KONINGSBERGER, D.C.
Department of Inorganic Chemistry
Utrecht University, Debye Institute
Sorbonnelaan 16
P.O. Box 80083
NL-3505 TB Utrecht

Tel: +30 31 253 74 00
Fax: +31 30 251 10 27
Eml: d.c.koningsberger@chem.uu.nl

NORWAY

GROPEN, Odd
Department of Chemistry
Faculty of Natural Sciences
University of Tromso
N-9037 Tromso

Tel: +47 (0)77644082
Fax: +47 (0)77644765
Eml: oddg@chem.uit.no

PORTUGAL

GASCHE, Teresa A.
Departamento de Quimica
Instituto Tecnologica e Nuclear
Estrada Nacional 10
P-2686 Sacavem Codex

Tel: +351 1 9550021 /1349
Fax: +351 1 9941455
Eml: teresag@itn1.itn.pt

PAIVA, Isabel
DPSR
DGA
Estrada Nacional 10
P-2686 Sacavem Codex

Tel: +351 1 955 0021
Fax: +351 1 994 1995
Eml: dpsr@dga.min-amb.pt

RUSSIAN FEDERATION

GRIGORIEV, Timofei V.
Department of Radiochemistry
St. Petersburg University
University nab 7/9
Saint Petersburg, 199034

Tel: +7 (0)812 218 2835
Fax: +7 (0)812 218 2835
Eml: test@sensor.chem.lgu.spb.su

LEBEDEV, Alexandre
Russian Research Center
Kurchatov Institute
Kurchatov sq.1
123182 Moscow

Tel:
Fax: +7 (0)95 882 5804
Eml: orlov@mbslab.kiae.ru

NEFEDOV, Vadim
Institute of Gen. Inorg. Chemistry RAS
Leninski pr 31
117 907 Moscow

Tel: +7 (0)95 9542230
Fax: +7 (0)95 9541279
Eml: isn@rikky.msk.su

TETERIN, Anton
Russian Research Center
Kurchatov Institute
Kurchatov sq.1
123182 Moscow

Tel:
Fax: +7 (0)95 882 5804
Eml: orlov@mbslab.kiae.ru

SWEDEN

GRENTHE, Ingmar R.
Department of Chemistry (Inorg. Chemistry)
The Royal Institute of Technology
Teknikringen 30
S-10044 Stockholm

Tel: +46 (0)8 7908144
Fax: +46 (0)8 212626
Eml: ingmarg@inorg.kth.se

MOLL, Henry
Department of Chemistry (Inorg. Chemistry)
The Royal Institute of Technology
Teknikringen 30
S-10044 Stockholm

Tel: +46 (0)8 7908293
Fax: +46 (0)8 212626
Eml: henrym@inorchem.kth.se

WAHLGREN, Ulf
Fysikum
Stockholm University
Box 6730
S-113 85 Stockholm

Tel:
Fax:
Eml: uw@physto.SE

SWITZERLAND

DAEHN, Rainer
Waste Management Laboratory
CH-5232 Villigen PSI

Tel: +41 56 310 4451
Fax: +41 56 310 4438
Eml: rainer.daehn@psi.ch

HADERMANN, Joerg
Paul Scherrer Institut
CH-5232 Villigen PSI

Tel: +41 (0)56 310 2415
Fax: +41 (0)56 310 2821
Eml: hadermann@psi.ch

JOLIE, Jan
Physics Institute
University of Fribourg
Perolles
CH-1700 Fribourg

Tel: +41 37 29 9079
Fax: +41 37 29 9747
Eml: jan.jolie@unifr.ch

SCHEIDEGGER, André M.
Waste Management Laboratory PSI
OHLB/411
CH-5232 Villigen

Tel: +41 56 310 21 84
Fax: +41 56 310 44 38
Eml: andre.Scheidegger@psi.ch

UNITED KINGDOM

BUTLER, Richard J.
Department of Chemistry
The University of Manchester
Oxford Road
Manchester M13 9PL

Tel: +44 (0)161 275 4647
Fax: +44 (0)161 275 4598
Eml: richard.j.butler@stud.man.ac.uk

IVESON, Peter B.
University of Reading
Department of Chemistry
Whiteknights
Reading RG6 2AD

Tel:
Fax: +44 (0)118 931 6529
Eml: p.b.iveson@reading.ac.uk

LIVENS, Francis R.
Department of Chemistry
The University of Manchester
Oxford Road
Manchester M13 9PL

Tel: +44 (0)161 275 4647
Fax: +44 (0)161 275 4598
Eml: francis.livens@man.ac.uk

MAY, Iain
BNFL Sellafield
B319.1
Seascale CA20 1PG

Tel: +44 (0)1 9467 74747
Fax: +44 (0)1 9467 75698
Eml:

REED, Wendy A.
Department of Chemistry
The University of Manchester
Oxford Road
Manchester M13 9PL

Tel: +44 (0)161 275 4647
Fax: +44 (0)161 275 4598
Eml: w.a.reed@stud.man.ac.uk

SWANTON, Stephen W.
AEA Technology
220.32 Harwell
Didcot, Oxfordshire
OX11 0RA

Tel: +44 235 434368
Fax: +44 235 432278
Eml: steve.swanton@aeat.co.uk

DENT, Andrew
CLRC Daresbury Laboratory
Daresbury
Warrington
Cheshire WA4 4AD

Tel: +44 (0)1925 603629
Fax: +44 (0)1925 603124
Eml: A.J.Dent@dl.ac.uk

UNITED STATES OF AMERICA

ALLEN, Patrick G.
Lawrence Livermore Laboratory
Seaborg Institute of Transactinium Science
MS L-231, P.O. BOX 808
Livermore CA 94551-9900

Tel: +1 925 423 8955
Fax: +1 925 422 3160
Eml: allen42@llnl.gov

BERTSCH, Paul M.
AACES
University of Georgia
SREL, Drawer E
Aiken, SC 29802

Tel: +1 803 725 56 37
Fax: +1 803 725 00 77
Eml: bertsch@srel.edu

CLARK, David L.
Seaborg Institute
Los Alamos National Laboratory
NMT-DO, MS E500
Los Alamos, NM 87545

Tel: +1 505 665 6690
Fax: +1 505 667 7966
Eml: dlclark@lanl.gov

EDELSTEIN, Norman M.
Lawrence Berkeley Nat. Lab.
Chemical Sciences Division
MS 70A-1150
Berkeley CA 94720

Tel:
Fax: +1 510 486 5596
Eml: NMEdelstein@lbl.gov

EVANS, Ian
Stanford Synchrotron Rad. Laboratory
P.O. Box 4349, MS 99
Stanford CA 94309-0210

Tel: +1 650 926 3110
Fax: +1 650 926 3600
Eml: evans@slac.stanford.edu

KEOGH, D. Webster
Los Alamos National Laboratory
MS G739
Los Alamos, NM 87545

Tel: +1 505 665 4622
Fax: +1 505 665 4624
Eml: wkeogh@lanl.gov

PAVIET-HARTMANN, Patricia
Los Alamos National Laboratory
CST-7, MS J514
Los Alamos, NM 87545

Tel: +1 505 667 5711
Fax: +1 505 665 4955
Eml: ppaviet-hartmann@lanl.gov

RUSSELL, Mark L.
University of Reading
Department of Chemistry
Whiteknights
Reading RG6 2AD

Tel: +44 (0)118 931 6717
Fax: +44 (0)118 931 6529
Eml: m.l.russell@reading.ac.uk

SHUH, David K.
LBNL
MS 70A-1150
1 Cyclotron Road
Berkeley CA 94720

Tel: +1 510 486 6937
Fax: +1 510 486 5596
Eml: dkshuh@lbl.gov

SODERHOLM, Lynda
Argonne National Laboratory
CHM/200
Argonne IL 60439

Tel: +1 630 252 43 64
Fax: +1 630 252 9289
Eml: ls@anl.gov

VEIRS, Kirk D.
Los Alamos National Laboratory
MS E 510
Los Alamos NM 87545

Tel: +1 505 667 5385
Fax: +1 505 665 4459
Eml: veirs@lanl.gov

HAIRE, Richard
Oak Ridge National Laboratory
P.O. Box 7008
MS 6375
Oak Ridge, TN 37831-6375

Tel: +1 423 574 5007
Fax: +1 423 574 4987
Eml: hairerg@ornl.gov

INTERNATIONAL ORGANISATIONS

NORDBORG, Claes
OECD/NEA, Nuclear Science Division
Le Seine St.-Germain
12, Bd. des Iles
F-92130 Issy-les-Moulineaux

Tel: +33 (0)1 4524 1009
Fax: +33 (0)1 4524 1106
Eml: nordborg@oecd.org

SAKURAI, Satoshi
OECD/NEA, Nuclear Science Division
Le Seine St.-Germain
12, Bd. des Iles
F-92130 Issy-les-Moulineaux

Tel: +33 (0)1 45 24 11 10
Fax: +33 (0)1 45 24 11 52
Eml: sakurai@nea.fr

SAVELLI, Philippe
OECD/NEA, Nuclear Science Division
Le Seine St.-Germain
12, Bd. des Iles
F-92130 Issy-les-Moulineaux

Tel: +33 (0)1 45 24 10 06
Fax: +33 (0)1 45 24 11 06
Eml: savelli@oecd.org

Annex 2
ORGANISING COMMITTEE

Dr. T. Reich (FZR, Germany)

Dr. H. Nitsche (LBL, USA)

Dr. H.M. Edelstein (LBL, USA)

Dr. C. Madic (CEA, France)

Dr. C. Kunz (ESRF, France)

Mr. S. Sakurai (OECD/NEA, France)

